Università degli Studi di Cagliari

DOTTORATO DI RICERCA

Scienze e Tecnologie Fisiche

Curriculum: Fisica Nucleare, Subnucleare e Astrofisica

XXIV Ciclo

Intracluster magnetic fields

Settore scientifico disciplinare di afferenza

Area 02 - FIS/05

Presentata da: Valentina Vacca
Coordinatore Dottorato: Prof. G. Usai
Tutor: Prof. L. Burderi
Relatori: Dr. F. Govoni, Dr. M. Murgia

Esame finale Anno Accademico 2010 - 2011

THIS THESIS HAS BEEN DONE IN THE CONTEXT OF THE SCIENTIFIC RESEARCH ACTIVITY OF THE “OSSERVATORIO ASTRONOMICO DI CAGLIARI - ISTITUTO NAZIONALE DI ASTROFISICA”

Abstract

Magnetic fields are ubiquitous in the Universe. They have been detected in planets, stars, galaxies, groups and clusters of galaxies, and recently also along filaments, in the large scale structure of the Universe.

The aim of this PhD thesis is to study magnetic fields in clusters of galaxies in different evolutionary stages. The presence of magnetic fields in the intracluster medium is clearly indicated by the discovery of diffuse synchrotron emission in the central region and in the outskirts of a larger and larger number of galaxy clusters. These sources, called radio halos and relics, are generated by high energy relativistic electrons moving along the flux lines of weak magnetic fields. These magnetic fields are deeply linked to the dynamical state and the energy transport in the system, and the study of their power spectrum gives information about the energy, the capacity to diffuse, and the ordered motion in the plasma of the relativistic particles.

The origin of intracluster magnetic fields is still debated. The most reliable theories suppose a cosmological or a galactic (at z≃2-3) origin. In both cases, to match the strengths presently observed, an amplification of the field is required, probably due to cluster formation processes. From the present day observations, intracluster magnetic fields appear to fluctuate over a range of scales and their strength seems to decrease with the distance from the cluster center as a function of the thermal gas density. Merging clusters show low magnetic field central strengths ($\sim 1\,\mu$G), while relaxed systems are characterized by higher values (up to some $10\,\mu$G).

In the radio band, the investigation of the intracluster magnetic field power spectrum can be performed by means of two techniques. Large scale ($\sim$ Mpc) studies can be carried out through the analysis of the emission of large-scale diffuse synchrotron sources. Higher resolution investigations ($\sim$ kpc) are allowed by the analysis of the Faraday rotation of the signal coming from galaxies within or behind galaxy clusters. The coexistence in a galaxy cluster of small and large scales of fluctuation of the magnetic field requires a combination of the two approaches. In fact, in this way, it is possible to follow with continuity the power spectrum of the magnetic field fluctuations from Mpc scales down to kpc scales. Up to now, a detailed study of the magnetic field power spectrum has been performed just in few galaxy clusters.

In this work we present the results we obtained by applying these different approaches and their contribution to the present day knowledge of intracluster magnetic fields.

To perform this kind of studies, we analyzed *Very Large Array* (VLA, New Mexico, USA) multi-frequency polarimetric data of diffuse radio halos and of discrete sources within or behind galaxy clusters. To constrain the magnetic field fluctuation power spectrum, we compared the observations with the expectations of two- and three-dimensional simulations obtained with the FARADAY software package.

The structure of this manuscript is the following. Three main sections can be identified:

- in **Chapter 1** we introduce clusters of galaxies, with particular care to radio emission originating from galaxies and diffuse synchrotron sources (radio halos, relics and mini-halos);
- in **Chapters 2** and **3** we present the contribution of this thesis to the still scanty radio halo

statistics and to the study of radio halo properties. We describe the discovery of six new radio halos and the investigation of the X-ray -radio correlation in systems hosting radio halos both on an individual and on a statistical point of view;

- in **Chapter 4** we give an overview about intracluster magnetic fields and the main techniques applied for their investigation and we present statistical studies based on the Faraday rotation effect on the polarimetric properties of radio galaxies. The modeling we adopt and its application to the detailed investigation of the magnetic field in two galaxy clusters are described in **Chapters 5**, **6**, and **7**.

Finally in **Chapter 8** we summarize our conclusions.

Throughout this thesis we adopt a ΛCDM cosmology with $H_0 = 71\,\mathrm{km\ s^{-1}\ Mpc^{-1}}$, $\Omega_\mathrm{m} = 0.27$, and $\Omega_\Lambda = 0.73$.

Contents

1 Clusters of galaxies

Cluster of galaxies are the largest gravitationally bound systems in the Universe: they cover linear sizes of some Mpc[1] and are characterized by masses of about $10^{15} M_{\odot}$. According to the hierarchical model of structure formation, they originate from the gravitational merger of smaller sub-units. In Fig. 1.1 an example of this kind of systems is presented. In blue the optical emission from the cluster galaxies is shown. Their number ranges between few tens and thousands, but they account just for 3-5% of cluster total mass. They move at speeds of about 1000 km s^{-1}, too large to preserve the gravitational pull due to their mutual attraction.

In order to account for the observed dispersion of the cluster galaxy velocities and hence redshifts[2], not explainable just considering the galaxy mutual attraction, Zwicky (1937) suggested for the first time the presence of dark matter in galaxy clusters. The nature and characteristics of dark matter are not yet well understood. The structures observed in the Universe can be explained in the context of cold dark matter (CDM) scenario that supposes dark matter to be cold and collisionless. Nevertheless, present observations indicate that the existence of warm dark matter (WDM) particles at the beginning of the early Universe cannot be completely excluded (see Markovic et al. 2011, and references therein). A powerful instrument to study dark matter distribution is the gravitational lensing distortion that cluster total mass produces in the images of background galaxies (e.g. Bartelmann & Schneider 2001). The other fundamental contribution to the total mass of the cluster is given by the intracluster medium (ICM) that fills the space between the galaxies (Kellogg et al. 1972; Forman et al. 1972). It is characterized by low densities ($n_e \simeq 0.01 - 0.001\,\mathrm{cm}^{-3}$) and high temperatures ($T \simeq 10^7$–10^8 K) whose combination causes its emission in the X-ray band (red color in Fig. 1.1), predominantly through thermal bremsstrahlung, with luminosities $L_X \simeq 10^{43} - 10^{45}\,\mathrm{erg\,s}^{-1}$. Overall, dark matter and ICM account respectively for 80% and 15-17% of the total mass of the cluster.

Galaxy clusters have been observed also in the radio band (green contours in Fig. 1.1) because of the emission of their galaxies (see § 1.3). In addition, in some cases, diffuse synchrotron radio sources (see § 1.4) with no obvious optical counterpart have been detected (e.g. Feretti & Giovannini 2008; Ferrari et al. 2008). They are called halos, relics, or mini-halos according to their morphology and location (e.g. Kempner et al. 2004; Feretti et al. 2004a). Their emission is not

[1] 1 pc= $3.09 \cdot 10^{18}$cm.

[2] For a source moving away from the observer at velocity $v \ll c$, the redshift is given by $z \approx \frac{v}{c}$.

related to the galaxies but to the ICM and their origin is still debated. They are a direct proof of the presence in the intracluster medium of a weak magnetic field and a population of relativistic electrons. An example of a powerful and extended radio halo is shown in Fig. 1.1.

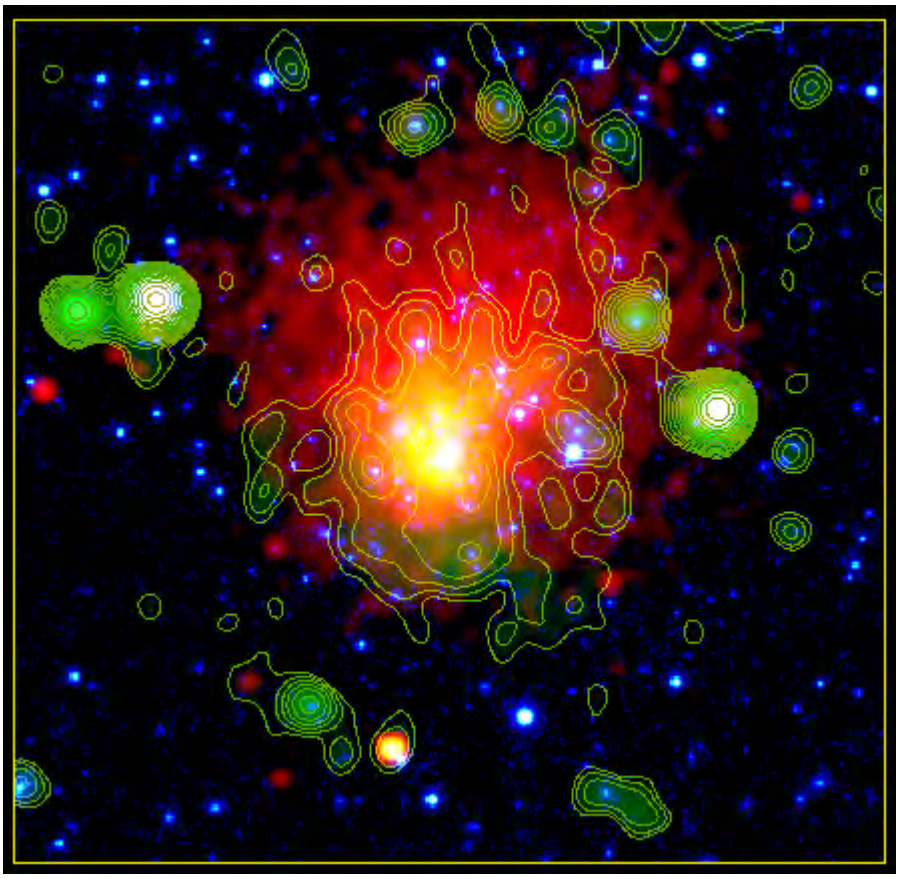

Figure 1.1 Superposition of the optical (blue), X-ray (red), and radio (green) emission from the galaxy cluster Abell 665 (Vacca et al. 2010, and references therein). This galaxy cluster hosts an extended and diffuse radio halo at its center. The optical emission comes from the galaxies, while the thermal gas in between emits in the X-ray band. The low brightness central source is the radio halo, while the bright sources are powerful radio galaxies. The image has a field of view of $2\times2\,\mathrm{Mpc}^2$.

1.1 Dynamical state

Galaxy clusters are characterized by different evolutionary stages: they merge to produce larger systems and then relax in few Gyrs. Frames from this time-sequence are presented in Fig. 1.2, where the X-ray emission of two clusters before the collision (*left panel*), a merging cluster (*central panel*), and a relaxed cluster (*right panel*) are shown.

1.1.1 Merging clusters

According to the hierarchical scenario of structure formation (e.g. Navarro et al. 1996), massive galaxy clusters form through the merger of galaxy groups and sub-clusters, and the continuous

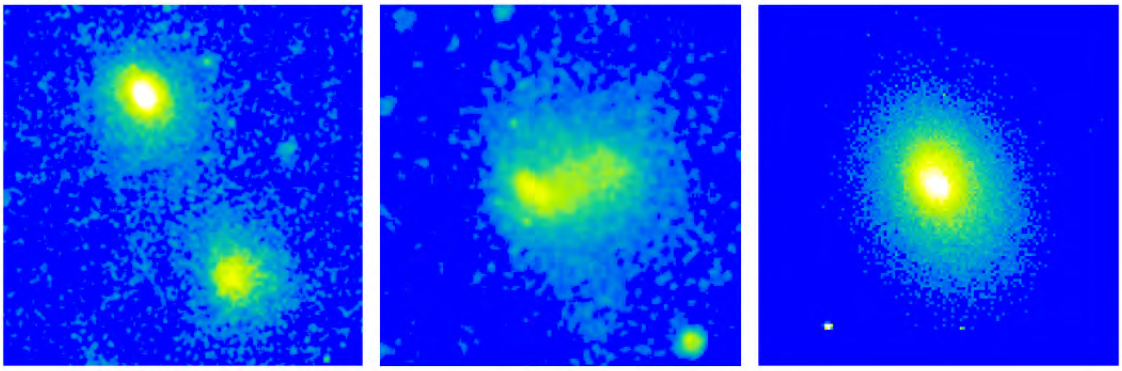

Figure 1.2 X-ray images of galaxy clusters in different evolutionary stages. *Left panel*: Abell 399 and Abell 401 are two approaching systems close to merge. *Middle panel*: Abell 754 is a cluster in the central phases of a merger event. *Right panel*: Abell 2029 is a relaxed cluster. Image taken from Markevitch & Vikhlinin (2007).

accretion of field galaxies. Merger events are the most energetic phenomena in the Universe since the Big Bang, involving gravitational energies up to 10^{64} erg (Sarazin 2002). A relevant amount of this gravitational energy is dissipated in the ICM in some Gyr, through turbulence, shocks, bulk motion that heat the thermal gas.

Mergers deeply affect the physical properties of clusters, generating typical signatures that can be detected by means of X-ray, optical, and radio observations, as for example shocks and cold fronts (Markevitch et al. 2000; Buote 2002; Kolokotronis et al. 2001, and references therein). Shocks are originated by the infalling subclusters and identified by discontinuities in the X-ray image. They are characterized by an abrupt change in pressure, temperature, and density, with a higher temperature in correspondence of the denser parts of the medium. Cold fronts (see also § 4.2.4) are supposed to be originated during the collision between two subclusters when one of the two cores is disturbed but not disrupted by the merger. In fact, they appear as sharp X-ray surface brightness discontinuities between the gas from the cluster core that survived the merger and the less dense, hotter, and shocked gas from the surrounding environment. The pressure is continuous across this kind of discontinuities, while the temperature and the entropy[3] are lower inside the edge, exactly the contrary than in a shock (Markevitch & Vikhlinin 2007).
The dissipation in the thermal plasma of the energy released during the merger originates spatial variations in ICM temperature, pressure, entropy, and metallicity images (e.g. Kapferer et al. 2006). Hints of an ongoing merger are also a non-Gaussian radial velocity distribution of cluster galaxies, as well as variations in their spatial distribution, dynamics and star-formation rate (Girardi & Biviano 2002, and references therein). In addition, shocks and the turbulence associated with a major cluster merger event are thought to compress magnetic field in the ICM and to accelerate the relativistic particle population coexisting with the thermal one (e.g. Roettiger et al. 1999b; Brunetti & Lazarian 2007; Skillman et al. 2008, 2011; Vazza et al. 2011).

1.1.2 Relaxed clusters

The passage of shocks causes a heating and an adiabatic expansion of the gas until a pressure imbalance is reached. Then, in the pretty ideal case that other merger events do not occur in the

[3] $S \equiv T n_e^{-2/3}$.

meanwhile, the cluster starts to relax getting in a completely relaxed state in few Gyr. Relaxed clusters are characterized by highly symmetrical and smooth X-ray surface brightness distribution with a central peak. Since the X-ray surface brightness scales as n_e^2, this implies high central densities and, consequently, a cooling time due to the bremsstrahlung emission calculated within an inner radius $\simeq$100 kpc

$$t \sim 5 \times 10^3 \frac{T^{0.5}(K)}{n_e(\mathrm{cm}^{-3})} \mathrm{yr} \simeq 10\,\mathrm{Gyr} \tag{1.1}$$

that is less than the actual Hubble time (H_0^{-1} ~13 Gyr). The higher density of the central regions with respect to the outskirts causes the first to cool faster than the second. This should imply a huge inward gas flux to preserve the hydrostatic equilibrium. The balance between the thermal energy emitted and the work done by the external gas layers on the internal ones causes an expected mass deposition rate (see Fabian 1994, and references therein)

$$\dot{M} = \frac{2\mu m_p}{5kT} L_{\mathrm{cool}} \tag{1.2}$$

where μ is the the average molecular mass, m_p is the proton mass, k is the Boltzmann constant, and L_{cool} is the X-ray luminosity within the cooling radius[4] r_{cool}. Typical $L_{\mathrm{cool}} \sim 10^{42} - 10^{44}$ erg s^{-1} corresponds to a mass deposition rate $\dot{M} \sim 50 - 100 M_\odot$ yr^{-1}, but values up to $\dot{M} \sim 500 M_\odot$ yr^{-1} have been observed.

Actually, the classical cooling flow model is not confirmed by observations. In fact, the inward gas flux necessary to preserve the hydrostatic equilibrium would be responsible of even more higher central densities and shorter cooling times, ideally leading to the collapse of the cluster (cooling catastrophe). Since this collapse has never been observed and cool core clusters appear characterized by higher temperatures than predicted by this model, it has been supposed that some heating mechanism prevents the ICM from cooling (e.g. Tucker & Rosner 1983; Gaetz 1989; David et al. 2000). Its nature is still debated. One of the most reliable hypothesis is the heating due to active galactic nuclei (AGNs) activity. In more than 70% of cooling core clusters the central galaxy is a radio-loud source (Burns 1990). Sometimes, these radio sources have been revealed to strongly interact with the intracluster gas with the injection of mechanical energy (see § 1.3.1). The comparison of this energy with the X-ray luminosity of the cooling core shows that the radio power could be enough to balance the cooling flow, even if this mechanism alone cannot furnish a general solution of this problem (e.g. Bîrzan et al. 2004).

1.2 The intracluster medium

The intracluster medium accounts for 15-17% of the total mass of the cluster. It is characterized by densities of about 10^{-2}–10^{-3} cm^{-3} in the central regions that decrease to 10^{-4} cm^{-3} in the outskirts. This gas is mainly composed by hydrogen and helium, but also traces of heavier elements have been detected. These elements are kept in an ionized state because of the extremely high temperatures, ranging between 10^7 and 10^8 K (1-10 keV). In fact, a big fraction of the gravitational energy released during cluster formation is converted into thermal energy by shocks, turbulence and bulk motions that heat the intracluster medium. The combination of low density and of high temperature makes these particles to emit in the X-ray band through the bremsstrahlung mechanism.

[4]The cooling radius r_{cool} is the distance from the cluster center that corresponds to a cooling time shorter than the age of the system, supposed to be about equal to the Hubble time.

In the hypothesis that the gas is isothermal and in hydrostatic equilibrium, its distribution can be described by means of the β-model (Cavaliere & Fusco-Femiano 1976):

$$n_e(r) = n_0 \left[1 + \left(\frac{r}{r_c}\right)^2\right]^{-\frac{3}{2}\beta}. \tag{1.3}$$

Here, r is the distance from the cluster X-ray center, r_c is the cluster core radius that identifies the linear size of the central part of the cluster, n_0 is the central thermal gas density, β is the ratio between the specific galaxy and gas kinetic energy:

$$\beta = \frac{\sigma^2 \mu m_p}{kT} \tag{1.4}$$

where σ is the galaxy velocity dispersion, assumed to be isotropic. An average typical value for β is 0.7 (Jones & Forman 1984). As Sarazin & Bahcall (1977) showed, the X-ray brightness distribution corresponding to this thermal gas distribution is:

$$S_X(r) = S_0 \left[1 + \left(\frac{r}{r_c}\right)^2\right]^{-3\beta+\frac{1}{2}} \tag{1.5}$$

where S_0 is the central X-ray brightness.

In Fig. 1.3 an example of the X-ray brightness profile fit based on a single β-model is shown for the merging galaxy cluster A520 (*top right panel*). In the *bottom right panel* a similar fit is reported for the cooling core galaxy cluster RX J1347.5-1145 (dashed line), a nearly relaxed system whose central region is not significantly affected by a minor merger (see Ferrari et al. 2011, and references therein). This thermal gas model does not allow a good description of the data when a central density excess is present, as in cooling core clusters. In this case a better result (see Fig. 1.3, *bottom right panel*, continuous line) is obtained when one empirically attempts to represent the thermal gas density profile with a double β-model profile (e.g. Mohr et al. 1999):

$$n_e(r) = n_{0\mathrm{int}} \left[1 + \left(\frac{r}{r_{\mathrm{cint}}}\right)^2\right]^{-\frac{3}{2}\beta_{\mathrm{int}}} + n_{0\mathrm{ext}} \left[1 + \left(\frac{r}{r_{\mathrm{cext}}}\right)^2\right]^{-\frac{3}{2}\beta_{\mathrm{ext}}} \tag{1.6}$$

where r_{cint} and r_{cext} are the internal and external cluster core radii, while $n_{0\mathrm{int}}$ and $n_{0\mathrm{ext}}$ are the internal and external central gas densities, respectively. The total central density is $n_0 = n_{0\mathrm{int}} + n_{0\mathrm{ext}}$.

Actually, merging clusters are nor in equilibrium neither isothermal. Indeed, during cluster merger events a significant amount of energy is injected on large scales in the intracluster medium and then turbulently cascades. This turbulence accounts for at least the 10% of the total pressure in the intracluster medium (Schuecker et al. 2004). Moreover, off-center merger are responsible of bulk motions of massive and dense gas clouds with velocities $\gtrsim 1000\,\mathrm{km/s}$ that affect the equilibrium of the cluster. The magnetic pressure can be important as well, if magnetic strength are high enough ($B \simeq 50 - 100\,\sqrt{h}\,\mu\mathrm{G}$, e.g. Felten 1996, and references therein). By using magneto hydrodynamic simulations, for a random magnetic field tangled on small scales and with initial strengths able to reproduce the present rotation measure observations, Dolag et al. (2001a) find a magnetic to thermal pressure ratio

$$\frac{p_B}{p_{\mathrm{th}}} = 2.5\% \left(\frac{|B|}{3\,\mu\mathrm{G}}\right)^2 \left(\frac{n_e}{10^{-3}\,\mathrm{cm}^{-3}}\right)^{-1} \left(\frac{T}{10^8\,\mathrm{K}}\right)^{-1} \tag{1.7}$$

of about 5%. Therefore, the simple assumption of an isothermal gas is not correct. Nevertheless, as shown in Fig. 1.3, the β-model profile gives a simple and working representation of the thermal gas density distribution in clusters of galaxies and for this reason it is still widely used from several authors.

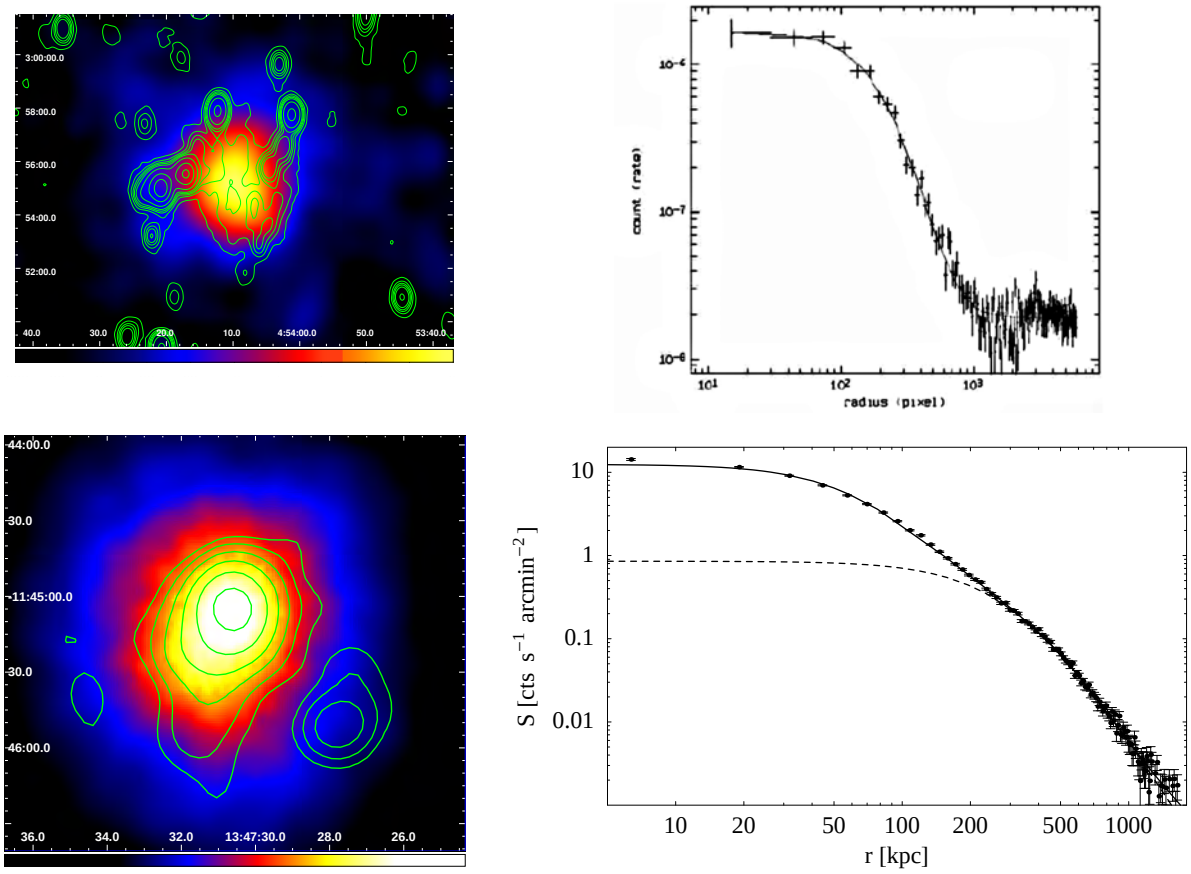

Figure 1.3 *Top panels*: on the left the superposition of the radio (contours) and the X-ray (colors) emission in the merging galaxy cluster A520 and on the right the fit of its X-ray brightness radial profile with a single β-model are shown (Govoni et al. 2001b). *Bottom panels*: on the left the superposition of the radio (contours) and the X-ray (colors) emission in the nearly relaxed galaxy cluster RX J1347.5-1145. On the right the fit of its X-ray brightness radial profile with a single (dashed line) and a double (continuous line) β-model are shown (Gitti et al. 2007a,b).

1.3 Non-thermal continuum radio emission from galaxies in clusters

The radio emission of spiral and elliptical galaxies is mainly due to the synchrotron mechanism.

Spiral galaxy radio emission follows the optical one: a disk, a halo (observed just in few spiral galaxies), a nucleus, and spiral arms can be clearly identified. This emission is polarized, characterized by a steep spectrum ($S(\nu) \propto \nu^{-\alpha}$, with $\alpha \sim 0.7$) and by radio powers at 1.4 GHz of $P_{1.4\mathrm{GHz}} \simeq 10^{18}$–$10^{23}$W Hz^{-1}.

While a radio signal from spiral galaxies is commonly observed, radio emission from elliptical galaxies is not a common phenomenon, being detected just in the 10% of the elliptical galaxies. In this class of sources, optical and radio emission do not have the same spatial location, the first covering regions of few tens of kpc, the second reaching distances of ∼100 kpc. Elliptical radio galaxies are characterized by powers of $P_{1.4\mathrm{GHz}} \simeq 10^{24}$–$10^{27}$W Hz^{-1} at 1.4 GHz and by a doubled peculiar structure: two jets depart from a central nucleus, inflating two lobes and terminating in two brigth hot spots. The jets inject in the surrounding environment energy in the form of mass,

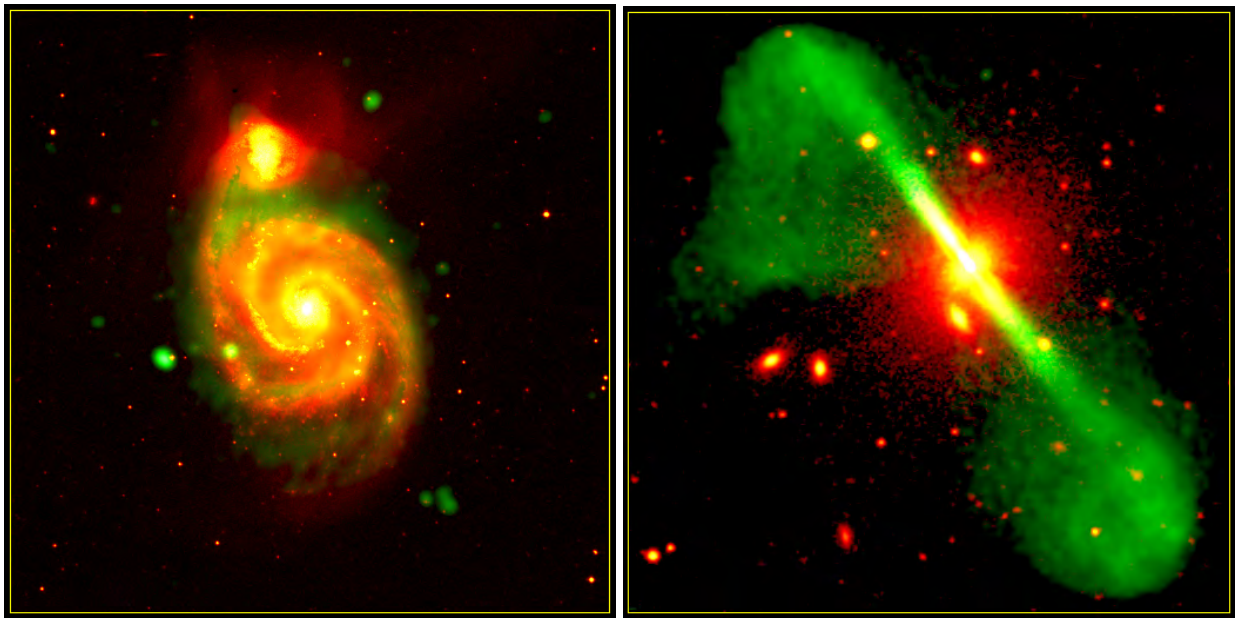

Figure 1.4 Example of the radio emission coming from the spiral galaxy M 51 (*left panel*, Klein et al. 1984) and the elliptical galaxy 3C 296 (*right panel*, Leahy & Perley 1991) in green overlaid on the optical image from the Digitized Sky Survey in red. The radio signal coming from the spiral galaxy follows the optical one. In particular, a central powerful nucleus and the spiral arms can be clearly identified. On the contrary, the radio emission in the elliptical galaxy extends beyond the optical counterpart, with a central nucleus that originates two jets terminating in two lobes.

magnetic field and momentum. Elliptical galaxies can be distinguished in *Fanaroff & Riley I* (FR I), faint sources ($P_{1.4GHz}$<$10^{24.5}$W Hz^{-1}) where the bulk of the radio emission is due to the central core and the jets, and *Fanaroff & Riley II* (FR II), brighter sources ($P_{1.4\mathrm{GHz}} > 10^{24.5}$W Hz^{-1}) with strong hot spots (Fanaroff & Riley 1974).

An example of the different radio emission from spiral and elliptical galaxies is shown in Fig. 1.4.

A general difference in the emission of field radio galaxies and cluster radio galaxies have been first observed by De Young (1972). Field galaxies emit almost without interferences from the surrounding environment, while cluster galaxy radio emission is strongly disturbed by the interaction with the intracluster medium and with other cluster galaxies. At radio wavelengths, the interaction between galaxies and the intracluster thermal gas is responsible of distorted galaxy morphologies. Moreover, because of the surrounding environment, a general suppression of the star-formation rate have been observed in cluster galaxies with respect to similar field galaxies (Balogh et al. 1998). However, high-pressure due to the intracluster medium can compress galactic molecular clouds with a local enhancement of the star-formation rate (Bekki & Couch 2003).

1.3.1 Interaction between galaxies and ICM

Spiral and elliptical galaxies moving at velocities v_{gal} strongly interact with the intracluster medium characterized by a density ρ_{ICM} via ram pressure

$$P_{\mathrm{ram}} = \rho_{\mathrm{ICM}} v_{\mathrm{gal}}^2 \tag{1.8}$$

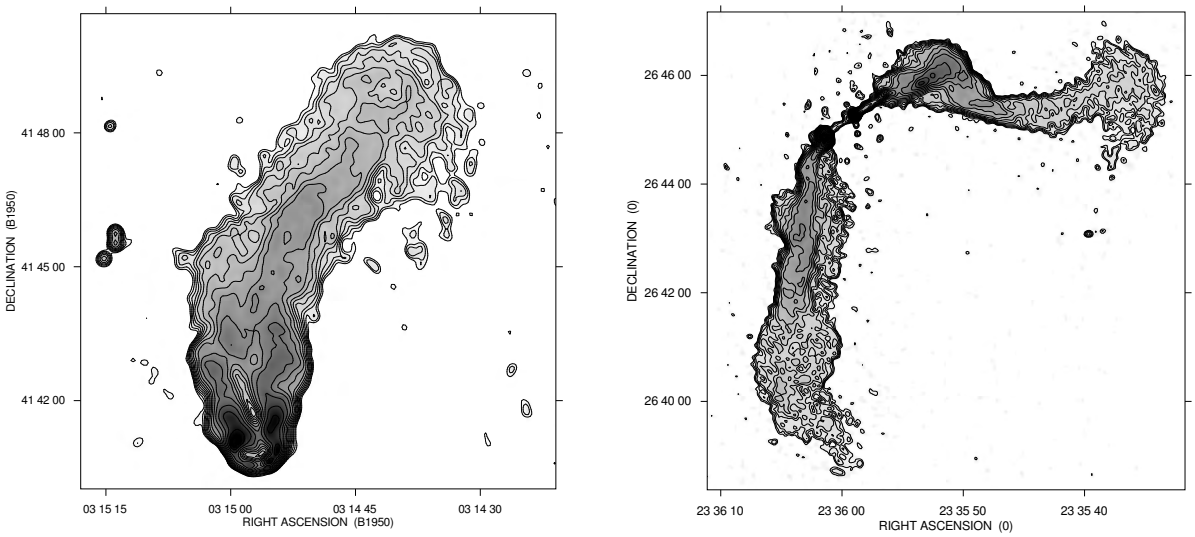

Figure 1.5 Radio emission from the narrow-angle tailed galaxy NGC 1265 (*left panel*) and the wide-angle tailed galaxy 3C 465 (*right panel*). These are clear examples of the interaction between the radio galaxy emission and the surrounding environment. Indeed, the jets have been blended by the pressure of the intracluster medium instead than naturally dispose as in Fig. 1.4. Images taken from the "3CRR" sample of Laing et al. (1983).

with a consequent distortion of the radio galaxy morphology and via the static pressure

$$P_{\rm static} = 2 n_{\rm e} k T \tag{1.9}$$

exerted by the ICM on the radio lobes. A dramatic example of the interplay between elliptical radio galaxies and intracluster medium is given by the tailed radio galaxies and by the X-ray cavities filled with non-thermal plasma.

1.3.1.1 Tailed radio galaxies

Tailed radio galaxies are elliptical galaxies whose jets have been bent in the same direction forming two tails because of the dynamic interaction with the ICM. Two classes of tailed radio galaxies can be identified:

- the *narrow-angle tailed sources* (NAT), characterized by small angles between the tails, with a "U" shape;
- the *wide-angle tailed sources* (WAT), characterized by wide angles and a "V" shape.

An example of NAT and WAT sources is given in Fig. 1.5.

The bending is explained as due to the action of the ram pressure of the ICM, because of high velocities of radio galaxies. The angle between the tails should be related to the relative velocity of the radio galaxy respect to the ICM ($\sim$1000 km s^{-1}) and to the density of the ICM and of the jet. Actually, NAT sources have been found not to be characterized by such high velocities but rather to be associated to clusters with ongoing merger. On the basis of these features, Bliton et al. (1998) proposed that the bulk motions originated during cluster mergers play a fundamental role in bending the jets of these sources. In addition, cluster mergers originate ram-pressure gradients

that could be responsible also of the shape of WAT sources, whose velocities respect to the cluster velocity centroid are lower than 100 km s^{-1} (Gomez et al. 1997; Loken et al. 1995). Also other mechanisms, as buoyancy forces and gas sloshing, have been proposed as responsible of this phenomenon (see e.g. Giacintucci et al. 2008, and references therein). However, at present, it is not yet clear if one of them is predominant or if they all concur to produce distortions in the radio galaxy morphology.

1.3.1.2 Dying radio galaxies

The radio emission coming from elliptical galaxies is powered by the nucleus that channels energy and plasma through the jets. After 10^7–10^8 yr the activity in the core stops or weakens, probably because of variations in the accretion rate of the central massive black hole in the AGN (Lara et al. 2002). A fading phase follows and, at the end, the source disappears completely. During the fading phase the core, jets, and hot spots are not anymore detectable since they are though to be originated by the continuing activity, while the lobes keep to be visible until relativistic electrons injected through the jets during the active phase run out all their energy. If the emitting electrons are subject just to radiative losses, this phase can last $\sim 10^8$ yr (Murgia et al. 2011). These sources are called *AGN relics* or *dying radio galaxies* (see e.g. Parma et al. 2007; Ferrari et al. 2008) and the first example is B2 0924+30 (Cordey 1987). In Fig. 1.6 we show the dying radio galaxy B2 1610+29. The radio lobes displaced from the host optical galaxy can be identified.

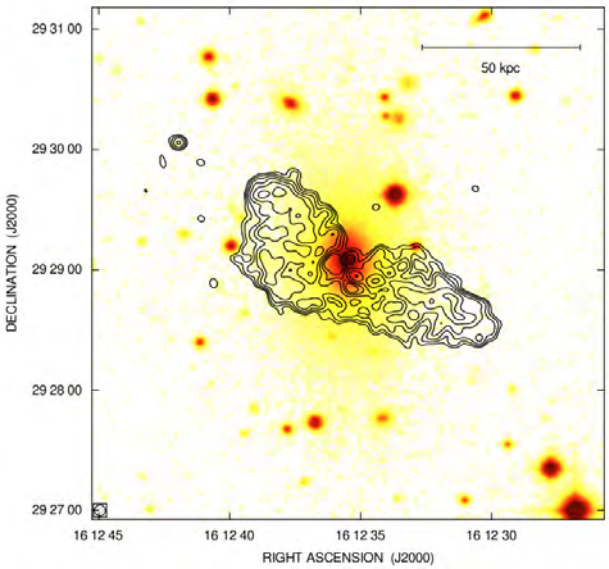

Figure 1.6 Radio contours of B2 1610+29 overlaid on the optical DSS2 image (Murgia et al. 2011). This is a dying radio source. Indeed, a clear displacement between the radio lobes and the host galaxy is present.

Dying radio galaxies have sizes of tens of kpc, steep spectral indexes ($2 \lesssim \alpha \lesssim 4$), degrees of polarization up to about 30% and are generally located in the proximity of the brightest central galaxy of some galaxy clusters, even if sometimes their ages do not allow a direct association with the cD galaxy but rather with other nearby bright galaxies of the cluster (Slee et al. 2001). Dying radio galaxies are very elusive, probably due to the fast spectral evolution during the dying phase. Because of synchrotron losses and Compton scattering, the high energy electrons are

quickly depleted without to be replaced by new particles. This produces an exponential cut-off in the spectrum. Then, the following expansion of the radio lobes shifts the break in the spectrum at lower and lower frequencies with the consequent disappearance of the source. Slee et al. (2001) find that cluster dying radio galaxies are in pressure equilibrium with the surrounding environment. This interplay of the radio source with the intracluster medium can affect the expansion of the lobes through adiabatic compression, allowing to detect the radio lobes at least at low frequencies. This explains why this kind of sources seems preferentially found in clusters of galaxies (Murgia et al. 2011).

1.3.1.3 X-ray cavities

An important evidence of the interaction between radio galaxies and the surrounding medium is given by the observation of X-ray cavities, detected for the first time near NGC 1275 in the Perseus cluster (Branduardi-Raymont et al. 1981; Fabian et al. 1981; Boehringer et al. 1993). X-ray cavities have been observed in 75% of galaxy clusters with strong cooling core or that need some form of heating at the center (Dunn et al. 2005). The observation of cavities is simpler if they

Figure 1.7 Radio (red), X-ray (blue), and optical (white) emission from the galaxy cluster Hydra A. The jets of the central radio galaxy have swept away some thermal plasma, giving rise to pronounced X-ray cavities coincident with the radio galaxy lobes. Image taken from http://chandra.harvard.edu/graphics/resources/desktops/2009/hydra_640.jpg.

are large, at the center of bright X-ray clusters and near to the plane of the sky. To date, in about 40 galaxy clusters, X-ray bubbles with size up to few hundreds of kpc have been observed, as e.g. in Perseus, A2052, A496, A2199, and Hydra A (see e.g. McNamara et al. 2008, and references therein). Usually, two cavities are present, often associated with the lobes of the central elliptical galaxy or of a dying radio galaxy, but sometimes multiple pairs have been identified, thought to be generated by different AGN outbursts. The pressure due to the synchrotron emission of cosmic ray electrons carried by the jets of the AGN inflates the thermal plasma giving rise to these features. X-ray cavities allow to derive information about the nature of the AGN jets. Indeed, according to

Guo & Mathews (2011), the quasi-spherical shape of the observed X-ray cavities suggests that they are produced by jets with low thermal gas densities ($n \sim 10^{-5}$ cm^{-3}) and energetically dominated by cosmic rays. The material swept away during these phenomena has typically a mass of $10^{10} M_{\odot}$, but also masses $\gtrsim 10^{12} M_{\odot}$ can be removed. The total energy required to create a cavity is about $10^{55} - 10^{62}$ erg (e.g. McNamara & Nulsen 2007; McNamara et al. 2008, and references therein). The work done during the cavity formation could solve the cooling catastrophe (see § 1.1.2) by heating the central region of cooling core galaxy clusters (e.g. Jones et al. 2002; Roychowdhury et al. 2004).

In Fig. 1.7 the X-ray cavities at the center of the Hydra A cluster are shown. They are characterized by a diameter of about 200 kpc and are a representative example of X-ray holes filled by the non-thermal radio emission.

1.4 Radio emission from diffuse sources in clusters

According to the hierarchical scenario of structure formation, massive galaxy clusters form from the merger of galaxy groups and sub-clusters. During these mergers, gravitational energies as large as $\gtrsim 10^{64}$ ergs are released (e.g. Sarazin 2002) . This significant amount of energy drives shocks and turbulence into the thermal intracluster medium: the energy is injected on large spatial scales, and then cascades turbulently to smaller scales. Shocks and turbulence associated with a major cluster merger event are thought to accelerate particles and compress magnetic field in the ICM (e.g. Roettiger et al. 1999b; Skillman et al. 2008, 2011). These non-thermal components are expected to lead to large-scale diffuse synchrotron emission associated with the ICM - an expectation confirmed by sensitive radio observations. In fact, in an increasing number of galaxy clusters, diffuse sources known as radio halos, radio relics, and radio mini-halos have been detected (Feretti & Giovannini 2008; Ferrari et al. 2008). While merging clusters typically host radio halos and radio relics, a few nearly relaxed, cool-core, galaxy clusters exhibit signs of a diffuse synchrotron emission called mini-halo. Burns et al. (1992) was the first to recognize a distinction between cluster-wide halos such as in Coma and mini-halos associated with cool cores such as in Perseus. The physical properties of radio halos, relics, and mini-halos reveal very weak large scale magnetic fields, with central strengths $\sim \mu$G, and rarefied and very energetic populations of relativistic electrons, with Lorentz factor $\gamma >> 1000$.

The study of these sources is important because they are related to the history and physical properties of the hosting cluster, as suggested by the deep link observed between radio, X-ray and optical emission of clusters. Therefore, a better understanding of these rare and elusive sources could allow a better understanding of galaxy cluster formation processes and to clarify the role of non-thermal components in the ICM. In the last years the higher sensitivity of radio observations and the development of theoretical models allowed to improve our knowledge of these sources.

1.4.1 Halos in merging clusters

Radio halos are diffuse, low-surface-brightness ($\simeq 1\,\mu$Jy·arcsec^{-2} at 1.4 GHz) synchrotron radio sources with no obvious optical counterpart, permeating the central regions of some merging galaxy clusters (e.g. Feretti & Giovannini 2008; Ferrari et al. 2008). Their morphology is quite regular, with a brightness distribution generally peaked in the X-ray cluster center and then decreasing towards the cluster outskirts. The prototype of this kind of sources is Coma C (see Fig. 1.8) in the Coma cluster, observed first by Large et al. (1959).

Usually radio halos appear to be not polarized. In fact, just in two cases polarized filaments

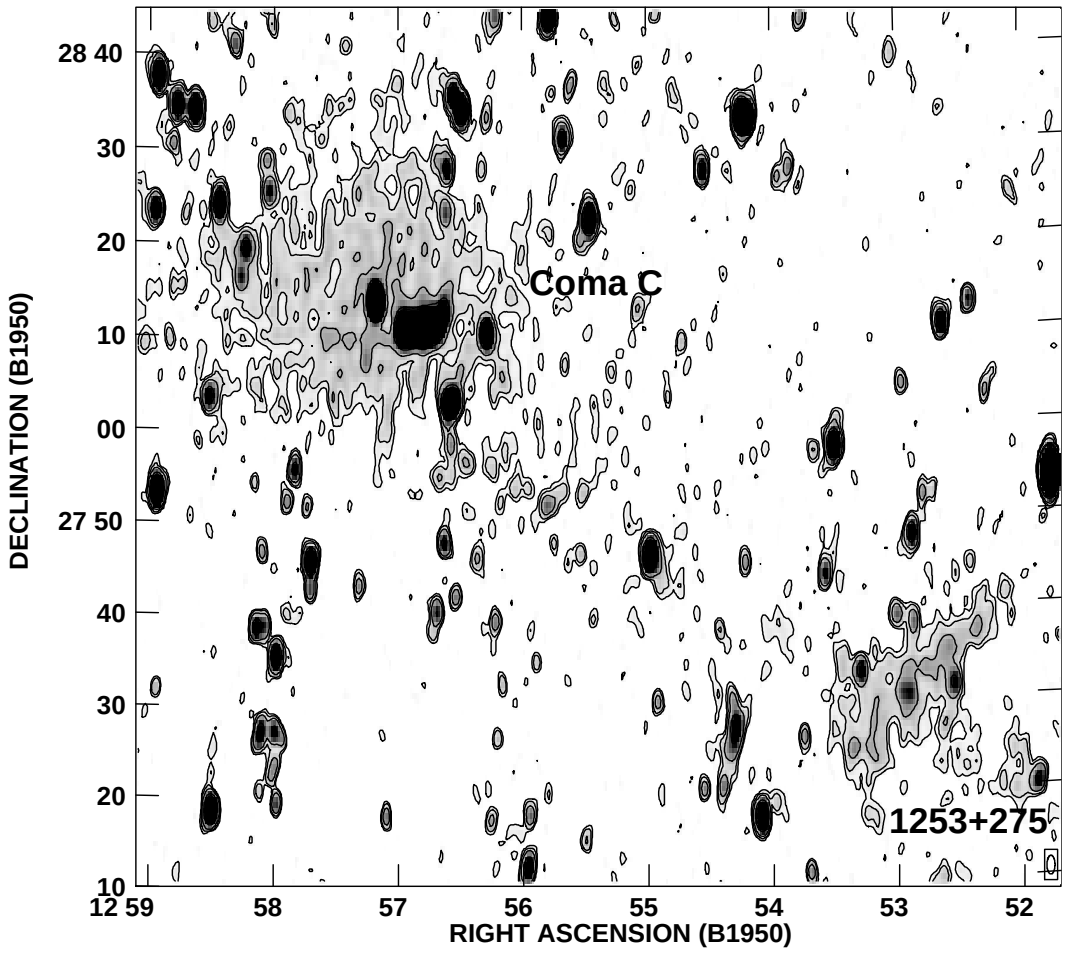

Figure 1.8 Radio emission at 90 cm (Westerbork Synthesis Radio Telescope) in the Coma cluster. The bright sources are powerful radio galaxies while the low brightness large scale structures in the central region (top left corner) and in the outskirts (bottom right corner) of the cluster are respectively the radio halo Coma C and the radio relic 1253+275 (Giovannini et al. 1993). The contour levels are drawn at 3, 5, 10, 30, 50 mJy/beam and the gray-scale ranges between 2 and 30 mJy/beam. The HPBW is $55'' \times 125''$.

have been detected: in A2255 (Govoni et al. 2005; Pizzo et al. 2011), and in MACS J0717.5+3745 (Bonafede et al. 2009a). Radio halos can cover linear sizes up to 2 Mpc, but also smaller halos have been detected, as in A2218 (Giovannini & Feretti 2000), A3562 (Venturi et al. 2003), and A1213 (Giovannini et al. 2009). The spectral index has been investigated for a few of them revealing integrated spectral slopes $\alpha \gtrsim 1$. In some cases a spectral index radial steepening has been observed, as in Coma (Giovannini et al. 1993), A665 and A2163 (Feretti et al. 2004b), while in others cases a flat patchy structure is present, as in A2744 and A2219 (Orrù et al. 2007). A steepening of the spectral index with frequency has also been detected in some clusters: Coma (Thierbach et al. 2003), A2319 (Feretti et al. 1997), A754 (Bacchi et al. 2003), and A3562 (Giacintucci et al. 2005).

The morphology of the radio halos and of the X-ray emission of their hosting clusters show strong similarities (Deiss et al. 1997; Feretti 1999; Liang et al. 2000; Govoni et al. 2001c; Feretti et al. 2001). Most of radio halos have been found in galaxy clusters with high X-ray luminosity ($L_{\mathrm{X}\,[0.1-2.4\,\mathrm{keV}]} \simeq 10^{44} - 10^{45}\,\mathrm{erg\,s^{-1}}$), in presence of an intense merger activity (e.g. Buote 2001; Feretti 2002; Govoni et al. 2004; Cassano et al. 2010; Rossetti et al. 2011), and the radio halo power

$P_{1.4\,\mathrm{GHz}}$ at 1.4 GHz strongly correlates with the X-ray cluster temperature (e.g. Colafrancesco 1999; Liang 1999) and luminosity L_X (e.g. Feretti 2002; Giovannini et al. 2009). In addition, the X-ray luminosity correlates with the mass of the cluster (e.g. Reiprich & Böhringer 2002), suggesting a dependence of the radio halo power on the cluster mass $P_{1.4\,\mathrm{GHz}} \propto M^{2.3}$ (Govoni et al. 2001b; Feretti 2003). Since not all clusters currently undergoing mergers host a radio halo, the cluster mass could be a fundamental parameter concerning the formation of these diffuse structures. A meaningful example is given by the galaxy cluster A2146. This cluster is undergoing a strong merger and is the first system observed to contain shock fronts not associated to diffuse radio emission. A possible explanation can be the low mass of the cluster (Russell et al. 2011). Indeed, only massive clusters, originating from several major mergers, could allow the formation of radio halos. In this scenario, both past and present mergers could play a role in the formation and evolution of this kind of diffuse sources (see Feretti & Giovannini 2008, and references therein).

Recently, some radio halos have been observed also in low X-ray luminosity galaxy clusters, as e.g. in A1213 (Giovannini et al. 2009) and 0217+70 (Brown et al. 2011), indicating a situation more complex than described by the present models and numerical simulations of radio halo formation (see § 3.6.3).

1.4.1.1 Radio halo origin

Radio halos are the clearest evidence of the presence of magnetic fields and cosmic ray mixed with the thermal ICM in the central regions of clusters of galaxies. The relativistic particles are injected in the ICM by shock fronts (in supernova remnant and during cluster formation processes), radio galaxies, AGN, and galactic winds (Ensslin et al. 1997; Völk & Atoyan 2000; Hoeft & Brüggen 2007; Vazza et al. 2009). After the injection, they start to lose energy. Relativistic proton energy losses are due to *pp* inelastic scattering and Coulomb interactions, implying lifetimes $\sim 10^{10}$ yr comparable to the diffusion time scale over the cluster size (Völk et al. 1996; Berezinsky et al. 1997), so that they can be accumulated in the cluster volume. On the other hand, relativistic electrons lose energy mainly because of synchrotron emission and inverse Compton scattering with the Cosmic Microwave Background (CMB) photons, but also Coulomb interactions and bremsstrahlung emission. Therefore, the relativistic electron radiative lifetime is shorter than the Hubble time. For $\gamma < 10^8$, it is (e.g. Longair 1981; Meisenheimer et al. 1989; Slee et al. 2001):

$$\tau \approx 2 \cdot 10^{12} \gamma^{-1} \left[(1+z)^4 + \left(\frac{B}{3.3\mu\mathrm{G}} \right)^2 \right]^{-1} \mathrm{yr} \tag{1.10}$$

that is about 10^8yr for a Lorentz factor $\gamma = 10^4$. Since their diffusion speed is limited by the Alfvén speed ($\sim$100km s^{-1}), during their lifetimes they can cover distances of about 10 kpc. Radio halos are extended over larger scales (1–2 Mpc), therefore, in order to explain their emission, a mechanism of *in situ* generation or (re-)acceleration of relativistic electrons has to be considered. Two main models have been proposed:

- *primary models* (Schlickeiser et al. 1987; Petrosian 2001; Brunetti et al. 2004; Brunetti & Blasi 2005; Brunetti & Lazarian 2007, 2011a). In these models Magneto Hydro Dynamical (MHD) turbulence due to cluster mergers is supposed to stochastically (re-)accelerate pre-existing electrons through Fermi-II processes. The main predictions of primary models are: 1. the presence of radio halos only in massive merging clusters, where enough energy is available for particle (re-)acceleration. This would imply the absence of radio diffuse emission in clusters with low X-ray luminosity (Cassano et al. 2006, 2008);

2. a high frequency cut-off in the radio halo spectrum. In fact, the scarce efficiency of this acceleration mechanism should produce in the electron spectrum a break at $\gamma \sim 10^5$, responsible of a steepening in the synchrotron source spectra. Therefore, a population of ultra-steep radio halos is expected (see Blasi 2004; Brunetti 2004, and references therein). They should be detected by surveys performed by the next generation of low frequency radio telescopes (LWA, LOFAR);
3. a radial steepening and a complex spatial distribution of the spectral index α due to different (re-)acceleration processes in different cluster regions;
4. complex radio halo morphologies due to intermittence of turbulence;

- *secondary models* (Dennison 1980; Vestrand 1982; Blasi & Colafrancesco 1999; Dolag & Enßlin 2000; Pfrommer & Enßlin 2004b,a; Pfrommer 2008; Pfrommer et al. 2008; Kushnir et al. 2009; Keshet 2010; Donnert et al. 2010a,b; Enßlin et al. 2011). Secondary models propose a continuous generation of pions through the collision between relativistic protons (accelerated during the cluster history) and thermal protons in the ICM. Then, the charged and neutral pions decay respectively into secondary electrons and neutrinos and into gamma rays. The main predictions of this scenario are:
  1. radio halos should be present in all galaxy clusters because of the proton confinement is expected to take place in every galaxy cluster. This problem has been addressed by Enßlin et al. (2011) (see the following);
  2. a uniform distribution of the radio halo spectral index because of a continuous and uniform injection of electrons;
  3. a smooth radio halo morphology because relativistic protons have enough time during their lives to diffuse over all the cluster volume;
  4. γ-ray and neutrino emission from the decay of secondary π^0.

An overview of the two scenarios is given by e.g. Feretti & Giovannini (2008) and Enßlin et al. (2011).

Observational results seem to be more in agreement with the (re-)acceleration scenario. In fact, radio halos have been observed not in all galaxy clusters, but just in massive merging galaxy clusters. During cluster mergers, the energy can be channeled from the ICM to the relativistic electrons by either shock wave acceleration (Fermi-I processes) or cluster turbulence (similar to Fermi-II processes). Radio halo observational properties suggest that their emission is mainly sustained by turbulence, while shocks appear not effective enough to accelerate relativistic electrons (Gabici & Blasi 2003). In addition, shocks detected in some galaxy clusters hosting radio halo are localized. Even if sometimes they have been found to be coincident with the edges of radio halos, as e.g. in 1E 0657-56 (Markevitch et al. 2002) and in A520 (Markevitch et al. 2005), in some galaxy clusters they do not correspond to a flattening of the spectral index (e.g. in A665, see Feretti et al. 2004b; Markevitch & Vikhlinin 2001), as expected if they were responsible of the energy supply. Actually the radio halo-merger connection could not be related to the supposed model for radio halo formation. In fact, in a recent work, Enßlin et al. (2011) give an alternative explanation (see also Brunetti 2011; Pfrommer et al. 2011). They show that the radio halo formation could be explained by means of a high central energy density concentration of cosmic rays that should be typical of cluster undergoing major mergers and strongly turbulent. Anyway, also other elements support the (re-)acceleration scenario. Indeed, the steep integrated spectra and the radial steepening of the spectral index of radio halos are not explainable in the context of secondary models. Finally, up to now, only an upper limit has been derived for the γ-ray emission in galaxy clusters (e.g. Reimer

et al. 2003; Aharonian et al. 2009a,b; Aleksić et al. 2010). The minimal flux predicted by hadronic models is under these values but would require atypically high magnetic field strengths. More reliable magnetic field strengths imply a γ-ray flux above the present upper limit (see e.g. the study about A2256 performed by Brunetti 2009).

We have to note that also primary models do not allow a complete description of the observational characteristics of radio halos. In fact, turbulence is a quite inefficient mechanism, so that it is expected to drive radio halo emission just during the most recent ongoing mergers. Moreover, it is intermittent, in such a way that is not able to account for the observed regular morphology of radio halos. Since relativistic protons are anyway accumulated in galaxy clusters, it seems more reliable that relativistic electrons continuously generated by hadronic collision and present in all galaxy clusters coexist with a population of relativistic electrons (re-)accelerated through MHD turbulence due to cluster mergers (see Cassano 2009, and references therein). The global picture has become even more complex owe to the recent discovery of radio halos in low X-ray luminosity clusters that opens new questions concerning the radio halo formation processes.

1.4.2 Relics in merging clusters

Radio relics are diffuse, low-surface-brightness ($\simeq$1 μJy·arcsec^{-2} at 1.4 GHz), steep spectrum ($\alpha > 1$), filamentary synchrotron radio sources related to the ICM and usually located in the peripheral regions of galaxy clusters (e.g. Giovannini & Feretti 2002, 2004). The prototype of this kind of sources is 1253+275 in the Coma cluster, first classified by Ballarati et al. (1981), see Fig. 1.8. Radio relics are an important proof of the presence of relativistic electrons and magnetic fields also in the cluster outskirts, at the boundary of the X-ray emission, where the ICM density is low.

Most of radio relics are elongated perpendicularly to the cluster radius, have linear sizes between 400 and 1500 kpc, and typical degree of polarization at 1.4 GHz between 10 and 30%. Radio relics with a circular shape have been observed as well, as e.g. in A1664 (Govoni et al. 2001b) and A548b (Feretti et al. 2006). Both elongated and circular radio relics show substructures if observed at high resolution.

In about 10 galaxy clusters both a radio relic and a radio halo emission have been observed, connected sometimes by a bridge of diffuse radio emission, as for example in A2744 (Govoni et al. 2001b). In some galaxy clusters double radio relic sources are present with a symmetric position respect to the cluster center as in the case of A3667 (Roettgering et al. 1997), A2345, A1240 (Bonafede et al. 2009b), CIZA J2242.8+5301 (van Weeren et al. 2010), and ZwCl 0008.8+5215 (van Weeren et al. 2011b). For three of them also a radio halo emission at the center of the cluster has been detected: RXCJ1314.4-2515 (Feretti et al. 2005; Venturi et al. 2007), 0217+70 (Brown et al. 2011), and PLCK G287.0+32.9 (Bagchi et al. 2011).

Sometimes radio relics are located at huge distances from the cluster center, so that an identification with a galaxy cluster could be not straightforward. This is the case for example of the relic source located at a projected distance of 4.6 Mpc from the center of A2069 (Giovannini et al. 1999).

The origin of radio relics is still debated. Enßlin & Gopal-Krishna (2001) investigated the possibility that aged radio plasma from AGN can be revived due to the adiabatic compression by shock waves during cluster formation processes. A different scenario has been proposed by Ensslin et al. (1998), Roettiger et al. (1999a), and Hoeft & Brüggen (2007). They state that these synchrotron sources could be produced by the acceleration of electrons by means of Fermi-I processes during cluster mergers. According to this model, double radio relics should often be observed symmetrically located respect to the cluster center along the axis of the merger where the shock waves propagate.

A study based on a sample of 35 relics has been recently performed by van Weeren et al. (2011a). They find that relics are generally located perpendicularly to the merger axis, in agreement with the scenario that relics trace shock waves which form along the merger axis of clusters. The second scenario seems also to be confirmed by the work of Bonafede et al. (2009b).

1.4.3 Mini-halos in relaxed clusters

Radio mini-halos are diffuse, low surface brightness, steep spectrum synchrotron sources, extended over linear size of 500 kpc and sometimes polarized at 1.4 GHz at levels of 10-20%. The prototype of this kind of sources has been found at the center of the galaxy cluster Perseus (Burns et al. 1992), see Fig. 1.9.

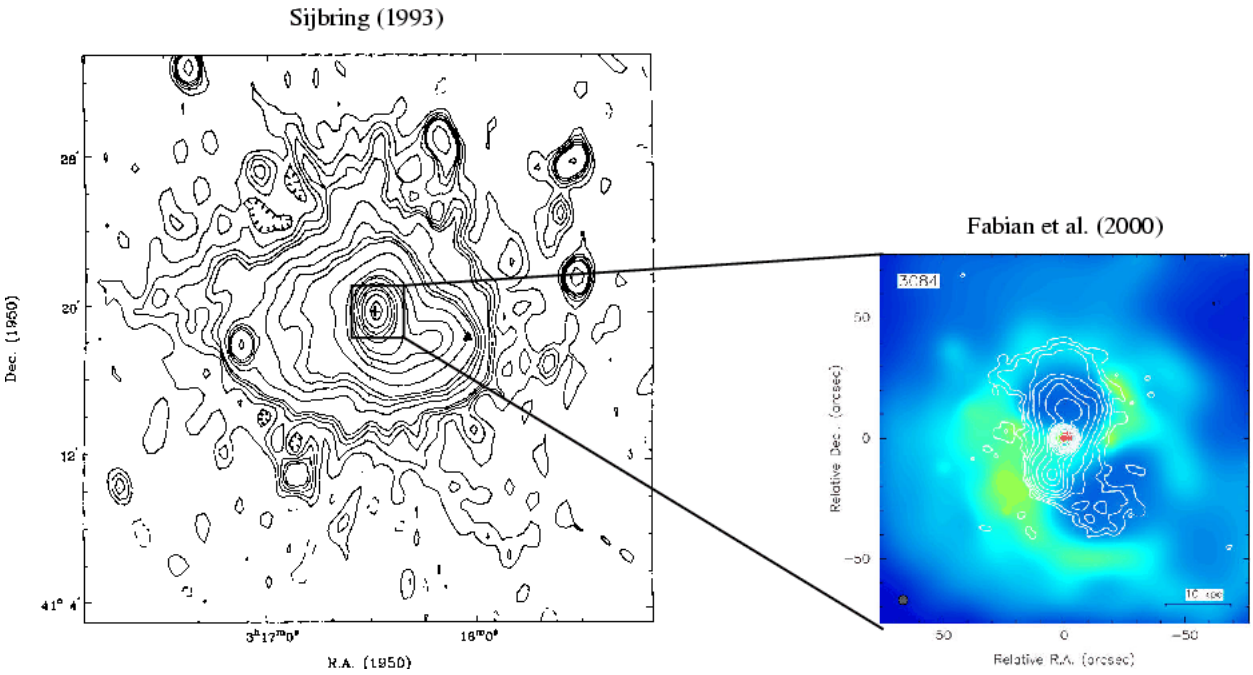

Figure 1.9 *Left*: diffuse mini-halo radio emission at 90 cm in the Perseus cluster. *Right*: superposition of the radio contours of the cD galaxy NGC 1275 located at the center of the radio mini-halo and X-ray emission of the cluster in colors. The images have been taken from Sijbring (1993), Fabian et al. (2000), and Gitti et al. (2004b).

They are always found to be located at the center of cool core clusters, surrounding the brightest cluster galaxy, even if, sometimes, the hosting cluster shows features of moderate merger activity in the central regions, as e.g. in A2142 (Giovannini & Feretti 2000), and in RXJ1347.5-1145 (Gitti et al. 2007a), suggesting a possible link between these minor mergers and the diffuse radio emission. Indeed, Burns et al. (2008) simulated the formation of both cool core and non-cool core clusters in the same numerical volume. These simulations confirmed that non-cool clusters are formed via major mergers early in their history which destroyed the cool cores and left significant residual kinetic energy in the gas which might be used to power the radio halos. In contrast, cool core clusters do not suffer any major mergers, thus preserving the central cool regions. However, the cool core clusters do experience regular smaller mergers which still inject energy in the intracluster medium, but more modestly than in the non-cool core clusters. These minor mergers might power the mini-halos. Indeed, recently, for the first time, an unambiguous correspondence

between a high-pressure region probably related to a shock and a radio excess in a mini-halo has been shown by Ferrari et al. (2011) at the center of the galaxy cluster RX J1347-1145.

Because of the small size of these elusive sources and the strong radio emission of the central radio galaxy, the study of mini-halos is quite difficult. In fact, up to now, less than ten mini-halos have been detected (Gitti et al. 2004a; Govoni et al. 2009). Higher resolution and dynamic range observations are required to improve the statistics.

It has not yet been clarified if halos and mini-halos are different phenomena or if they are different manifestations of the same processes. On this regard, a quantitative comparison is fundamental. One of the main difficulties is to estimate the size of diffuse synchrotron sources, because the size derived from the 3σ-isophotes of the radio image can be deeply affected from the sensitivity of the observations. A criterion to distinguish between radio halo and mini-halo emission has been introduced by Murgia et al. (2009). Following the approach presented by Orrù et al. (2007), they fit the azimulthally averaged brightness profile of the diffuse radio sources with an exponential law:

$$I(r) = I_0 e^{-\mathrm{r}/\mathrm{r_e}} \tag{1.11}$$

where I_0 and r_e are respectively the central radio surface brightness and the e-folding radius i.e., the radius at which the brightness drops to I_0/e. This is the only contribution for radio halos. Concerning radio mini-halos, the central radio galaxy has to be taken into account. To separate the central radio galaxy contribution from the radio mini-halo emission, Murgia et al. (2009) include a central point source:

$$I(r) = I_{0_\mathrm{PS}} e^{-(\mathrm{r}^2/2\sigma^2_\mathrm{PS})} + I_0 e^{-\mathrm{r}/\mathrm{r_e}} \tag{1.12}$$

where the point source emission has been characterized by a Gaussian.

The e-folding radius r_e can be used to define a length scale for the diffuse emission not deeply affected by the sensitivity of the radio image, as the 3σ isophotes of the radio image. This length scale allows to distinguish between mini-halos and halos, permitting a better classification. By using this approach, Murgia et al. (2009) perform a comparison of a representative sample of the two classes of diffuse radio sources. They find that radio halos with higher central brightness show larger scale lengths, with I_0 between 0.4 and $3\,\mu$Jy/arcsec^2 and r_e ranging between 70 and 400 kpc. Anyway, all radio halos appear characterized by a similar radio emissivity of about 10^{-42}erg s^{-1}cm^{-3}Hz^{-1} at 1.4 GHz. On the other hand, mini-halos show scale lengths smaller than 100 kpc with a larger spread in central brightness and in radio emissivity respect to large halos.

2

The diffuse radio emission in the galaxy cluster Abell 1689

In this Chapter we present the detection of a new diffuse synchrotron radio source in the complex galaxy cluster A1689.

As mentioned in the previous Chapter, sometimes the classification of a diffuse large-scale synchrotron source as radio halo or radio mini-halo is not straightforward as, for example, in the case of A1689, because of the small size of the diffuse source and the still debate dynamical state of the cluster. Therefore, we carry out an analysis of the radio properties of this cluster based on the approach proposed by Murgia et al. (2009) and described in § 1.4.3. In addition, a quantitative comparison between the radio and X-ray emission of the cluster is performed, since it permits to investigate a possible correlation of the radio and X-ray properties of the galaxy cluster.

This work is presented in Vacca et al. (2011).

2.1 The galaxy cluster A1689

A1689 (z=0.1832, Struble & Rood 1999)[1] is a galaxy cluster characterized by a complex optical and X-ray structure. At first inspection, it has a regular spherical shape and a strong peak in the X-ray surface brightness profile (Peres et al. 1998), features that apparently indicate a cooling core. Indeed, Chen et al. (2007) found a short central cooling time for A1689 ($t_{\rm cool} = 4.7 \pm 0.4$ Gyr) and a high accretion rate ($\dot{M} = 683^{239}_{-182} M_{\odot}$ yr^{-1}). Its Einstein radius[2] is the largest known so far (Tyson et al. 1990; Miralda-Escude & Babul 1995; Clowe & Schneider 2001; Broadhurst et al. 2005b,a; Umetsu & Broadhurst 2008), a characteristic that has made it attractive for lensing analysis. Strong and weak lensing studies have revealed discrepant mass values. Differences in the mass estimations have also been found between lensing and X-ray observations.

By means of *XMM-Newton* observations, Andersson & Madejski (2004) find evidence of an ongoing merger. They find a nonuniform radial temperature of the X-ray emitting gas across the

[1] $1''$=3.05 kpc, $D_{\rm L}$=880 Mpc.

[2] The Einstein radius indicates approximately the distance between images of a source produced by a gravitational lens.

cluster, and these features suggest a complex dynamical state. A major merger in which a subcluster moves along the line-of-sight could also explain the different mass estimates from X-ray and lensing analysis. An alternative explanation of this difference has been given by Lemze et al. (2008). By using a model-independent approach based on a simultaneous fit of lensing and X-ray surface brightness data, they find good agreement between the lensing mass profile and the X-ray emission profile. Their model, however, implies a temperature discrepancy with respect to the one derived solely from X-ray observations. The authors state that their result could support the presence of colder, denser, and more luminous small-scale structures that could be responsible for a bias in the observed temperature (Kawahara et al. 2007). Peng et al. (2009) refute this view and show that X-ray and lensing estimates can be made consistent by considering a prolate distribution for the gas temperature and density with the major axis aligned with the line-of-sight.

By using the Hubble's Advanced Camera for Surveys (ACS) and combining the strong and weak lensing approaches, Limousin et al. (2007) apply an accurate mass model to describe the observed substructures, obtaining good agreement between the strong and weak lensing analysis. To reduce the discrepancy between X-ray and lensing approaches, Riemer-Sørensen et al. (2009) combine this lensing analysis with high-resolution X-ray *Chandra* temperature and hardness ratio images. They find consistent mass profiles and indications that the main clump is in a hydrostatic equilibrium. By means of the same ACS observations, Coe et al. (2010) trace the most detailed mass distribution with a resolution of 25 kpc. They estimate a mass $M_{200} = 1.8^{+0.4}_{-0.3} \times 10^{15} M_{\odot}\, h_{70}^{-1}$ within a radius $r_{200} = 2.4^{+0.1}_{-0.2}\mathrm{Mpc}\, h_{70}^{-1}$. In addition, their results agree with the presence of a high mass along the line-of-sight, confirming previous studies present in the literature. Analyzing the same ACS dataset, Leonard et al. (2011) detect two dominant peaks of mass concentration that they identify as possible remnants of a recent merger.

The head-on merger scenario also seems supported by other optical observations. In fact, the central region of the cluster lacks a dominant galaxy at its centroid, while it hosts multiple nuclei/galaxies. Indeed, Girardi et al. (1997) find that A1689 appears to consist of three distinct groups of galaxies possibly aligned and well separated in velocity space ($\Delta V_{1-2} \sim 1200\,\mathrm{km\,s^{-1}}$ and $\Delta V_{2-3} \sim 1500\,\mathrm{km\,s^{-1}}$), suggesting a merger along the line of sight.

2.2 Radio observations and data reduction

We present archival observations of A1689 at 1.2 and 1.4 GHz performed at the Very Large Array (VLA) in spectral line mode in the A, C, and DnC configurations. The details of the observations are summarized in Table 2.1. The data were reduced following standard procedures using the NRAO's Astronomical Image Processing System (AIPS) package. Surface brightness images were produced using the AIPS task IMAGR. In the C and DnC configuration the data were collected with a total bandwidth of 12.5 MHz, subdivided into seven channels with a band-with of ∼1.6 MHz each. The source 1331+305 (3C286) was used as flux and bandpass calibrator. The nearby source 1354−021 was observed for complex gain calibration. Radio interference was carefully excised channel by channel, and several cycles of self-calibration and imaging were applied to remove residual phase variations. We averaged the seven channels together in the gridding process using IMAGR. The A configuration was calibrated by using the source 1331+305 as flux calibrator, and the nearby source 1246-075 as phase reference. The two IFs were averaged to obtain the surface brightness image.

Table 2.1 Details of the VLA observations of A1689.

R.A. (J2000)	Decl. (J2000)	Obs. frequency, ν (MHz)	Bandwidth (MHz)	VLA Configuration	Time (h)	Date	Project
13 11 30.2	−01 20 10.6	1365/1435	25.0	A	3.0	Mar 29,30,31 2002	AI0098
13 11 30.2	−01 20 35.4	1193	12.5	C	6.0	Jan 13, 1999	AZ0111
13 11 30.2	−01 20 35.4	1193	12.5	DnC	7.8	Feb 03,05 1999	AZ0111

Col. 1, Col. 2: Pointing position; Col. 3: Observing frequency; Col. 4: Observing bandwidth; Col. 5: VLA configuration; Col. 6: Time on source; Col. 7: Dates of observations; Col. 8: VLA project name.

2.3 Diffuse emission in A1689

The radio iso-contours at 1.2 GHz of A1689 are shown in Fig. 2.1. This image was obtained with the VLA in DnC configuration, and it was convolved with a circular FWHM beam of 30″. To compare the radio and X-ray cluster emission, the radio contours are overlaid on the *Chandra* image in the 0.1−10 keV band. We found that the central region of A1689 is permeated by a low-surface brightness diffuse emission with a few discrete sources embedded. The radio morphology of the diffuse emission is quite regular with a pretty round shape, following the regular structure of the cluster X-ray emission. As measured from the 3σ radio isophote, the overall diffuse emission has an angular extension of about 4′ (the Largest Linear Size is $LLS \simeq 730$ kpc at the cluster distance). However, as pointed out in Murgia et al. (2009), we note that the size of the diffuse emission calculated from the contour levels should be considered carefully, since it depends on the sensitivity of the radio image.

To separate the diffuse radio emission from discrete sources, we produced images at higher resolution. In Fig. 2.2 we present the radio contours of A1689 at 1.2 GHz taken with the VLA in C configuration, convolved with an FWHM beam of 20″. The discrete sources are labeled in the figure. A few discrete radio sources (labeled A, B, C) are embedded in the diffuse cluster emission, and their positions and flux densities are given in Table 2.2. Source B is located close to the cluster X-ray peak. In the *bottom* and *right-hand panels* of Fig. 2.2, their radio contours at 1.4 GHz taken with the VLA in A configuration (convolved with an FWHM beam of 2″) are overlaid on the optical Sloan Digital Sky Survey[3]. From this figure it is evident that source A, when observed at high resolution, is indeed composed of two distinct discrete sources: a wide-angle tailed radio source and a point source, shown respectively in the top right and bottom left-hand corners of the *top right-hand panel* of Fig. 2.2 (the flux density of source A given in Table 2.2 includes both sources). All these discrete sources have an optical counterpart.

To ensure that the large-scale diffuse emission is not caused by the blending of discrete sources, in Fig. 2.3 we present the total intensity radio contours at 1.2 GHz with the VLA in DnC configuration after subtraction of discrete sources. We produced an image of the discrete sources by using only the longest baselines of the DnC configuration dataset and uniform weighting. The clean components of this image were then subtracted in the (u, v) plane by using the AIPS task UVSUB. The image with the discrete sources subtracted confirms the presence of a low-surface brightness diffuse radio emission at the cluster center. The radio contours are overlaid on the *Chandra* X-ray image presented in Fig. 2.1. Crosses indicate the positions of the subtracted discrete sources.

The total flux density is calculated from the DnC dataset after a primary beam correction by integrating the total intensity surface brightness in the region of the diffuse emission down to 3σ level. The resulting total flux density at 1.2 GHz is estimated to be $\simeq (91.6\pm2.7)$ mJy. By

[3]http://www.sdss.org/

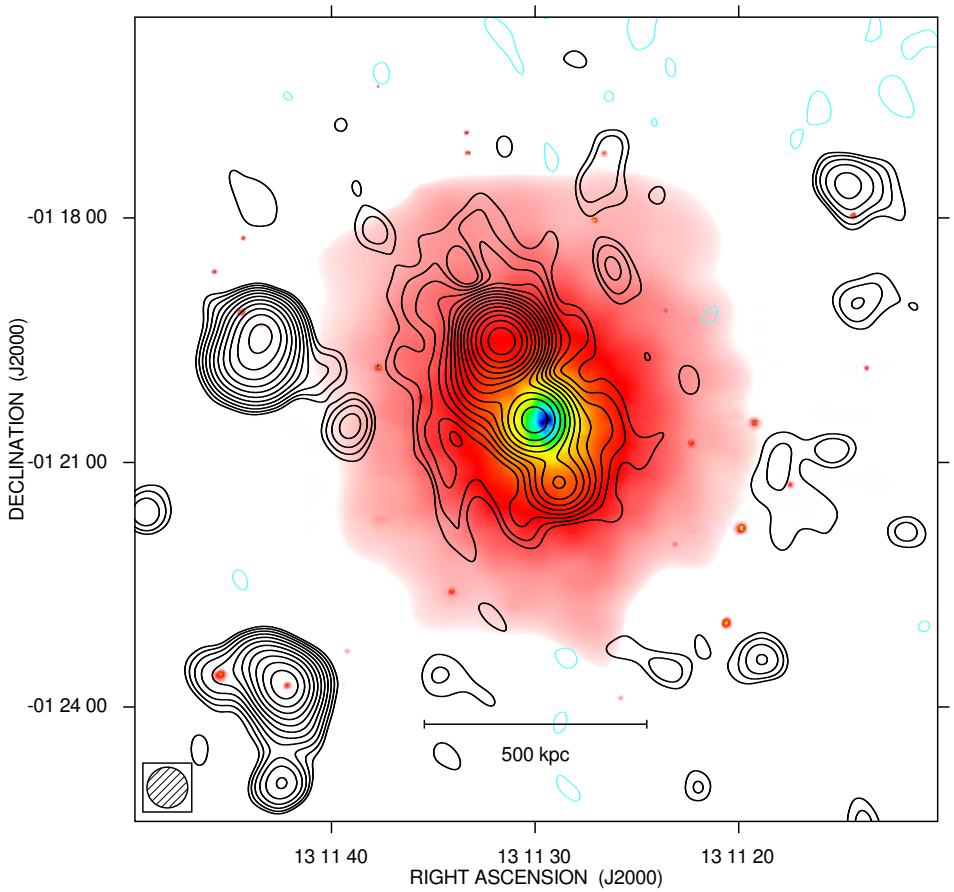

Figure 2.1 Total intensity radio contours at 1.2 GHz (VLA in DnC configuration) with an FWHM of 30″×30″. The contour levels are drawn at -3×10^{-4} Jy/beam, 3×10^{-4} Jy/beam, and the rest are spaced by a factor $\sqrt{2}$. The sensitivity (1σ) is 1×10^{-4} Jy/beam. The contours of the radio intensity are overlaid on a *Chandra* X-ray 0.1−10 keV band, adaptively smoothed count image (Obs. ID 6930).

subtracting the flux density of the embedded discrete sources A, B, and C as derived in the C configuration dataset (see Table 2.2), a flux density of $\simeq$ (11.7±3.4) mJy appears to be associated with the low-brightness diffuse emission. This flux density value corresponds to a radio power of $P_{1.2\,\mathrm{GHz}} = 1.08\times10^{24}$ W Hz^{-1}. To compare this result with studies of other radio halos, we rescaled the corresponding radio power at 1.4 GHz $P_{1.4\,\mathrm{GHz}} = 9.21\times10^{23}$ W Hz^{-1}, correcting by a factor 0.85 as estimated assuming a spectral index $\alpha = 1$.

A1689 is part of an X-ray flux-limited galaxy cluster sample selected from the ROSAT All-Sky Survey by Reiprich & Böhringer (2002). Its X-ray luminosity (corrected for our cosmology) in the 0.1-2.4 keV band is 1.2×10^{45} erg/sec. Therefore, the radio power ($P_{1.4\,\mathrm{GHz}}$), the radio's largest linear size (*LLS*), and the X-ray luminosity (L_{X}) of A1689 agree with the $P_{1.4\,\mathrm{GHz}} - LLS$ and $P_{1.4\,\mathrm{GHz}} - L_{\mathrm{X}}$ relations known for the other halos in clusters (see § 3.6.3).

2.3.1 Azimuthally averaged brightness profile of the radio emission

In Fig.2.4 we show the azimuthally averaged radio halo brightness profile at 1.2 GHz obtained from the DnC configuration image after subtracting the discrete sources (see Fig.2.3) and correcting for

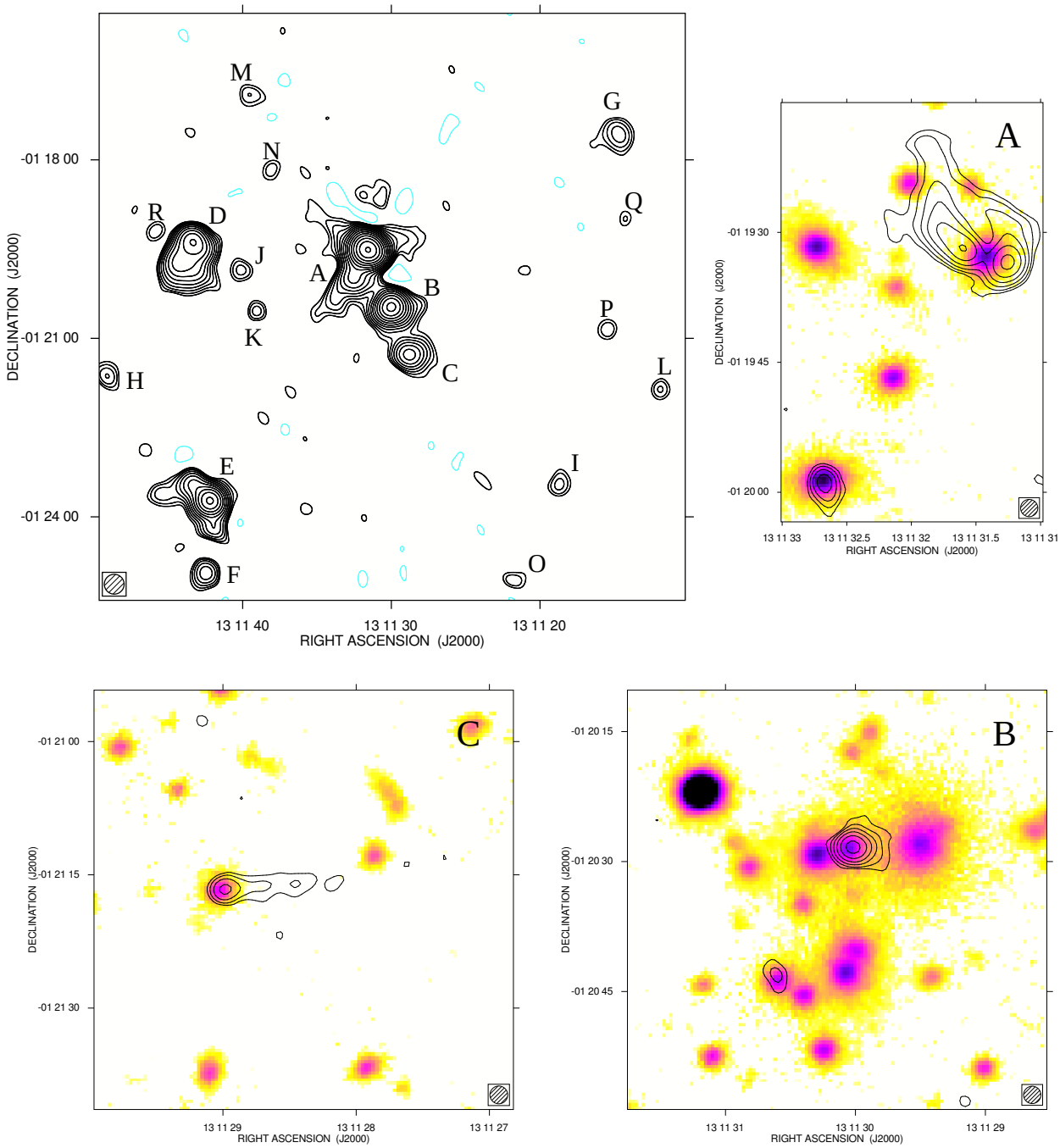

Figure 2.2 *Top left panel*: Total intensity radio contours at 1.2 GHz (VLA in C configuration) with an FWHM of 20″×20″. The contour levels are drawn at -3.3×10^{-4} Jy/beam, 3.3×10^{-4} Jy/beam, and the rest are spaced by a factor $\sqrt{2}$. The sensitivity (1σ) is 1.1×10^{-4} Jy/beam. *Bottom, top right panels*: Total intensity radio contours at 1.4 GHz (VLA in A configuration) with an FWHM of 2″× 2″. The first contour level is drawn at 13.5×10^{-5} Jy/beam, and the rest are spaced by a factor 2. The sensitivity (1σ) is 4.5×10^{-5} Jy/beam. The contours of the radio intensity are overlaid on the red plate of the Sloan Digital Sky Survey.

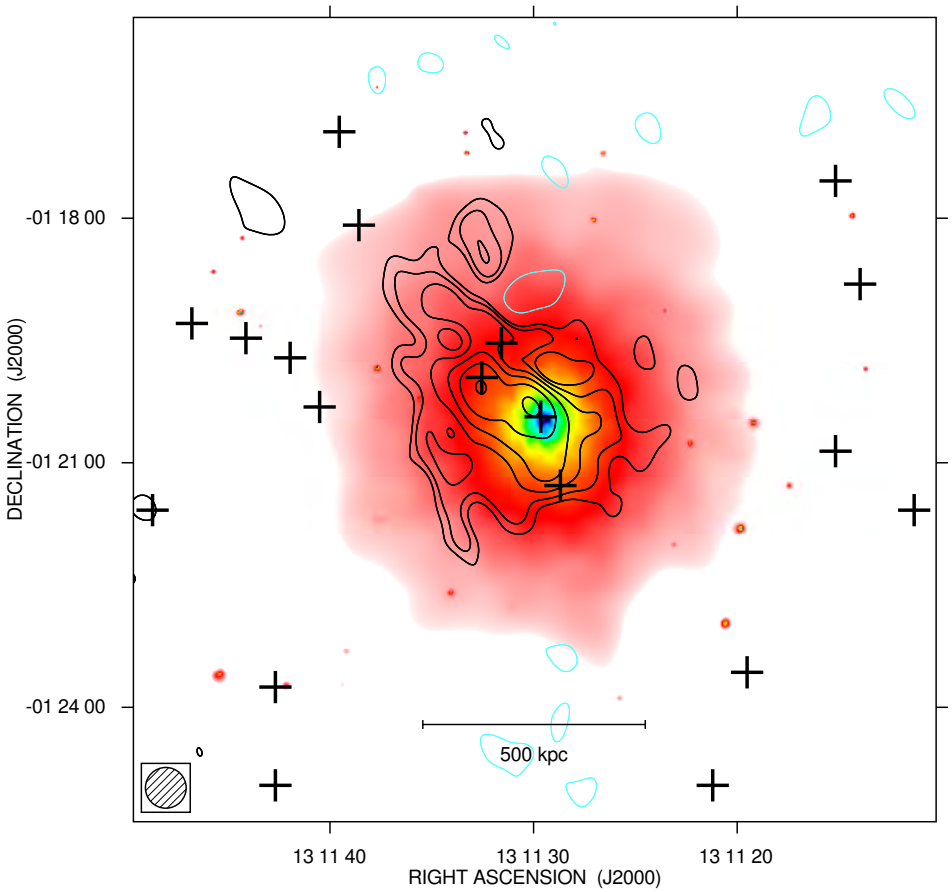

Figure 2.3 Total intensity radio contours at 1.2 GHz with the VLA in DnC configuration after subtraction of discrete sources. The image has an FWHM of 30″×30″. The contour levels are drawn at -3×10^{-4} Jy/beam, 3×10^{-4} Jy/beam, and the rest are spaced by a factor $\sqrt{2}$. The sensitivity (1σ) is 1×10^{-4} Jy/beam. Crosses indicate the positions of the subtracted discrete sources. The contours of the radio intensity are overlaid on the *Chandra* X-ray image shown in Fig. 2.1.

the primary beam attenuation. Each data point represents the average brightness in concentric annuli of half beam width (≃15″) centered on the cluster X-ray peak. The observed brightness profile is traced down to a level of 3σ.

Following Murgia et al. (2009) (see also § 1.4.3), we modeled the radio halo brightness profile, $I(r)$, with an exponential of the form $I(r) = I_0 e^{-r/r_e}$, whose best-fit is shown in Fig.2.4. The proposed method for deriving the radio brightness, the lengthscale, hence the radio emissivity of diffuse sources, is relatively independent of the sensitivity of the radio observation. The exponential model is attractive in its simplicity and involves a minimal set of free parameters. Obviously, it can not account for the local deviations from the circular symmetry of the diffuse emission. Indeed, an elliptical model would be more suitable to describe the slightly elongated shape of this radio halo. Nevertheless, to compare our results with those in literature we will suppose a perfect circular symmetry.

The fit is performed in the image plane as described in Murgia et al. (2009). To properly take the resolution into account, the exponential model is first calculated in a 2-dimensional image, with the same pixel size and field of view as observed, and then convolved with the same beam by means of a fast Fourier transform. Finally, the model is azimuthally averaged with the same set of annuli used

Table 2.2 Information on discrete radio sources embedded in the central diffuse cluster emission.

Label	R.A. (J2000)	Decl. (J2000)	$S_{1.2\,GHz}$ (mJy)
A	13 11 31.5	-01 19 31	62.0± 2.0
B	13 11 30.0	-01 20 28	14.0± 0.4
C	13 11 29.0	-01 21 17	3.9± 0.1

Col. 1: Source label; Col. 2, 3: Source position (R.A., Decl.); Col. 4: Source flux density at 1.2 GHz.

to obtain the observed radial profile. All these functions are performed at each step during the fit procedure. As a result, the values of the central brightness, I_0, and the e-folding radius r_e provided by the fit are deconvolved quantities, and their estimate includes all the uncertainties related to the sampling of the radial profile in annuli of finite width. The fit procedure has been implemented in the software FARADAY (Murgia et al. 2004). The best-fit of the exponential model at 1.2 GHz yields a central brightness [4] of I_0=$(1.70^{+0.20}_{-0.23})$ μJy/arcsec^2 and a lengthscale r_e=(149^{+25}_{-22}) kpc. The average radio emissivity $\langle J \rangle$ over the volume V of a sphere of radius $3r_e$ can be calculated following Murgia et al. (2009). Since

$$\langle J \rangle = \frac{\int_V J dV}{\int_V dV}$$

and since for a source with a power-law spectrum and at redshift z the monochromatic luminosity and brightness are related by:

$$dL = 4\pi I (1+z)^{3+\alpha} d\Sigma$$

where $d\Sigma$ is the infinitesimal surface element, the average emissivity results:

$$\langle J \rangle = \frac{\int_S dL}{\int_V dV}$$

$$\langle J \rangle = \frac{8\pi(1+z)^{3+\alpha} \int_0^{3r_e} I_0 e^{-r/r_e} r dr}{4\pi \int_0^{3r_e} r^2 dr}$$

$$\langle J \rangle = \frac{2\pi}{9}(1+z)^{3+\alpha}(1-4e^{-3}) \cdot \frac{I_0}{r_e}$$

where S is the surface of a section of the sphere of volume V. By expressing r_e and I_0 are in units of kpc and μJy/arcsec^2 finally we have

$$\langle J \rangle \simeq 7.7 \times 10^{-41} (1+z)^{3+\alpha} \cdot \frac{I_0}{r_e} \ (\mathrm{erg\,s^{-1}cm^{-3}Hz^{-1}}). \quad (2.1)$$

From the central brightness and the e-folding radius, we obtained for A1689 an average radio emissivity calculated over the volume of a sphere with radius of $3r_e$, k-corrected with α=1, of $\langle J \rangle = 1.7 \times 10^{-42}$ ergs^{-1}cm^{-3}Hz^{-1}.

In Fig.2.5, we show the best-fit central brightness I_0 rescaled at 1.4 GHz with $\alpha = 1$ versus the lengthscale r_e of A1689 in comparison with the set of radio halos and mini-halos analyzed in Murgia et al. (2009) and Murgia et al. (2010b). As previously pointed out, radio halos can have

[4] We checked that the fit of the exponential disk performed by masking, and not subtracting, the discrete sources is consistent within the uncertainties with the reported values for I_0 and r_e.

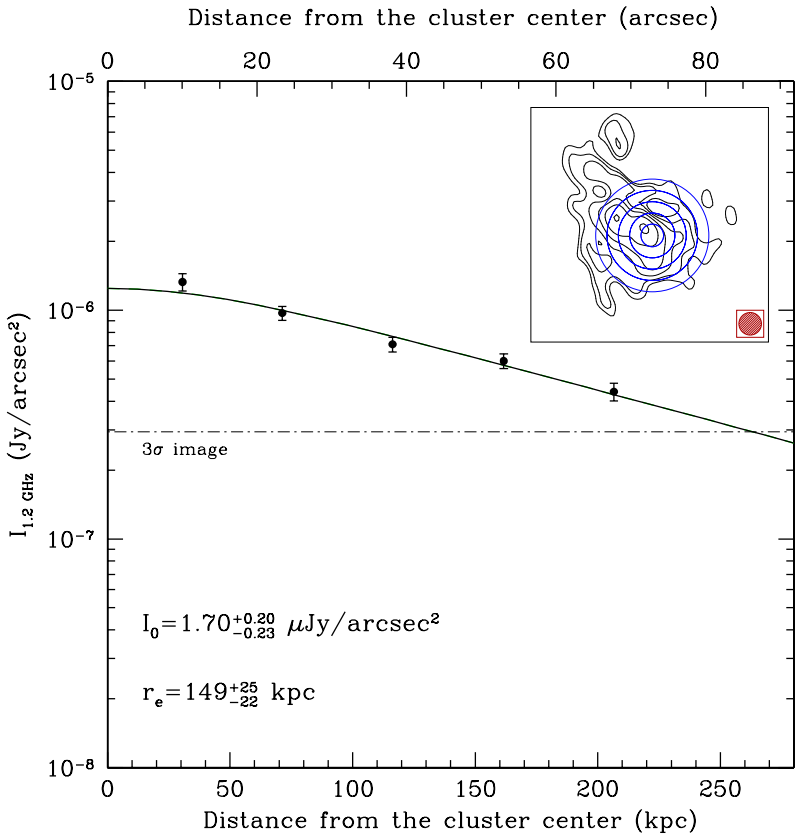

Figure 2.4 The azimuthally averaged brightness profile of the radio halo emission in A1689 at 1.2 GHz. The profile has been calculated in concentric annuli centered on the cluster X-ray peak, as shown in the inset panel. The horizontal dashed-dotted line indicates the 3σ noise level of the radio image, while the continuous line indicates the best-fit profile described by an exponential law (see text).

quite different lengthscales, but their emissivity is remarkably similar from one halo to another. In contrast, mini-halos span a wide range of radio emissivity. Some of them, like Perseus (Pedlar et al. 1990; Burns et al. 1992), RXJ1347.5-1145 (Gitti et al. 2007a) and A2390 (Bacchi et al. 2003) are characterized by a radio emissivity that is more than two orders of magnitude greater than that of radio halos. On the other hand, the mini-halos in cooling core clusters like A2029, Ophiuchus, and A1835 (Govoni et al. 2009) have a radio emissivity that is much more typical of halos in merging clusters rather than to the mini-halos previously known. A1689 populates the same region of the $I_0 - r_e$ plane of the other radio halos known in the literature. Although the e-folding radius of A1689 is not particularly extended, it is larger than the e-folding radius of the other mini-halos (they typically have $r_e \lesssim 100$ kpc). Therefore, the physical properties of the diffuse emission in A1689 seem in good agreement with the extrapolation of the properties of the other radio halos known in the literature.

2.3.2 Comparison of thermal and non-thermal emission

To investigate the possible presence of a radio - X-ray correlation in A1689, in Fig. 2.6 we present a quantitative comparison between the radio halo emission at 1.2 GHz after the correction for the primary beam attenuation and the *Chandra* X-ray image in the 0.1−10 keV band. Only regions

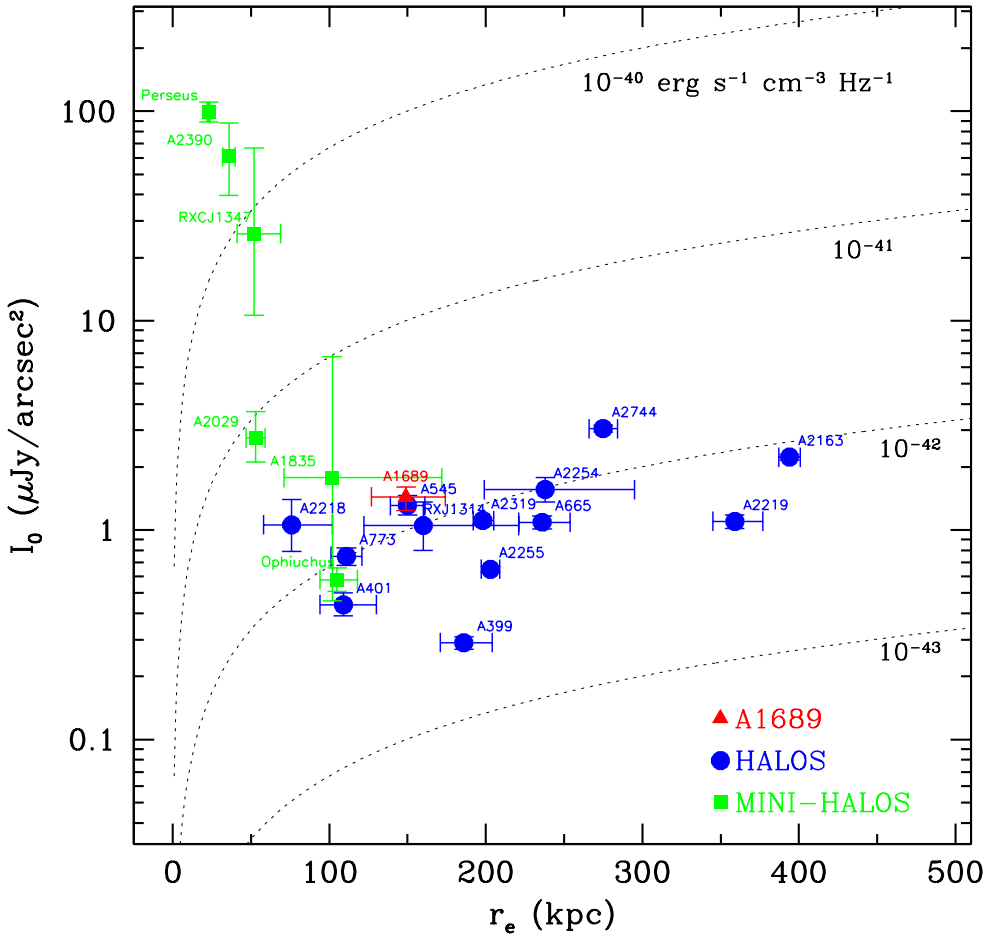

Figure 2.5 Best-fit central brightness I_0 at 1.4 GHz versus the lengthscale r_e of A1689 in comparison with azimuthally averaged brightness profiles of radio halos and mini-halos taken from the literature (Murgia et al. 2009, 2010b, and references therein). The dotted lines indicate regions of constant synchrotron emissivity. The central brightness of A1689 has been rescaled at 1.4 GHz with $\alpha = 1$ (see text).

where the radio halo emission is higher than a level of 3σ have been considered. The radial profile was produced by using the same concentric annuli presented in Fig. 2.4. Each dot represents the average emission in each annulus. By fitting the trend with a power law relation

$$I_{1.2\,\mathrm{GHz}} \propto I_{\mathrm{X}}^{\mathrm{a}}, \tag{2.2}$$

we obtained a=0.42±0.02 (Fig. 2.6, *left panel*), reinforcing the turbulence model of particle acceleration (e.g. Xu et al. 2010). The sublinear slope comes from the radial profile of the radio emission being flatter than the X-ray one, as shown in the *right panel* of Fig. 2.6, as in Coma and in A2319 (Govoni et al. 2001a; Brown & Rudnick 2011). A similar analysis was performed for the mini-halo in the Ophiuchus cluster, where a superlinear correlation has instead been observed (Govoni et al. 2009).

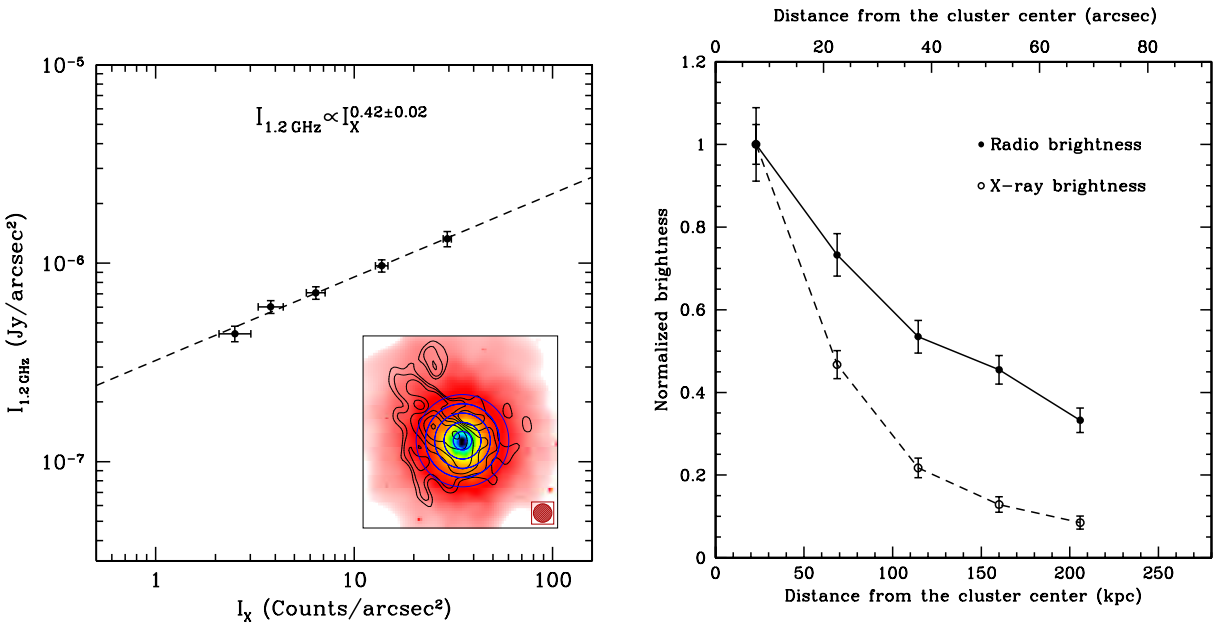

Figure 2.6 *Left*: Azimuthal average of the radio brightness at 1.2 GHz versus the *Chandra* X-ray brightness in A1689. Each dot represents the average of the emission in an annulus of half beam-width size (15″) centered on the cluster X-ray peak, as shown in the inset. *Right*: Normalized radio and X-ray radial profiles.

2.4 Discussion and conclusion

As a part of an ongoing program aimed at finding new diffuse sources in galaxy clusters, we have investigated the radio emission of the complex galaxy cluster A1689. We analyzed deep radio observations carried out with the Very Large Array at 1.2 and 1.4 GHz in different configurations. To properly map these diffuse sources, high sensitivity to the extended features is needed, along with modest (∼50 kpc) linear resolution in order to distinguish a real diffuse source from the blend of unrelated discrete sources. The availability of sensitive radio images at different resolutions revealed that at the center of A1689 a few discrete sources are surrounded by a diffuse low surface brightness emission associated with the intracluster medium.

We studied the morphological and physical radio properties (i.e., lengthscale, central brightness, average emissivity) of the diffuse emission in A1689 in comparison with that of other halos known in the literature, by fitting their azimuthally averaged brightness profile with an exponential law. The best-fit of the exponential model at 1.2 GHz yields a central brightness of I_0=1.7 μJy/arcsec^2 and r_e = 149 kpc. From the central brightness and the e-folding radius, we derived an average radio emissivity of $\langle J \rangle = 1.7 \times 10^{-42}$ erg s^{-1}cm^{-3}Hz^{-1}. This value is consistent with that of all the other radio halo clusters known to date since Murgia et al. (2009) find that radio halo emissivities are characterized by a narrow distribution with mean value $\langle J \rangle \sim 10^{-42}$ erg s^{-1}cm^{-3} Hz^{-1}. Moreover, we investigated the possible presence of a radio - X-ray correlation in A1689. We found a sub-linear slope, which comes from the radial profile of the radio emission being flatter than the X-ray one.

The presence of a radio halo in A1689 strongly supports the cluster merger scenario discussed by Leonard et al. (2011). Detecting a diffuse non-thermal emission in a high-mass, merging structure agrees with the evidence that radio halos are mostly found in massive merging systems.

3

New radio halo sources

Radio halos are very faint and rare. At the detection limit of the NVSS, the radio halo detection rate is only 5% for a complete cluster sample and increases up to 35% when clusters with high X-ray luminosity ($L_{X\,0.1-2.41\,\mathrm{keV}} > 0.6\,10^{45}\mathrm{erg\cdot s^{-1}}$) are considered (Giovannini et al. 1999). Up to now, only about 40 radio halos have been observed (e.g. Giovannini et al. 2009; van Weeren et al. 2011a), among which the most powerful and distant is MACS J0717.5+3745 (Bonafede et al. 2009a; van Weeren et al. 2009). Because of the scanty statistics, the discovery of new halos provides important information on this class of sources. As part of an ongoing program aimed to investigate the presence of radio halo emission from clusters in merger belonging to complex X-ray systems, we have analyzed archival VLA observations (VLA Programs AM0469, AB1180, AB0699, AO0048, AM0702 and AD0509). We found 6 new radio halos in the galaxy clusters A781 (Govoni et al. 2011), A523 (Giovannini et al. 2011), A800, A1550, and CL1446+26 (Govoni et al. in preparation) described in this Chapter, and A1689 (Vacca et al. 2011) presented in Chapter 2. In the following we present the results.

3.1 Abell 800

Very little radio, X-ray, and optical information exists in the literature for A800 and nothing is reported regarding the dynamical state of the cluster. A800 (RXCJ0928.6+3747) is a low X-ray luminosity cluster which is part of the Northern ROSAT All-Sky (NORAS) Galaxy Cluster Survey by Böhringer et al. (2000). Its redshift is z=0.2223 and its X-ray luminosity (corrected for our cosmology) in the 0.1–2.4 keV band is 2.25×10^{44} erg/sec.

Low resolution radio contours at 1.4 GHz of A800 are shown in the *left-hand panel* of Fig. 3.1. This image was obtained with the VLA in D configuration and has an FWHM beam of $62.45'' \times 41.59''$. The radio contours are overlaid on the cluster X-ray image taken from the ROSAT All Sky Survey in the 0.1–2.4 keV band. The X-ray image shows a disturbed, irregular structure with an elongation in the Northwest-Southeast direction, indicating an ongoing merger activity. Slightly displaced from the X-ray center, we detected a diffuse low-surface brightness radio emission, which we classify as a radio halo. Although in most of the radio halos known in the literature the radio morphology is very similar to the thermal gas density distribution, in the case of A800

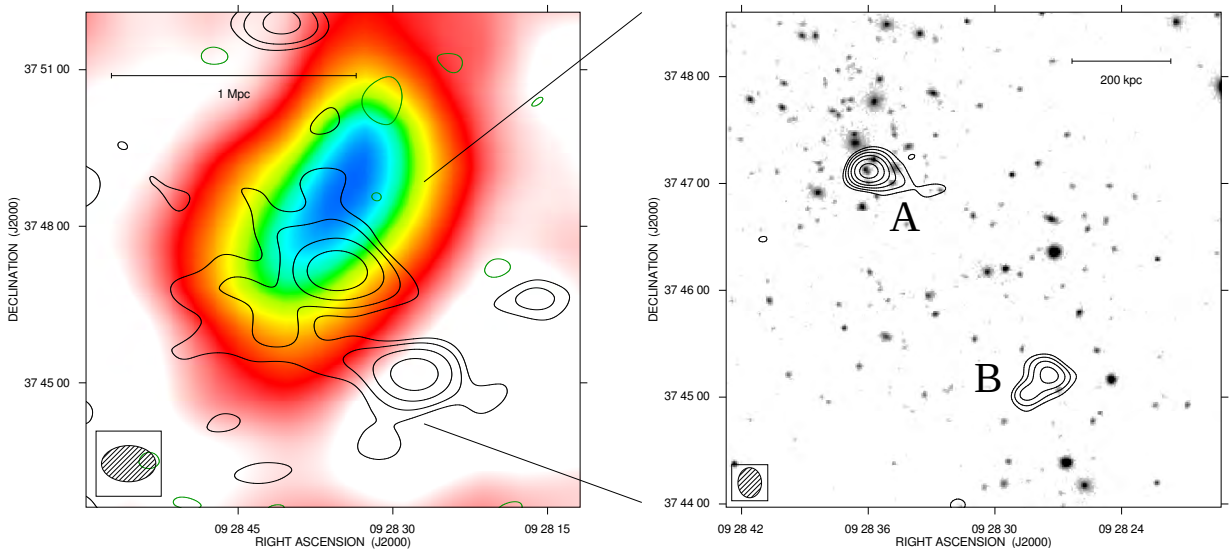

Figure 3.1 **Abell 800.** *Left*: total intensity radio contours of A800 at 1.4 GHz with the VLA in D configuration (VLA Program AM469). The image has an FWHM of 62.45″×41.59″ (PA=-89.52°). The contour levels are drawn at −0.3 (green), 0.3 mJy/beam, and the rest are spaced by a factor of 2. The sensitivity (1σ) is 0.1 mJy/beam. Total intensity radio contours are overlaid on the ROSAT PSPC X-ray image in the 0.1–2.4 keV band, taken from the ROSAT All Sky Survey. The X-ray image has been convolved with a Gaussian of σ=45″. *Right*: zoom of total intensity radio contours in the center of A800 at 1.4 GHz with the VLA in C configuration (VLA Program AO0048). The image has an FWHM of 13.26″ × 16.88″ (PA=-89.81°). The first contour level is drawn at 0.3 mJy/beam, and the rest are spaced by a factor $\sqrt{2}$. The sensitivity (1σ) is 0.1 mJy/beam. The contours of the radio intensity are overlaid on the optical image taken from the SLOAN Digital Sky Survey (red plate).

this similarity is not present.

To separate the diffuse radio emission from discrete sources we produced an image at higher resolution. In the *right-hand panel* of Fig. 3.1 we present the radio contours of A800 at 1.4 GHz taken with the VLA in C configuration. This image has an FWHM beam of 13.26″ × 16.88″. The radio contours are overlaid on the optical image taken from the SLOAN Digital Sky Survey[1]. Two discrete radio sources (labeled with A and B) are embedded in the diffuse cluster emission. Source A is located on south of the cluster X-ray center, in coincidence with the concentration of likely cluster members. Its flux density (primary beam corrected) is (3.5±0.3) mJy. Source B is located on south-west of source A and its flux density is (2.3±0.2) mJy.

The total flux density is calculated from the D dataset after a primary beam correction by integrating the total intensity surface brightness in the region of the diffuse emission down to the 3σ level. The resulting total flux density is estimated to be (16.4±0.8) mJy. By subtracting the flux density of the embedded discrete sources A, and B, as derived in the C configuration dataset, a flux density of (10.6±0.9) mJy appears to be associated with the low brightness diffuse emission. This flux density value corresponds to a radio power of $P_{1.4\,\mathrm{GHz}} = 1.51 \times 10^{24}$ W Hz^{-1}.

[1] http://www.sdss.org/

3.2 Abell 1550

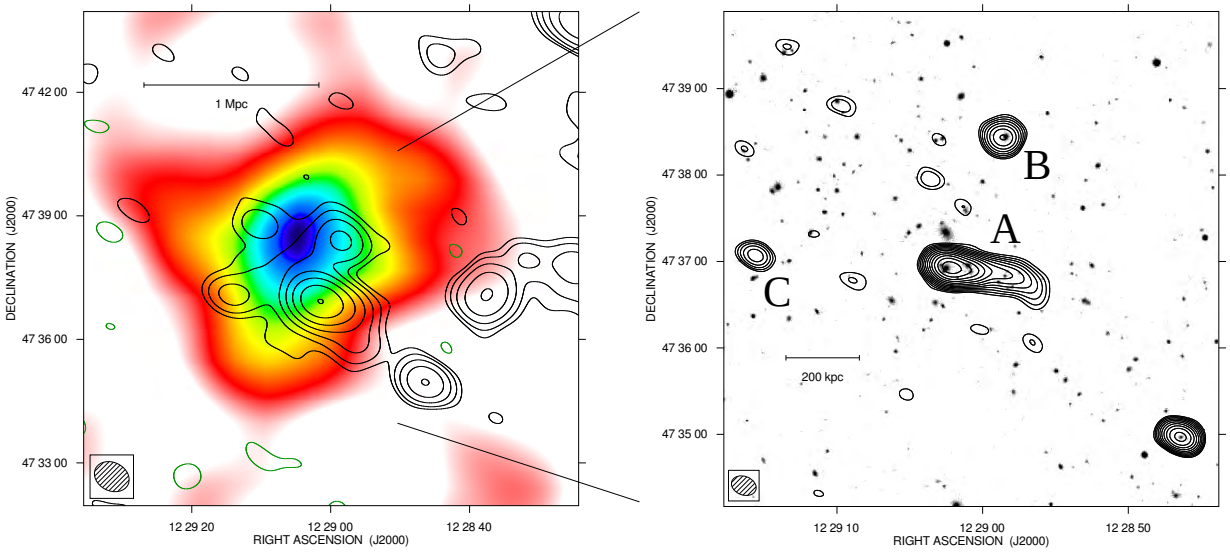

Figure 3.2 **Abell 1550.** *Left*: total intensity radio contours of A1550 at 1.4 GHz with the VLA in D configuration (VLA Program AM469). The image has an FWHM of $52.70'' \times 41.22''$ (PA=63.08°). The contour levels are drawn at -0.2, 0.2 mJy/beam, and the rest are spaced by a factor of 2. The sensitivity (1σ) is 0.07 mJy/beam. Total intensity radio contours are overlaid on the ROSAT PSPC X-ray image in the 0.1–2.4 keV band, taken from the ROSAT All Sky Survey. The X-ray image has been convolved with a Gaussian of σ=45″. *Right*: zoom of total intensity radio contours in the center of A1550 at 1.4 GHz with the VLA in C configuration (VLA Program AM0702). The image has an FWHM of $17.71'' \times 12.94''$ (PA=69.19°). The first contour level is drawn at 0.15 mJy/beam, and the rest are spaced by a factor $\sqrt{2}$. The sensitivity (1σ) is 0.04 mJy/beam. The contours of the radio intensity are overlaid on the optical image taken from the SLOAN Digital Sky Survey (red plate).

A1550 (RXCJ1229.0+4737) is a galaxy cluster at a redshift z=0.254 with an X-ray luminosity (corrected for our cosmology) in the 0.1–2.4 keV band of 3.51×10^{44} erg/sec (Böhringer et al. 2000).

Low resolution radio contours at 1.4 GHz of A1550 are shown in the *left-hand panel* of Fig. 3.2. This image was obtained with the VLA in D configuration and has an FWHM beam of $52.70'' \times 41.22''$. The radio contours are overlaid on the cluster X-ray image taken from the ROSAT All Sky Survey in the 0.1–2.4 keV band. The external X-ray emission is elongated in the east-west direction, while the inner region is extended along north-south. As in the case of A800, the complex X-ray morphology is believed to be the result of a recent or ongoing major merger. Surrounding the X-ray center we detected a diffuse low-surface brightness radio emission, which we classify as a radio halo.

To separate the diffuse radio emission from discrete sources we produced an image at higher resolution. In the *right-hand panel* of Fig. 3.2 we present the radio contours of A1550 at 1.4 GHz taken with the VLA in C configuration. This image has an FWHM beam of $17.71'' \times 12.94''$. The radio contours are overlaid on the optical image taken from the SLOAN Digital Sky Survey. Three discrete radio sources (labeled with A, B, and C) are clearly embedded in the radio halo. Spots of very faint emission are also detected in the C configuration dataset and, since they do not coincide

with any discrete source detected in the FIRST survey (Becker et al. 1995), we consider these emission associated with the peaks of the radio halo detected in the D configuration dataset.

A total flux density of (26.5±1.3) mJy is calculated from the D dataset, after primary beam correction, by integrating the total intensity surface brightness in the region of the diffuse emission down to the 3σ level. By subtracting the flux density (primary beam corrected) of the three embedded discrete sources A (15.8±0.8) mJy, B (2.2±0.2) mJy, and C (0.8±0.2) mJy as calculated from the C configuration dataset, a flux density of (7.7±1.5) mJy appears to be associated with the low brightness diffuse emission. This flux density value corresponds to a radio power of $P_{1.4\,\mathrm{GHz}} = 1.49 \times 10^{24}\,\mathrm{W\,Hz^{-1}}$.

3.3 CL 1446+26 - CL 1447+26 - ZwCl 1447.2+2619

CL 1446+26, known also as CL 1447+26 or ZwCl 1447.2+2619, is a rich galaxy cluster located at z=0.370 (Dressler et al. 1997). The X-ray emission of this cluster has been investigated by Wu et al. (1999)[2] that found an X-ray luminosity in the 0.1–2.4 keV band of 3.42×10^{44}erg/sec (corrected for our cosmology), while at radio wavelengths, CL 1446+26 has been studied by Owen et al. (1999) and Giovannini et al. (2009). By using a VLA dataset in C configuration, Giovannini et al. (2009) found the presence of diffuse radio emission in-between the two X-ray peaks in the NE of the cluster plus several head-tail radio galaxies. Because of its location, they classified the diffuse source as a radio relic.

Low resolution radio contours at 1.4 GHz of CL 1446+26 are shown in the *left-hand panel* of Fig. 3.3. This image was obtained with the VLA in D configuration and has an FWHM of 51.85″×43.05″. The radio contours are overlaid on the cluster X-ray image taken from the ROSAT All Sky Survey in the 0.1–2.4 keV band. The X-ray emission reveals the presence of two substructures, one to the NE and one to the SW, with a double-peaked morphology each. A peculiar diffuse radio emission, unrelated from the activity of discrete sources, is clearly visible. Our lower resolution image shows in coincidence with the Northern clump a radio emission more extended than that obtained by Giovannini et al. (2009). In particular, this new image seems to indicate that the diffuse emission is indeed a central radio halo rather than a peripheral relic source, as previously stated. In addition, a new elongated diffuse radio emission in correspondence of the Southern sub-cluster has been detected. This diffuse emission is not regular as in giant radio halos (e.g. Coma, Kim et al. 1990; Giovannini et al. 1993) and it has the same spatial location of the less bright X-ray sub-structure.

To separate the diffuse radio emission from discrete sources we used the image at 1.4 GHz taken with the VLA in C configuration presented by Giovannini et al. (2009) (*right panel* of Fig. 3.3). This image has an FWHM beam of 15″ × 15″. Radio contours are overlaid on the optical image taken from the SLOAN Digital Sky Survey. Six radio galaxies (labeled with A, B, C, D, E and F) are embedded in the diffuse emission. The diffuse source in the NE region of the cluster is still detectable in the C array dataset, as previously pointed by Giovannini et al. (2009). Given their location and morphology, in the following we define the norther emission as a radio halo and the elongated southern emission as a relic. The radio halo appears to be connected through a low brightness diffuse bridge to the relic. However, a deeper follow-up is necessary to clarify the nature of this system.

In the Northern emission a total flux density of (42.0±2.1) mJy is calculated from the D dataset, after a primary beam correction, by integrating the total intensity surface brightness in the region of

[2]The bolometric X-ray luminosity has been converted to the 0.1−2.4 keV band using Table 5 of Böhringer et al. (2004), assuming an intracluster temperature of T≃5 keV.

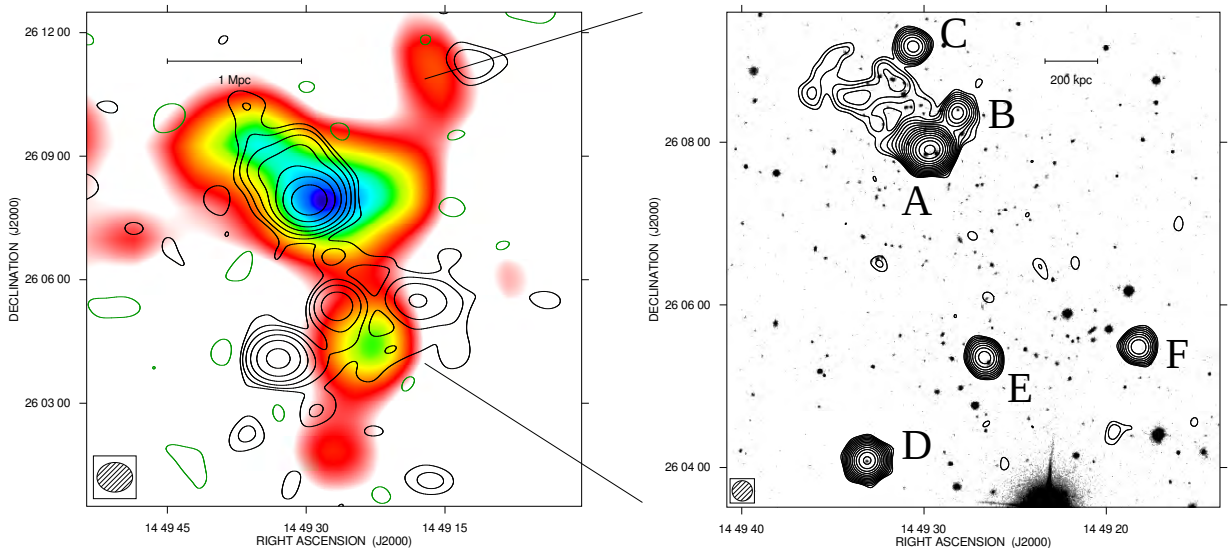

Figure 3.3 **CL 1446+26.** *Left*: total intensity radio contours of CL 1446+26 at 1.4 GHz with the VLA in D configuration (VLA Program AM469). The image has an FWHM of 51.85″ × 43.05″ (PA=-89.28°). The contour levels are drawn at −0.25 (green), 0.25 mJy/beam, and the rest are spaced by a factor of 2. The sensitivity (1σ) is 0.08 mJy/beam. Total intensity radio contours are overlaid on the ROSAT PSPC X-ray image in the 0.1–2.4 keV band, taken from the ROSAT All Sky Survey. The X-ray image has been convolved with a Gaussian of σ=45″. *Right*: zoom of total intensity radio contours in the center of CL 1446+26 at 1.4 GHz with the VLA in C configuration, image (VLA program AO0149) taken from Giovannini et al. (2009). The image has an FWHM of 15″ × 15″ (PA=0°). The first contour level is drawn at 0.15 mJy/beam, and the rest are spaced by a factor $\sqrt{2}$. The sensitivity (1σ) is 0.05 mJy/beam. The contours of the radio intensity are overlaid on the optical image taken from the SLOAN Digital Sky Survey (red plate).

the diffuse emission down to the 3σ level. By subtracting the flux density (primary beam corrected) of the discrete sources A (29.7±1.5) mJy, B (2.4±0.2) mJy , and C (2.2±0.2) mJy as derived in the higher resolution image, a flux density of (7.7±2.6) mJy appears to be associated with the radio halo. This flux density value corresponds to a radio power of $P_{1.4\,\mathrm{GHz}} = 3.57 \times 10^{24} \mathrm{W\,Hz^{-1}}$. In the southern emission by subtracting the flux density of the discrete sources D (11.0±0.5) mJy, E (3.2±0.2) mJy, and F (2.5±0.2) mJy from the total flux density (22.0±1.1) mJy, a flux density of (5.3±1.2) mJy appears to be associated with the relic.

3.4 Abell 523

A523 is a very rich cluster with a low X-ray luminosity: Ebeling et al. (1998) reported a cluster X-ray luminosity in the 0.1–2.4 keV band of 1.07×10^{44} erg/sec, while Böhringer et al. (2000) reported a slightly lower value of 0.9×10^{44} erg/sec (after cosmological corrections). To date, only the redshift for the brightest cluster galaxy [RA=04^{h}:59^{m}:12.97^{s}, DEC=+08^{d}:49^{m}:41.3^{s} (J2000.0)] has been acquired (z=0.1036, Crawford et al. 1999), whose radio emission has not yet been detected.

Low resolution radio contours at 1.4 GHz of A523 are shown in the *left-hand panel* of Fig. 3.4. This image was obtained with the VLA in D configuration and has an FWHM beam of 65″ × 65″. The radio contours are overlaid on the cluster X-ray image taken from the ROSAT All Sky Survey

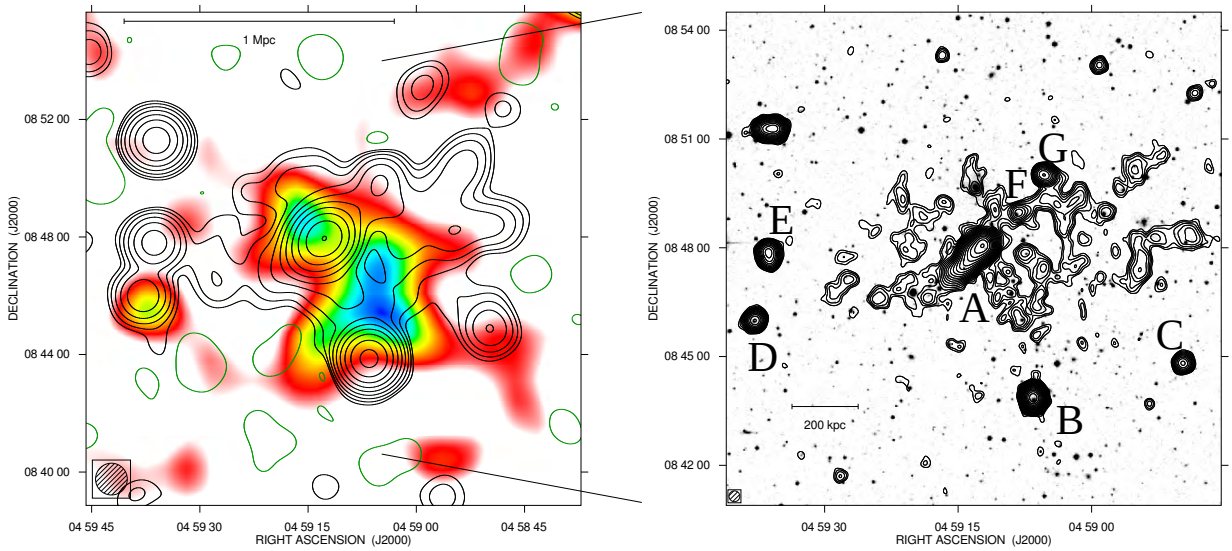

Figure 3.4 **Abell 523.** *Left*: total intensity radio contours of A523 at 1.4 GHz with the VLA in D configuration (VLA Program AB1180). The image has an FWHM of $65'' \times 65''$ (PA=0°). Contour levels are drawn at -0.18 (green), 0.18 mJy/beam, and the rest are spaced by a factor of 2. The sensitivity (1σ) is 0.06 mJy/beam. Total intensity radio contours are overlaid on the ROSAT PSPC X-ray image in the 0.1–2.4 keV band, taken from the ROSAT All Sky Survey. The X-ray image has been convolved with a Gaussian of σ=45″. *Right*: zoom of total intensity radio contours in the center of A523 at 1.4 GHz with the VLA in C configuration (VLA Program AB1180). The image has an FWHM of $18'' \times 18''$ (PA=0°). The first contour level is drawn at 0.102 mJy/beam, and the rest are spaced by a factor $\sqrt{2}$. The sensitivity (1σ) is 0.034 mJy/beam. The contours of the radio intensity are overlaid on the optical image taken from the Digitized Sky Surveys 2 (red plate).

in the 0.1–2.4 keV band. The X-ray data indicate a merging cluster structure, where the main cluster is identified with a SSW structure. As shown by its irregular shape and lack of a dominant galaxy, the SSW cluster is not in a relaxed stage, and is now strongly interacting (major merging) with a more compact cluster on the NNE direction, dominated by the brightest cluster galaxy (BCG). The radio morphology is irregular and elongated in the EW direction with a largest angular size of ∼12′. The radio emission permeates both merging clumps, corresponding to ∼1.3 Mpc, as found e.g. in the Bullet cluster (Liang et al. 2000). This is also similar to the case e.g. of A2255 (Govoni et al. 2005) or A665 (Giovannini & Feretti 2000) where the radio halos are elongated in the direction of the cluster merger. The radio structure in A523 is therefore typical of radio halos.

To separate the diffuse radio emission from discrete sources we produced an image at higher resolution. In the *right-hand panel* of Fig. 3.4 we present the radio contours of A523 at 1.4 GHz taken with the VLA in C configuration. This image has an FWHM beam of $18'' \times 18''$. The radio contours are overlaid on the optical image taken from the Digitized Sky Survey 2[3]. At this relatively high angular resolution, discrete sources are well separated and the diffuse emission is still visible.

The radio emission does not show any morphological feature typical of radio relics such as high brightness filamentary structures or a transverse flux asymmetry (see e.g. van Weeren et al. 2011b). Therefore, its classification as a radio relic is very unlikely and we classify the diffuse radio emission in A523 as a giant radio halo. Seven discrete sources (labeled with A, B, C, D, E, F, and G) can be identified in the radio halo emission. Their flux density are respectively: (104±3) mJy,

[3] http://archive.eso.org/dss/dss

(61±2) mJy,(2.25±0.07) mJy,(5.3±0.2) mJy,(7.9±0.2) mJy, (0.59±0.05) mJy, and (4.81±0.1) mJy. By subtracting embedded discrete sources, the estimated halo flux density is (59±5) mJy, corresponding to a total radio power $P_{1.4\,\mathrm{GHz}}$=1.58×10^{24} W/Hz.

3.5 Abell 781

A781 belongs to a complex system that is characterized by extended X-ray sources that may form part of a line of clusters along a filament (e.g. Jeltema et al. 2005). As previously pointed out by Sehgal et al. (2008), the X-ray image reveals that A781 consists of a large main cluster (z=0.3004) connected to a subcluster. The X-ray and weak-lensing analysis by Sehgal et al. (2008) suggest that the main cluster may be undergoing a merger with the subcluster to the southwest. A781 is part of the ROSAT brightest cluster sample by Ebeling et al. (1998). Its X-ray luminosity in the 0.1–2.4 keV band is 1.1×10^{45} erg/sec, corrected for our cosmology.

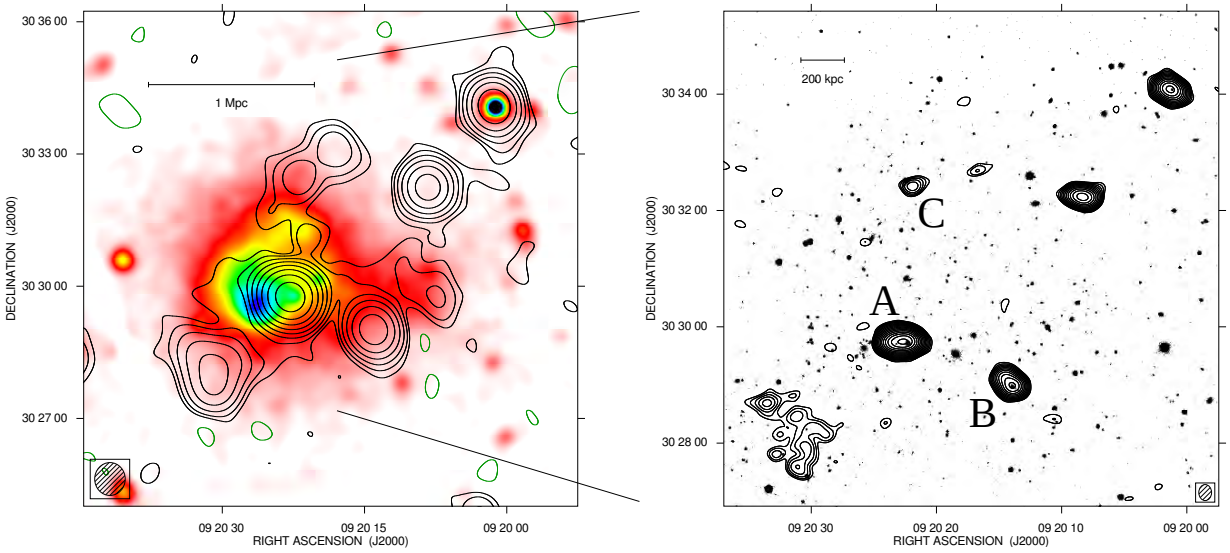

Figure 3.5 **Abell 781.** *Left*: total intensity radio contours of A781 at 1.4 GHz with the VLA in D configuration (VLA Program AM469). The image has an FWHM of 41.6″ × 44.8″ (PA=16.6°). The contour levels are drawn at −0.3 (green), 0.3 mJy/beam, and the rest are spaced by a factor of 2. The sensitivity (1σ) is 0.1 mJy/beam. Total intensity radio contours are overlaid on the XMM X-ray image in the 0.2–12 keV band. The X-ray image has been convolved with a Gaussian of σ=8″. *Right*: zoom of total intensity radio contours in the center of A781 at 1.4 GHz with the VLA in C configuration (VLA Program AO0048). The image has an FWHM of 13.2″ × 16.5″ (PA=-84.9°). The first contour level is drawn at 0.27 mJy/beam, and the rest are spaced by a factor $\sqrt{2}$. The sensitivity (1σ) is 0.09 mJy/beam. The contours of the radio intensity are overlaid on the optical image taken from the SLOAN Digital Sky Surveys (red plate).

The A781 system was observed with the Giant Metrewave Radio Telescope at 610 MHz by Venturi et al. (2008). A peripheral patch of diffuse emission, with no obvious optical counterpart, peaking at RA(J2000)=09^{h}:20^{m}:32.2^{s} and DEC(J2000)=30^{d}:27^{m}:34.2^{s} has been detected, and the authors suggested that it might be a relic source, but no hint of radio halo emission was found. The presence of diffuse cluster-scale radio emission close to the main cluster X-ray centroid, indicative

of a radio halo, was suggested by Rudnick & Lemmerman (2009), by reprocessing radio images from the Westerbork Northern Sky Survey (WENSS, Rengelink et al. 1997) at 327 MHz.

Low resolution radio contours at 1.4 GHz of A781 are shown in the *left-hand panel* of Fig. 3.5. This image was obtained with the VLA in D configuration and has an FWHM beam of 41.6″ × 44.8″. The radio contours are overlaid on the cluster X-ray image taken with the XXM-*Newton* satellite in the 0.2–12 keV band. We found that the central region of the main cluster is permeated by diffuse low-surface brightness emission, which we classified as a radio halo. The radio halo appears to be linked to the brighter peripheral patch previously found by Venturi et al. (2008). In addition, the diffuse radio emission of the main cluster is elongated toward the subcluster. As measured from the 3σ radio isophote, the overall diffuse emission has an angular extension of about 7′ (≃1.8 Mpc at the cluster distance).

To separate the diffuse radio emission from discrete sources we produced an image at higher resolution. In the *right-hand panel* of Fig. 3.5 we present the radio iso-contours of A781 at 1.4 GHz, taken with the VLA in C configuration. This image has an FWHM beam of 13.2″×16.5″. The radio contours are overlaid on the optical image taken from the SLOAN Digital Sky Survey. Although the relatively high resolution of this image is not particularly suitable for detecting diffuse cluster emission, the peripheral patch of diffuse emission is clearly visible in the C array dataset too. The discrete sources embedded in the radio halo emission (labeled with A, B, and C) show an optical counterpart and their flux densities are (67.0±2.0) mJy, (14.7±0.5) mJy, and (1.50±0.005) mJy, respectively. Source A, which is located about 50″ west of the X-ray peak of the main cluster, is the brightest radio source in the field. The total flux density in the region of the main and subcluster is (119±4) mJy. By subtracting the flux density of the embedded discrete sources A, B, and C as derived in the C configuration dataset, a flux density of (36±5) mJy appears to be associated with the low brightness diffuse emission. This flux density value corresponds to a radio power $P_{1.4\,\mathrm{GHz}}$=1.0×10^{25} W/Hz. The peripheral patch alone has a flux density (15.5±0.5) mJy. Thus, if we consider the radio halo separated by the peripheral patch, it results in a flux density of (20.5±5) mJy. This value corresponds to a radio power $P_{1.4\,\mathrm{GHz}}$=5.9×10^{24} W/Hz.

3.6 Statistics of the physical properties of clusters hosting radio halos

The radio halos recently discovered and presented in this thesis (see references in the previous Sections and in Chapter 2) contribute to improve the scanty statistics, increasing the total number of sources to 45. In Table 3.1 a complete list of all radio halos presently known is given, inclusive of literature and new radio halos. The study of this sample from a statistical point of view is useful to better understand this still enigmatic class of sources. In this Section we present some discussion about the statistics of radio halos versus redshift, the relation between their radio power and largest linear scale at 1.4 GHz, and the similarities between the X-ray and radio properties at 1.4 GHz.

3.6.1 Radio halos and redshift

Usually, radio halos are found in nearby clusters. Up to now, among the 45 radio halos observed, 34 are located at z <0.3, 7 at 0.3< z <0.4, and 3 at z >0.4, with an overall average redshift $\langle z\rangle$=0.21 (see Fig. 3.6). The most distant ones are the powerful radio halos MACSJ0717.5+3745 and CL0016+16. The observed redshift distribution is certainly affected by several biases. Nearby large halos could be missing due to baseline limitations of current interferometric surveys. A Mpc halo at redshift < 0.1 is larger than 10′ while the angular size limit for the VLA at 1.4 GHz is 7′

for snapshot observations like the NVSS and 1′ for snapshot observations like the FIRST. On the other hand, at high redshift only the most luminous halos can be observed because of sensitivity limits. For these reasons, at low redshifts just the smallest radio halos can be detected, while at high redshifts just the brightest ones (see Giovannini et al. 2009).

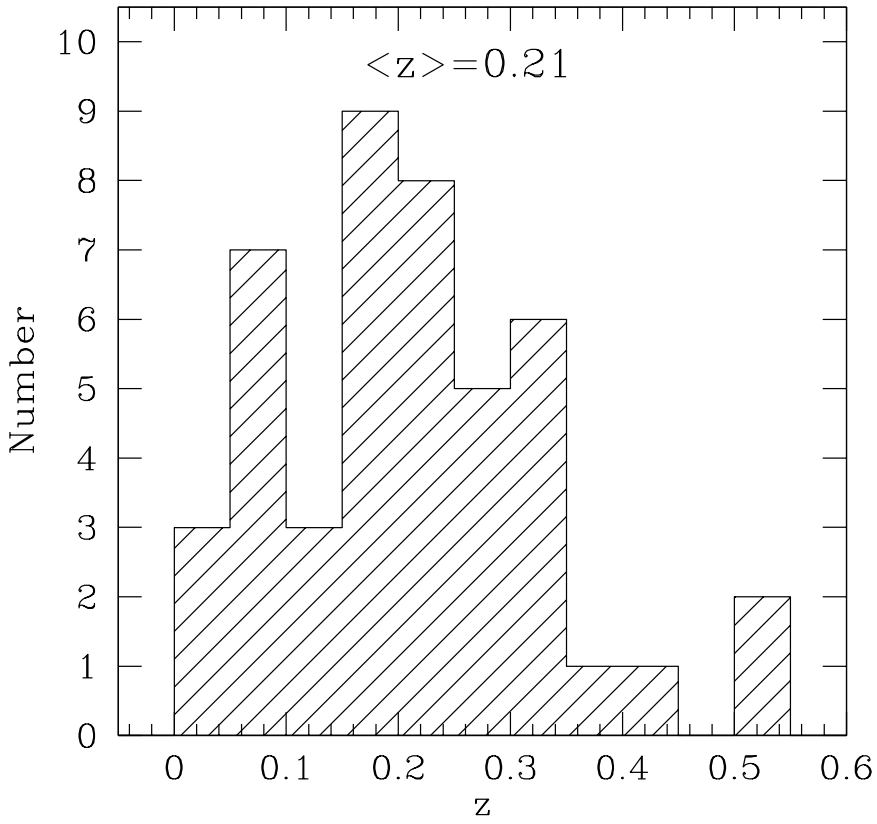

Figure 3.6 Histogram of the redshift values for the clusters containing a radio halo. Clusters hosting a radio halo appear to have an average redshift of 0.21 and just three radio halos have been observed at a redshift larger than 0.4.

3.6.2 Radio halo power and largest angular size

In Fig. 3.7 the radio halo power $P_{1.4\,\mathrm{GHz}}$ versus the largest linear size of the radio halo *LLS* at 1.4 GHz is shown. Blue dots indicate the radio halos from literature (see Table 3.1 and references therein), while red triangles identify the new radio halos found by Govoni et al. (2011), Giovannini et al. (2011), Vacca et al. (2011) and Govoni et al. in preparation (see also this thesis). A correlation can be observed: the most powerful radio halos are, the most they are extended. Indeed, on average the radio halo power scales as LLS^3, as suggested by the black dashed line. This scaling of the radio power with LLS^3 has been already found by Murgia et al. (2009). They note that since the radio power of the source is given by the product of the radio halo emissivity and the volume and they find a radio halo emissivity quite constant among all radio halos, a consequent scaling of the radio halo power with the volume is expected. Just few outsiders can be identified: the most evident is MACSJ0717.5+3745.

Recently, the trend between the radio halo power and their size has been investigated by Giovannini et al. (2009). They pointed out that both small and large radio halos seem to follow the correlation, suggesting a common origin and physical mechanism for radio halos of different size. A similar approach has been previously presented by Cassano et al. (2007) by using the geometric mean of the minimum and maximum radius of the diffuse emission instead than *LLS*. Since the *LLS* and the minimum and maximum radius have been measured by using the 3σ isophotes, they depend on the sensitivity of the radio image and therefore should be considered carefully. A better analysis could be performed by adopting as physical size of radio halos their *e*-folding radius r_e, i.e. the radius at which the brightness drops of a factor e^{-1} respect to the central value (Murgia et al. 2009, see also 1.4.3). In fact, this parameter is relatively independent on the sensitivity of the observations. Since detailed and deep observations are not available for all radio halos, this parameter has been calculated just for a dozens of these sources.

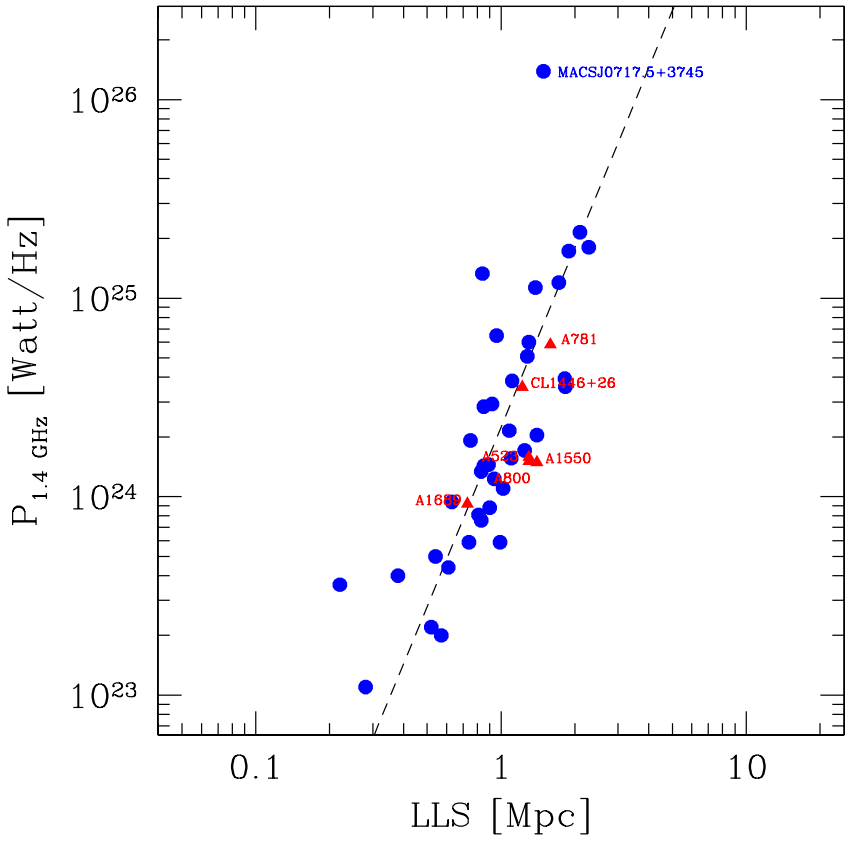

Figure 3.7 Radio halo power $P_{1.4\,GHz}$ versus the largest linear size (*LLS*) at 1.4 GHz. Blue dots are radio halos taken from the literature, while red triangles are the new radio halos presented in this thesis (see Chapter 2, this Chapter and Table 3.1). The dashed black line corresponds to a radio halo power that scales as LLS^3.

3.6.3 Radio halo power and cluster X-ray properties

As pointed out in the introduction to this Chapter, present observations show that radio halo physical properties appear deeply connected with the X-ray properties of their host clusters. In Fig. 3.8

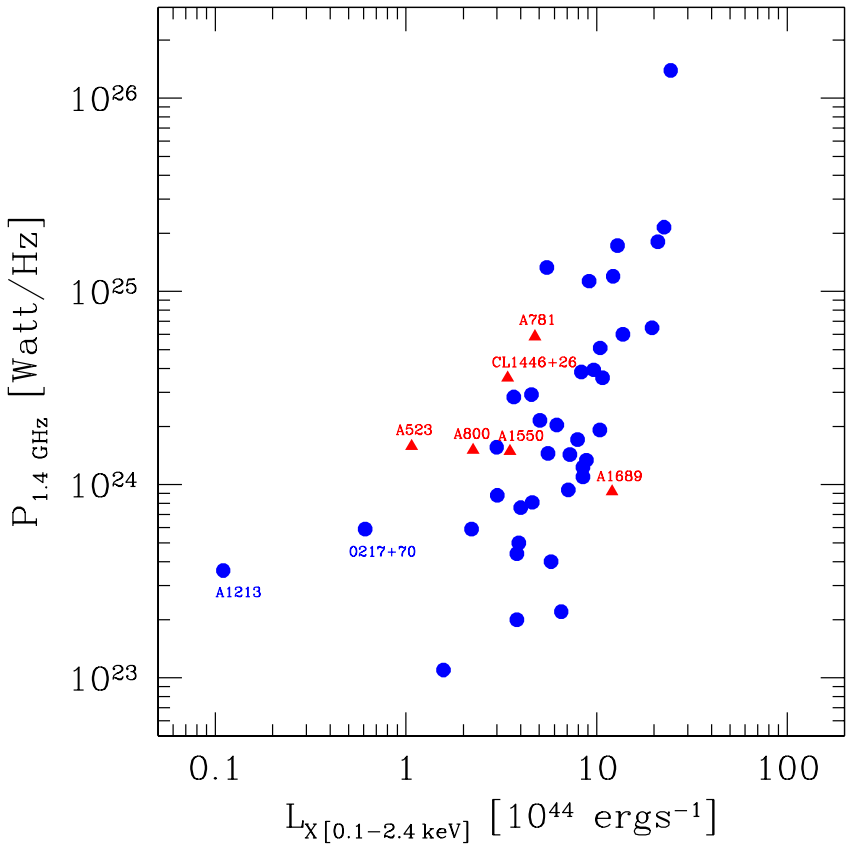

Figure 3.8 Radio halo power at 1.4 GHz $P_{1.4\,GHz}$ versus cluster X-ray luminosity in the 0.1-2.4 keV band $L_{X\,[0.1-2.4\,keV]}$. Blue dots are radio halos taken from the literature, while red triangles are the new radio halos presented in this thesis (see Chapter 2, this Chapter and Table 3.1).

and in Fig. 3.9, the radio halo power at 1.4 GHz $P_{1.4\,GHz}$ versus the X-ray luminosity in the 0.1-2.4 keV band $L_{X\,[0.1-2.4\,keV]}$ and the X-ray temperature T are respectively shown. As before, blue dots indicate radio halos from literature, while red triangles identify new radio halos. All radio halos have been observed in clusters showing clear distortion in the X-ray morphology, hint of a strong link between the radio halo phenomenon and the dynamical state of the cluster. The strong correlation between the radio power at 1.4 GHz $P_{1.4\,GHz}$ and the X-ray luminosity in the 0.1-2.4 keV band $L_{X\,[0.1-2.4\,keV]}$, as well as the broader correlation between the radio power at 1.4 GHz $P_{1.4\,GHz}$ and the X-ray temperature T, confirm the deep connection between X-ray and radio properties in clusters. These empirical relationships indicate that the most powerful radio halos are expected to be found in the most X-ray luminous and hot clusters. Recently, some powerful radio halos with a radio power higher than predicted by the radio - X-ray correlation have been observed. The most robust example is represented by A523 (Giovannini et al. 2011, see § 3.4). Giovannini et al. (2009) were the first to discuss the presence of radio halos in under-luminous X-ray clusters with the discovery in A1213 of a possible radio halo, located well outside the $P_{1.4\,GHz}$-$L_{X\,[0.1-2.4\,keV]}$ correlation. A similar case was found in the cluster 0217+70 by Brown et al. (2011). They discussed whether the low X-ray luminosity in 0217+70 could be due to an underestimate of the X-ray luminosity because of the hydrogen column density, which might be patchy at low Galactic latitudes, as that of this cluster. The existence of radio halos, associated with clusters of low X-ray luminosity raises

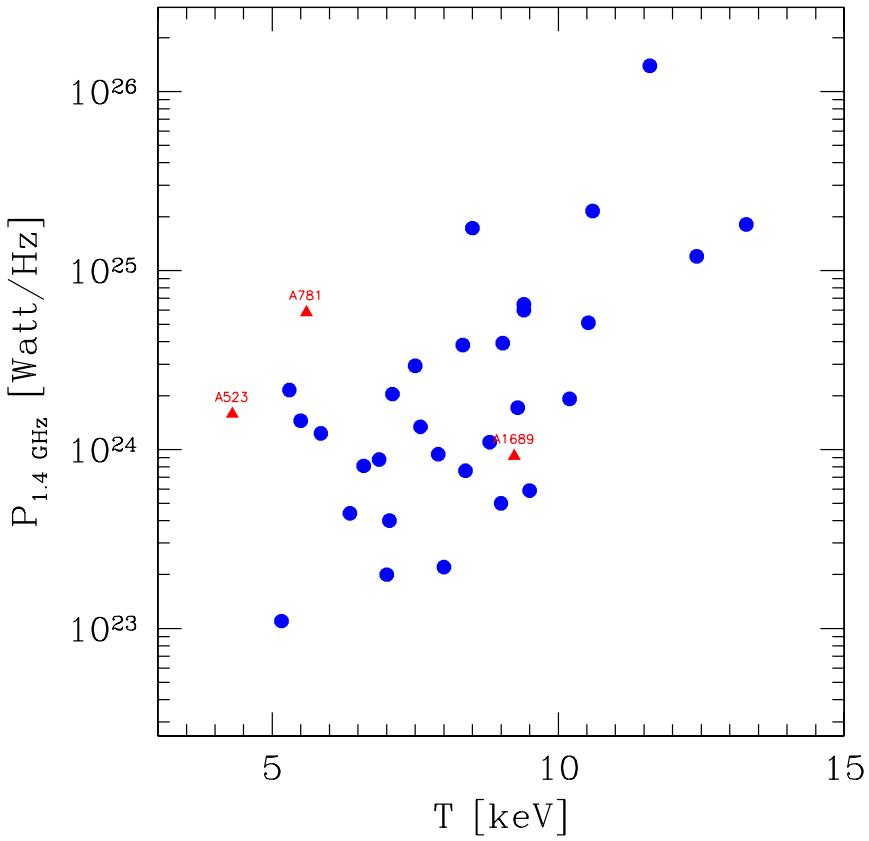

Figure 3.9 Radio halo power at 1.4 GHz $P_{1.4\,\mathrm{GHz}}$ versus cluster temperature T. Blue dots are radio halos taken from the literature, while red triangles are the new radio halos presented in this thesis (see Chapter 2, this Chapter and Table 3.1).

new questions about the origin of radio halos. They could be either young halos or clusters at a special time of the merger event, when particle acceleration processes have a higher efficiency (see Brunetti & Lazarian 2011b). Another possibility is that the X-ray luminosity might not be in these cases a good indicator of the previous cluster merging activity. Further studies are necessary to understand the conditions that give rise to these over-luminous radio halos that need to be studied in better detail with more sensitive X-ray and multi-frequency radio observations.

Table 3.1. Radio halos observed at 1.4 GHz

Source	z	kpc/″	$S_{1.4\,GHz}$	L_{rad}	LLS[a]	D_L	$L_{X\,[0.1-2.4keV]}$	T	Ref. radio	Ref. L_X,T
			mJy	10^{24}W/Hz	Mpc	Mpc	10^{44}erg/s	keV		
A209	0.206	3.34	16.9	2.04	1.40	1003	6.17	7.10	1	26,27
A399	0.0718	1.35	16.0	0.20	0.57	320	3.81	7.00	2	28,29
A401	0.0737	1.38	17.0	0.22	0.52	329	6.52	8.00	3	28,29
A520	0.1990	3.25	34.4	3.83	1.11	965	8.30	8.33	4	30,31
A521	0.2533	3.91	6.4	1.23	0.94	1268	8.47	5.85	5	26,32
A523	0.1036	1.88	59.0	1.58	1.30	472	1.07	4.30	6 (*)	30
A545	0.1540	2.64	23.0	1.45	0.89	726	5.55	5.50	3	26,33
A665	0.1819	3.03	43.1	3.93	1.82	873	9.65	9.03	7	30,31
A697	0.282	4.23	5.2	1.92	0.75	1435	10.40	10.20	8	30,34
A746	0.232	3.67	18.0	2.84	0.85	1147	3.68	-	8	8
A754	0.0542	1.04	86.0	0.59	0.99	239	2.21	9.50	3	28
A773	0.2170	3.48	12.65	1.71	1.25	1064	7.95	9.29	4	30,31
A781	0.3004	4.42	20.5	5.84	1.59	1543	4.74	5.60	9 (*)	35,36
A800	0.2223	3.55	10.6	1.51	1.3	1093	2.25	-	10 (*)	35
A851	0.4069	5.40	3.7	2.15	1.08	2205	5.04	5.3	1	35,37
A1213	0.0469	0.91	72.2	0.36	0.22	205	0.11	-	1	38
A1300	0.3072	4.49	20.0	6.00	1.3	1584	13.73	9.40	11	26,39
A1351	0.3224	4.65	39.6	13.30	0.84	1676	5.47	-	1	35
A1550	0.2540	3.92	7.7	1.49	1.4	1272	3.51	-	10 (*)	35
A1656	0.0231	0.46	640.0	0.76	0.83	99	3.99	8.38	12	28
A1689	0.1832	3.05	9.95	0.92	0.73	880	12.07	9.23	13 (*)	28
A1758a	0.279	4.20	3.9	0.94	0.63	1417	7.09	7.90	1	40,27
A1914	0.1712	2.88	64.0	5.10	1.28	816	10.42	10.53	3	28
A1995	0.3186	4.61	4.1	1.34	0.83	1653	8.83	7.59	1	35,41
A2034	0.113	2.03	13.6	0.44	0.61	519	3.81	6.36	1	30,41
A2163	0.2030	3.31	155.0	18.06	2.28	987	20.93	13.29	14	28
A2218	0.1756	2.94	4.7	0.40	0.38	839	5.77	7.05	7	30,31
A2219	0.2256	3.59	81.0	11.98	1.72	1112	12.19	12.42	3	30,31
A2254	0.1780	2.98	33.7	2.93	0.92	852	4.55	7.50	4	30, 30[b]
A2255	0.0806	1.50	56.0	0.88	0.90	362	3.01	6.87	15	28
A2256	0.0581	1.11	103.4	0.81	0.81	256	4.59	6.60	16	28
A2294	0.178	2.98	5.8	0.50	0.54	852	3.90	9.00	1	30,36
A2319	0.0557	1.07	153.0	1.10	1.02	245	8.46	8.80	17	28
A2744	0.3080	4.50	57.1	17.25	1.89	1589	12.86	8.50	4	26,39
A3562	0.0490	0.95	20.0	0.11	0.28	215	1.57	5.16	18	28
0217+70	0.0655	1.24	58.6	0.59	0.74	291	0.61	-	19	20
1E0657-56	0.2960	4.38	78.0	21.48	2.10	1517	22.59	10.6	20	26,42
CIZAJ0107.7+5408	0.1066	1.93	55.0	1.56	1.10	487	2.99	-	8	43
CIZAJ2242.8+5301	0.1921	3.17	-	-	3.1	928	6.8	9	21	21
CL0016+16	0.5456	6.37	5.5	6.48	0.96	3138	19.49	9.4	7	44
CL1446+26	0.370	5.09	7.7	3.57	1.22	1970	3.41	-	10 (*)	45
MACSJ0717.5+3745	0.5458	6.37	118.0	139.14	1.49	3139	24.46	11.6	22	44
RXCJ1314.4-2515	0.2439	3.81	20.3	3.58	1.83	1215	10.75	-	23	26
RXCJ1514.9-1523	0.2226	3.55	10.0	1.43	0.85	1095	7.23	-	24	26
RXCJ2003.5-2323	0.3171	4.59	35.0	11.31	1.38	1643	9.12	-	25	26

Col. 1: Cluster Name; Col. 2: Redshift; Col. 3: Angular to linear conversion; Col. 4: Luminosity distance; Col. 5: Flux at 20 cm;
Col. 6: Power at 20 cm in 10^{24} units; Col. 7: X-ray luminosity in the 0.1-2.4 keV band in 10^{44} units; Col. 8: Radio largest linear size estimated at a 3σ noise level;
Col. 9: References for radio data: * = This work; 1 = Giovannini et al. (2009); 2 = (Murgia et al. 2010b); 3 =Bacchi et al. (2003); 4 =Govoni et al. (2001b); 5 = Dallacasa et al. (2009);
6 = Giovannini et al. (2011); 7 =Giovannini & Feretti (2000); 8 = van Weeren et al. (2011a); 9 = Govoni et al. (2011); 10 = Govoni et al. in preparation; 11 = Reid et al. (1999);
12 = Deiss et al. (1997); 13 = Vacca et al. (2011); 14 = Feretti et al. (2001); 15 = Govoni et al. (2005); 16 = Clarke & Ensslin (2006); 17 = Feretti et al. (1997); 18 = Venturi et al. (2003);
19 = Brown et al. (2011); 20 = Liang et al. (2000); 21 = van Weeren et al. (2010); 22 = Bonafede et al. (2009a); 23 = Feretti et al. (2005); 24 = Giacintucci et al. (2011);
25 = Giacintucci et al. (2009); Col. 10: X-ray temperature; Col. 11: Reference for X-ray data: 26 = Böhringer et al. (2004); 27 =Zhang et al. (2008); 28 =Reiprich & Böhringer (2002);
29 = Markevitch et al. (1998); 30 = Ebeling et al. (1998); 30[b] = Ebeling et al. (1998), estimated from $L_X - kT$ relation; 31 =Allen (2000); 32 =Ferrari et al. (2006); 33 =David et al. (1993);
34 =Girardi et al. (2006); 35 =Böhringer et al. (2000); 36 =Maughan et al. (2008); 37 = Kotov & Vikhlinin (2005); 38 = Ledlow et al. (2003); 39 = Ebeling et al. (2010);
40 = Ebeling et al. (1996); 41 = Baldi et al. (2007); 42 = Zhang et al. (2006); 43 = Ebeling et al. (2002); 44= Ebeling et al. (2007); 45 =Wu et al. (1999);
[a] The *LLS* has been measured from the 3-σ radio isophote. Since it depends on the sensitivity of the radio image, it should be considered carefully.

4 Intracluster magnetic field

Over all the cluster volume, thermal particles and relativistic electrons are mixed with an intracluster magnetic field. Its origin and evolution is still debated, but there is a global agreement about a magnetic field seed amplified to the values presently observed by cluster formation processes through adiabatic compression, turbulence and shear flows. To discriminate between different models of intracluster magnetic field origin and evolution, the comparison with observations plays a key role.

In the following we present the current theories about the generation and evolution of intracluster magnetic fields. In addition, we give an overview of the theory at the basis of the investigation techniques applied in this work and of the present knowledge about magnetic fields in galaxy clusters. A more complete description of intracluster magnetic fields can be found in some reviews (e.g. Carilli & Taylor 2002; Govoni & Feretti 2004).

4.1 Origin and evolution

Different scenarios have been proposed to explain the origin of intracluster magnetic fields (see e.g. Dolag et al. 2008; Widrow 2002). They can be identified in three classes:

- *galactic* scenarios. They include:
  - *low-redshift* models. The intracluster medium of proto-clusters can be magnetized by galactic winds produced during star-burst phases of galaxies (Völk & Atoyan 2000; Donnert et al. 2009) or by AGN outflows (Furlanetto & Loeb 2001; Kronberg et al. 2001; Xu et al. 2010, 2011) at $z \sim 2$–3;
  - *high-redshift* models. According to these models magnetic field can be produced during early population galaxy star-burst or in the accretion flow around the black hole in an early population of AGNs, before proto-cluster formation (Kronberg et al. 1999), at $z \gtrsim 4$;

  The high degree of metallicity of the ICM (~30% solar) seems to support this scenario because, when magnetic field is injected by galactic winds or AGN outflows, matter can also be transferred in the ICM;

- *early-universe* scenarios. The generation could have taken place either in the early universe due to phase transition, with the formation of baryons and mesons from quarks and gluons, or to neutrino/photon decoupling, or during the inflation (see Grasso & Rubinstein 2001). Primordial magnetic fields can also have been produced by means of the Biermann battery effect (Biermann 1950; Kulsrud et al. 1997). This effect consist in the generation of thermionic electric currents during accretion shocks. These currents are responsible of the production of a magnetic field. This scenario could be supported by the presence of magnetic fields everywhere in the Universe.

The fields produced in these ways are characterized by strengths that are lower than those presently observed. Therefore, to match the values presently observed, an amplification mechanism is required. Such an amplification can take place during cluster mergers, thanks to shocks, bulk motions, shear flows and turbulence (e.g. Roettiger et al. 1999b; Dolag et al. 2002; Ryu et al. 2008). During cluster formation processes, shear flows drive Kelvin-Helmholtz instabilities, supposed to be able to amplify seed magnetic fields in timescales of about 10^7yr. In addition, MHD simulations performed by Roettiger et al. (1999b) indicate that during merger phenomena, shocks and bulk motions compress and stretch the field, making it filamentary. Then turbulence amplifies the magnetic field further and faster, albeit mainly locally, implying a magnetic field strength and a coherence length reconcilable with observations (Subramanian et al. 2006).

MHD simulations that trace the evolution of seed magnetic fields have recently been performed with high numerical resolution, both for the case of a galactic and of primordial origin. By following the evolution of primordial magnetic fields in cluster mergers, Dolag et al. (2005) find that the geometry of the seed magnetic field is completely changed by the cluster formation processes, almost independently on the mechanism of generation of the seed magnetic field, if it is generated before $z \sim 3$. According to their simulations, after the amplification the magnetic field strength radial profile scales as the thermal gas density in the cluster outskirts, while at the cluster center a strong dependence on the temperature has been predicted. By supposing magnetic fields injected by galactic outflows during star-burst phase of galactic evolution and later processed by structure formation, Donnert et al. (2009) find a final magnetic field that depends just weakly on the exact magnetic structure of the assumed initial magnetic field, while mainly influenced by the velocity field induced by structure formation. The possibility that intracluster magnetic fields can originate from AGNs has been investigated by Xu et al. (2009) as well. They find that, during cluster formation process, magnetic field ejected from AGNs can be spread over all the cluster volume and further be amplified by the turbulence in the intracluster medium. Xu et al. (2010) point out that this scenario requires that the injection of the magnetic field by the AGNs occurs at a previous epoch than major mergers ($z \geq 1$). Moreover, they show that the turbulence in the intracluster medium can amplify the magnetic field energy by a factor up to 1000. Therefore, the values presently observed can be explained also considering AGN injected-magnetic fields with low energy density over the cluster volume . The final magnetic energy associated to the intracluster medium depends on the turbulent energy of the intracluster medium and on the mass of the cluster rather than on the AGN injection energy(Xu et al. 2010, 2011). In addition, Xu et al. (2011) note that also the cluster dynamical state plays an important role in the intracluster magnetic field evolution and distribution. Young clusters appear less magnetized than older relaxed clusters, because the amplification requires longer time scales.

All these theories, even if different, predict rotation measure values in good agreement with the observations. This makes the understanding of the origin and evolution of intracluster magnetic fields a problem difficult to manage, since it becomes quite hard to discriminate which is the most reliable scenario.

4.2 Investigation

Intracluster magnetic fields can be investigated by means of different approaches based both on X-ray and radio observations.

In the X-ray domain, the most powerful technique relies on the analysis of the non-thermal emission due to the inverse Compton scattering of the cosmic microwave background by the synchrotron electrons, detected in the hard X-ray band (Blumenthal & Gould 1970; Harris & Grindlay 1979; Rephaeli et al. 1987; Feigelson et al. 1995; Bagchi et al. 1998). Studies of cold fronts allow as well magnetic field measurements, even if not over all the cluster volume but just locally (Vikhlinin et al. 2001b; Markevitch & Vikhlinin 2007). However, the most relevant and detailed investigations of intracluster magnetic fields are provided by observations in the radio band. The Faraday rotation of the signal produced by galaxies located behind or belonging to clusters of galaxies gives important constraints on the strength and structure of the magnetic field associated with the intracluster medium in galaxy clusters (Kim et al. 1991; Enßlin & Vogt 2003; Murgia et al. 2004, and references therein). Recently, an alternative and complementary approach based on the analysis of total and polarized brightness fluctuations of the synchrotron signal coming from diffuse radio sources has been applied (Tribble 1991b; Murgia et al. 2004).

In the following we give a description of the theory at the base of these approaches.

4.2.1 Synchrotron emission

Intracluster magnetic fields in astrophysical sources emit radio waves by the synchrotron radiation produced by the motion of ultra-relativistic[1] electrons. If an electron moves with a velocity **v** in a magnetic field with strength **B**, the electron experiences the Lorentz force:

$$\frac{d(m_e \mathbf{v})}{dt} = \frac{e}{c}\mathbf{v} \times \mathbf{B} \tag{4.2}$$

where e is the charge of the particle. The electron will start a helical motion around the magnetic field lines and it will emit in a cone with half-angle $1/\gamma$ around its instantaneous velocity. From the relativistic Larmor formula, the power emitted results to be:

$$-\frac{d\epsilon}{dt} = \frac{2e^4}{3m_e^4 c^7}\epsilon^2 B^2 \sin^2\theta \tag{4.3}$$

where θ is the angle between the magnetic field and the electron velocity, called pitch angle, and ϵ is the particle energy. When the emission is originated by a population of ultra-relativistic electrons, the observer gets a continuum emission mainly concentrate around a critical frequency (see Fig. 4.1):

$$\nu_c = \frac{3e}{4\pi m_e^3 c^5}\epsilon^2 B \sin\theta. \tag{4.4}$$

If the relativistic electrons have a power law energy distribution:

$$N(\epsilon,\theta)d\epsilon = N_0 \epsilon^{-\delta}\frac{\sin\theta}{2}d\epsilon \tag{4.5}$$

[1] An electron with a Lorentz factor γ and an energy ϵ is defined ultra relativistic if

$$\gamma = \frac{\epsilon}{m_e c^2} >> 1 \tag{4.1}$$

where m_e is the electron rest mass and c the speed of light.

the total synchrotron emissivity of the ultra-relativistic electrons population will be (see Murgia et al. 2004):

$$J(\nu) = C_{\rm f} \frac{N_0 B \sin^2\theta}{2} \int_{\epsilon_{\rm min}}^{\epsilon_{\rm max}} F\left(\frac{\nu}{C_\nu B \sin\theta \epsilon^2}\right) \epsilon^{-\delta} d\epsilon \tag{4.6}$$

where $\epsilon_{\rm min}$ and $\epsilon_{\rm max}$ are the limits in the electron energy spectrum, $C_{\rm f} = 2.34 \times 10^{-22}$ and $C_\nu = 6.26 \times 10^{18}$ in cgs units, $\alpha = (\delta - 1)/2$ is the spectral index of the source and $F(x)$ is the synchrotron radiation kernel:

$$F(x) = x \int_{\rm x}^{\infty} K_{5/3}(z) dz \tag{4.7}$$

where $K_{5/3}$ is the 5/3-order modified Bessel function. For sources optically thin to their own radiation the brightness distribution is given by the integral of the emissivity in Eq. 4.6 across the source:

$$I(\nu) = \frac{1}{4\pi} \int_{-{\rm L}/2}^{{\rm L}/2} J(\nu) dl \tag{4.8}$$

where L is the source depth along the line of sight.

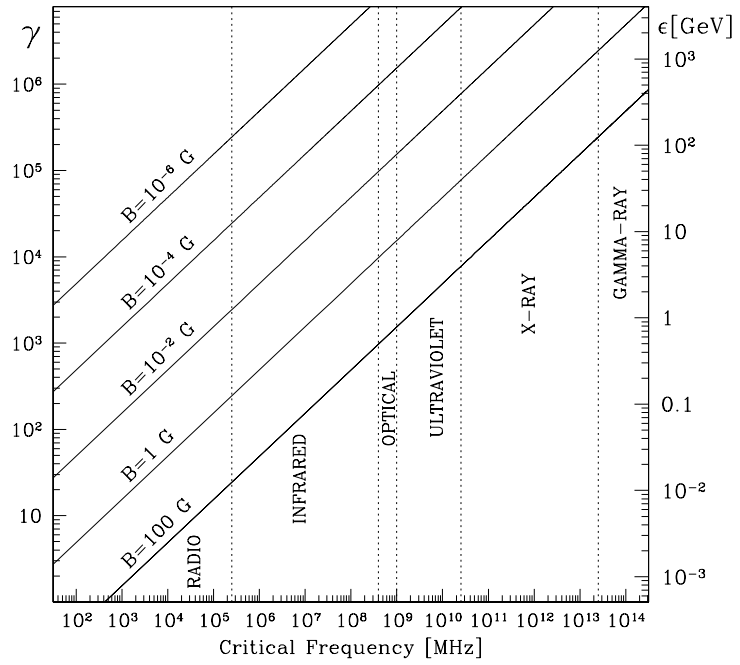

Figure 4.1 Lorentz factor γ and energy ϵ of emitting electrons versus the critical frequency $\nu_{\rm c}$ (see Eq. 4.4). Continuous lines indicate magnetic field strengths ranging between 1 μG and 100 G. Electrons with $\gamma \simeq 10^5$ in a magnetic field of 1 μG generate synchrotron radiation in the radio domain (see Eq. 4.4). Image taken from Govoni & Feretti (2004).

The synchrotron radiation from a single electron is elliptically polarized. When a population of ultra-relativistic electrons is considered, a linearly polarized emission is expected. For optically thin sources, the degree of intrinsic linear polarization is given by:

$$P(\nu) = J(\nu) \frac{\int_{\epsilon_{\rm min}}^{\epsilon_{\rm max}} G\left(\frac{\nu}{C_\nu B \sin\theta \epsilon^2}\right) \epsilon^{-\delta} d\epsilon}{\int_{\epsilon_{\rm min}}^{\epsilon_{\rm max}} F\left(\frac{\nu}{C_\nu B \sin\theta \epsilon^2}\right) \epsilon^{-\delta} d\epsilon} \tag{4.9}$$

where $G(x) = xK_{2/3}(x)$ (see Murgia et al. 2004, and references therein). By supposing a uniform magnetic field and a power law energy distribution for the relativistic electron population, the intrinsic degree of polarization is related just to the spectral index of the energy distribution δ:

$$P_{\rm int} = \frac{3\delta + 3}{3\delta + 7}. \tag{4.10}$$

If the magnetic field direction in the source varies along the line of sight or its fluctuations are on smaller scales than the beam of the radio images, the observed degree of linear polarization is lower than the intrinsic value. Therefore, the analysis of the emission of a synchrotron source can give important information about the magnetic field strength and structure. Both total and polarized intensity are related to the relativistic electron distribution, but because of its scalar nature, the total intensity emission is directly related to the magnetic field strength, while because of its vectorial nature the polarized emission is mainly affected by the degree of order of the magnetic field. Therefore, the ratio between total and polarized brightness has just a marginal dependence from the relativistic electron distribution and directly constrains the magnetic field strength and structure.

4.2.1.1 Equipartition magnetic field

The observed radio halo intensity is directly related to the integral of the magnetic field and relativistic particle distribution along the line-of-sight. When the relativistic particle energy distribution is unknown, disentangling the two contributions is not possible from radio observations alone. Then, a quite common hypothesis is a minimum total energy density condition for the system (Pacholczyk 1970), sometimes equivalent to energy equipartition between the magnetic field and the relativistic particles (see the following). Under this and some other assumptions about physical properties of the radio source, the derivation of average magnetic field strengths in radio sources as a function of the radio source luminosity is possible. Up to the last decade, the estimation of magnetic fields in clusters of galaxies was obtained through this approach. Since several assumptions are necessary and their validity is not unquestionable, the values obtained have to be carefully considered. The main uncertainties concern the electron energy spectrum and pitch-angle distribution (Petrosian 2001; Carilli & Taylor 2002), while Beck & Krause (2005) consider improbable the possibility that the system is not in an equipartition condition since, in that case, it would rapidly tend to this stable state.

The total energy $U_{\rm tot}$ of a synchrotron source includes different contributions:

$$U_{\rm tot} = (1 + \kappa)U_{\rm el} + U_{\rm B} \tag{4.11}$$

where $U_{\rm B}$ is the energy in magnetic field, while $(1 + \kappa)U_{\rm el}$ is the energy in relativistic particles expressed as a function of the relativistic electron energy $U_{\rm el}$. Conventionally κ is the ratio of the heavy particle to electron energy densities. The magnetic field energy is:

$$U_{\rm B} = \phi V \frac{B^2}{8\pi} \tag{4.12}$$

where V is the volume of the radio source and ϕ is the filling factor that is the fraction of the volume of the source occupied by the magnetic field. The total energy of relativistic electrons is:

$$U_{\rm el} = V \int_{\epsilon_{\rm min}}^{\epsilon_{\rm max}} N(\epsilon, \theta)\epsilon d\epsilon = V N_0 \frac{\epsilon_{\rm max}^{1-2\alpha} - \epsilon_{\rm min}^{1-2\alpha}}{1 - 2\alpha} \frac{\sin\theta}{2}. \tag{4.13}$$

To express the total energy just in terms of the magnetic field, VN_0 can be expressed as a function of the synchrotron luminosity $L_{\rm syn}$:

$$L_{\rm syn} = V \int_{\epsilon_{\rm min}}^{\epsilon_{\rm max}} \left(-\frac{d\epsilon}{dt}\right) N(\epsilon,\theta) d\epsilon = C_\alpha V N_0 B^{1+\alpha} \nu^{-\alpha} \frac{\sin\theta}{2} \tag{4.14}$$

where C_α is a constant just related to the spectral index of the radio source. By substituting in the relativistic electron energy:

$$U_{\rm el} = \frac{\epsilon_{\rm max}^{1-2\alpha} - \epsilon_{\rm min}^{1-2\alpha}}{1-2\alpha} \frac{1}{C_\alpha \nu^{-\alpha}} \frac{L_{\rm syn}}{B^{1+\alpha}}, \tag{4.15}$$

the total energy becomes:

$$U_{\rm tot} = (1+\kappa) \frac{\epsilon_{\rm max}^{1-2\alpha} - \epsilon_{\rm min}^{1-2\alpha}}{1-2\alpha} \frac{1}{C_\alpha \nu^{-\alpha}} \frac{L_{\rm syn}}{B^{1+\alpha}} + \phi V \frac{B^2}{8\pi}. \tag{4.16}$$

This function has a minimum for a magnetic field given by (Brunetti et al. 1997; Beck & Krause 2005):

$$B_{\rm min} = \left(\frac{4\pi}{C^\alpha} \frac{\epsilon_{\rm max}^{1-2\alpha} - \epsilon_{\rm min}^{1-2\alpha}}{1-2\alpha} (1+\alpha)(1+\kappa) \nu^\alpha \frac{L_{\rm syn}}{\phi V} \right)^{\frac{1}{3+\alpha}}. \tag{4.17}$$

When α=1, this value of the magnetic field guarantees a perfect equipartition of the energy between the magnetic field and the relativistic particles.

4.2.2 Faraday rotation

Intracluster magnetic fields can be investigated by means of multi-wavelength observations of radio galaxies located behind or belonging to the clusters. Radio galaxy emission is well know to be linearly polarized and the presence of a magnetic field in an ionized plasma creates a difference in the phase velocities for left versus right circularly polarized radiation. As a consequence, the polarized emission from a radio source propagating through a plasma experiences a phase shift between the two components. This corresponds to a rotation in the polarization angle (see Fig. 4.2).

For a completely foreground screen (Burn 1966), the rotation is

$$\Delta\Psi = \Psi_{\rm obs}(\lambda) - \Psi_{\rm int} = \lambda^2 {\rm RM}, \tag{4.18}$$

where $\Psi_{\rm obs}(\lambda)$ is the observed position angle at wavelength λ, $\Psi_{\rm int}$ the intrinsic polarization angle of the polarized emission, and RM the rotation measure. By considering an electron density $n_{\rm e}$ (cm^{-3}), a magnetic field $\mathbf{B}$ (μG), and a path length $\mathbf{l}$ (kpc), the Faraday RM is

$${\rm RM} = 812 \int_0^{\rm L} n_{\rm e[cm^{-3}]} \mathbf{B}_{[\mu{\rm G}]} \cdot \mathbf{dl}_{\rm [kpc]} \quad {\rm rad\ m^{-2}} \tag{4.19}$$

where L is the path along the cluster. By convention, RM is assumed positive when the magnetic field is directed toward the observer, negative in the contrary case. Therefore, by observing radio galaxies at different wavelengths, the rotation measure can be derived from a linear fit of the observed polarization position angle $\Psi_{\rm obs}(\lambda)$ versus λ^2. To remove ambiguities on the position angle ($\Psi_{\rm obs} = \Psi_{\rm obs} + n\pi$) and determine accurately RM, the polarization angle should be measured at least at three wavelengths.

The rotation measure seen along the line of sight is the result of the combination of different contributions due to the intracluster medium, our Galaxy and the radio source. The investigation

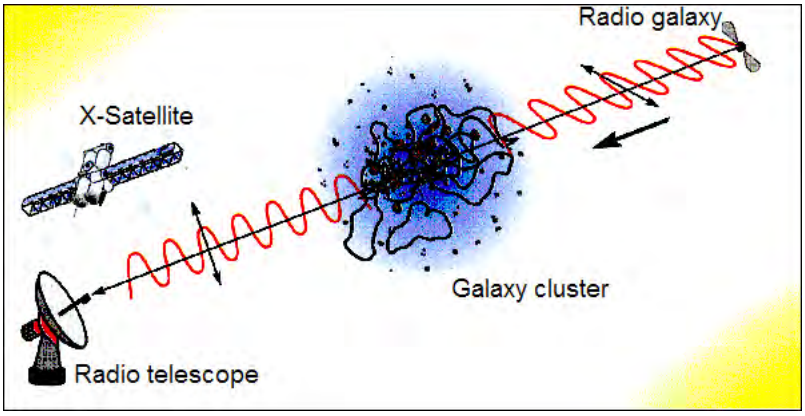

Figure 4.2 The polarization angle of the signal coming from a radio source suffers a rotation passing through a magnetized plasma. This rotation is proportional to the integral of the product of the thermal gas density and the magnetic field in the medium along the line of sight (see text). Image taken from Kronberg (2002).

of the intracluster magnetic field can be performed only when the ICM contribution dominates. The Galactic contribution in the direction of the source can be evaluated and subtracted (Simard-Normandin et al. 1981; Taylor et al. 2009), while the possible internal contribution inside the radio lobes can be neglected if a linearity of the polarization angle Ψ_{obs} versus λ^2 is observed (Burn 1966). Then, by combining the rotation measure with X-ray observations of the thermal gas, the intracluster magnetic field can be constrained by inverting Eq. 4.19. For a uniform magnetic field and a constant thermal gas density, the rotation of the position angle is directly proportional to the rotation measure mean value:

$$\langle RM \rangle = 812 B_{\parallel} n_e L. \tag{4.20}$$

Observations suggest that this view is quite simplistic. A more complex picture considers a magnetic field tangled on a single scale Λ_C. In each cell the thermal gas density and magnetic field strength are supposed to be uniform and different cells are characterized by a random orientation of the magnetic field (Lawler & Dennison 1982; Tribble 1991a; Feretti et al. 1995; Felten 1996). The combination of the different contributions along the line of sight can be described by means of a random walk process. The resulting RM distribution is a Gaussian characterized by mean value $\langle RM \rangle$ and variance σ^2_{RM}:

$$\langle RM \rangle = 0 \qquad \sigma^2_{RM} = \langle RM^2 \rangle = 812^2 \Lambda_C \int (n_e B_{\parallel})^2 dl. \tag{4.21}$$

If the thermal gas density is supposed to decrease with the distance from the cluster center according a β-model profile (Cavaliere & Fusco-Femiano 1976, , see § 1.2), the integral in Eq. 4.21 gives the following variance (for the detailed mathematical derivation we refer to Appendix B):

$$\sigma^2_{RM}(r_\perp) = \frac{K^2 B^2 \Lambda_C n_0^2 r_c}{\left(1 + \frac{r_\perp^2}{r_c^2}\right)^{\frac{6\beta-1}{2}}} \frac{\Gamma(3\beta - \frac{1}{2})}{\Gamma(3\beta)} \tag{4.22}$$

where $r_\perp$ indicate the projected distance from the cluster center and K is a constant depending on the integration path:

- $K = 624$ for a source located behind the cluster;
- $K = 441$ for a source located at the center of the cluster.

By knowing the thermal gas density profile through X-ray observations, the evaluation of $\sigma_{\rm RM}$ gives precious information about the magnetic field strength and fluctuation scale.

Actually, a more realistic model requires a magnetic field tangled on a range of scale. In this case a numerical approach is necessary (see Chapter 5).

4.2.2.1 Depolarization

The observations of radio sources at different frequencies or at the same frequency but with different spatial and frequency resolution reveal that the observed degree of polarization can be lower than the intrinsic. This decrease of the polarization degree is called depolarization and can be distinguished in:

- *intrinsic depolarization*. The signal coming from different locations in the source is characterized by a given orientation of the polarization angle and degrees of polarization up to 70%. The observed polarized emission is due the vectorial sum of these different contributions along the same line of sight. This results in a reduction of the polarization degree due to the combination of two effects. Indeed, a depolarization is observed both if the RM is null and the field is tangled and if the RM is non-null and the field is completely ordered. Usually both the contributions are present;
- *observational depolarization*. The observations are performed with a fixed bandwidth and spatial resolution. The polarization angle rotates as a function of the wavelength, therefore there is a rotation across the bandwidth that causes the so called bandwidth depolarization. In addition, unresolved density and/or magnetic field fluctuations in the medium between the observer and the source originate a gradient in the Faraday RM that is responsible of the beam depolarization.

While a completely homogeneous foreground screen does not prevent the intrinsic depolarization, it would avoid the beamwidth depolarization. Therefore, the observed beamwidth depolarization suggests a fluctuating intervening medium. The depolarization of the signal due to the Faraday rotation effect results in a radial decrease of the degree of polarization towards the cluster center, see § 4.3.2 and § 7.5.

4.2.3 Inverse Compton scattering

To investigate the intracluster magnetic field, a technique based on the combination of the synchrotron radio and inverse Compton emission coming from galaxy clusters can be applied (Blumenthal & Gould 1970; Harris & Grindlay 1979; Rephaeli et al. 1987; Feigelson et al. 1995; Bagchi et al. 1998). The inverse Compton effect takes place when high-energy electrons transfer energy to low-energy photons. In clusters of galaxies the population of ultra-relativistic electrons responsible for the diffuse non-thermal synchrotron radio emission can scatter the microwave background photons, producing in this way hard X-ray radiation. In fact, the frequency of the outcoming and incoming radiation are related by (Blumenthal & Gould 1970):

$$\nu_{\rm out} = \frac{4}{3}\gamma^2 \nu_{\rm in} \tag{4.23}$$

where γ is the Lorentz factor of the electron. For ultra-relativistic electrons with $\gamma \sim 10^3$ and incoming photons with $\nu_{\rm in} \sim 10^{11}$Hz, Eq. 4.23 implies that radiation with $\nu_{\rm out} \sim 10^{18}$Hz will be generated.

In Fig. 4.3 the Spectral Energy Distribution (SED) of the non-thermal radio and inverse Compton emission (10^7–10^{21} Hz) from the Ophiuchus galaxy cluster is shown (Murgia et al. 2010a). The inverse Compton luminosity $L_{\rm IC}$ is directly proportional to the energy density in the photon field $u_{\rm ph}$, while the synchrotron luminosity $L_{\rm syn}$ to the energy density in the magnetic field $u_{\rm B}$. Therefore, their ratio is directly related to the intracluster magnetic field of the source:

$$\frac{L_{\rm IC}}{L_{\rm syn}} \propto \frac{u_{\rm ph}}{u_{\rm B}} = \frac{8\pi u_{\rm ph}}{B^2}. \tag{4.24}$$

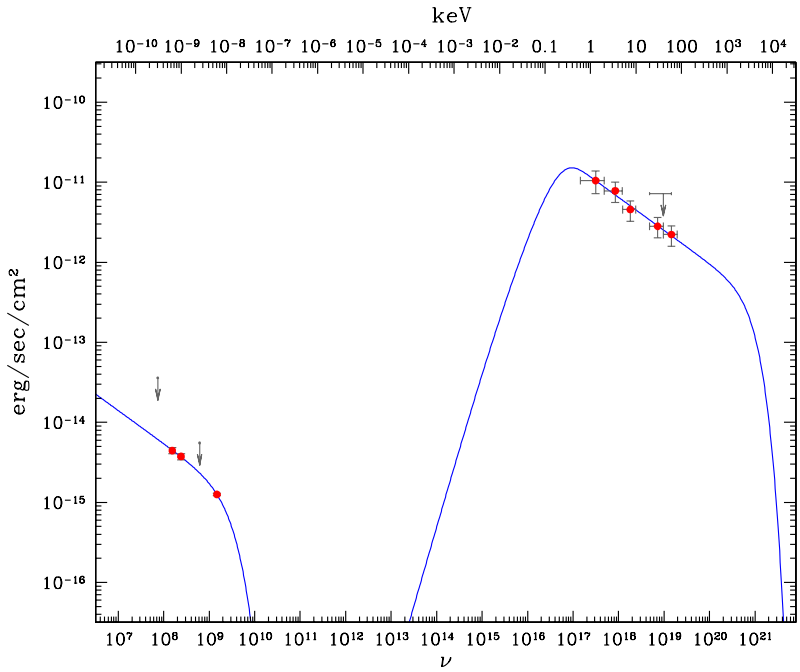

Figure 4.3 Spectral Energy Distribution of the non-thermal emission from the Ophiuchus galaxy cluster in the frequency range from the radio to the γ-ray band (Murgia et al. 2010a).

Sometimes, this technique can not be easy applied because of the difficulties to discern between the thermal and non-thermal hard X-ray emission from the source. With the Beppo/Sax and RXTE instruments this problem has been partly overcome thanks to the increased sensitivities above 10 keV where the inverse Compton emission dominates (Rephaeli 2001). If the detection of the inverse Compton radiation is not possible just a magnetic field lower limit can be given (Rephaeli et al. 1987).

4.2.4 Cold fronts

An alternative method that allows a local investigation of the magnetic field relies on the analysis of cold fronts. They are sharp discontinuities in the ICM density distribution, located at the separation between dense cool cores and the hotter less dense surrounding gas, that can be observed in some merging galaxy clusters and around central density peaks of some relaxed clusters (see also

§ 1.1.1). The most famous observed cold fronts are in the galaxy clusters A2142 (Markevitch et al. 2000) and A3667 (Vikhlinin et al. 2001a).

Cold fronts appear very stable features on the dynamical point of view. In correspondence of cold fronts the magnetic field is expected to be parallel to the front direction and amplified respect to the rest of the cluster. Such a magnetic field configuration suppresses every heat transport process across the discontinuity. At the same time it guarantees the dynamical stability of the front. For a dynamically stable cold front, where the Kelvin-Helmholtz instability has been suppressed by the magnetic surface tension, a local estimation of the magnetic field strength can be inferred, as in the case of A3667 (Vikhlinin et al. 2001b).

Markevitch & Vikhlinin (2007) pointed out that when the magnetic and thermal pressure near to the front reach the equipartition, some plasma should be removed from a layer near the front. The width of the layer Δr results to be:

$$\Delta r \simeq \frac{R}{M}\frac{p_{\rm gas}}{p_{\rm B}} \tag{4.25}$$

where R is the radius of the front, M is the Mach number of the cloud, and $p_{\rm gas}$ and $p_{\rm B}$ are respectively the thermal and magnetic pressure in the undisturbed gas ahead of the front (Lyutikov 2006). If the plasma depletion layer could be observed and its width estimated by means of X-ray observation, it would allow an independent estimate of the magnetic field strength in undisturbed regions of the cluster.

4.2.5 Magnetic fields derived through different approaches

In the last decade significant progress has been done in the study of magnetic fields in galaxy clusters. Analyses based on the different approaches described in this Chapter agree about a complex magnetic field structure, characterized by fluctuations on a range of scales and filaments. On the other hand, the field strengths derived with these techniques are, sometimes, difficult to reconcile. In the following we briefly summarize the main results.

Equipartition magnetic field strengths derived through synchrotron radio emission can be up to few μG, both at the center and in the outskirts of galaxy clusters: 0.7 and 4.3 μG have been found respectively in the central region of A2254 and in A773 (Govoni et al. 2001b) through radio halo emission, and 0.8 and 1.9 μG in A1664 (Govoni et al. 2001b) and Coma (Ensslin et al. 1998) periphery through radio relic sources. Similar values have been inferred with inverse Compton hard X-ray observations. By means of the combination of co-spatial non-thermal X-ray and radio fluxes, averaged magnetic field strength in the range 0.05–1 μG have been estimated. Some examples are given by 0.3 μG in the Ophiuchus cluster (Murgia et al. 2010a) and 1 μG in A85 (Bagchi et al. 1998).

Higher values have been revealed by cold fronts and RM studies. Indeed, magnetic fields of $\sim$10 μG have to be supposed along the cold front in A3667 (Vikhlinin et al. 2001b). Rotation measure studies generally show central magnetic field strengths of a few μG in merging galaxy clusters and values up to several tens μG in the central regions of cooling-core galaxy clusters where the extreme RM magnitudes observed appear to be roughly proportional to the cooling flow rate (Taylor et al. 2002). Some examples are given by Hydra A, where magnetic field central strengths between 19 and 85 μG have been found by Laing et al. (2008) and Kuchar & Enßlin (2011), and in 3C 295, where 12 and 30 μG strengths have been indicated respectively by Allen et al. (2001) and Perley & Taylor (1991).

The reasons at the base of these gaps can be different. Rotation measure values correspond to magnetic field strengths averaged along the line of sight and weighted by the thermal gas density

and cold fronts furnish local estimates in regions where compression is at work, likely leading to the amplification of the field. On the other hand, equipartition estimates rely on several assumptions and, as inverse Compton values, they are averaged over the volume occupied by diffuse synchrotron sources. Moreover, we have to note that the relativistic electron population responsible of synchrotron and hard X-ray emission is not the same. The analysis of the hard X-ray emission due to inverse Compton reveals Lorentz factors $\gamma \sim 5000$ for the relativistic electrons, while for μG intracluster magnetic field strengths the observed radio halo emission at 1.4 GHz can be explained just considering relativistic electrons with $\gamma \sim 18000$ (Carilli & Taylor 2002; Beck & Krause 2005).

Recently, more sophisticated studies have been performed based on a combination of observational and numerical approaches, aiming at finding a more realistic description of the intracluster magnetic field both in strength and in structure (e.g. Tribble 1991b; Enßlin & Vogt 2003; Murgia et al. 2004, see also Chapter 5).

4.3 Intracluster magnetic field properties from statistical studies

As described in § 4.2.2, information on the intracluster magnetic fields can be obtained through the analysis of the effect of the Faraday rotation on the radio signal coming from radio galaxies in the background or embedded in the galaxy clusters themselves. RM studies of radio galaxies on both statistical samples and individual galaxy clusters and galaxy groups have been carried out. In parallel to detailed intracluster magnetic field analysis in single galaxy clusters, statistical studies allow to get information about the average properties of the intracluster magnetic field in this class of systems.

In the following we will present the main results available in literature from statistical studies based on the rotation measure effect. Moreover, the results on a statistical investigation about the connection between the magnetic field and the thermal gas temperature will be described (Govoni et al. 2011), while a study performed on a specific galaxy cluster on the basis of a rotation measure analysis will be discussed in Chapter 6.

4.3.1 Rotation measure statistics

An important statistical rotation measure analysis has been performed by Clarke et al. (2001) on a sample of clusters without cooling flows and extended radio halos. They consider 16 low redshift ($z \leqslant 0.2$) clusters, located at high latitudes ($|b| > 20°$), and characterized by an X-ray luminosity $L_{\mathrm{X[0.1-2.4\,keV]}} > 5\,10^{42}\,\mathrm{erg\,s^{-1}}$. For each cluster, polarized radio galaxies have been selected at different distances from the cluster center. Moreover, a control sample is considered, formed by radio sources located outside the cluster thermal gas emission. To investigate possible difference for radio galaxies in and out galaxy clusters, they analyze the RM of these radio galaxies as a function of the impact parameter by using multi-wavelength VLA observations. Their results are shown in Fig. 4.4. The figure indicates an increasing dispersion of the rotation measure distribution moving towards smaller impact parameters. The rotation measure in cluster galaxies is higher than in sources not belonging to galaxy clusters. Indeed, the cluster radio source rotation measures range from -200 rad m^{-2} to +200 rad m^{-2}, on the contrary the control sample rotation measures vary in the range $\pm$50 rad m^{-2}. This result confirms the presence of magnetic field associated to the intracluster medium. Clarke (2004) investigate a larger sample of RM including data from Kim et al.

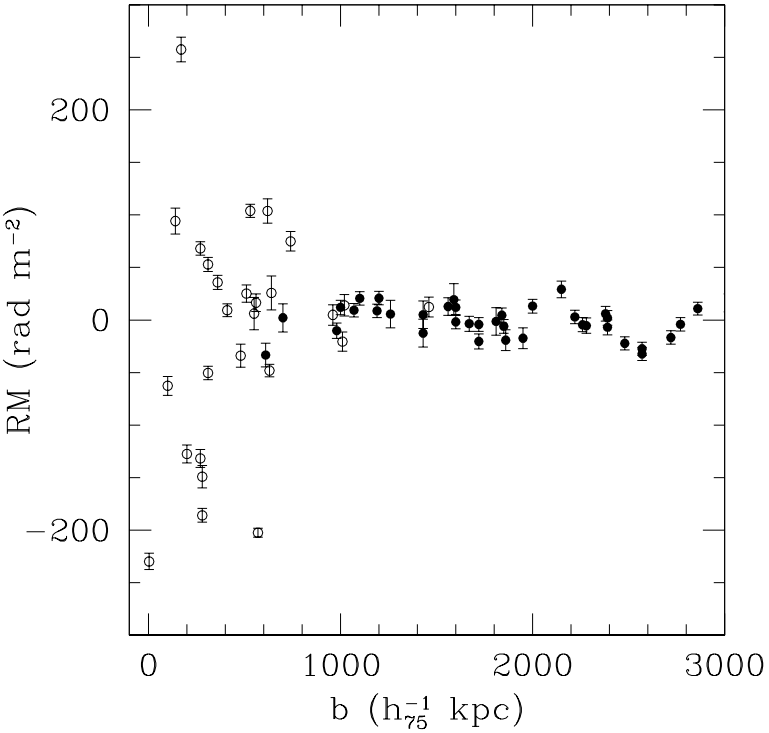

Figure 4.4 Radio galaxy RM versus the projected distance from the cluster center *b*. The sample comprises radio galaxies belonging to clusters (open dots), and located outside the cluster thermal gas emission (fill dots). Image taken from Clarke et al. (2001).

(1991). They do not find differences in the rotation measure of background and embedded sources, indicating that a possible contribution local to the source is negligible.

For a magnetic field tangled on a single scale (see § 4.2.2), they derive magnetic field strengths of about 5–10 μG and a magnetic field to thermal gas energy ratio equal to about 2.5%. In addition, they discuss the origin of the intracluster magnetic field energy. They consider as possible primary sources the AGN/accretion disk energy (see also Colgate & Li 2000), the gravitational energy and the energy from past merger, while they exclude a possible thermonuclear origin.

4.3.1.1 Magnetic field - gas temperature connection

An increasing attention is given in the literature to the possible connection between the magnetic field strength and the cluster temperature. Smoothed-particle hydrodynamics (SPH) simulations predict that galaxy clusters should have different central magnetic field strengths depending on their dynamical state, mass, and hence temperature, with a very steep correlation, e.g. $B \propto T^2$ (Dolag et al. 1999, 2002, 2005). The temperature has been observed to strongly correlate with the cluster mass $M_{\rm gas} \propto T^{1.94}$ (Neumann & Arnaud 1999, 2001). Since, on average, the effect of the magnetic field is to change the temperature values of about 5% with respect to non-magnetized clusters, this increases the scatter in the observed mass-temperature relation (Dolag et al. 2001a).

Dolag et al. (2001b) show that the observed correlation between the dispersion of the rotation measure distribution

$$\sigma_{\rm RM} \propto \int_{\rm LOS} n_{\rm e} B_{\parallel} dl \tag{4.26}$$

and the X-ray surface brightness of the cluster in the source location

$$S_X \propto \int_{LOS} n_e^2 \sqrt{T} dl \tag{4.27}$$

reflects a correlation between the magnetic field and the thermal gas density if the temperature is neglected. Therefore, the possible dependence of the magnetic field on the temperature suggested by the simulations should produce an offset in this relation for cool with respect to hot galaxy clusters. However, there is also the possibility that the magnetic field strength is only mildly dependent on the cluster temperature, as recently pointed out by Donnert et al. (2009). Kunz et al. (2011) predict a dependence in cool-core clusters ($B \propto n_e^{0.5} T^{0.75}$) but not in isothermal clusters ($B \propto n^{0.5}$).

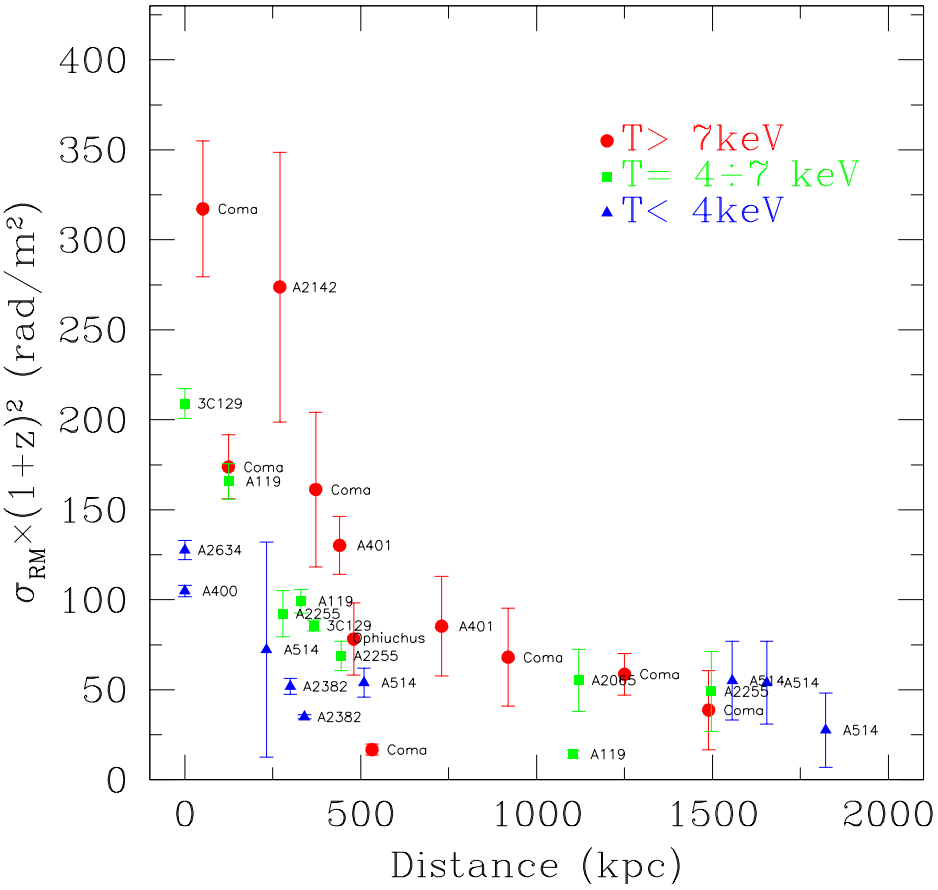

Figure 4.5 Dispersion of the rotation measure distribution as a function of the projected distance from the cluster X-ray center. The different symbols represent the cluster temperature taken from the literature (red > 7 keV, green 4–7 keV, blue < 4 keV).

We present here an investigation of the possible connection between the intracluster magnetic field strength and the thermal gas temperature (see Govoni et al. 2010). We reduced sensitive polarimetric VLA multi-frequency observations of polarized radio galaxies embedded within or in the background of the hot, nearby galaxy clusters A401, Ophiuchus, A2142, and A2065. We combined these new data with the high quality and high sensitivity RM images of extended radio galaxies present in the literature for cooler galaxy clusters. Only radio sources at large projected distance from the cluster center have been considered for cooling core galaxy clusters, therefore

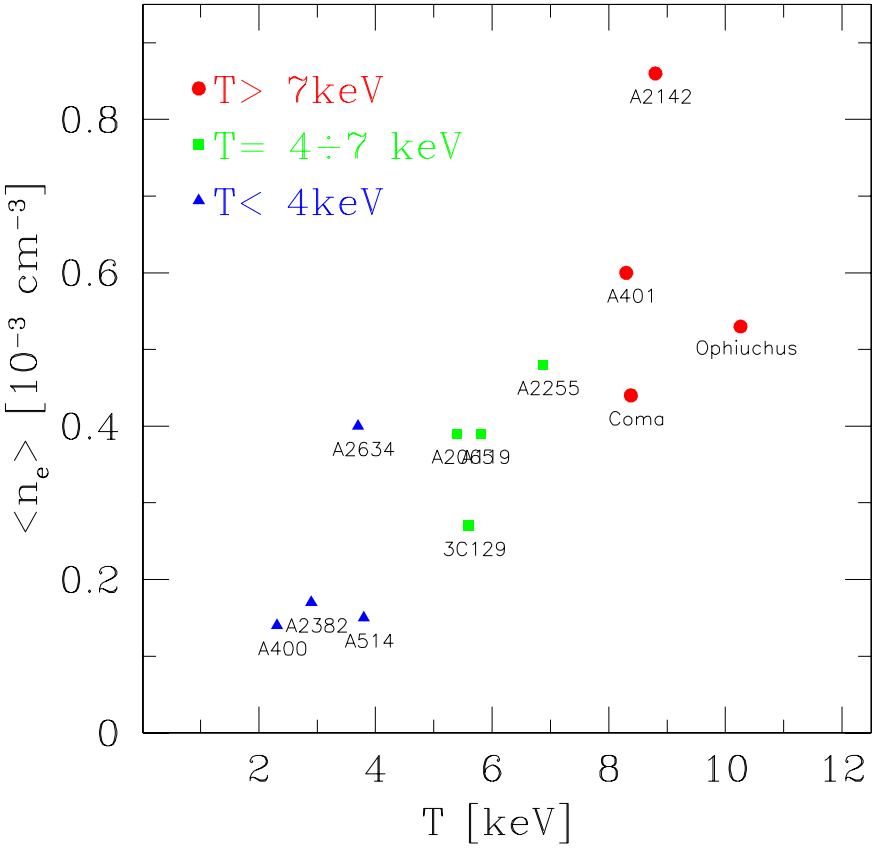

Figure 4.6 Plot of the mean gas density versus the temperature of the clusters in the sample.

the contribution of the dense cool core to the RM is likely to be negligible. Overall, we could investigate a sample of 12 systems with a temperature ranging between 3 and 10 keV. As Clarke et al. (2001) and Clarke (2004), we found a broadening of $\sigma_{\rm RM}$ toward small projected distances, in agreement with an excess of Faraday rotation due to a magnetized intracluster medium (see Fig. 4.5). Moreover, a positive trend has been found between the cluster temperature and the $\sigma_{\rm RM}$. Indeed, for a fixed projected distance from the cluster center, clusters with higher temperature show a higher $\sigma_{\rm RM}$. In the context of a magnetic field tangled on a single scale $\Lambda_{\rm B}$ and constant along the cluster

$$\sigma^2_{\rm RM} \propto n_0^2 B^2 \Lambda_{\rm B} \tag{4.28}$$

as reported in § 4.2.2, for a fixed $\Lambda_{\rm B}$, this trend can be explained if hotter clusters have a higher magnetic field strength and/or a higher gas density. In Fig. 4.6, we show the mean gas density versus the temperature of the cluster. Clusters with higher temperatures show a higher gas density indicating that the trend in Fig. 4.5 may reflect just a correlation between the thermal gas density and the temperature. In Fig. 4.7 we report the $\sigma_{\rm RM}$-$S_{\rm X}$ plot showing the trend of $\sigma_{\rm RM}$ values as a function of the cluster X-ray surface brightness $S_{\rm X}$ calculated in the corresponding source location. The new RM data confirm the $\sigma_{\rm RM}$-$S_{\rm X}$ relation previously known in the literature (Dolag et al. 2001b), and just an offset comparable to the intrinsic scatter of the correlation has been found for clusters with different temperatures. Therefore, a possible connection between the magnetic field strength and the gas temperature, if present, is very weak. This result indicates that in our sample

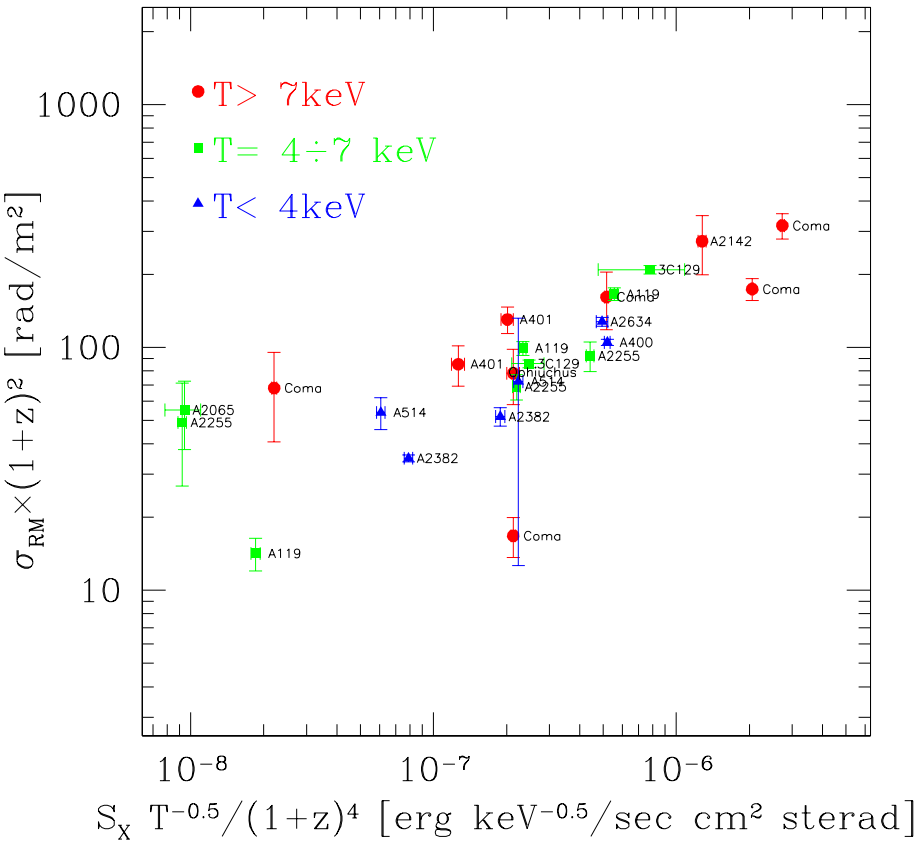

Figure 4.7 Dispersion of the rotation measure distribution as a function of the X-ray surface brightness of the intracluster gas in the source location. The different symbols represent the cluster temperature taken from the literature (red > 7 keV, green 4–7 keV, blue < 4 keV).

hotter clusters have higher σ_{RM} mostly because of their higher gas density. In addition, although the statistics is still limited, we note that in the σ_{RM}-S_X relation clusters with extended diffuse emission (e.g. Coma, A2255, A401) seem to show a behavior similar to that of clusters without diffuse synchrotron emission.

4.3.2 Fractional polarization statistics

A slightly different approach has been adopted by Bonafede et al. (2011), based on the consequences of the rotation of the polarization angle at 1.4 GHz due to the Faraday rotation effect rather than on a multi-frequency analysis. Indeed, by using full polarization single frequency VLA observations taken from the NVSS, they investigate the observed polarized emission versus the distance from the cluster center, aiming at finding possible relations with the dynamical state of the cluster and to constrain the magnetic field power spectrum. They select from the HIghest X-ray FLUx Galaxy Cluster Sample (HIFLUGCS) by Reiprich & Böhringer (2002) a sample of 39 galaxy clusters in different dynamical states with an X-ray luminosity $L_{X[0.1-2.4\,keV]} \geq 1.5\,10^{44}$ erg s^{-1}. The fractional polarization as a function of the impact parameter is shown in Fig. 4.8 for all the galaxies of the sample. A clear trend is present, with low degrees of polarization at the cluster center and values up to 35% in the outskirts, indicating a larger impact of the Faraday effect at the center of

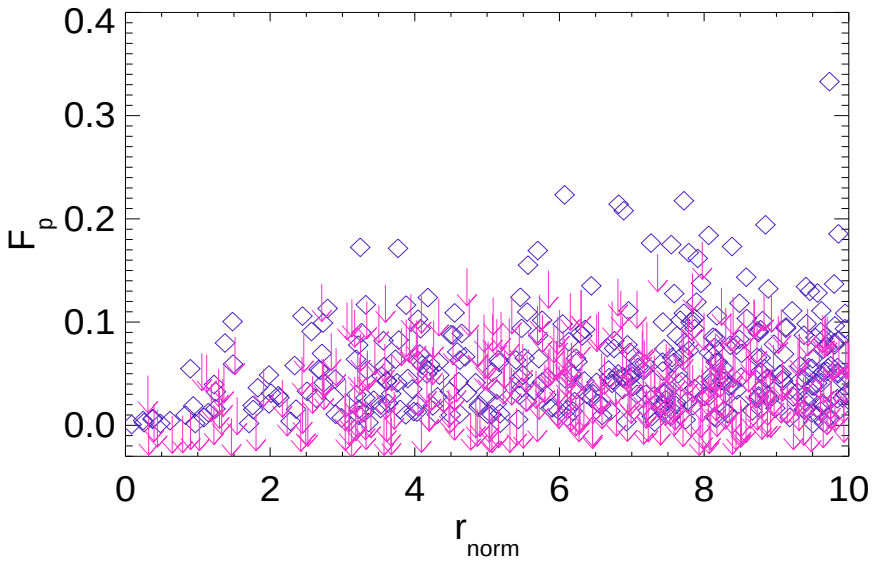

Figure 4.8 Fractional polarization versus the projected distance from the cluster center. The arrows indicate upper limits. Image taken from Bonafede et al. (2011).

the cluster. This result strongly confirms the presence of a magnetic field spread in the intracluster medium, in agreement with the work of Clarke et al. (2001) and Clarke (2004). Moreover, by comparing fractional polarization trends in galaxy clusters with or without a radio halo, they find on a statistical point of view that they share the same properties. On the contrary, a similar comparison between cool core and non-cool core galaxy clusters reveals with a high level of confidence that these systems on average are not characterized by the same behavior. As a consequence, cool core and non-cool core clusters do not share the same magnetic properties, in agreement with the results of Parrish et al. (2009), Parrish et al. (2010), and Ruszkowski & Oh (2010). Differently, clusters with and without radio halos show similar magnetic field strengths and structures. According the authors, this disfavors the hadronic model for radio halo formation. Indeed, Keshet & Loeb (2010) account for the bimodality of radio synchrotron emissivities in clusters in the context of hadronic models by means of different magnetic properties for clusters with and without radio halo. In particular, they suppose an amplification of the magnetic field strength due to cluster merger phenomena in clusters hosting radio halos. Actually, an alternative explanation that does not exclude the hadronic scenario has be given by Enßlin et al. (2011). They propose as responsible of radio halo formation the higher central energy density concentration of cosmic rays that should be typical of cluster undergoing major mergers and strongly turbulent.

Finally, to constrain the average intracluster magnetic field, Bonafede et al. (2011) compare the observed fractional polarization trend with the prediction of 3D numerical simulations, obtained with the FARADAY software package (Murgia et al. 2004). By assuming a random Gaussian multi-scale magnetic field decreasing with the radius as a function of the thermal gas density (see Chapter 5), they infer that the observed trend can be explained by supposing a central strength of $5\,\mu$G, whit a mean of $2.6\,\mu$G over the central Mpc^3.

5 Numerical approach

The studies of Faraday rotation measures of radio galaxies in individual clusters and radio halos performed in the last decade reveal an intracluster magnetic field fluctuating on scales between tens and hundreds of kpc and decreasing with the distance from the cluster center.

In this thesis we present a detailed study of the intracluster magnetic field strength and structure in galaxy clusters in different evolutionary stages: a relaxed cool core cluster and a cluster undergoing a strong merger phenomenon. In the cool core galaxy cluster A2199 (see Chapter 6), famous for the central powerful radio galaxy 3C338, we investigate the magnetic field power spectrum by exploiting the radio galaxy total and polarized emission at different frequencies. In the merging galaxy cluster A665 (see Chapter 7), known to host a powerful and extended radio halo at its center, we use the radio halo brightness fluctuation information, following an original idea of Tribble (1991b) and Murgia et al. (2004). The approach we adopted has been already applied to investigate the power spectrum of the intracluster magnetic field in the galaxy clusters A119 (Murgia et al. 2004), A2255 (Govoni et al. 2006), A2382 (Guidetti et al. 2008), and Coma (Bonafede et al. 2010). It consists in the comparison of observed images of the cluster radio total and polarized emission with synthetic images obtained with the dedicated C++ code FARADAY (Murgia et al. 2004). By this comparison, the magnetic field power spectrum that better describes the data can be found.

5.1 Modeling

To constrain the magnetic field power spectrum through rotation measure studies and the analysis of the radio halo signal, we produce synthetic images of the total and polarized emission of radio galaxies and radio halos. This requires three models:

- a magnetic field model;
- a thermal gas model;
- a relativistic electron model.

The synthetic RM images rely on the magnetic field and thermal gas models, while the synthetic images of synchrotron total intensity and polarized radio halo emission rely also on the relativistic electron model.

5.1.1 Magnetic field

We investigate the power spectrum of the magnetic field fluctuations following the 3-dimensional numerical approach proposed by Tribble (1991b) and Murgia et al. (2004).

We simulate a multi-scale random magnetic field in a cubical box[1]. The simulations begin in Fourier space by extracting the amplitude of the magnetic field potential vector, $\tilde{A}(k)$, from a Rayleigh distribution (that is, real and imaginary parts follow a Gaussian distribution) and by taking its phase ϕ to be completely random between 0 and 2π:

$$P(A,\phi)dAd\phi = \frac{A}{2\pi|A_{\rm k}|^2}\exp\left(-\frac{A^2}{2|A_{\rm k}|^2}\right)dAd\phi. \tag{5.1}$$

This Rayleigh distribution is supposed to have a standard deviation that varies as a power law

$$|A_k|^2 \propto k^{-\zeta} \tag{5.2}$$

where the wave number $k = 2\pi/\Lambda$ ranges from $k_{\rm min} = 2\pi/\Lambda_{\rm max}$ to $k_{\rm max} = 2\pi/\Lambda_{\rm min}$ ($\Lambda_{\rm min}$ and $\Lambda_{\rm max}$ are the minimum and maximum scale of the magnetic field fluctuations). Outside this range:

$$|A_k|^2 = 0. \tag{5.3}$$

The magnetic field is formed in Fourier space via the cross product

$$\mathbf{B}(\tilde{\mathbf{k}}) = i\mathbf{k}\times\mathbf{A}(\tilde{\mathbf{k}}). \tag{5.4}$$

This ensures that the magnetic field is effectively divergence free and implies a magnetic field power spectrum

$$|B_k|^2 = Ck^{-n} \tag{5.5}$$

where C is the normalization and $n = \zeta - 2$ is the spectral index of the magnetic field power spectrum. The magnetic field power spectrum represents the magnetic field energy associated with each wave number. The magnetic field in the real space domain is obtained by a 3D fast Fourier transform (Press et al. 1986) inversion. The resulting magnetic field components have a Gaussian distribution with mean $\langle B_{\rm i}\rangle = 0$ and dispersion $\sigma^2_{\rm B_i} = \langle B^2_{\rm i}\rangle$ (where i=x,y, or z). The field is isotropic, in the sense that there is no privileged direction in space for the random fluctuations. The amplitude of the magnetic field has a Maxwellian distribution with $\langle B\rangle = 2\sqrt{\frac{2}{\pi}}\sigma_{\rm B_i}$ and $\sigma_{\rm B} = \sqrt{\frac{3\pi-8}{\pi}}\sigma_{\rm B_i}$. From the conservation of energy expressed through the Parseval's Theorem

$$\int |B_{\rm i}|^2 dV = \int |B_{\rm k}|^2 d^3k, \tag{5.6}$$

for $n \neq 3$ one obtains:

$$U_{\rm B} = \frac{C}{8\pi}\frac{k^{3-{\rm n}}_{\rm max} - k^{3-{\rm n}}_{\rm min}}{3-n}, \tag{5.7}$$

while for $n = 3$:

$$U_{\rm B} = \frac{C}{8\pi}\ln\left(\frac{k_{\rm max}}{k_{\rm min}}\right). \tag{5.8}$$

If the spectral index is $n < 3$ the energy is distributed on small scales, while when $n > 3$ the energy is distributed on large scales. When $n = 3$, the energy is uniformly distributed on small and large scales.

[1]Throughout this thesis the power spectra are expressed as vectorial forms in k-space. The one-dimensional forms can be obtained by multiplying by $4\pi k^2$ and $2\pi k$ the three and two-dimensional power spectra respectively.

The power spectrum normalization is set such that the average magnetic field strength scales as a function of the thermal gas density

$$\langle B(r)\rangle = \langle B_0\rangle\left[\frac{n_e(r)}{n_0}\right]^{\eta}, \tag{5.9}$$

where $\langle B_0\rangle$ is the average magnetic field strength at the cluster center, η is the slope of the radial profile, and $n_e(r)$ is the thermal electron gas density profile. To reduce the computational burden, this operation is performed in the real space domain by multiplying the magnetic field by Eq. 5.9. However, to preserve the null divergence of the field exactly, this operation should be better performed as a convolution in the Fourier space domain before the cross product is formed. Moreover, the convolution with the radial profile in Eq. 5.9 alters the input power spectrum shape. If the size of the cluster core radius is comparable to the size of the computational grid the above effects are acceptably negligible. However, if the cluster core radius is much smaller than the size of the computational grid, one should consider that the shape of the magnetic-field power-spectrum may deviate from a perfect power law. On the other hand, if the gas density profile changes smoothly, the effect is mostly seen at the edges of the power spectrum (see Fig. 6.10).

Overall, the 3-dimensional multi-scale power-law magnetic field power spectrum model with a radial scaling depends on five parameters:

- $\langle B_0\rangle$, the average magnetic field strength at the center of the cluster;
- η, the magnetic field radial profile index;
- n, the power spectrum index;
- $\Lambda_{\rm min}$, the minimum scale of magnetic field fluctuations;
- $\Lambda_{\rm max}$, the maximum scale of magnetic field fluctuations.

5.1.2 Thermal gas density

The thermal electrons distribution can be modeled from X-ray observations of the hot gas. A widely used representation is given by the β-model (Cavaliere & Fusco-Femiano 1976):

$$n_e(r) = n_0\left[1+\left(\frac{r}{r_c}\right)^2\right]^{-\frac{3}{2}\beta} \tag{5.10}$$

while a double β-model:

$$n_e(r) = n_{0\rm int}\left[1+\left(\frac{r}{r_{\rm cint}}\right)^2\right]^{-\frac{3}{2}\beta_{\rm int}} + n_{0\rm ext}\left[1+\left(\frac{r}{r_{\rm cext}}\right)^2\right]^{-\frac{3}{2}\beta_{\rm ext}} \tag{5.11}$$

is more suitable for relaxed cool core galaxy cluster (e.g. Mohr et al. 1999).

A more exhaustive description of the intracluster medium is given in § 1.2.

5.1.3 Relativistic electrons

We assume as electron energy spectrum a power law of the form

$$N(\epsilon,\theta) = N_0\epsilon^{-\delta}\frac{\sin\theta}{2} \tag{5.12}$$

with the energy ϵ ranging from $\gamma_{\rm min} m_{\rm e} c^2$ and $\gamma_{\rm max} m_{\rm e} c^2$, with $\gamma_{\rm max} \gg \gamma_{\rm min}$. The index δ is related to the observed spectral index throughout the relation $\delta = 2\alpha + 1$. The relativistic electrons are supposed to have an isotropic distribution of the pitch angle θ, between the direction of their velocity and the magnetic field. We set the normalization N_0 supposing a perfect equipartition condition between magnetic field and relativistic particle energy density at each point in the intracluster medium.

5.2 Synthetic images

The models presented in the previous Section are used to predict the total and polarized emission of diffuse synchrotron radio sources and radio galaxies in galaxy clusters.

As noted in § 4.2.2, the rotation measure is defined as

$$RM \propto \int_{\rm LOS} n_{\rm e} B_{\parallel} dl. \tag{5.13}$$

Therefore, a rotation measure image can be produced through the integration along the line of sight of a magnetic field and a thermal gas model. In Fig. 5.1, synthetic rotation measure images corresponding to three different spectral indices are shown (Murgia et al. 2004). Spectral indices $n < 3$ generate rotation measure structures on small scales (*left panel*), while spectral indices $n > 3$ generate rotation measure structures on large scales (*right panel*). A spectral index $n = 3$ generates rotation measure structures on intermediate scales (*middle panel*).

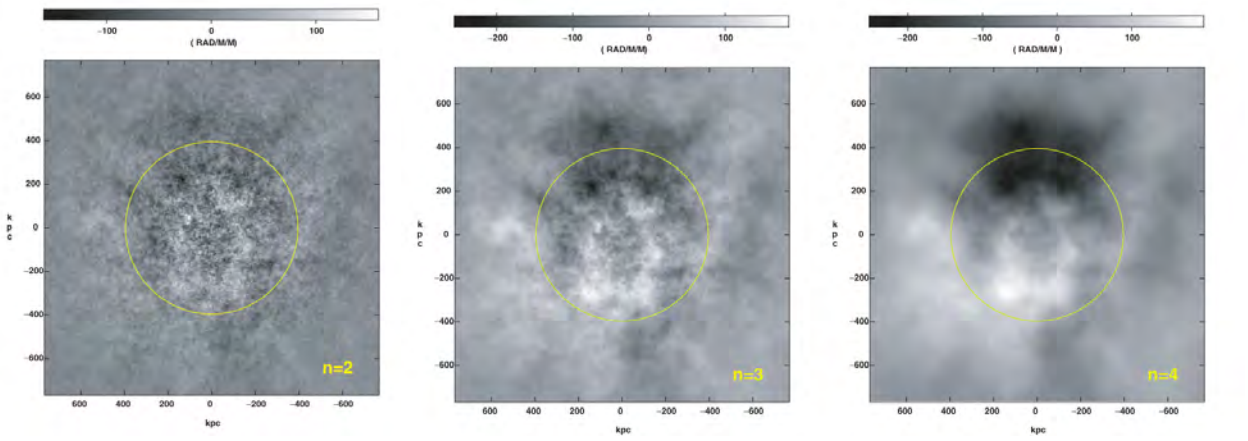

Figure 5.1 Synthetic rotation measure images obtained with the software FARADAY (Murgia et al. 2004). The images correspond to a power spectrum fluctuating between 6 and 770 kpc and to three different indices n ($|B_k|^2 \propto k^{-n}$, with $n = 2, 3, 4$). The average magnetic field strength at the center of the cluster is $\langle B_0 \rangle = 1 \mu$G and decreases with the distance from the cluster center as $n_{\rm e}^{0.5}$. The circles indicate the core radius of the thermal gas distribution. The field of view is $1.5 \times 1.5\,{\rm Mpc}^2$.

The prediction of synchrotron total intensity and polarization images of a radio halo requires the integration along the line of sight of a magnetic field and a relativistic electron distribution. Indeed, the total synchrotron emissivity is

$$J(\nu) \propto N_0 B^{(\alpha+1)} \nu^{-\alpha} \tag{5.14}$$

implying a brightness distribution

$$I(\nu) \propto N_0 B^{(\alpha+1)} \nu^{-\alpha} L \tag{5.15}$$

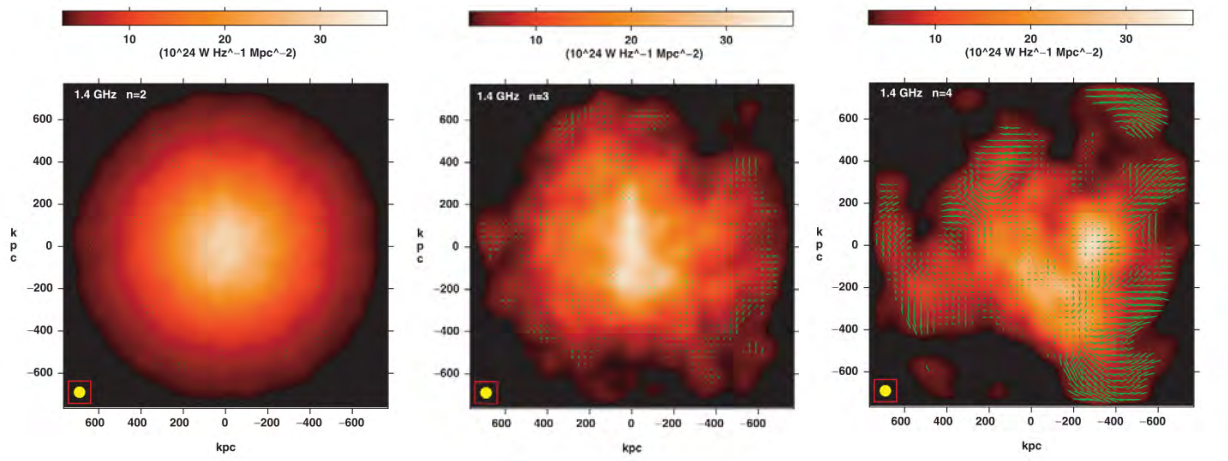

Figure 5.2 Synthetic synchrotron radio halo emission obtained with the software FARADAY (Murgia et al. 2004). The images correspond to a power spectrum fluctuating between 6 and 770 kpc and to three different indices n ($|B_k|^2 \propto k^{-n}$, with $n = 2, 3, 4$). The average magnetic field strength at the center of the cluster is $\langle B_0 \rangle = 1\mu$G. Color describes radio halo total intensity. Green vector length indicates the degree of polarization, their orientation the electric field direction.

where L is the source depth along the line of sight, see § 4.2.1. In Fig. 5.2, the synthetic total and polarized synchrotron emission from a radio halo at 1.4 GHz is shown for three different spectral indices n (Murgia et al. 2004). When the spectral index is $n < 3$ (e.g. $n = 2$, *left panel*), the radio halo emission is smooth and regular and lacks of polarization (energy on small scales), while when $n > 3$ (e.g. $n = 4$, *right panel*) the radio morphology is disturbed and the degree of polarization is higher (energy on large scales). If $n = 3$, the energy is uniformly distributed on small and large scales (*middle panel*).

We note that a number of degeneracies between the intracluster magnetic field parameters exists. In particular, the most relevant are the degeneracies between $\Lambda_{\rm max}$ and n, and between $\langle B_0 \rangle$ and η. Different combinations of these parameters lead to similar properties in the expected radio halo emission and rotation measure distribution. These degeneracies are presented in Fig. 5.3 (Bonafede et al. 2010). The *left panel* describes the degeneracy between $\Lambda_{\rm max}$ and n. The average value of the RM to $\sigma_{\rm RM}$ ratio observed in the Coma cluster (continuous line) can be explained with different combinations of $\Lambda_{\rm max}$ and n. In the *right panel*, the χ^2 plane obtained by comparing the $\sigma_{\rm RM}$ from synthetic and observed radio galaxy rotation measure images in the same galaxy cluster is shown. Different combinations of $\langle B_0 \rangle$ and η give equally good representations of the intracluster magnetic field in the cluster, since high values of the central strength of the magnetic field $\langle B_0 \rangle$ and of the index of the radial profile η can produce synthetic images similar to those obtained with low $\langle B_0 \rangle$ and η. These degeneracies can be reduced by improving the quality of data and by combining the RM analysis with the investigation of the radio halo emission (see Murgia et al. 2004).

5.3 Characterization of the magnetic field power spectrum

In the following, we define the rotation measure structure and auto-correlation functions and the corresponding auto-correlation lengths. The mathematical details can be found in the Appendix B.

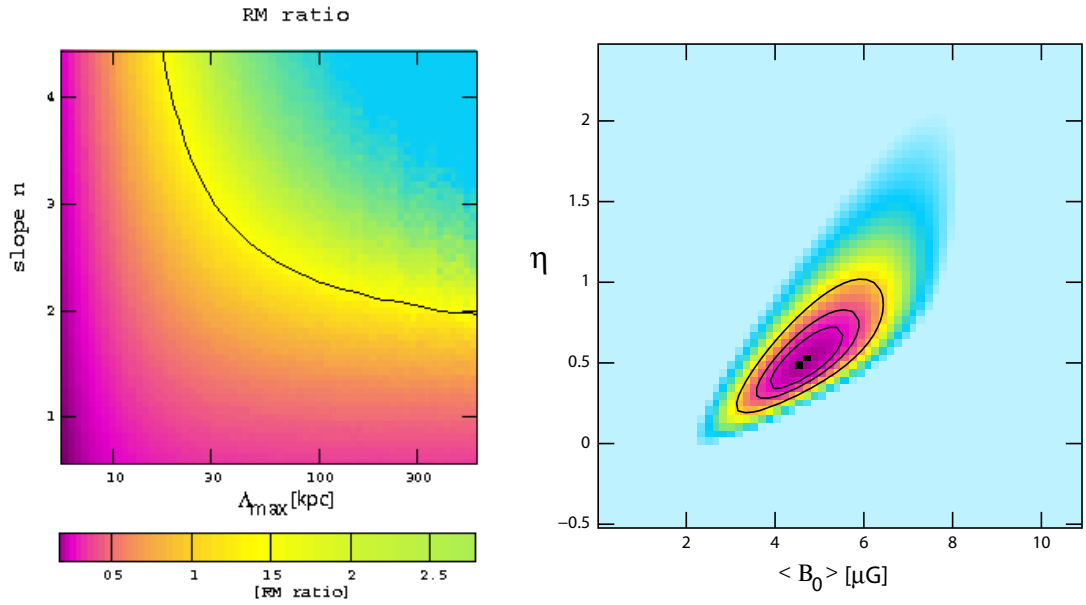

Figure 5.3 *Left panel*: synthetic RM to $\sigma_{\rm RM}$ ratio as a function of $\Lambda_{\rm max}$ and n. The continuous line indicates the average value of this ratio observed in the Coma cluster. *Right panel*: χ^2 plane for the two magnetic field parameters $\langle B_0 \rangle$ and η, obtained comparing synthetic and observed images in the galaxy cluster Coma. Contours indicate 1σ, 2σ, 3σ confidence level respectively. Images taken from Bonafede et al. (2010).

5.3.1 Structure and auto-correlation function

The rotation measure structure function $S_{\rm RM}$ is obtained by averaging the difference in RM values corresponding to pixels located at the scale distance $r_\perp = \sqrt{\Delta x^2 + \Delta y^2}$:

$$S_{\rm RM}(r_\perp) = \langle [RM(x,y) - RM(x+\Delta x, y+\Delta y)]^2 \rangle_{\rm (x,y)}. \tag{5.16}$$

The structure function is related to the RM auto-correlation function $C_{\rm RM}$

$$C_{\rm RM}(r_\perp) = \langle RM(x,y) \cdot RM(x+\Delta x, y+\Delta y) \rangle_{\rm (x,y)}, \tag{5.17}$$

by the simple relation:

$$S_{\rm RM}(r_\perp) = 2(\sigma^2_{\rm RM} + \langle RM \rangle^2) - 2C_{\rm RM}(r_\perp) = 2[C_{\rm RM}(0) - C_{\rm RM}(r_\perp)]. \tag{5.18}$$

For an isotropic field, the RM auto-correlation function and power spectrum are related by the Hankel transform

$$C_{\rm RM}(r_\perp) = 2\pi \int_0^\infty J_0(kr_\perp) |RM_{\rm k}|^2 k dk, \tag{5.19}$$

where

$$J_0(kr_\perp) = \frac{1}{2\pi} \int_0^{2\pi} e^{-{\rm i}kr_\perp \cos\theta} d\theta \tag{5.20}$$

is the zero-order Bessel function (Abramowitz & Stegun 1970).

Moreover, the rotation measure auto-correlation function is related to the magnetic field auto-correlation function $C_{\rm B_z}$ by the Abel transform (Enßlin & Vogt 2003),

$$C_{\rm RM}(r_\perp) = 812^2 n_{\rm e}^2 L \times \left(2 \int_{\rm r_\perp}^{\sqrt{({\rm L}/2)^2 + r_\perp^2}} \frac{C_{\rm B_z}(r) r}{\sqrt{r^2 - r_\perp^2}} dr \right), \tag{5.21}$$

where L is the linear size of the integration domain and, for simplicity, the thermal gas density n_e is considered constant here.

5.3.2 Auto-correlation length

If the characteristic fluctuation scale of the magnetic field is much smaller than the physical depth of the Faraday screen (such that $\langle B \rangle = 0$ and $\langle RM \rangle = 0$), in the limit $r_\perp \to 0$, the Eq. 5.21 gives

$$\sigma^2_{\rm RM} = 812^2 n_e^2 L \, \Lambda_B \, \sigma^2_{B_z}, \tag{5.22}$$

where Λ_B is the magnetic field auto-correlation length

$$\Lambda_B = \frac{3\pi}{2} \frac{\int_0^\infty |B_k|^2 k dk}{\int_0^\infty |B_k|^2 k^2 dk}. \tag{5.23}$$

This is a particularly important result, since it implies that we must know the power spectrum of the magnetic field fluctuations to determine the strength of the field from the RM image.

Similarly we can define the rotation measure auto-correlation length

$$\Lambda_{\rm RM} = 2 \frac{\int_0^\infty |RM_k|^2 dk}{\int_0^\infty |RM_k|^2 k dk}. \tag{5.24}$$

For a power law magnetic field power spectrum, the rotation measure auto-correlation length is larger than the magnetic field auto-correlation length. Therefore, the assumption of a magnetic field auto-correlation length equal to the rotation measure fluctuation scale determined through the observed images leads to an underestimation of the magnetic field strength.

6

The intracluster magnetic field power spectrum in Abell 2199

In this Chapter we investigate the magnetic field power spectrum in the cool core galaxy cluster A2199 by analyzing the polarized emission of the central radio source 3C 338.

It is well established that the polarized radiation from radio emitting plasma is modified by the Faraday rotation as it passes through the magneto-ionic intracluster medium. The radio galaxy 3C 338 in A2199 is a suitable target for this kind of study because this source is powerful, extended and located at the center of the cluster, allowing to constrain directly the magnetic field in this region.

We use VLA observations between 1665 and 8415 MHz to produce detailed Faraday rotation measure and fractional polarization images of the radio galaxy. Following Murgia et al. (2004), we simulate Gaussian random three-dimensional magnetic field models with different power-law power spectra and we compare the synthetic and the observed images in order to constrain the strength and structure of the magnetic field associated with the intracluster medium.

This work is presented in Vacca et al. (2012).

6.1 The cluster of galaxies A2199

A2199 (z=0.0311, Smith et al. 1997)[1] is a nearby cool-core galaxy cluster. *Chandra* observations by Johnstone et al. (2002) reveal X-ray cavities in the cluster center. The temperature of the intracluster medium decreases from 4.2 keV to 1.6 keV over radii from 100 kpc to 5 kpc, implying a drop in the radiative cooling time from 7 Gyr to 0.1 Gyr. These features seem to be consistent with a cooling flow, even if the action of radiative cooling should leave the central ICM with kT<1 keV. Therefore, as in many other cool core clusters, in A2199, it has been proposed that some heating mechanism (e.g. Tucker & Rosner 1983; Gaetz 1989; David et al. 2000) prevents the ICM from cooling down to temperatures below 1 keV. Kawano et al. (2003) suggest that previous AGN activity could be responsible for such heating in A2199.

[1] 1″=0.61 kpc, D_L=135 Mpc.

The radio source 3C 338 (otherwise known as B2 1626+39) is associated with the multiple nuclei cD galaxy NGC 6166, the brightest galaxy at the center of the cluster (Burns et al. 1983; Fanti et al. 1986), and it is classified as a restarting Fanaroff-Riley type I radio galaxy (see Murgia et al. 2011, and references therein). On parsec scales, 3C 338 is the first established example of a symmetric, two-sided source in a radio galaxy (Feretti et al. 1993), consisting of a compact core and two symmetric relativistic jets (Giovannini et al. 2001). On kiloparsec scales, Burns et al. (1983) and Giovannini et al. (1998) show that the radio structure consists of an active region, which includes the core and two symmetric jets terminating in two faint hot spots and two steep-spectrum radio lobes. The radio lobes are clearly associated with cavities in the central X-ray emission, as shown by Johnstone et al. (2002) and Gentile et al. (2007). Burns et al. (1983) pointed out a displacement between the large-scale structure with respect to the restarted symmetric jets, which could indicate a possible motion of the central AGN inside the galaxy, but we speculate that the displacement could also be due to an interaction between the old radio lobes with bulk motions in the surrounding medium caused by the sloshing of the cluster core (Markevitch & Vikhlinin 2007).

A2199 is an interesting target for Faraday rotation studies because the presence of X-ray cavities associated with the radio galaxy lobes indicates that the rotation of the polarization plane is likely to occur entirely in the intracluster medium, since comparatively little thermal gas should be present inside the radio-emitting plasma. A previous rotation measure study has been done by Ge & Owen (1994) based on 5000 MHz VLA data. These authors show that 3C 338 radio emission suffers a significant depolarization and is characterized by high RM values. By combining the information from this rotation measure image with deprojected ROSAT data, and assuming a very simple magnetic field model, Eilek & Owen (2002) infer an averaged magnetic field value along the line of sight of 15 μG.

In this work we try to improve upon the previous estimate by analyzing additional data and by performing a numerical modeling of the intracluster magnetic field fluctuations.

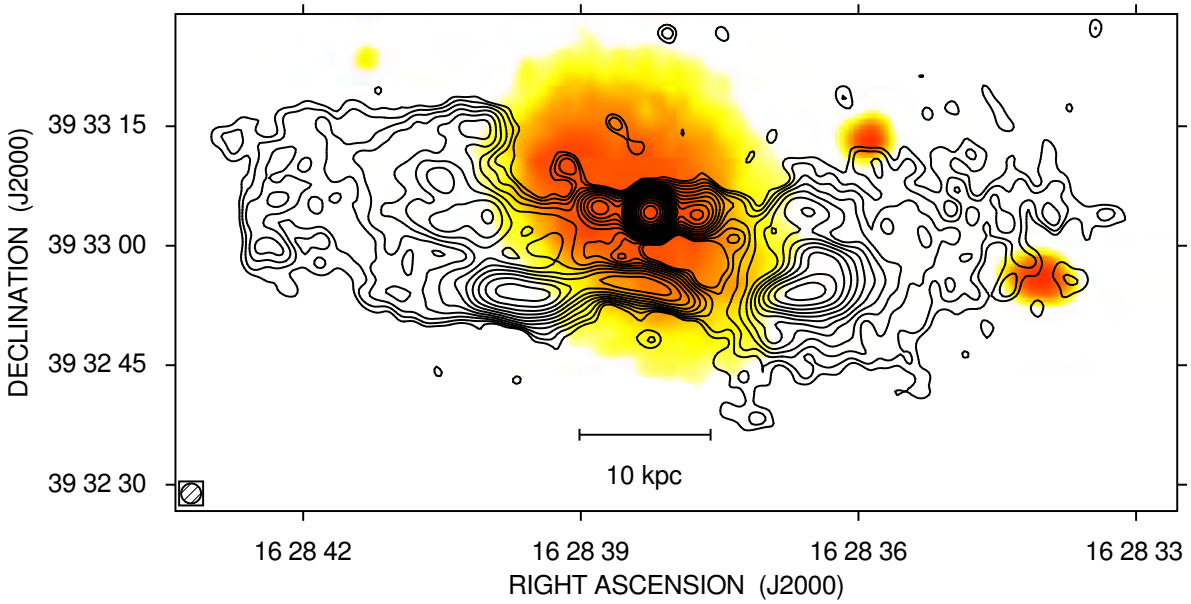

Figure 6.1 Total intensity radio contours of 3C 338 at 8415 MHz with an FWHM of 2.5″ × 2.5″. The first contour level is drawn at 0.06 mJy/beam and the rest are spaced by a factor $\sqrt{2}$. The sensitivity (1σ) is 0.02 mJy/beam. The contours of the radio intensity are overlaid on the DSS2 red plate.

Table 6.1 Details of the VLA observations of 3C 338.

Obs. frequency, ν (MHz)	Bandwidth (MHz)	VLA Configuration	Time (h)	Data	Project
1665	50	A	8.5	91-Jun-18/19	GG0005
4585/4685/4885	50	B	7.0	89-Apr-03	AG0269
4885	50	B	1.5	87-Dec-21	AS0309
4985	50	C	3.0	94-Nov-17	BG0012
4985	50	AB	3.5	95-Sep-11/12	BV0017
8415	50	C	3.0	94-Nov-17	BG0012
8415	50	BC	3.8	00-Feb-26	GG0038

Col. 1: Observing frequency; Col. 2: Observing bandwidth;

Col. 3: VLA configuration; Col. 4: Time on source; Col. 5: Dates of observations; Col. 6: VLA project name.

Table 6.2 Relevant parameters of the total intensity and polarization images between 1665 and 8415 MHz.

ν (MHz)	Beam ($'' \times ''$)	σ(I) (mJy/beam)	σ(Q) (mJy/beam)	σ(U) (mJy/beam)	S_ν (mJy)
1665	2.5×2.5	0.25	0.029	0.029	1490± 40
4585	2.5×2.5	0.06	0.033	0.032	520± 20
4685	2.5×2.5	0.06	0.025	0.026	470± 10
4885	2.5×2.5	0.06	0.026	0.027	440± 10
4985	2.5×2.5	0.08	0.037	0.037	400± 10
8415	2.5×2.5	0.02	0.015	0.015	170± 10

Col. 1: Observation frequency; Col. 2: FWHM; Col. 3,4,5: RMS noise of the I, Q, U images;

Col. 6: Flux density.

6.2 Radio observations and data reduction

We present polarimetric archival observations of 3C 338 at 1665, 4585, 4685, 4885, 4985, and 8415 MHz performed at the VLA in the A, B, and C configurations between 1987 December and 2000 February. All observations were made with a bandwidth of 50 MHz. The pointing center is identified by the coordinates RA(J2000)=$16^h28^m38^s$, and DEC(J2000)=$+39^d33^m04^s$, the details are provided in Table 6.1.

All data were reduced using the NRAO's Astronomical Image Processing System (AIPS) package. The radio source 3C 286 was used both as primary flux density calibrator and as reference for the absolute polarization angles. Phase calibration was derived from nearby sources, periodically observed over a wide range in parallactic angle to separate the source polarization properties from the antenna polarizations. We proceeded with the standard calibration procedures, imaging and self calibration. Once all the data were calibrated for each configuration and frequency, all visibilities corresponding to the same frequency were combined using the task DBCON in order to improve (u, v) coverage and sensitivity. The combined data were then self-calibrated to produce the final images. The images of total intensity I and Stokes parameters Q and U were restored with a circular beam of 2.5″. The noise levels of I, U, and Q are summarized in Table 6.2. Polarized intensity (corrected for the positive bias), $P = \sqrt{Q^2 + U^2}$, polarization angle, $\Psi = 0.5 tan^{-1}(U/Q)$, and fractional polarization $FPOL = P/I$ images were produced for each frequency.

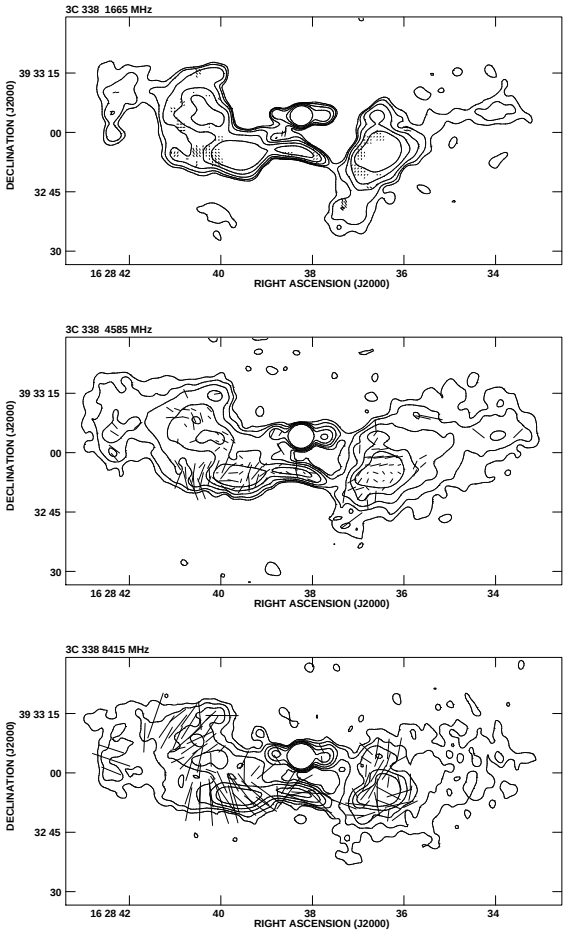

Figure 6.2 Total intensity contours and polarization vectors at 1665 (*top*), 4585 (*middle*), and 8415 MHz (*bottom*). The angular resolution is $2.5'' \times 2.5''$. Contour levels start at $3\sigma_{\rm I}$, and increase by factors of two. The lines give the orientation of the electric vector position angle (E-field) and are proportional in length to the fractional polarization ($1'' \sim 5\%$).

The total intensity contours of the radio galaxy 3C 338 overlaid on the DSS2 red plate[2] are showed in Fig. 6.1. The 8415 MHz radio galaxy emission peaks at RA(J2000)=$16^{\rm h}28^{\rm m}38^{\rm s}$ and DEC(J2000)=$+39^{\rm d}33^{\rm m}04^{\rm s}$. It is also the same location of the X-ray peak to within the image resolution. Therefore we chose this reference location for our analysis.

6.3 Polarization analysis

In Fig. 6.2 we present the total intensity radio contours and polarization vectors at 1665, 4585, and 8415 MHz at a resolution of $2.5'' \times 2.5''$. The length of the vectors is proportional to the fractional polarization, while their orientation is the same as the projected E-field. The fractional polarization and the polarization angle were obtained by considering only those pixels where the fractional polarization is above $3\sigma_{\rm FPOL}$ at the corresponding frequency. The total intensity emission of the source extends out to about $1'$ from the cluster center. The total flux density of the radio source and all the relevant parameters of the I, Q, and U images, are reported in Table 6.2.

[2] http://archive.eso.org/dss/dss

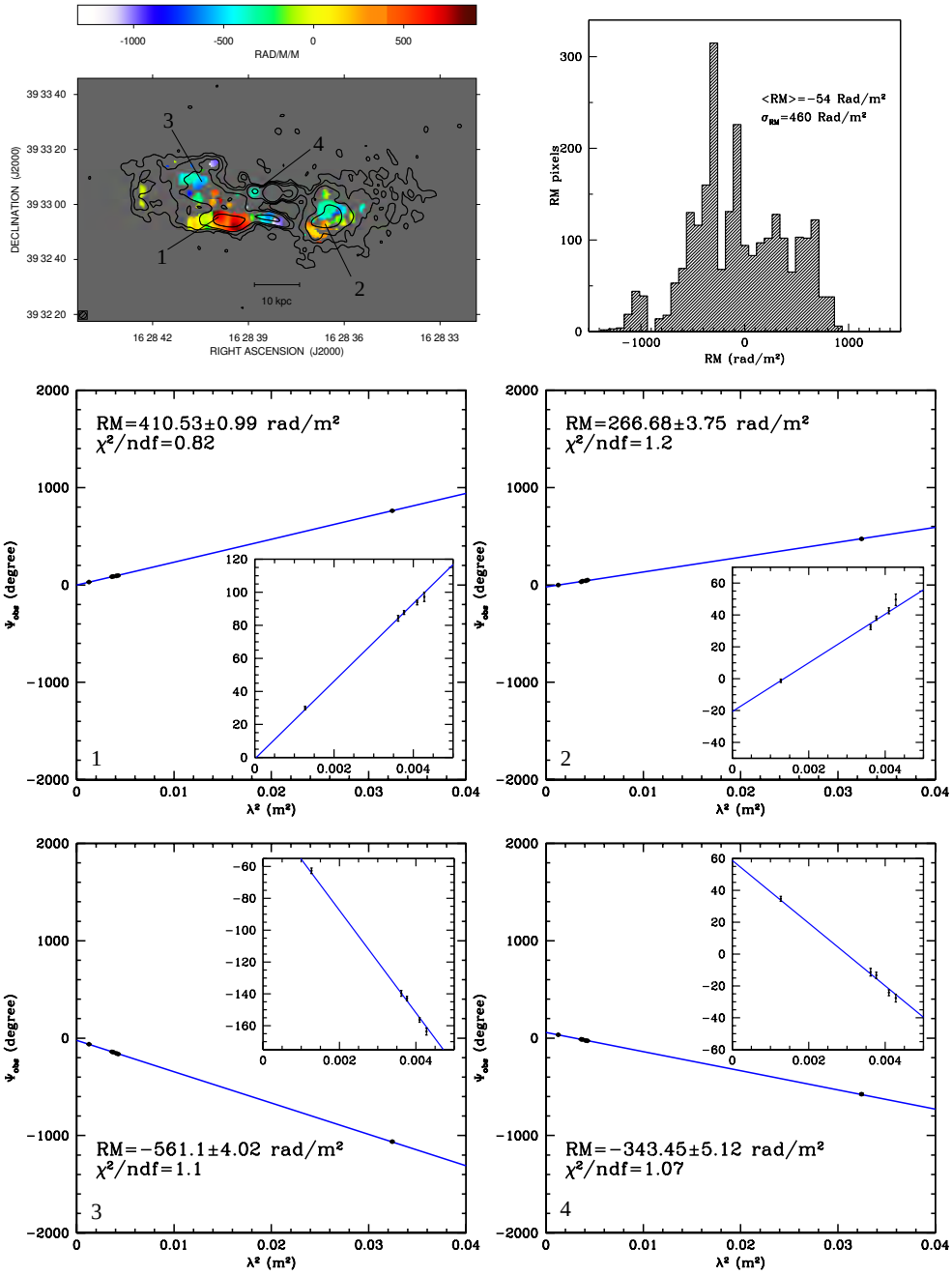

Figure 6.3 *Top left*: total intensity radio contours of 3C 338 at 8415 MHz overlaid on the RM image in colors. The angular resolution is 2.5″ × 2.5″. Contour levels are drawn at: 0.06, 0.12, 0.24, and 0.96 mJy/beam. *Top right*: histogram of the RM values. *Bottom*: sample plots of the observed position angle versus the squared wavelength at different source locations. The inset is a zoom of the observed polarization angle corresponding to frequencies between 4585 and 8415 MHz.

6.3.1 Rotation measure

As described in § 4.2.2, a foreground magneto-ionic screen changes the polarimetric properties of radio sources embedded or in its background. Therefore, rotation measure studies of these radio sources are a precious tool to investigate the magnetic field in the screen.

We produced the Faraday RM image by running the FARADAY code (Murgia et al. 2004). The

Table 6.3 Statistics of the rotation measure distribution.

Component	$\langle RM \rangle$ (rad/m^2)	$\sigma_{\rm RM}$ (rad/m^2)	$\mid RM_{\rm max} \mid$ (rad/m^2)	$Err_{\rm fit}$ (rad/m^2)	$\langle RM^2 \rangle^{1/2}$ (rad/m^2)
Total	-54	460	903	18	463
E-Lobe	66	473	903	20	478
W-Lobe	-251	356	581	16	436

Col. 1: Component of the source; Col. 2: Mean value of the RM distribution;

Col. 3: Standard deviation of the RM distribution; Col. 4: Maximum absolute value of the RM distribution;

Col. 5: Mean value of the RM fit error; Col. 6: Total power, $\langle RM^2 \rangle^{1/2} = (\langle RM \rangle^2 + \sigma^2_{\rm RM})^{1/2}$.

software requires as input Q and U images for each frequency and outputs the RM, the intrinsic polarization angle $\Psi_{\rm int}$, their errors images, and χ^2 maps. The RM image is created pixel by pixel by fitting the observed polarization angle $\Psi_{\rm obs}$ versus the squared wavelength λ^2 for all the frequencies. To reduce the problems associated with $n\pi$ ambiguities, the fitting algorithm can perform a sequence of improvement iterations. In the first iteration, only a subset of high signal-to-noise pixels is considered. In the successive iterations, lower signal-to-noise pixels are gradually included and the information from the previous iteration is used to assist the fit of the λ^2 law.

We considered only those regions of the radio source where the total intensity emission at 8415 MHz is above $5\sigma_{\rm I}$. Only pixels with an uncertainty in polarization angle below 10° at each wavelength were considered. The RM fit is generated if this condition is satisfied for at least five frequency maps. Almost half of the total number of the pixels in the RM image are based on a five-frequency fit. The remainder are based on a six-frequency fit.

The final rotation measure image of 3C 338 is shown in Fig. 6.3 (*top left panel*) with total intensity contours at 8415 MHz overlaid. The image has a resolution of 2.5″, which corresponds to 1.5 kpc at the distance of 3C 338. The RM has a patchy structure with values ranging from −1300 to 900 rad/m^2. As shown by the histogram in Fig. 6.3 (*top right panel*), the RM distribution is characterized by a mean value of $\langle {\rm RM} \rangle = -54$ rad/m^2 and a standard deviation $\sigma_{\rm RM} = 460$ rad/m^2. The RM fit is characterized by a mean error $Err_{\rm fit}$=18 rad/m^2. In Table 6.3 we report the statistics of the RM distribution of the entire source and, separately, of the east and west lobes. The mean and dispersion of the RM are quite different, but the "total power" $\langle RM^2 \rangle^{1/2} = (\langle RM \rangle^2 + \sigma^2_{\rm RM})^{1/2}$ is very similar. As a consequence, we cannot constrain the inclination to the line of sight of the source, since an inclination of the source to the line of sight would correspond to different Faraday depths for the two lobes that should result in different total powers. Therefore, in the following analysis we assume that 3C 338 is on the plane of the sky. Examples of the observed position angle $\Psi_{\rm obs}$ as a function of λ^2 for four high signal-to-noise pixels are shown in the *bottom panels* of Fig. 6.3. The observed fits are linear, as expected in the case of a foreground Faraday screen.

We have estimated the contribution of our own Galaxy to the Faraday rotation in the direction of 3C 338. In galactic coordinates, the radio source is located at $l = 62.9°$ and $b = 43.7°$. We computed the average of the RM values reported in Taylor et al. (2009) for a region of about 3° around this direction and from this we estimated a Galactic contribution of ∼13 rad/m^2. Since the Galactic foreground is small compared to the RM intrinsic to 3C 338, it has a negligible impact on the RM.

Table 6.4 Fractional polarization between 1665 and 8415 MHz

ν (MHz)	FPOL (%)
1665	1.1±0.3
4585	13.6±0.3
4685	15.8±0.2
4885	18.2±0.3
4985	23.0±0.4
8415	41.7±0.6

Col. 1: Observational frequency;

Col. 2: Fractional polarization.

6.3.2 Depolarization

In Table 6.4 we report the average fractional polarization levels of 3C 338 obtained by considering the same pixels as we used to calculate the RM image. The radio source is less polarized at longer wavelengths. This behavior can be interpreted in terms of variations in the RM on smaller scales than the beam of the radio images.

These unresolved RM structures in the foreground screen cause a depolarization of the signal which, to first order, can be approximated by

$$FPOL = FPOL_0 \exp(-a\lambda^4), \tag{6.1}$$

where a is a value related to the RM gradient within the observing beam and $FPOL_0$ is the intrinsic fractional polarization (Burn 1966, see also Laing et al. 2008 for a more recent derivation). We fitted the Burn law only between 4585 and 8415 MHz (6 and 3.6 cm) observations, since the formula is not applicable in the long-wavelength regime (20 cm/1665 MHz) (see Tribble 1991a, and §6.5). We find a=(66±6)×10^3 rad^2/m^4.

6.4 Faraday rotation modeling

Our aim is to constrain the intracluster magnetic field strength and structure in A2199 by using the information from the radio galaxy RM and polarization images presented in the previous Section. Our modeling is based on the assumption that the Faraday rotation is occurring entirely in the intracluster medium. In particular, we suppose that there is no internal Faraday rotation inside the radio lobes, as suggested by the X-ray cavities detected by Johnstone et al. (2002) and by the observed linearity of the polarization angle Ψ_{obs} versus λ^2 (see Fig. 6.3). Moreover, we suppose that any possible local RM enhancement occurring at the interface between the radio lobes and the surrounding medium is negligible compared to the total RM across the cluster (but see Rudnick & Blundell 2003, for a contrary viewpoint).

As shown in Eq. 4.19, the rotation measure is the integral along the line-of-sight of the intracluster magnetic field and the thermal gas density. To derive useful information about the intracluster magnetic field we firstly need a model for the spatial distribution of the thermal electron density.

6.4.1 Thermal gas modeling

The distribution of the thermal electrons was modeled using the *Chandra* X-ray observation of A2199 by Johnstone et al. (2002). In the *left panel* of Fig. 6.4 we show a superposition of the

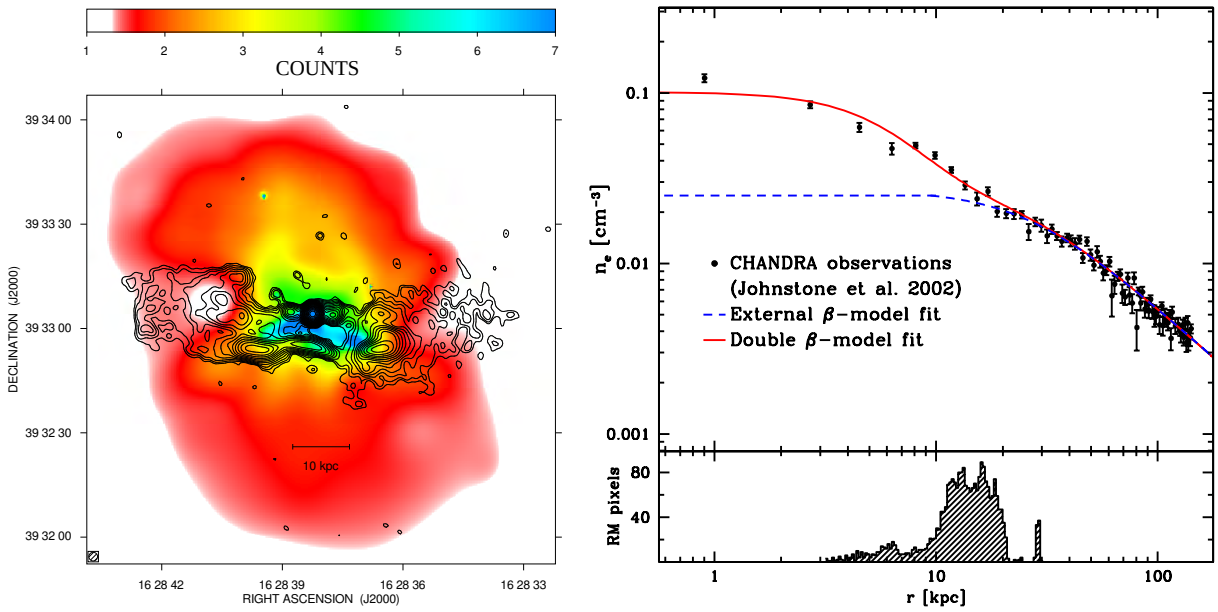

Figure 6.4 *Left panel*: Adaptively smoothed *Chandra* X-ray image (Obs. ID 497) in the 0.2-10 keV band of the galaxy cluster A2199 with the VLA contour levels at 8415 MHz overlaid. Pronounced X-ray cavities can be identified in correspondence of the radio galaxy lobes. *Top right panel*: deprojected thermal gas density profile (Johnstone et al. 2002). *Bottom right panel*: pixel distribution of the rotation measure image as a function of the distance from the cluster center.

VLA 8415 MHz contour levels on the *Chandra* X-ray image in the 0.2-10 keV band of the central region of A2199. In the *top right-hand panel* of Fig. 6.4 we show the deprojected thermal gas density $n_e(r)$ profile derived by Johnstone et al. (2002). In the *bottom right-hand panel* we show the rotation measure pixel distribution as a function of the distance from the cluster center. The RM pixels are sampled at distances from the cluster core in the range 3 to 30 kpc, with a higher concentration between 10 and 20 kpc.

We initially fitted the deprojected thermal gas density profile with a single β-model (Cavaliere & Fusco-Femiano 1976, see Eq. 5.10), but this thermal gas model does not allow a good description of the central jump owing to the high central density, typical of cooling core galaxy clusters. Therefore, we tried to improve the fit by considering a double β-model (Mohr et al. 1999, see Eq. 5.11). We do not discuss the physical validity of this model here. Our purpose is to empirically obtain an analytic profile that provides a reasonable continuous description of the deprojected gas density observed by Johnstone et al. (2002). This analytic profile can be conveniently extrapolated to both the cluster center and to large radii so that the integral in Eq. 4.19 can be performed.

The double β-model best-fit parameters are reported in Table 6.5, while the best-fit profile is shown as a continuous line in the *top right-hand panel* of Fig. 6.4. In the same plot we also show, as a dashed line, the external part of the model that has been constrained by a fit of the data points with $r > 18$ kpc. The total central density we found is $n_0 = n_{0_{\rm int}} + n_{0_{\rm ext}} = 0.101\,{\rm cm}^{-3}$.

Table 6.5 Double β- model parameters.

PARAMETER	VALUE	UNITS
$\beta_{\rm int}$	$1.5^{+0.2}_{-0.5}$	
$r_{c_{\rm int}}$	9^{+2}_{-3}	kpc
$n_{0_{\rm int}}$	$0.074^{+0.004}_{-0.01}$	cm^{-3}
$\beta_{\rm ext}$	$0.39^{+0.01}_{-0.03}$	
$r_{c_{\rm ext}}$	$26.0^{+0.8}_{-6.0}$	kpc
$n_{0_{\rm ext}}$	$0.027^{+0.003}_{-0.003}$	cm^{-3}

Table 6.6 Magnetic field model parameters.

Parameter	Description	Means of investigation
$\langle B_0 \rangle$	strength at the cluster center	3D simulations
η	radial slope, $\langle B(r) \rangle = \langle B_0 \rangle \left(\frac{n_e(r)}{n_e(0)}\right)^{\eta}$	3D simulations
n	power spectrum index, $\lvert B_k \rvert^2 \propto k^{-n}$	2D simulations
$\Lambda_{\rm min}$	minimum scale of fluctuation, $\Lambda_{\rm min} = 2\pi/k_{\rm max}$	2D simulations
$\Lambda_{\rm max}$	maximum scale of fluctuation, $\Lambda_{\rm max} = 2\pi/k_{\rm min}$	2D simulations

6.4.2 Magnetic field modeling

In this work we chose to model a power-law power spectrum whose normalization varies with the distance from the cluster center such that the average magnetic field strength scales as a function of the thermal gas density, as described in § 5.1.1. The tapering of the magnetic field power spectrum due to the thermal gas density may not preserve exactly the magnetic-field power-spectrum power-law shape at the edges (see §6.6).

Overall, our magnetic field model depends on the five parameters listed in Table 6.6: the strength at the cluster center $\langle B_0 \rangle$, the radial slope η, the power spectrum index n, and finally the minimum and maximum scale of fluctuations, $\Lambda_{\rm min} = 2\pi/k_{\rm max}$ and $\Lambda_{\rm max} = 2\pi/k_{\rm min}$, respectively.

6.4.3 Bayesian inference

To constrain the magnetic field strength and structure, we proceeded in two steps. First, we performed a two-dimensional analysis of the RM fluctuations and of the source depolarization to constrain the slope n and the range of scales of the power spectrum. Second, we performed three-dimensional numerical simulations to constrain the strength of the field and its scaling with the gas density. In both cases, we made use of the FARADAY code to produce synthetic polarization images of 3C 338 and to compare them to the observed ones. We compared model and data using the Bayesian inference, whose use was first introduced in the RM analysis by Enßlin & Vogt (2003). Because of the random nature of the intracluster magnetic field, the RM image we observe is just one possible realization of the data. Different realizations of magnetic field characterized by the same power spectrum will generate different RM images. Thus, rather than try to determine the particular set of power spectrum parameters that best reproduces the given realization of the data, it is perhaps more meaningful to search for that distribution of model parameters that maximizes the probability of the model given the data. The Bayesian inference offers a natural theoretical framework for this approach.

The Bayesian rule relates our prior information on the distribution $P(\vec{\theta})$ of model parameters $\vec{\theta}$ to their posterior probability distribution $P(\vec{\theta} \mid D)$ after the data D have been acquired

$$P(\vec{\theta} \mid D) = \frac{L(D \mid \vec{\theta})P(\vec{\theta})}{P(D)}, \tag{6.2}$$

where $L(D \mid \vec{\theta})$ is the likelihood function, while $P(D)$ is called the evidence. The evidence acts as a normalizing constant and represents the integral of the likelihood function weighted by the prior over all the parameters space

$$P(D) = \int L(D \mid \vec{\theta})P(\vec{\theta})d\vec{\theta}. \tag{6.3}$$

The most probable configuration for the model parameters is obtained by maximizing the joint posterior given by the product of the likelihood function with the prior probability. We used a *Markov Chain Monte Carlo* (MCMC) method to extract samples from the posterior probability distribution. In particular, we implemented the Metropolis−Hastings algorithm, which is capable of generating a sample of the posterior distribution without the need to calculate the evidence explicitly, which is often extremely difficult to compute since it would require exploring the entire prior space. The MCMC is started from a random initial value $\vec{\theta}_0$ and the algorithm is run for many iterations by selecting new states according to a transitional kernel, $Q(\vec{\theta}, \vec{\theta}')$, between the actual, $\vec{\theta}$, and the proposed position, $\vec{\theta}'$. The proposed position is accepted with probability

$$h = \min\left[1, \frac{L(D \mid \vec{\theta}')P(\vec{\theta}')Q(\vec{\theta}', \vec{\theta})}{L(D \mid \vec{\theta})P(\vec{\theta})Q(\vec{\theta}, \vec{\theta}')}\right]. \tag{6.4}$$

We chose for Q a multivariate Gaussian kernel. The MCMC starts with a number of "burn-in" steps during which, according to common practice, the standard deviation of the transitional kernel is adjusted so that the average acceptance rate stays in the range 25%−50%. After the burn-in period, the random walk forgets its initial state and the chain reaches an equilibrium distribution. The burning steps are discarded, and the remaining set of accepted values of $\vec{\theta}$ is a representative sample of the posterior distribution that can be used to compute the final statistics on the model parameters.

6.5 2D analysis

We performed a preliminary two-dimensional analysis of the RM fluctuations and of the source depolarization to constrain the slope n and the range of scales of the power spectrum. The two-dimensional analysis relies on the proportionality between the magnetic field and the rotation measure power spectra. On the basis of this proportionality, the index n of the two-dimensional rotation measure power spectrum is the same as the three-dimensional magnetic field power spectrum (see Appendix B):

$$|RM_{\mathrm{k}}|^2 \propto k^{-\mathrm{n}}. \tag{6.5}$$

At this stage, we are only interested in the shape of the power spectrum and not in the exact value of the normalization. Indeed, as a first approximation, we do not consider the effect of the spatially variable gas density; i.e., we suppose that the depth of the Faraday screen is on average the same over all of the source. We simulated synthetic images with a given power spectrum in a two-dimensional grid. The simulations start in the Fourier space, where the amplitudes of the RM components are selected according to Eq. 6.5 while the phases are completely random. The RM image in the real space is obtained by a fast Fourier transform (FFT).

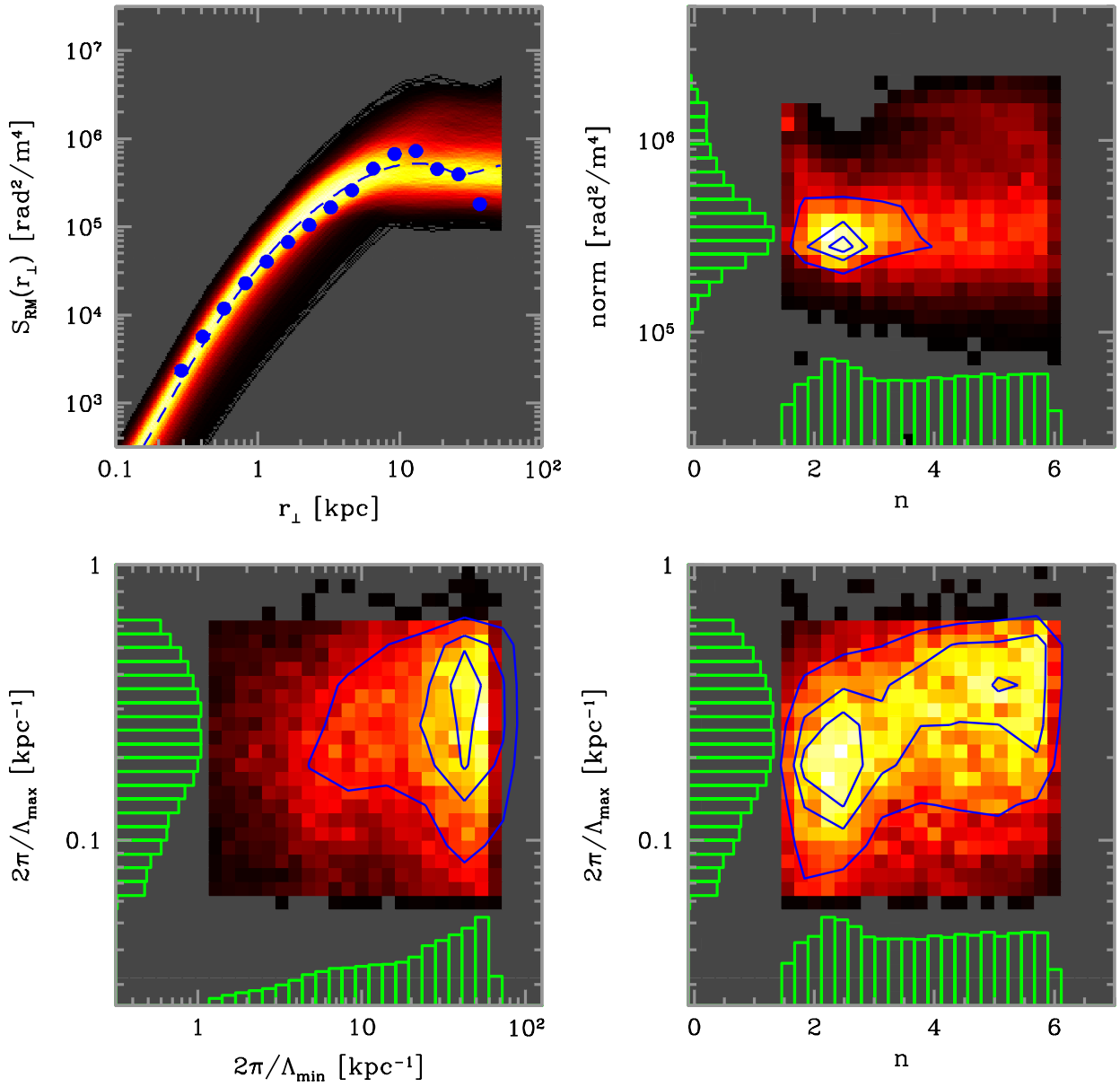

Figure 6.5 *Top left panel*: Bayesian analysis of the RM structure function. The dots represent the data (error bars are comparable to the size of the symbols). The shaded area represents the population of synthetic RM structure functions from the posterior distribution. The dashed line corresponds to the most probable value for the model parameters (see text). *Top right, bottom left, and bottom right panel*: one-dimensional (histograms) and two-dimensional (colors and contours) marginalization of the posterior for the model parameters. The contours are traced at 0.9, 0.75, and 0.5 of the peak value.

As a compromise between computational speed and spatial dynamical range, we adopted a computational grid of 2048×2048 pixels with a pixel size of 0.05 kpc. This grid allowed us to explore RM fluctuations on scales as small as $\Lambda_{min} \simeq 0.1$ kpc, i.e. one order of magnitude smaller than the beam of the observations ($FWHM \simeq 1.5$ kpc). Simultaneously, we were able to investigate fluctuations as large as $\Lambda_{max} \simeq 100$ kpc, i.e., comparable to the linear size of 3C 338. We determined the distribution of the best-fit parameters using the Bayesian approach outlined in §6.4.3. In particular, we characterized the RM image by its structure function (Eq. 5.16). The observed struc-

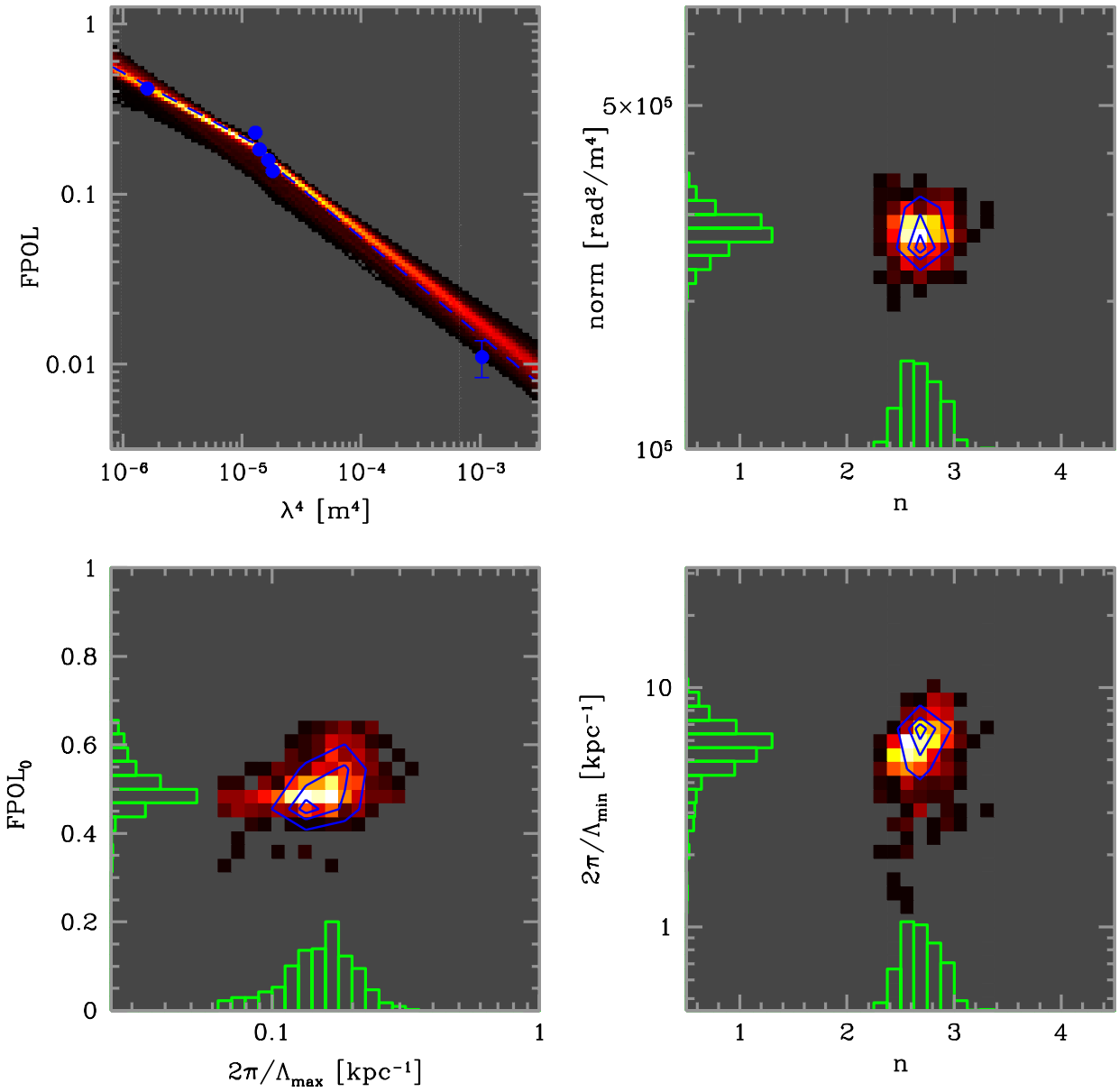

Figure 6.6 *Top left panel*: Bayesian analysis of the source depolarization. The dots represent the data. The shaded area represents the population of synthetic polarization from the posterior distribution. The dashed line corresponds to the most probable value for the model parameters (see text). *Top right, bottom left, and bottom right panel*: one-dimensional (histograms) and two-dimensional (colors and contours) marginalization of the posterior for the model parameters. The contours are traced at 0.9, 0.75, and 0.5 of the peak value.

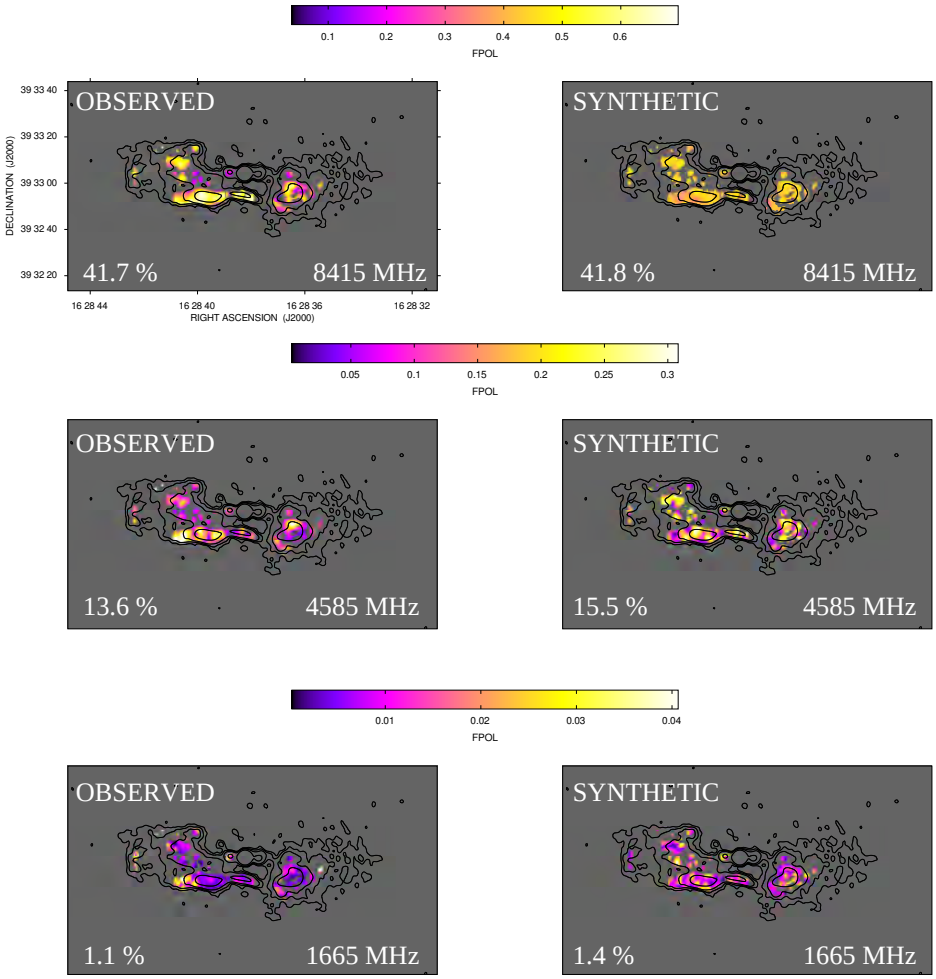

Figure 6.7 Examples of observed (*left*) fractional polarizations images at 8415, 4585, 1665 MHz compared with synthetic realizations (*right*) corresponding to the best fit parameters from the depolarization analysis.

ture function is shown in the *top left-hand panel* of Fig. 6.5, the formal error bars are comparable to the size of the dots. As noticed in Appendix B, for the power-law power-spectrum in Eq. 6.5, we can identify three regimes in the RM structure function. In the asymptotic small-separation regime, $r_\perp \ll 2\pi/k_{\rm max}$, the structure function increases as $S_{\rm RM}(r_\perp) \propto r_\perp^2$. In the intermediate regime, where $2\pi/k_{\rm max} \ll r_\perp \ll 2\pi/k_{\rm min}$, $S_{\rm RM}(r_\perp) \propto r_\perp^{\rm n-2}$. Finally for $r_\perp \gg 2\pi/k_{\rm min}$, the structure function saturates to the constant value of $S_{\rm RM} \simeq 2\sigma_{\rm RM}^2$. However, it can be hard to discern these three regimes directly from the observed structure function because of the coarse resolution of the radio images and the undersampling of the large separations because of the finite size of the RM image. Indeed, we need to resort to numerical simulations in order to account for the effects of these window functions. The synthetic images were thus gridded to the same geometry as the data and were convolved to the same angular resolution. Moreover, we masked the synthetic images using the observations to reproduce the window function imposed by the shape of 3C 338, and we added Gaussian noise with an rms value of $Err_{\rm fit}$, in order to mimic the noise of the observed RM image.

We then applied the Bayesian method described in § 6.4.3 by choosing uniform priors for the four power spectrum parameters: the normalization *norm*, the slope *n*, the minimum, and the maximum wave number $k_{\rm min}$ and $k_{\rm max}$. The statistics of the simulated RM fluctuations are Gaussian,

so their structure function at a given separation has a log-normal distribution. At each step of the MCMC, we performed 30 realizations of the same power spectrum with different random seeds and evaluated the average and the dispersion of the logarithm of the model structure function. We averaged the offsets and the dispersions at all the individual separations. From these values we computed the likelihood of the observed structure function.

In Fig. 6.5 we show the results of the Bayesian analysis of the rotation measure structure function. The output from the MCMC is a 4-dimensional hypercube containing a sample of the posterior distribution of the power spectrum parameters. The *top-right*, *bottom-left*, and *bottom right-hand panels* show the two-dimensional marginalization of this hypercube as color images. In addition, one-dimensional marginalizations are shown as histograms along each axis of these images. The two-dimensional marginalizations represent the projected density of samples in the MCMC, which is proportional to the posterior probability of that particular couple of model parameters. The maximum scale of the fluctuation, the normalization, and the slope of the power spectrum appears to be characterized by a peak that corresponds to the maximum posterior probability for that configuration of parameters, while for the minimum scale of fluctuation we only have an upper limit.

To provide a visual comparison between model and data, in the *top left-hand panel* of Fig. 6.5 we show the observed structure function along with the population of synthetic structure functions contained in the posterior sample, and the structure function for which posterior is maximum (best fit). The brighter pixels in the shaded image occur where many different synthetic structure functions overlap each other. The probability of the model given the data is higher in the brighter regions and is lower in the darker regions. The shaded region is relatively narrow for small separations but widens significantly for $r_\perp > 10$ kpc, indicating that our sensitivity to the large-scale separations is lower. Overall, the data stay close to the high-probability region, indicating that the model is doing a good job reproducing the observed RM structure. However, for $r_\perp > 20$ kpc the observed structure function decreases while the model stays relatively constant. The turnover of the observed structure function is very likely due to the lower gas density at large distances from the cluster center which results in a systematic decrease in the power spectrum normalization, hence of the Faraday rotation on large scales. This effect is not included in the current modeling, but it will be investigated with the aid of three-dimensional simulations in §6.6.

The power spectrum used to model the RM image should also be consistent with the observed depolarization of the radio source at increasing wavelengths (see §6.3.2). The depolarization is caused by RM variations on smaller scales than the beam that results in an incoherent sum of the radio signal. Indeed, modeling of the polarization amplitude can be used to place more stringent constraints on the minimum scale of fluctuation of the magnetic field and on the slope of the power spectrum. Using the same simulation set-up presented above, we reproduced the expected polarized signal from 3C 338 as a function of the wavelength. We first constructed an image of the source polarization at $\lambda = 0$, which is characterized by an intrinsic degree of polarization $FPOL_0$. We then simulated different RM images at full resolution and used them to rotate the intrinsic polarization vectors according to Eq. 4.18. These full-resolution images were finally convolved at the same resolution as the observations, resulting in beam depolarization of the signal at longer wavelengths.

We used the Bayesian inference and a Gaussian likelihood to estimate the distribution of the power spectrum parameters, which maximizes the probability that the observed depolarization is a realization of the model. In Fig. 6.6 the posterior from the depolarization analysis is shown for the five free parameters: the intrinsic degree of polarization $FPOL_0$, the normalization *norm*, the slope n, the minimum, and the maximum scale of fluctuation $\Lambda_{\rm min}$, and $\Lambda_{\rm max}$ of the magnetic field power spectrum. In the *top right* and *bottom panels* the two-dimensional (colors and contours)

and one-dimensional (histograms) marginalization of the posterior are shown for three different combinations of the model parameters. All the model parameters appear to be well constrained, and their values are consistent with the structure function analysis. In the *top left-hand panel*, the observed fractional polarization as a function of the fourth power of the wavelength is shown, together with the sample of realizations from the posterior and the best fit. In Fig. 6.7 the observed fractional polarization images are compared with synthetic realizations corresponding to the best fit parameters. The synthetic fractional polarization trend at higher frequencies (4585 to 8415 MHz) is consistent with a Burn law, $FPOL = FPOL_0 \exp(-a\lambda^4)$, with $a_{\rm synth}$=(61±3)×10^{3}rad^2/m^4, in very good agreement with the observed value $a_{\rm obs}$=(66±6)×10^{3}rad^2/m^4. However, it is clear from the *top left-hand panel* of Fig. 6.6 that our simulations are also able to explain the observed polarization levels reasonably well at low frequencies (1665 MHz) where the Burn law breaks down.

Overall, the combined two-dimensional analysis, RM image, and depolarization allowed us to obtain a first insight into the shape of the magnetic field power spectrum. We constrained the power spectrum index to n=(2.8±1.3), and the minimum and maximum scales in the range from $\Lambda_{\rm min}$=(0.7±0.1) kpc to $\Lambda_{\rm max}$=(35±28) kpc, where the given errors represent the dispersion of the one-dimensional marginalizations. In the next step we fix these values and constrain the strength of the magnetic field and its scaling with the gas density with the aid of three-dimensional simulations.

6.6 3D simulations

We constructed a three-dimensional model of the intracluster magnetic field by following the numerical approach described in Murgia et al. (2004) and presented in § 5.1.1. The gas density profile is described by the double-beta model in Eq. 5.11. Actually, we know that the gas density distribution in A2199 deviates from spherical symmetry because of the X-ray cavities corresponding to the radio lobes of 3C 338. Hence, we included the X-ray cavities in the three-dimensional simulations by removing from the gas density modeling all the magneto-ionic material inside two ellipsoidal regions centered on the radio lobes, as shown in the *top panel* of Fig. 6.8. In the *bottom panel* we trace the profile of the X-ray brightness along a horizontal slice passing through the radio lobes for the double beta-model with and without cavities. The model with cavities provides a better description of the observed X-ray brightness along the slice.

We simulated the random magnetic field by using a cubical grid of 1024^3 pixels with a cell size of 0.16 kpc/pixel. The synthetic RM images were obtained by integrating numerically the gas density and the magnetic field product along the line-of-sight accordingly to Eq. 4.19. In a similar way as in the two-dimensional simulations, the synthetic RM images were gridded, convolved, blanked, and noised as the observed RM image before the comparison with the data. We used the Bayesian approach to find the posterior distribution for $\langle B_0 \rangle$ and η, which maximizes the probability that the observed structure function is a realization of the model. The slope n and the scales $k_{\rm min}$ and $k_{\rm max}$ were kept fixed at the values found with the two-dimensional analysis.

We started with uniform priors for $\langle B_0 \rangle$ and η and we evaluated the likelihood of the structure function by mean of 30 different configurations for the magnetic field phases at each step of the MCMC. The result of the Bayesian analysis is shown in Fig. 6.9. In the *right panel* we present the two-dimensional (colors and contours) and one-dimensional marginalizations of the posterior. The two parameters appear well constrained. We found a magnetic field with a central strength $\langle B_0 \rangle$=(11.7±9.0) μG, and a radial slope η=(0.9±0.5). In the *left panel* we show the observed structure function along with the synthetic structure functions from the posterior and the best fit. The three-dimensional modeling represents a significant improvement over the two-dimensional analysis. In fact, we are now able to describe the overall shape of the observed structure function with

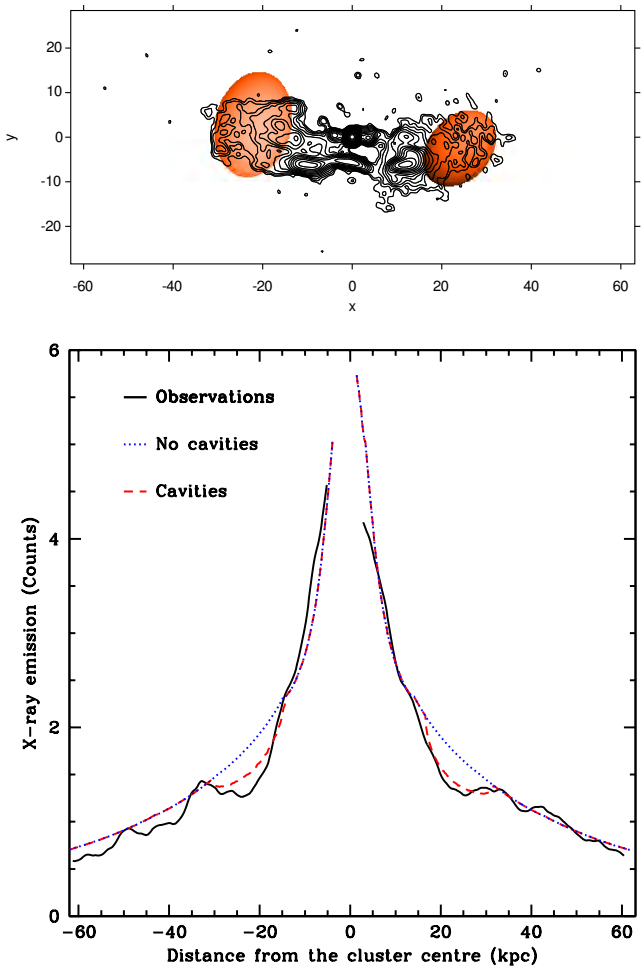

Figure 6.8 *Top panel*: X-ray cavity model. The darker region indicates the location where the thermal gas has been subtracted from the double β-model. *Bottom panel*: horizontal slice passing through the X-ray cavities at the cluster center. Continuous line represents the observations from the *Chandra* image, dashed line simulations with cavities, dotted line simulations without cavities.

good accuracy, including the turnover at large separations that is most likely due to the decrease in the Faraday rotation with radius. In the three-dimensional simulations we kept the maximum scale of the magnetic field fluctuation fixed to Λ_{max}=35 kpc, which is the value found from the two-dimensional analysis in § 6.5. The consequences of a different choice of this parameter are discussed in further detail in § 6.7 where we also tested the cases Λ_{max}=10 and 164 kpc. The value Λ_{max}=35 kpc still provides the best description of the observed RM structure function. In the *left panel* of Fig. 6.10 we plot the magnetic field power spectra corresponding to the maximum posterior for the three values of Λ_{max}. The original power law shape has been slightly modified by the tapering due to the thermal gas density (see §6.4.2). On the *right panel* the radial profiles corresponding to the maximum posterior for the three values of Λ_{max} are shown.

We performed the same Bayesian analysis also not taking the X-ray cavities into account (not shown). We found very similar results to those including the cavities and we conclude that the presence of these voids in the gas density distribution has a second-order impact on the Faraday rotation measures we are analyzing. This could be because most of the lines of sight sampled from our observed RM image do not intercept the regions of the cluster affected by the cavities.

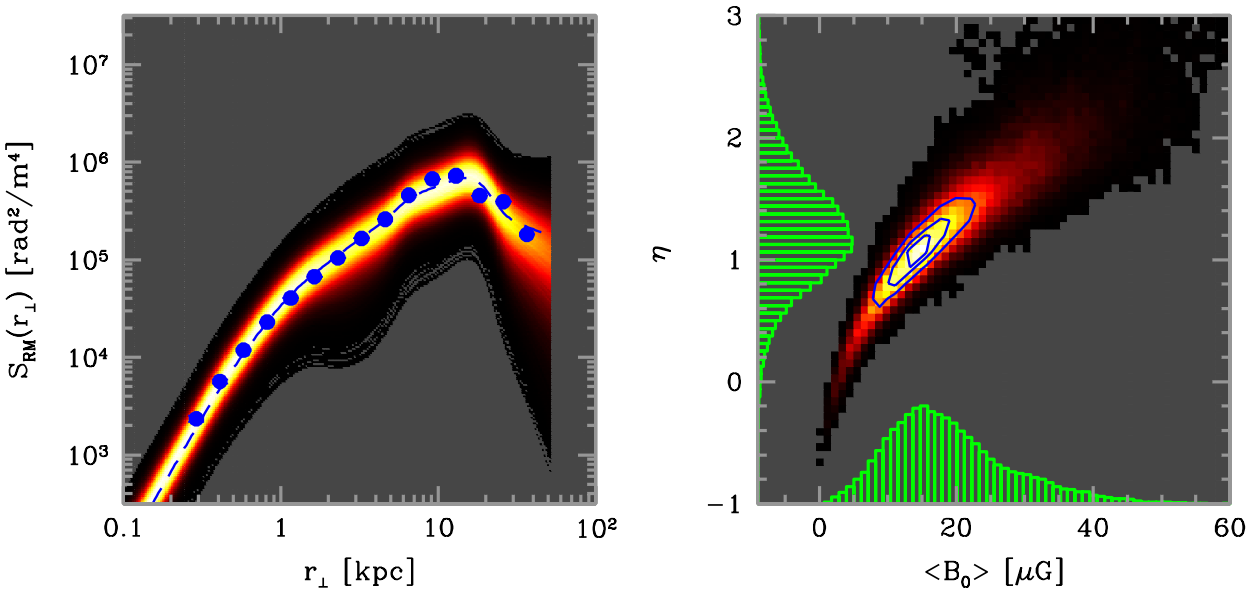

Figure 6.9 Bayesian three-dimensional analysis of the RM structure function for the model with Λ_{max}=35 kpc. *Left panel*: The dots represent the data (error bars are comparable to the size of the symbols). The shaded area represents the population of synthetic RM structure functions from the posterior distribution. The dashed line corresponds to the most probable value for the model parameters (see text). *Right panel*: one-dimensional (histograms) and two-dimensional (colors and contours) marginalizations of the posterior for the model parameters. The contours are traced at 0.9, 0.75, and 0.5 of the peak value.

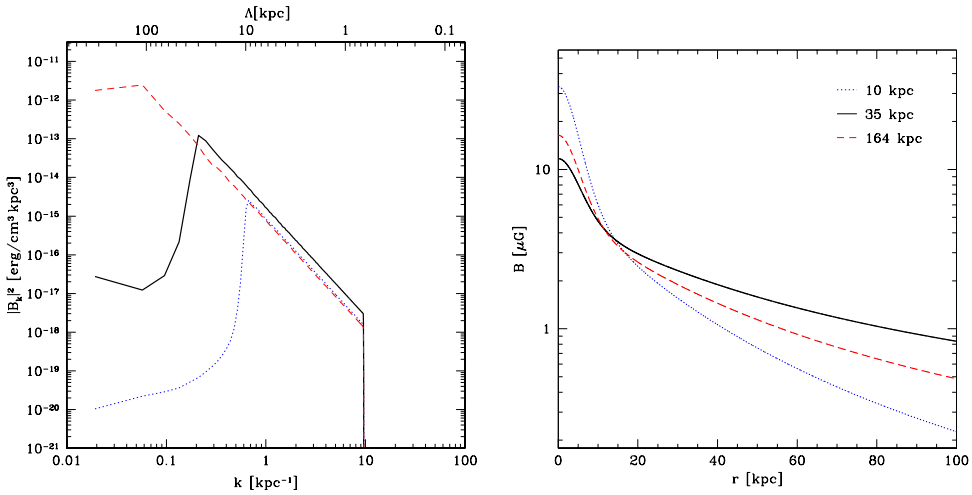

Figure 6.10 The magnetic field power spectra (*left panel*) and radial profiles (*right panel*) for the models corresponding to the three values of Λ_{max}=10, 35, and 164 kpc are shown as dotted, continuous, and dashed lines, respectively. The model with Λ_{max}=35 kpc provides the best description of the observed RM structure function, see text.

Finally, in Fig. 6.11 we present a qualitative comparison between the observed and a synthetic RM image taken from the simulations with cavities. Although very simple, the power-spectrum model adopted here provides a reasonable description of the patchy RM structure seen in the data.

It is interesting to compare our result with the independent estimate based on the theoretical

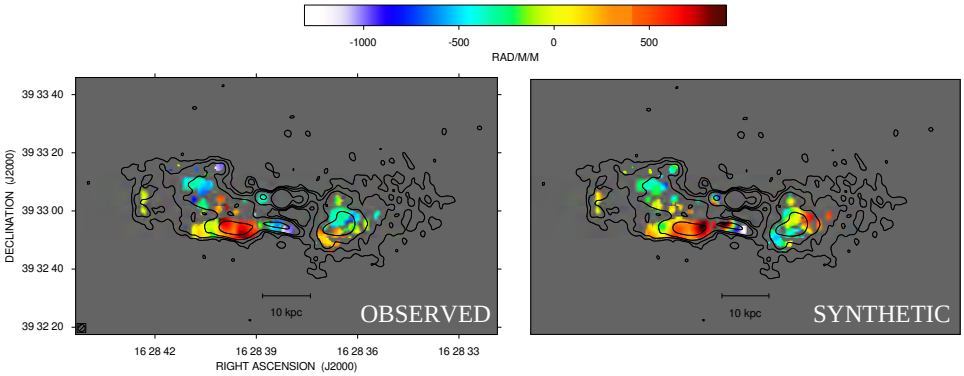

Figure 6.11 Qualitative comparison between the observed rotation measure image (*left*) and a synthetic three-dimensional realization (*right*).

work by Kunz et al. (2011). By assuming that turbulent dissipation balances radiative cooling at all radii inside the cluster core, Kunz et al. (2011) find in the bremsstrahlung regime (that is $T \gtrsim 1\,\mathrm{keV}$)

$$B(r) \simeq 11\xi^{-1/2}\left(\frac{n_{\rm e}(r)}{0.1\mathrm{cm}^{-3}}\right)^{1/2}\left(\frac{T(r)}{2\,\mathrm{keV}}\right)^{3/4}\mu\mathrm{G}, \tag{6.6}$$

where T is the temperature, while ξ is related to the kind of micro-scale instability whose evolution regulate the pressure anisotropy in the plasma (ξ^2 is expected to range between 0.25 and 1 in a turbulent plasma). By considering a central density $n_0 \simeq 0.1\,\mathrm{cm}^{-3}$ and a central temperature $T \simeq 2\,\mathrm{keV}$, according Johnstone et al. (2002), they find $B_0 \simeq 11\xi^{-1/2}\,\mu$G, very close to our estimate based on the Faraday rotation.

6.7 Maximum scale of fluctuation

In this section we briefly discuss the determination of the outer scale of the magnetic field fluctuations. On the basis of the two-dimensional and three-dimensional simulations, we find that a maximum fluctuation scale of $\Lambda_{\rm max}$=35 kpc provides a very good description of the observed structure function.

The observed rotation measure structure function is affected by a turnover in the large-separation regime ($r_\perp \gg 2\pi/k_{\rm min}$). The drop comes from a lowering of the gas density at large distances from the cluster center, resulting in a systematic decrease of the power of the Faraday rotation on large scales. This effect cannot be modeled by the two-dimensional simulations (see *top-left panel* of Fig. 6.5), while it is reproduced perfectly by the three-dimensional simulations (see *left panel* of Fig. 6.9). However, since we know that the tapering imposed by the gas density distribution on the RM structure function at large separations may limit the possibility to determine the maximum fluctuation scale of the magnetic field, we may ask which is our actual sensitivity on $\Lambda_{\rm max}$.

An accurate analysis would require considering $\Lambda_{\rm max}$ as a free model parameter also in the three-dimensional simulations, but the computational burden would be heavy. Indeed, we decided to explore only two more different values of $\Lambda_{\rm max}$, namely, a value of $\Lambda_{\rm max} = 10\,\mathrm{kpc}$, which is lower than the best-fit value, and a value of $\Lambda_{\rm max} = 164\,\mathrm{kpc}$, which is the maximum allowed by our computational grid of 1024^3 pixels.

We performed the Bayesian analysis of the RM structure function with the same magnetic field configuration as is described in § 6.5, except for the maximum scale of fluctuations. The results are presented in Fig. 6.12 for $\Lambda_{\rm max}$=10 kpc and $\Lambda_{\rm max}$=164 kpc (*left* and *right panels*, respectively).

In the *bottom panels* of Fig. 6.12 we present the two-dimensional (colors and contours) and one-dimensional (histograms) marginalizations of the posterior. The magnetic field central strength and radial decrease are constrained to

- $\langle B_0 \rangle$=(33.1±9.7) μG, and η=(1.7±0.4) for $\Lambda_{\rm max}$=10 kpc;
- $\langle B_0 \rangle$=(16.4±8.9) μG, and η=(1.2±0.5) for $\Lambda_{\rm max}$=164 kpc.

In the *top panels* we show the observed structure function (dots) along with the synthetic structure functions from the posterior. The blue line is the best fit. We note that $\Lambda_{\rm max}$ =10 kpc does not give a good description of the data because there is not enough power on large scales.

On the other hand, a maximum scale of fluctuation of $\Lambda_{\rm max}$ =164 kpc provides a better description of the observed structure function, even if it predicts slightly too much power for separations larger than $r_\perp > 20$ kpc. In this regime, the magnetic field model with $\Lambda_{\rm max}$ =35 kpc is still better.

Indeed, we may conclude that $\Lambda_{\rm max}$ should be surely larger than 10 kpc. Although the drop in the gas density limits our sensitivity, we may infer that $\Lambda_{\rm max}$ should be around 35 kpc, in any case lower than 164 kpc.

6.8 Conclusions

We investigated the magnetic field power spectrum in the cool core galaxy cluster A2199 by analyzing the polarized emission of the central radio source 3C 338. We used archival VLA observations between 1665 and 8415 MHz to produce detailed Faraday rotation measure and fractional polarization images of the radio galaxy. We observed a significant depolarization of the radio emission of the radio galaxy and high RM values. This agrees with the analysis performed by Ge & Owen (1994) at 5000 MHz, although our result takes the additional information at 1665 and 8415 MHz into account.

We simulated Gaussian random three-dimensional magnetic field models with different power-law power-spectra, and we assumed that the field strength decreases radially as a power of the thermal gas density as $n_{\rm e}^{\eta}$. By comparing the synthetic and the observed images with a Bayesian approach, we constrained the strength and structure of the magnetic field associated with the intracluster medium. We found that the Faraday rotation toward 3C 338 in A2199 is consistent with a magnetic field power-law power spectrum characterized by an index n=(2.8±1.3) between a maximum and a minimum scale of fluctuation of $\Lambda_{\rm max}$=(35±28) kpc and $\Lambda_{\rm min}$=(0.7±0.1) kpc, respectively. The corresponding magnetic field auto-correlation length is $\Lambda_{\rm B}$=5.2 kpc. In addition, by including in the modeling the presence of X-ray cavities in coincidence with the radio galaxy lobes, we found a magnetic field strength of $\langle B_0 \rangle$=(11.7±9.0) μG at the cluster center. Farther out, the field decreases with radius following the gas density to the power of η=(0.9±0.5). To a comparison with other values reported in the literature, the radially averaged magnetic field strength calculated over the central 1 Mpc^3 is ∼0.19 μG. The additional data and the numerical modeling of the intracluster magnetic field fluctuations allowed us to improve upon the previous estimate of 15 μG (Eilek & Owen 2002), with more stringent constraints not only on the magnetic field strength but also on its structure.

From the literature the central magnetic field strength found in merger galaxy clusters is a few μG, e.g. 2.5 μG in A2255 by Govoni et al. (2006) and 4.7 μG in Coma by Bonafede et al. (2010). In cooling-core galaxy clusters the magnetic field central strength is still uncertain. Typically it is a few tens μG (as in Hydra A, where values between 19 and 80 μG have been indicated, e.g. Laing et al. 2008; Kuchar & Enßlin 2011) even if lower values have also been found, for instance in the

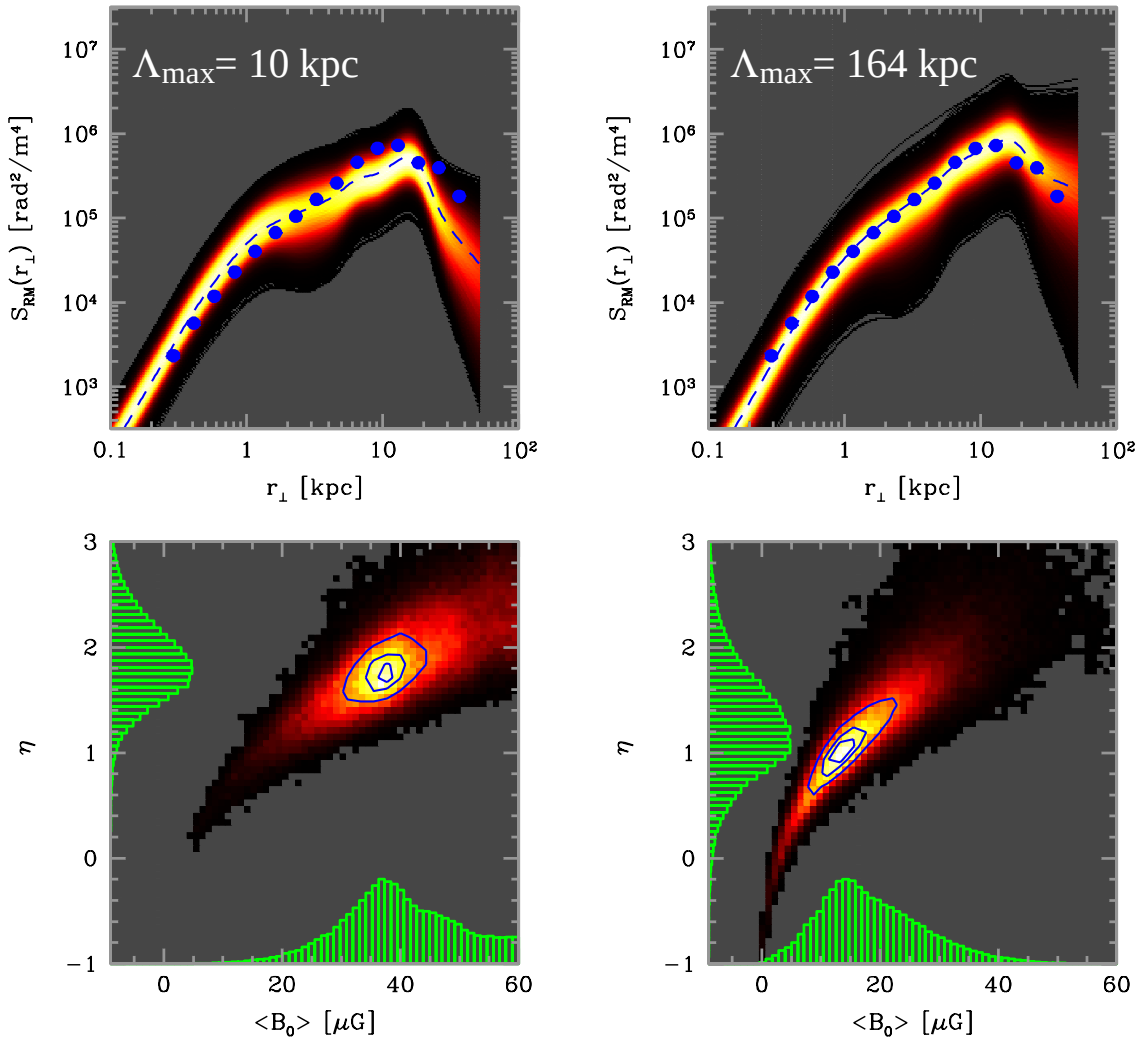

Figure 6.12 Bayesian three-dimensional analysis of the RM structure function for the model with cavities for Λ_{max}=10 kpc (*left*) and Λ_{max}=164 kpc (*right*). *Top panels*: The dots represent the data (error bars are comparable to the size of the symbols). The shaded area represents the population of synthetic RM structure functions from the posterior distribution. The dashed line corresponds to the most probable value for the model parameters (see text). *Bottom panels*: one-dimensional (histograms) and two-dimensional (colors and contours) marginalizations of the posterior for the model parameters. The contours are traced at 0.9, 0.75, and 0.5 of the peak value.

galaxy cluster A2634 (3 μG, Vogt & Enßlin 2003). In A2199 we found a magnetic field strength of about 10 μG that seems to confirm values of the magnetic field central strength in cooling-core galaxy clusters that are higher than in merging clusters.

7

The intracluster magnetic field power spectrum in Abell 665

In this Chapter we investigate the power spectrum of the large scale intracluster magnetic field in the merging galaxy cluster A665, which contains a known radio halo.

Following Tribble (1991b) and Murgia et al. (2004), we propose to study the cluster magnetic field strength and structure on the basis of the radio halo properties. Indeed, information on the cluster magnetic field can be derived from detailed images of the radio halo, since the halo brightness fluctuations and the polarization level are strictly related to the intracluster magnetic-field power spectrum. A665 is a suitable target for this kind of study since its radio halo is powerful, extended, and characterized by angular size suitable to VLA observations. In addition, the cluster declination is compatible with full synthesis.

We investigate the total intensity and the polarization properties of the A665 radio halo at 1.4 GHz by means of a new deep and high resolution VLA observation combined with previously published data (Giovannini & Feretti 2000). The power spectrum of the intracluster magnetic field fluctuations is constrained by comparing the data with the expectations of simulated random three-dimensional magnetic field models characterized by different power spectra.

This work is presented in Vacca et al. (2010).

7.1 The cluster of galaxies Abell 665

The cluster of galaxies A665 (z=0.1829, Gómez et al. 2000)[1] is well known to contain an extended diffuse radio halo first observed by Moffet & Birkinshaw (1989) and successively confirmed by Jones & Saunders (1996). At an angular resolution of about 1′, the radio halo is asymmetric because it is elongated in the southeast-northwest direction (Giovannini & Feretti 2000).

The total halo flux density at 1.4 GHz is 43.1 ± 0.8 mJy, while at 0.327 GHz the flux density is 197 ± 6 mJy. This results in an averaged spectral index of $\alpha_{0.3}^{1.4} = 1.04 \pm 0.02$ (Feretti et al. 2004b). Like all clusters containing a radio halo, A665 shows signatures of a major merger. Optical

[1] 1″=3.04 kpc, $D_L = 878$ Mpc.

(e.g. Gómez et al. 2000) and X-ray (e.g. Hughes & Birkinshaw 1994) studies reveal a disturbed dynamical state.

Chandra satellite data have provided a detailed gas temperature map revealing a shock region with a temperature jump from 8 keV to 15 keV, located near the southern boundary of the radio halo (Markevitch & Vikhlinin 2001; Govoni et al. 2004). The radio morphology seems to follow the X-ray elongation, trailing the shock wave direction. A spectral analysis of *Chandra* data by Million & Allen (2009) indicates the possibility of non-thermal (or quasi-thermal) X-ray emission, likely due to inverse Compton scatter between relativistic electrons responsible for radio halo emission and cosmic microwave background photons.

7.2 Radio observations and data reduction

We present a new deep, polarization sensitive, full-synthesis observation of A665 at 1.4 GHz obtained using the VLA in C configuration. The details of the observation are summarized in Table 7.1. The data were reduced following standard procedures using the NRAO's Astronomical Image Processing System (AIPS) package.

The nearby phase calibrator 0834+555 was observed over a wide range in parallactic angle to separate the source polarization properties from the feed parameters. The radio source 3C286 was used both as primary flux density calibrator and as reference for the absolute polarization angles. Radio interferences were carefully excised, and several cycles of self-calibration and CLEAN were applied to remove residual phase variations. A circular beam of 15″ was used to restore the final images of total intensity I and Stokes parameters Q and U. Images of polarized intensity $P = \sqrt{Q^2 + U^2}$ (corrected for the positive bias) and fractional polarization $FPOL = P/I$ were derived from the I, Q, and U images. The I image has an rms noise level of $\sigma_{\rm I} \simeq 25\,\mu$Jy/beam, while the P image has an rms noise level of $\sigma_{\rm P} \simeq 15\,\mu$Jy/beam.

In order to improve *uv*-coverage and sensitivity to the diffuse emission but still keeping a good angular resolution, we combined the new C configuration data with the D configuration data by Giovannini & Feretti (2000), see Table 7.1. The D configuration data have been calibrated in phase and amplitude by using the sources 0841+708 and 3C48, respectively. A circular beam of 55″ was applied to restore the final total intensity image I, which has a noise level of 60 μJy/beam. The combined C+D data were then self-calibrated to produce a final total intensity image. This image was restored with a circular beam of 25″ and has a noise level of 45 μJy/beam. Since the D configuration data were not polarization sensitive, no Q and U images were produced with the combined C+D dataset. The total intensity images at different resolution of the radio emission in A665 are shown in Fig. 7.1.

The central regions of the galaxy cluster are permeated by a low-surface brightness radio halo which is surrounded by many discrete radio sources. The full extent of the radio halo is readily visible in the D configuration image shown in Fig. 7.1a. However, the comparatively low resolution of this image does not permit easily distinguishing the contribution of the discrete radio sources from the diffuse radio halo.

The new C configuration image at a resolution of 15″ is shown in Fig. 7.1b. Here we can clearly separate the halo emission from the discrete radio sources. In particular, there are a few embedded sources in the central regions, and at least part of the northwestern elongation of the halo seen at lower resolution comes from a blending of several discrete sources distributed, in projection, along an arc-like structure. At the sensitivity level of our C configuration observation, we did not detect polarized emission from the radio halo. Since the innermost regions of the halo have an average brightness of $I \simeq 100$ μJy/beam, we can derive a 1σ upper limit to the fractional polarization of

Table 7.1 Details of the VLA observations of Abell 665.

Obs. pointing, RA (J2000)	Obs. pointing, DEC (J2000)	Obs. frequency, ν (MHz)	Bandwidth (MHz)	Config.	Date	Time (h)	Project
08:30:53.000	+65:51:30.000	1465, 1415	25	C	24-Jul-2005	13	AG690
08:30:54.830	+65:49:54.800	1365, 1435	50	D	14-Jul-1996	5	AF304

$FPOL \leq \sqrt{\sigma_{\rm P}^2/(I^2-\sigma_{\rm I}^2)} \simeq 15\%$. The polarization of the discrete sources in the field of view is discussed in § 7.5.

Finally, In Fig.7.1c we present the C+D configuration image at a resolution of 25″ (corresponding to 75 kpc at the cluster distance). The radio iso-contours[2] are overlaid on the adaptively smoothed *Chandra* X-ray image in the 0.8-4 keV band (Govoni & Feretti 2004). The X-ray and radio peaks do not overlap precisely. The distance between them is about 45″. The radio halo emission peaks at RA=$08^{\rm h}31^{\rm m}7^{\rm s}$ and DEC=$65^{\rm d}50^{\rm m}21^{\rm s}$, while the X-ray peak coordinates are RA=$08^{\rm h}30^{\rm m}59^{\rm s}$ and DEC=$65^{\rm d}50^{\rm m}21^{\rm s}$.

7.3 Magnetic field modeling

The halo brightness fluctuations and the polarization level can be related to the intracluster magnetic-field power spectrum. Following the approaches proposed by Tribble (1991b) and Murgia et al. (2004), we analyzed the radio images presented in the previous Section to constrain the intracluster magnetic field in A665. We proceeded in two steps. First, we performed a two-dimensional analysis to determine the radial scaling of the magnetic field, i.e. the average magnetic field strength at the cluster center and its radial decline. Second, we focused on the radio-halo total intensity and polarization fluctuations with respect to the average radial profiles to determine their power spectrum with the aid of three-dimensional numerical simulations.

7.3.1 The radial scaling of the equipartition magnetic field strength

In the following two-dimensional analysis, we want to infer the average magnetic field strength at the cluster center and possibly its scaling with the thermal gas density (see also Murgia et al. 2009). Since the synchrotron emissivity traces the product of electron and magnetic field energy densities and disentangling the two contributions is not possible from radio observations alone, in this work we assumed the electron energy spectrum described in § 5.1.3 with $\delta = 3$, in agreement with the observed spectral index $\alpha_{0.3}^{1.4} \simeq 1$ (see § 7.1). We set the normalization N_0 supposing a perfect equipartition condition between magnetic field and relativistic particle energy density at each point in the intracluster medium. In this case the radio source is on a minimum energy condition and the radio emissivity at 1.4 GHz is given by

$$J_{1.4\,\rm GHz} \simeq 8.12\times10^{-43}(\gamma_{\rm min}/100)B_{\mu\rm G}^4 \quad ({\rm erg\,s^{-1}cm^{-3}Hz^{-1}}). \tag{7.1}$$

In Eq. 7.1 we took the isotropy of the electron population into account and we averaged over all the possible directions between the magnetic field and the line-of-sight, i.e. the field is supposed to be completely tangled on an infinitesimally small scale (for a more realistic model see § 7.3.2). We furthermore assumed that the magnetic field strength scales as a function of the thermal gas density (see § 5.1.1), while the thermal electron gas density profile $n_{\rm e}(r)$ is taken to follow a single

[2] The reader can refer to Fig. 7.4a for an alternative visualization with contours and color scale of the radio emission at 1.4 GHz.

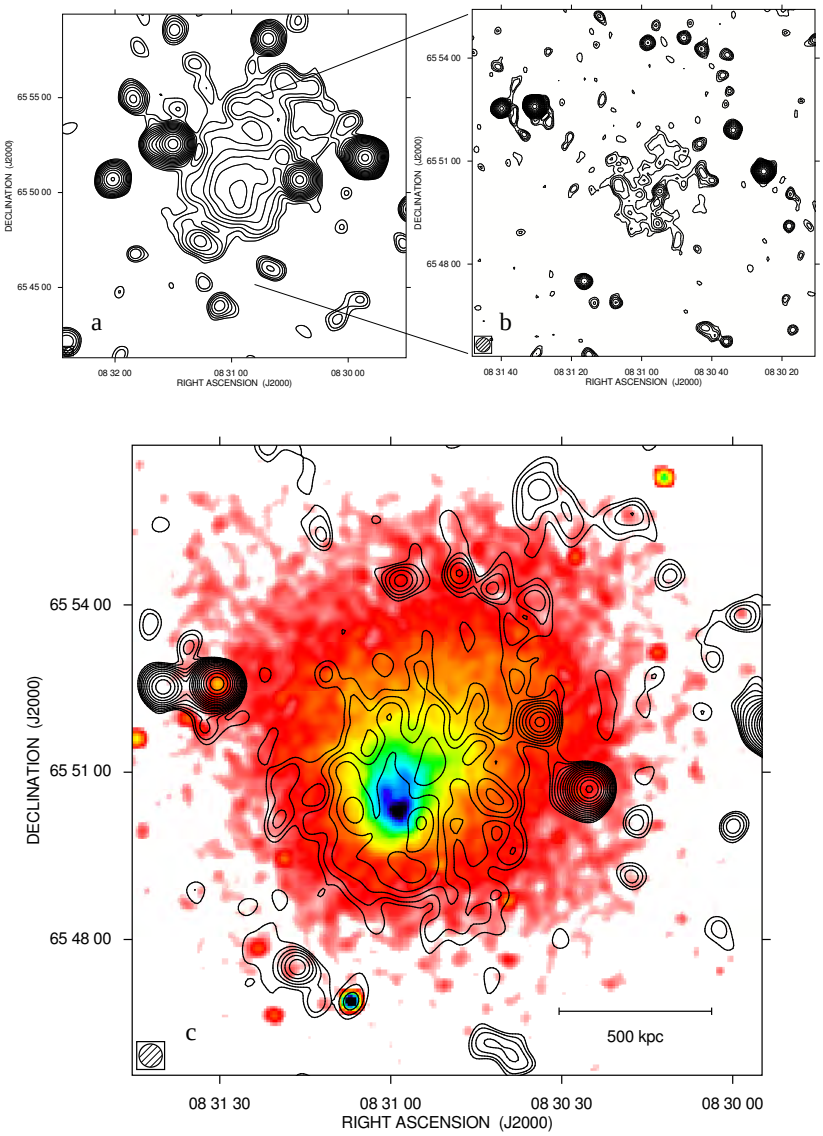

Figure 7.1 (a): Total intensity radio contours of A665 at 1.4 GHz (VLA in D configuration) with an FWHM of $55'' \times 55''$. The first contour level is drawn at 180 μJy/beam, and the rest are spaced by a factor $\sqrt{2}$. The sensitivity (1σ) is 60 μJy/beam. (b): Total intensity radio contours of A665 at 1.4 GHz (VLA in C configuration) with a FWHM of $15'' \times 15''$. The first contour level is drawn at 75 μJy/beam, and the rest are spaced by a factor $\sqrt{2}$. The sensitivity (1σ) is 25 μJy/beam. (c): Total intensity radio contours of A665 at 1.4 GHz (combining VLA data in C and D configuration) with an FWHM of $25'' \times 25''$. The first contour level is drawn at 135 μJy/beam, and the rest are spaced by a factor $\sqrt{2}$. The sensitivity (1σ) is 45 μJy/beam. The contours of the radio intensity are overlaid on the *Chandra* X-ray image. The adaptively smoothed X-ray image is in the 0.8-4 keV band (Govoni et al. 2004).

β-model (Cavaliere & Fusco-Femiano 1976, we refer also to § 5.1.2). In the case of A665, the gas density parameters have been taken as derived by Roussel et al. (2000) from ROSAT X-ray data and rescaled to our chosen cosmology ($\beta = 0.763$, $r_c = 112''$ and $n_e(0)$=3.25·10^{-3} cm^{-3}).

Under these hypotheses, the synchrotron emissivity scales as

$$J_{1.4\,\mathrm{GHz}}(r) = J_0 \left(1 + \frac{r^2}{r_c^2}\right)^{-6\beta\eta} . \tag{7.2}$$

Since radio halos are optically thin sources, the radio brightness profile results from the integral along the line-of-sight of the synchrotron emissivity in Eq. 7.2, which gives

$$I(r_\perp) = I_0 \left(1 + \frac{r_\perp^2}{r_c^2}\right)^{-6\beta\eta+0.5} \tag{7.3}$$

where $I(r_\perp)$ is the brightness value at the $r_\perp$ projected distance from the cluster center, and I_0 is the central radio halo brightness. By fitting the model in Eq.7.3 to the data, we obtain the value of I_0 and η, from which $\langle B_0 \rangle$ can be estimated. We calculated the equipartition magnetic field by neglecting the energy contribution from relativistic protons and other, non-emitting, heavy particles, i.e. we used $\kappa = 0$ (where κ is conventionally the ratio of the heavy particle to electron energy densities, see § 4.2.1). Adopting $\kappa > 0$ leads to a higher equipartition magnetic field strength: for $\delta = 3$, $B \propto (1+\kappa)^{0.25}$, see also Beck & Krause (2005). In this respect, the magnetic field values computed in this way should be considered as lower limits.

In Fig.7.2 we show the azimuthally averaged radio-halo brightness profile obtained from the C+D configuration image at 25″resolution. Data points represent the average brightness in concentric annuli of half beam width centered on the X-ray peak, as shown in the inset. Discrete sources have been masked out and excluded from the statistics. The observed brightness profile is traced down to a level of $3\sigma_I$ and the best fit of the analytical model in Eq. 7.3 is showed. The fit was performed in the image plane as described in Murgia et al. (2009). To properly take the resolution into account, the model in Eq. 7.3 was first calculated in a two-dimensional image, with the same pixel size and field of view as that observed, and then convolved with the same beam by means of a fast Fourier transform. The resulting image was masked exactly in the same regions as for the observations. Finally, the model was azimuthally averaged with the same set of annuli as were used to obtain the observed radial profile. All these functions were performed at each step during the fit procedure. As a result, the values of the central brightness, I_0, and the index η provided by the fit are deconvolved quantities, and their estimate includes all the uncertainties related to the masked regions and to the sampling of the radial profile in annuli of finite width.

The best fit of the analytical model yields a central brightness of $I_0 = 0.76^{+0.05}_{-0.05}\,\mu$Jy/arcsec^2 and $\eta = 0.47^{+0.03}_{-0.03}$, the corresponding equipartition magnetic strength at the cluster center is $\langle B_0 \rangle = 1.58^{+0.04}_{-0.04}\,\mu$G. Indeed, the value of η we found is very close to the physical situation in which the magnetic field energy density scales as the thermal gas density: $B^2 \propto n_e$.

The brightness profile is very sensitive to the value of η. To show this, we fixed the central brightness I_0 and we also traced the models corresponding to $\eta = 2/3$ (the magnetic field is frozen in the thermal gas) and $\eta = 1$ (the magnetic field radially decreases according to thermal gas density). The two cases are represented in Fig.7.2, but these two profiles are too steep for the data.

7.3.2 Numerical analysis of the magnetic field fluctuations

The analytic model presented in the previous Section provides a good description of the azimuthally averaged brightness radial profile. However, significant deviations of the diffuse emission from circular symmetry are observed. These fluctuations can be related to local fluctuations of the intracluster magnetic field strength and direction around the average. We characterized the

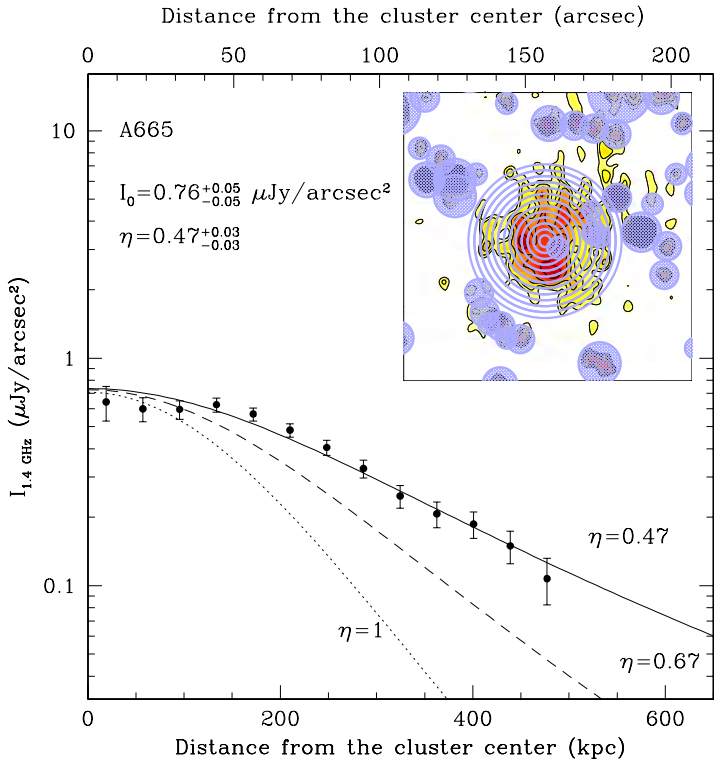

Figure 7.2 Analytical fit to the observed radio-halo brightness radial profile. Points represent the azimuthally averaged radio brightness at 1.4 GHz obtained in annuli, as shown in the inset. Discrete sources have been excluded from the statistics. The solid line represents the best fit of the magnetic field model described in the text. The dashed and dot-dashed lines are reference models, see text.

power spectrum of these fluctuations following the three-dimensional numerical approaches proposed by Tribble (1991b) and Murgia et al. (2004). We simulated a multi-scale random magnetic field in a cubical box by assuming the magnetic field model presented in Chapter 5.

This three-dimensional random magnetic field model was “illuminated" with the relativistic electron distribution in Eq. 5.12, to produce total intensity and polarization synthetic images of the radio halo. The magnetic field fluctuates in strength and direction from pixel to pixel in the grid. The integration of the total intensity straightforward: the contributions of the pixels in the computational grid are added together by considering the angle between the local magnetic field direction and the line-of-sight. Indeed, the total intensity at a given direction is proportional to the integral along the line-of-sight of the magnetic field projected on the plane of the sky, $B_\perp$.

The integration of the polarized intensity is not a simply scalar sum because of two distinct effects. One is that the magnetic field has random orientations, and the second is that the radio wave polarization plane is subject to the Faraday rotation as it traverses the magnetized intracluster medium. Therefore, the integration of the polarized intensity is performed as a vectorial sum in which the intrinsic polarization angle of the radiation coming in from the pixels located at a depth L is rotated by the amount given in the Eq. 4.18. The combination of the aforementioned effects lead to the intrinsic depolarization of the radio signal (see § 4.2.2.1). Finally, to be compared, both the synthetic and the observed images were convolved with a Gaussian beam. The convolution with the beam prevents observing the small-scale fluctuations of the radio halo and causes a further suppression of the polarized intensity (beam depolarization).

An example of synthetic A665 radio halo is shown in Fig. 7.3. A turbulent magnetic field is simulated in a grid of 1024^3 pixels with a cell size of 1 kpc/pixel. The magnetic field has a

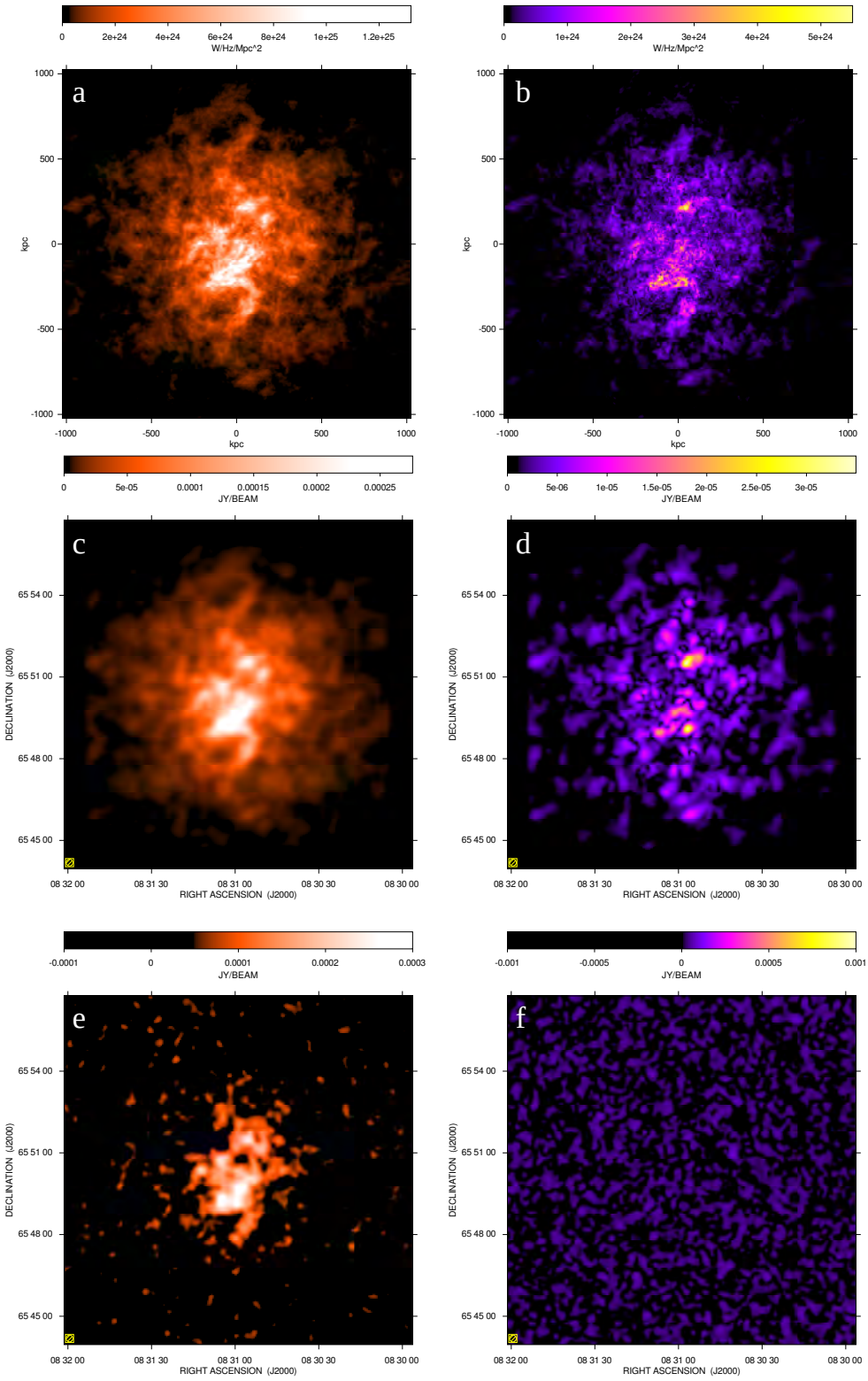

Figure 7.3 Example of simulated radio halo. *Left* and *right panels* refer to the total and polarized intensity, respectively. *Top panels*: images at full resolution. *Mid panels*: images at 15″ resolution. *Bottom panels*: as for *mid panels* but with noise added.

Kolmogorov power spectrum slope $n = 11/3$ and fluctuates in the range of spatial scales from $\Lambda_{\rm min}$=4 kpc and $\Lambda_{\rm max}$=512 kpc. The central magnetic field strength is $\langle B_0 \rangle = 1.3\,\mu$G and $\eta = 0.47$.

The simulated magnetic field is periodic at the grid boundaries, so the computational grid has been replicated to reproduce a field of view of 2048^2 kpc^2 around the galaxy cluster center. *Left* and *right panels* refer to the total and polarized intensity, respectively. *Top panels* refer to the simulations at full resolution and show all the fine structure of the radio halo. The expected theoretical fractional polarization for this power spectrum is about 24%. *Middle panels* show the images convolved at 15″ resolution. The radio halo appears smoother and the fractional polarization is reduced to about 7%. Finally, *bottom panels* show the synthetic radio images with the same noise level as in the observations. In total intensity, only the brightest central regions of the radio halo are visible, while in polarized intensity the halo emission falls below the noise level. This example illustrates how radio halos can be effectively polarized, but because of their faintness, detecting this polarized signal is a very hard task with current radio interferometers.

7.4 Simulations results

To constrain the power spectrum of the magnetic field fluctuations in A665, we compared the synthetic radio halo images obtained through the numerical procedure described in § 7.3 and the real radio images and polarization limits presented in § 7.2. Overall, the three-dimensional magnetic field and relativistic electron models depend on the eight parameters listed in Table 7.2. For a power-law magnetic field power spectrum with a radial scaling, we have five parameters: $\langle B_0 \rangle$, η, $\Lambda_{\rm min}$, $\Lambda_{\rm max}$, and n. As pointed out in Murgia et al. (2004) (see § 5.2), there is a degeneracy between $\langle B_0 \rangle$ and η, and between $\Lambda_{\rm max}$ and n. Different combinations of these parameters lead to similar radio halo total intensity and polarization distributions. We decided to concentrate our analysis on $\langle B_0 \rangle$ (by fixing $\eta = 0.47$ on the basis of the azimuthally averaged radial profile presented in § 7.3.1) and on $\Lambda_{\rm max}$ (by fixing $n = 11/3$ on the basis of the Kolmogorov theory for a turbulent medium[3]). Moreover, we fixed $\Lambda_{\rm min}$=4 kpc, the minimum allowed by our computational grid. However, we note that a higher $\Lambda_{\rm min}$ has a negligible impact on the simulation results since, for a Kolmogorov spectral index, most of the magnetic field power is on larger scales. The random magnetic field was illuminated with a population of relativistic electrons with Lorentz factors between $\gamma_{\rm min} = 100$ and $\gamma_{\rm max} = +\infty$. The electrons spectrum is a power law (see § 5.1.3) with index $\delta = 3$, according to the observed radio-halo spectral index $\alpha_{0.3}^{1.4} \simeq 1$ (see § 7.1), and its energy density is in local equipartition with the magnetic field energy density.

Because of the random nature of the intracluster magnetic field, the comparison between synthetic and observed images required several simulation runs with different seeds for each given couple of the fitting parameters $\langle B_0 \rangle$ and $\Lambda_{\rm max}$, this because the same set of the magnetic field power spectrum parameters results in a different realization of the same synthetic halo. Indeed, we chose to simulate 10 equally spaced values of the minimum wave number from $k_{\rm min} = 0.0061\,{\rm kpc}^{-1}$ to $k_{\rm min} = 0.061\,{\rm kpc}^{-1}$. Correspondingly, the outer scale of the magnetic field fluctuations ranges from $\Lambda_{\rm max} = 1024$ kpc (the maximum allowed by our computational grid) down to $\Lambda_{\rm max} = 102.4$ kpc (i.e. very close to the linear resolution of the radio images). For each value of $\Lambda_{\rm max}$, we realized 10 more simulation runs, with different seeds, in which we determined the value of $\langle B_0 \rangle$ by fitting the synthetic radio halo brightness profile to the observed one. Indeed, we realized a total of 100 simulations by running the FARADAY code (Murgia et al. 2004) in the CyberSAR-OAC computer cluster.

In Fig. 7.4 we show the observed radio halo in total emission at 25″ resolution (panel a) along

[3] In the past years, progress has been made by analyzing the state of turbulence of the intracluster medium. Signature of turbulence have been found by analyzing the gas pressure of the Coma cluster, where the pressure fluctuations are consistent with a Kolmogorov power spectrum (Schuecker et al. 2004).

Table 7.2 Parameters adopted in the radio halo simulation.

Parameter	Value	Description
$\langle B_0 \rangle$	*free*	magnetic field strength at the cluster center
η	0.47	magnetic field radial decrease, $\langle B(r) \rangle = \langle B_0 \rangle \left(\frac{n_e(r)}{n_e(0)} \right)^{\eta}$
n	11/3	magnetic field power spectrum index, $\lvert B_k \rvert^2 \propto k^{-n}$
Λ_{min}	4 kpc	minimum scale of fluctuation, $\Lambda_{min} = 2\pi/k_{max}$
Λ_{max}	*free*	maximum scale of fluctuation, $\Lambda_{max} = 2\pi/k_{min}$
γ_{min}	100	minimum relativistic electron Lorentz factor
γ_{max}	$+\infty$	maximum relativistic electron Lorentz factor
δ	3	power-law index of the energy spectrum of the relativistic electrons

with the synthetic radio-halo images corresponding to three different values Λ_{max} (panels b, c, and d). The synthetic images have the same resolution and noise level as the observed one and were obtained with the procedure described in § 7.3.2. At first glance, the synthetic images look quite similar to the observed one in terms of total extension and average brightness. In fact, the *top panel* of Fig. 7.4e shows that all three simulations fit the total intensity radial profile of the observed A665 radio-halo image remarkably well at 1.4 GHz at 25″ resolution. The different lines in the *bottom panel* of Fig. 7.4e represent the simulated fractional polarization at different radii from the cluster center as expected at 15″resolution before the noise is applied. The model fractional polarization is consistent with the upper limits derived on the base of the VLA C configuration observation presented in this work. The best-fit central magnetic field strength for the three simulations is around $\langle B_0 \rangle$ =1.3 μG, in good agreement with the value found on the basis of the two-dimensional analytical fit in § 7.3.1.

Although the examples of the synthetic halos shown in Fig. 7.4 visually appear similar to the observed halo, it is clear that, as Λ_{max} increases, the simulated radio halos change shape. In particular, when the outer scale of the magnetic field fluctuations is close to the observing beam, the halo is smooth and rounded (Fig. 7.4d). Increasing Λ_{max} results in a much distorted radio halo morphology and in a significant offset of the radio halo peak from the cluster center (particularly evident in Fig. 7.4b). The simulated clusters are centered on the observed X-ray peak.

We indeed tried to evaluate quantitatively the value of Λ_{max} which best reproduce the observed intensity fluctuations of the radio halo, as originally proposed time ago by Tribble (1991b). To do this, we analyzed the residual images obtained by fitting and then subtracting the analytical model in Eq. 7.3 to both the simulated and the observed halo images. Since the analytical model has a perfect circular symmetry, it is particular well-suited to highlighting the halo fluctuations around the average profile.

In the *top panels* of Fig.7.5 we show residuals corresponding to the images shown in Fig. 7.4 with the total intensity iso-contours overlapped. The higher Λ_{max}, the higher the residual levels and the larger the fluctuation patches.

In Fig. 7.5e the root-mean-square of the residual images, evaluated inside the inner $\sim$ 200 kpc from the cluster center, is plotted against Λ_{max}. The solid line and the shaded region represent the mean and the standard deviation of the mean derived from the simulations, respectively. First of all, the residuals approach the noise level as Λ_{max} approaches the observing beam. This result implies that, if Λ_{max} is smaller than $\lesssim$ 100 kpc, the expected rms of the halo intensity fluctuations is already below the noise level of the observations $\sigma_I = 0.06\,\mu$Jy/arcsec^2. As the maximum scale of the intracluster magnetic field power spectrum increases, the rms level of the radio halo fluctuations increases, reaching a value as high as 0.15 μJy/arcsec^2 for Λ_{max} = 1024 kpc.

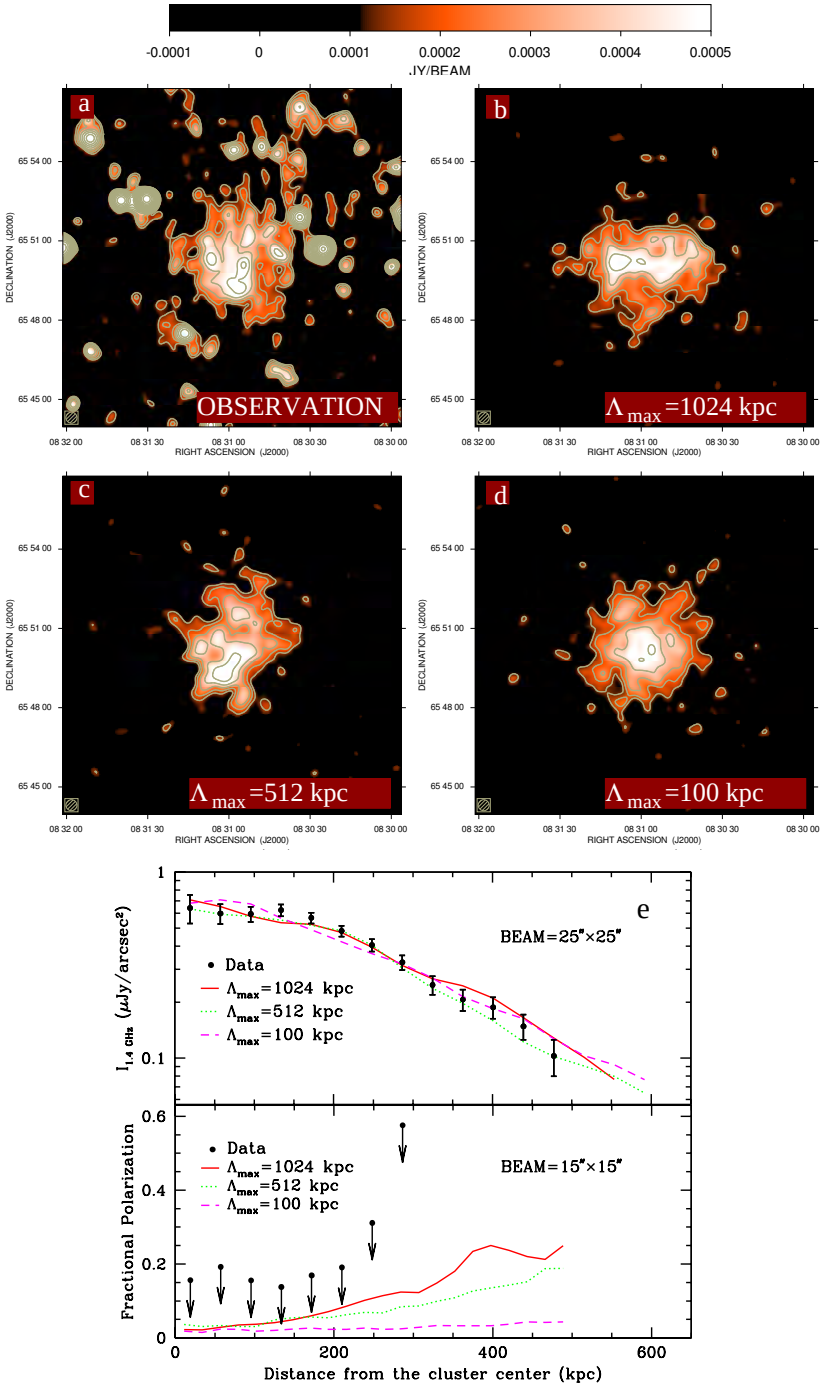

Figure 7.4 Observed (a) and simulated (b, c, d) surface brightness images, with FWHM of 25″× 25″. Both the observation and simulation first contour levels are drawn at 3σ and the rest are spaced by a factor $\sqrt{2}$. The simulations correspond to three different $\Lambda_{\rm max}$: 1024, 512, and 100 kpc. In the *bottom panels (e)*, the radial profiles of the radio brightness and the fractional polarization are shown. The polarization upper limits are at 1σ level.

By comparing the observed fluctuation rms level of 0.11 μJy/arcsec^2 with the simulated trend we estimate that the outer scale of the magnetic field fluctuations is $\Lambda_{\rm max} \simeq 400 \div 500$ kpc (i.e. $k_{\rm min} = 0.014 \div 0.012\,{\rm kpc}^{-1}$). In Fig. 7.5f the offset between the X-ray and radio peak is plotted against $\Lambda_{\rm max}$. This indicator has a larger dispersion but is much more direct since it does not involve

a specific handling of the observed and simulated images. As observed in Fig. 7.4, the offset of the radio peak from the cluster center (here assumed to be coincident with the X-ray peak) increases with Λ_{max}. By comparing the observed offset of 135 kpc with the simulated trend, it turns out that Λ_{max} should be about $500 \div 600$ kpc, in agreement with the residual analysis.

To summarize, the results of the three-dimensional simulations indicate that the radio halo emission in A665 is consistent with a central magnetic field strength of about $1.3\,\mu$G. To explain the azimuthally averaged radio brightness profile, the magnetic field energy density should decrease following the thermal gas density, leading to an averaged magnetic field strength over the central 1 Mpc^3 of about $0.75\,\mu$G. From the observed brightness fluctuations of the radio halo, we infer that the outer scale of the magnetic field power spectrum is ~450 kpc, the corresponding magnetic field auto-correlation length (see Eq. 5.23) is $\Lambda_B \simeq 100$ kpc.

7.5 The depolarization of discrete radio sources

In this Section we investigate the effects of the intracluster magnetic field in A665 on the polarization properties of the discrete radio sources belonging to the cluster of galaxies itself or situated in background (see Table 7.3). In particular, it is expected that radio sources whose emission crosses the central region of the cluster suffer a higher Faraday rotation, hence a higher beam depolarization, with respect to the sources at larger impact parameters (see e.g. Murgia et al. 2004). In the *left panel* of Fig. 7.6, we show a field of view of about $1.5^o \times 1.5^o$ around A665 taken from a $15''$ resolution image. All the discrete sources brighter than $500\,\mu$Jy/beam ($20\sigma_I$) are labeled. This severe cut guarantees a maximum error on the fractional polarization of 0.03.

For each of these sources we plotted the fractional polarization against the distance from the cluster center (*right panel* of Fig.7.6). At large impact parameters, $r_\perp > 2000$ kpc, the observed radio sources fractional polarization at 1.4 GHz and $15''$ resolution oscillates around 0.1. The plot also shows a hint that the discrete sources seen in projection close to the cluster center are more depolarized.

The continuous line is the expected depolarization trend calculated on the basis of the best magnetic field model derived from the fit of the radio halo image (see §7.4). The dashed lines represent the dispersion of the model. The depolarization model assumes that all the considered sources are situated at the cluster mid-plane and that the intrinsic polarization is fully ordered. As intrinsic value we assumed the mean of the fractional polarization of the radio galaxies located at more than 2 Mpc from the cluster center.

Although the relatively large scatter of the data and the simplicity of the model prevent us from deriving other useful constraints to the magnetic field properties in A665, we note that the model prediction broadly agrees with the observed depolarization trend. Studies at possibly higher resolution and sensitivity are required to measure the fractional polarization for many more sources so that this method can be applied successfully.

7.6 Conclusions

In this work we presented a new deep VLA observation at 1.4 GHz of the cluster of galaxies A665. By combining this observation with a previous VLA observation at lower resolution, we studied the intracluster magnetic-field power spectrum by analyzing the radio halo brightness fluctuations, following both an original idea by (Tribble 1991b) and the numerical approach proposed by Murgia et al. (2004).

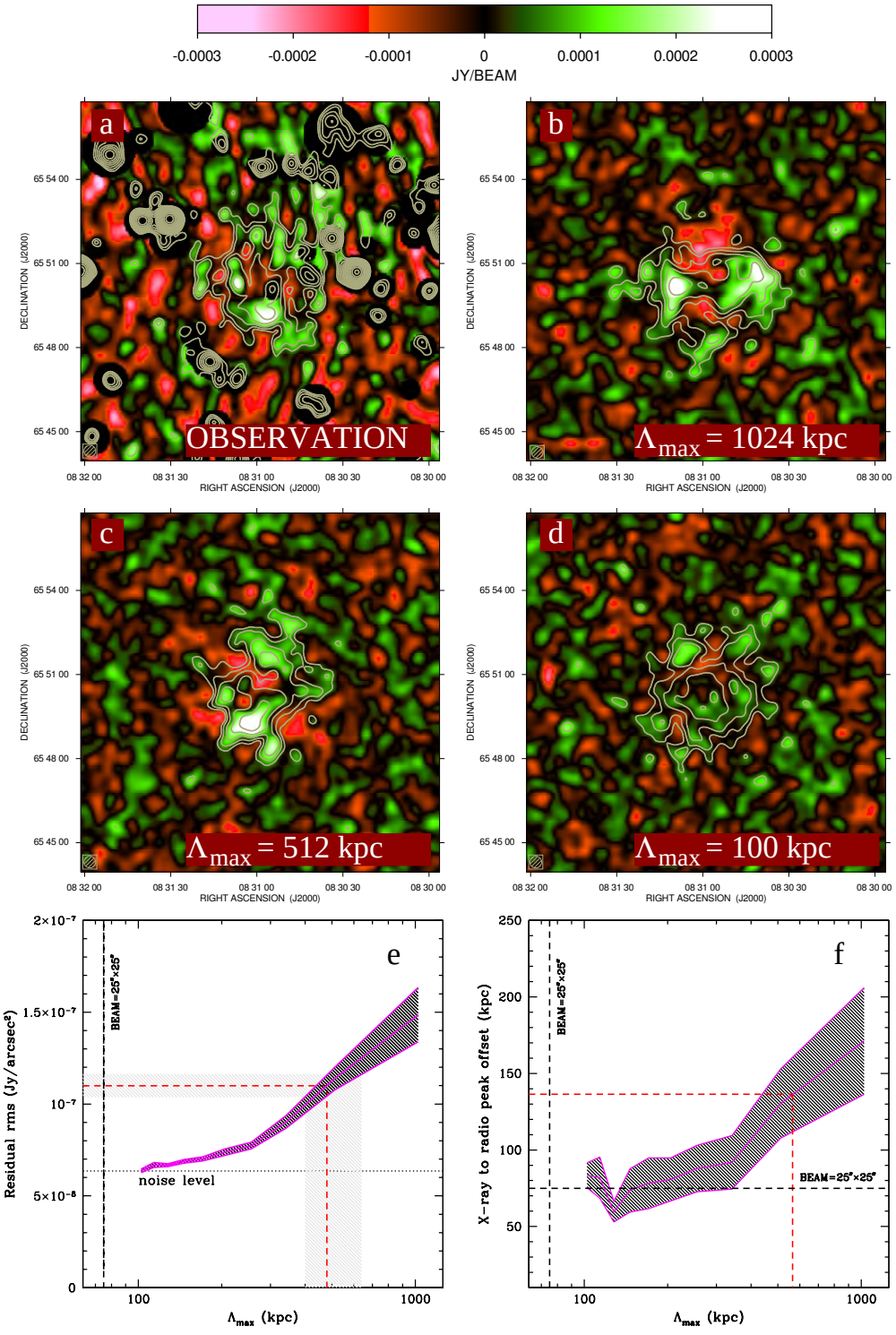

Figure 7.5 Observed (a) and simulated (b, c, d) residuals images, with FWHM of 25″×25″. Both the observation and simulation first contour levels are drawn at 3σ and the rest are spaced by a factor $\sqrt{2}$. Panel e) and f) show the residuals rms versus Λ_{max} and the X-ray to radio peak offset versus Λ_{max}, respectively.

Our findings are summarized as follows. We simulated Gaussian random three-dimensional turbulent magnetic-field models in order to reproduce the observed radio halo emission. By com-

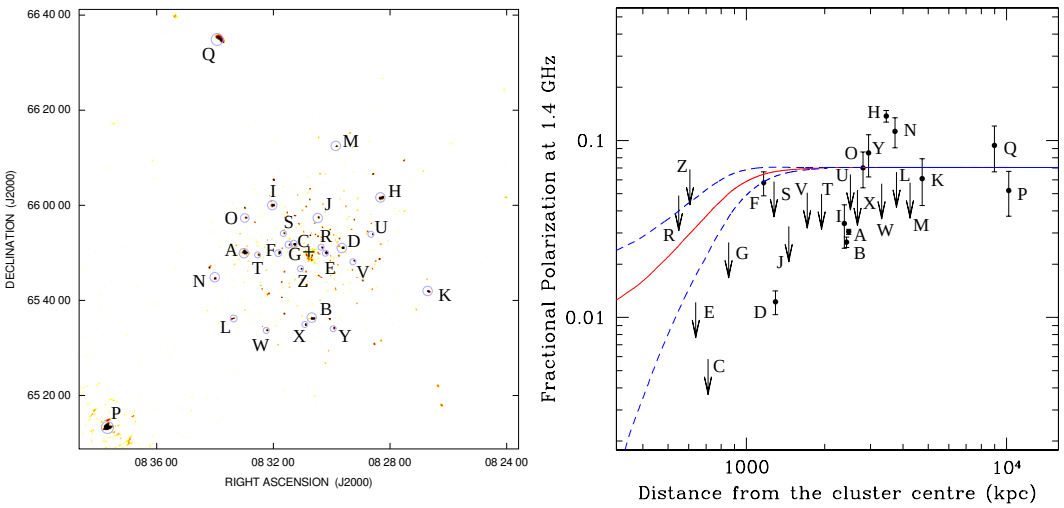

Figure 7.6 Depolarization of the brightest discrete radio sources as a function of the distance from the cluster center (marked by the cross). The upper limits are at the 3σ level. The solid and dashed lines respectively represent the mean and the dispersion of the depolarization trend expected on the basis of the magnetic field model that best reproduces the radio halo in A665, see text for details.

paring observed and synthetic radio halo images, we constrained the strength and structure of the intracluster magnetic field. We assumed that the magnetic field power spectrum is a power law with a Kolmogorov index, and we imposed a local equipartition of energy density between relativistic particles and the magnetic field. Under these assumptions, we found that the radio halo emission in A665 is consistent with a central magnetic field strength of about $1.3\,\mu$G. To explain the azimuthally averaged radio brightness profile, the magnetic field energy density should decrease following the thermal gas density, leading to an averaged magnetic field strength over the central $1\,\mathrm{Mpc}^3$ of about $0.75\,\mu$G. From the observed brightness fluctuations of the radio halo, we inferred that the outer scale of the magnetic field power spectrum is ~ 450 kpc, the corresponding magnetic field auto-correlation length is 100 kpc. We also found a hint that the discrete sources seen in projection close to the cluster center are more depolarized. The best-fit magnetic model broadly agrees with the observed depolarization trend.

More tightening constraints could be potentially obtained by detecting the radio halo polarization fluctuations, not just total intensity fluctuations. In fact, the ratio of two former quantities, i.e. the fractional polarization, is a very robust indicator of the intracluster magnetic-field power spectrum, because it only marginally depends on the shape of the energy spectrum of the synchrotron electrons and on the equipartition assumption. Therefore, it would be very important to improve the sensitivity of future observations in order to detect polarized signal in as many radio halos as possible. This is a science case for the new generation of instruments in radio astronomy.

Table 7.3 A665 radio galaxies used to study signal depolarization through intracluster medium.

Source	RA (J2000)	DEC (J2000)	$r_\perp$ (kpc)	$FPOL$ (%)	$S_{1.4\,\mathrm{GHz}}$ (mJy)
A	08:33:12	65:50:41	2474	3.0 ± 0.1	222± 7
B	08:30:53	65:36:60	2429	2.7 ± 0.2	122± 4
C	08:31:31	65:52:36	712	< 0.6	35± 1
D	08:29:51	65:51:53	1293	1.2 ± 0.2	41± 1
E	08:30:25	65:50:42	639	< 1.0	12.8± 0.4
F	08:32:02	65:50:38	1166	5.8 ± 0.9	6.4± 0.2
G	08:31:40	65:52:33	855	< 3	3.8± 0.1
H	08:28:34	66:02:17	3449	13.8 ± 1.0	27.2± 0.8
I	08:32:17	66:00:50	2382	3.4 ± 0.9	12.0± 0.4
J	08:30:42	65:58:09	1456	< 3	2.8± 0.09
K	08:26:57	65:42:31	4745	6.1 ± 1.8	19.9± 0.6
L	08:33:34	65:37:01	3779	4.0±2.2	5.9± 0.2
M	08:30:04	66:13:06	4259	3.2 ± 1.9	5.7± 0.2
N	08:34:13	65:45:25	3728	11.3 ± 2.2	3.7± 0.1
O	08:33:11	65:58:02	2810	7.0 ± 1.6	2.8± 0.09
P	08:37:44	65:13:31	10203	5.2±1.5	1275±2
Q	08:34:14	66:35:52	8991	9.4±2.7	341±2
R	08:30:34	65:51:54	550	< 5	1.05±0.04
S	08:31:52	65:54:53	1277	< 6	0.77±0.03
T	08:32:44	65:50:15	1946	< 5	1.77±0.06
U	08:28:51	65:54:36	2512	< 6	0.81±0.03
V	08:29:28	65:49:08	1713	< 5	1.19±0.04
W	08:32:26	65:34:28	3313	< 6	3.2±0.1
X	08:31:08	65:35:39	2676	< 5	2.31±0.07
Y	08:30:09	65:34:57	2952	8.5±2.2	1.22±0.04
Z	08:31:16	65:47:30	607	< 7	0.42±0.02

Col. 1: Radio galaxy labels; Col. 2 to Col. 3: Source's position;

Col. 4: Distance from cluster center; Col. 5: Polarization Percentage; Col. 6: Flux density.

8 Conclusions

The aim of this thesis was to improve the knowledge of the intracluster magnetic field power spectrum in galaxy clusters through interferometric radio observations. In this context, both statistical studies and careful analysis of individual galaxy clusters have been performed.

To contribute to the statistical studies, the presence of new diffuse synchrotron wide sources in complex X-ray systems has been investigated and polarimetric studies of the properties of radio galaxies located inside or behind galaxy clusters have been carried out.

Concerning the study of specific galaxy clusters, a careful analysis has been done for two of them. Indeed, following the approach of Tribble (1991b) and Murgia et al. (2004), the intracluster magnetic field fluctuation power spectrum has been investigated in the galaxy cluster A665, undergoing a strong merger event, and in the relaxed cool core galaxy cluster A2199, by means of a comparison between the observed images and the predictions of 3D numerical simulations.

In the following we present our main results and conclusion and the future perspectives.

8.1 Intracluster magnetic field in merging and relaxed clusters

Galaxy clusters undergoing strong merger events are supposed to be characterized by magnetic fields central values of few μG. Instead, in relaxed systems, typically higher central strengths ($\gtrsim$10 μG) are expected.

In this work, we investigated the intracluster magnetic field power spectrum in the merging galaxy cluster A665, known to host a powerful and extended radio halo, and in the relaxed cool core galaxy cluster A2199, hosting at its center the radio galaxy 3C338.

The intracluster magnetic field power spectrum in A665 has been constrained by comparing observed and synthetic images of the radio halo total brightness and polarization. We could infer a magnetic field auto-correlation length of 100 kpc. Moreover, we found that the radio halo emission in A665 is consistent with a central magnetic field strength of about 1.3 μG.

The intracluster magnetic field in the galaxy cluster A2199 has been investigated by studying the rotation measure and polarization images of the central radio galaxy 3C338. The analysis revealed an intracluster magnetic field power-law power-spectrum characterized by an index n=2.8 and fluctuating between a minimum and a maximum scale of fluctuation of $\Lambda_{\rm min}$=0.7 kpc and

Λ_{max}=35 kpc, respectively. The corresponding magnetic field auto-correlation length is Λ_B=5.2 kpc. In addition, we found a magnetic field strength of $\langle B_0 \rangle$=11.7 μG at the cluster center.

The magnetic field power spectrum parameters found in A665 and A2199 are in agreement with the results present in literature. Clusters undergoing merger events seem to have larger spatial scales of fluctuation and moderate magnetic field strength at the cluster center, while relaxed galaxy clusters appear characterized by fluctuations on smaller scales and higher central magnetic field values.

8.2 New radio halos in merging galaxy clusters

Fundamental information about the intracluster magnetic field can be obtained by means of statistical studies of radio halo properties. However radio halos are very faint and elusive, to date just few dozens of these sources are known. To improve the scanty statistics, a program aimed at investigating the presence of diffuse synchrotron sources in complex X-ray cluster systems is in progress. In this context, we found six new radio halos located in merging systems. We found an intriguing diffuse radio emission in A781, an exceptional complex of several clusters. A powerful and extended radio halo has been observed in A523, the first firm detection of a radio halo in an X-ray underluminous cluster. Diffuse radio halo emission has been detected in the complex galaxy cluster A1689, whose dynamical state is still debated. The presence of a radio halo in this cluster strongly supports the scenario of a merger event along the line of sight. Three further radio halos have been discovered, respectively in the galaxy clusters A800, A1550, and CL1446+26. Although, in most of the radio halos known in the literature the radio morphology is very similar to the thermal X-ray emission, in these clusters the two seem uncorrelated.

The discovery of these new radio halos implies a growth in the number of known radio halos of about 15%, for a total of 45 sources.

8.3 Intracluster magnetic field and cluster X-ray properties

Cosmological magneto-hydrodynamical simulations indicate that central magnetic field strengths depend on the cluster X-ray temperature and thermal gas density (Dolag et al. 1999, 2002, 2005). To investigate a possible connection between the magnetic field strength and the gas temperature of the intracluster medium, we analyzed new rotation measure images of radio galaxies in hot galaxy clusters. According to our analysis, the current data do not allow to establish a strict link between the magnetic field strength and the gas temperature of the intracluster medium. Moreover, we investigated the connection between the intracluster magnetic field strength and the cluster gas density in the relaxed cool core galaxy cluster A2199 and in the merging galaxy cluster A665. In this two galaxy clusters we found that the magnetic field and the magnetic field energy density respectively decreases with the radius almost following the gas density. A similar behavior has been observed in clusters as Coma, A2382, A119.

Hints of a link between thermal and non-thermal components in galaxy clusters are given also by the similarities between the X-ray and radio properties of galaxy clusters hosting radio halos. Indeed, all radio halos have been observed in merging clusters, and a global correlation between the radio power at 1.4 GHz and the X-ray cluster luminosity and temperature has been observed. These features indicate that the most powerful radio halos are expected to be found in the most X-ray luminous and hot clusters. On the other hand, a few halos more luminous than predicted by the radio - X-ray correlation have been recently found. The most robust example is represented by

A523, one of the radio halos presented in this thesis. Radio halos associated with clusters of low X-ray luminosity do not appear to be described well by current models (e.g. Giovannini et al. 2011). They could be either young halos or clusters at a special time of the merger event, when particle acceleration processes have a higher efficiency. Another possibility is that the X-ray luminosity might not be in these cases a good indicator of the mass distribution and therefore of the previous cluster merging activity.

8.4 Future perspectives

The knowledge of the intracluster magnetic field power spectrum is relevant to address key problems in galaxy clusters, like cosmic ray energy and diffusion, turbulence level and energy transfer in the intracluster medium. Moreover, understanding the formation and evolution of cosmological magnetic fields is, per se, a fundamental issue.

The most detailed studies of intracluster magnetic field power spectra present in literature come from radio observations. By means of the analysis of the total and polarized emission of diffuse sources and the rotation measure images of radio galaxies, magnetic fields with turbulent structures from Mpc to kpc scales have been revealed. The combination of the rotation measure and the radio halo approaches would allow to follow with continuity the power spectrum of the magnetic field fluctuations from Mpc scales (best studied through the halo intensity fluctuations and polarization information) down to kpc scale (derived from radio galaxies RM images), as done up to now just in the galaxy cluster A2255 (Govoni et al. 2006).

The new generation of radio interferometers (e.g., EVLA, SKA, LOFAR, LWA) will give high resolution and sensitivity polarimetric observations of radio halos, with a gain in sensitivity up to a factor 10^3. The enhanced sensitivity will allow to detect the polarized emission from radio halos. More tightening constraints about intracluster magnetic fields could be potentially obtained from the radio halo polarization fluctuations. In fact, the ratio of polarized and total intensity, i.e. the fractional polarization, is a very robust indicator of the intracluster magnetic field power spectrum, because it only marginally depends on the shape of the energy spectrum of the synchrotron electrons and on the equipartition assumption. In addition, these new instruments will allow to produce rotation measure images of several radio galaxies in and behind a galaxy cluster. In this way the intracluster magnetic field power spectrum will be studied both in the central and peripheral regions of galaxy cluster.

Moreover, the capabilities of the incoming radio interferometers will allow to extend the knowledge of magnetic fields to scales larger than those of galaxy clusters. Indeed, present cosmological magneto-hydro-dynamical simulations indicate that magnetic fields are present also in the large scale structure of the Universe, i.e. along the optical filaments connecting galaxy clusters (e.g. Dolag et al. 2008). This prediction has been confirmed by the observation of synchrotron diffuse radio emission in low density intergalactic environments between clusters of galaxies. Harris et al. (1993) and Giovannini & Feretti (2000) detected an elongate diffuse emission ~4 Mpc away from the galaxy cluster A786. Moreover, Bagchi et al. (2002) reported evidence of diffuse radio emission from the multi-Mpc scale filamentary network of galaxies in ZwCl 2341.1+0000, detection recently confirmed by the deeper observations performed by Giovannini et al. (2010). The study of the magnetic field in the large-scale filaments would allow a better understanding of the origin and properties of cosmological magnetic fields.

A

The Stokes parameters

Generally, to described the polarized emission coming from a radio source, the Stokes parameters are used:

- I, the total intensity of the signal;
- Q and U, related to the elliptical polarization;
- V, the circular polarization.

Actually, just three of them are independent parameters, because it results:

$$I \geqslant Q^2 + U^2 + V^2. \tag{A.1}$$

The polarized emission of the source is given by

$$P = \sqrt{Q^2 + U^2 + V^2} \tag{A.2}$$

therefore, the degree of polarization of the source is:

$$\Pi = \frac{P}{I} = \frac{\sqrt{Q^2 + U^2 + V^2}}{I} \tag{A.3}$$

while the polarization angle is defined as:

$$\Psi = \frac{1}{2}\text{arctg}\left(\frac{U}{Q}\right). \tag{A.4}$$

For the sources considered in this thesis the circular polarization is null, that is V=0.

B

Mathematical derivations

In this Appendix we collect some mathematical derivations omitted in the text.

In particular, we present the derivation of:

- the rotation measure dispersion for the single-scale magnetic field model;
- the auto-correlation length, the structure function, and the auto-correlation function of the magnetic field and rotation measure power spectra, and their relations;
- the proportionality of the magnetic field and rotation measure power spectra.

B.1 Single scale magnetic field model

The rotation measure distribution depends on the magnetic field and thermal gas density characteristics. As noted in § 4.2.2, for a magnetic field tangled on a single scale $\Lambda_{\rm C}$, the resulting RM distribution is a Gaussian characterized by a mean value $\langle RM \rangle$ and dispersion $\sigma_{\rm RM}$ given by:

$$\langle RM \rangle = 0 \quad \sigma^2_{\rm RM} = \langle RM^2 \rangle = 812^2 \Lambda_{\rm C} \int (n_{\rm e} B_{\parallel})^2 dl. \tag{B.1}$$

If the thermal gas density is supposed to decrease with the distance from the cluster center according to a β-model (Cavaliere & Fusco-Femiano 1976, see Eq. 5.10), and the magnetic field strength radial profile to be a function of the thermal gas density (see Eq. 5.9), the integral in Eq. B.1 becomes:

$$\begin{aligned}
\sigma^2_{\rm RM} = \frac{812^2}{3} \Lambda_C \int_0^\infty B^2 n_{\rm e}^2 dl = \frac{812^2}{3} B_0^2 \Lambda_{\rm C} n_0^2 \int_0^\infty \left(1 + \frac{r^2}{r_{\rm c}^2}\right)^{-3\beta(1+\eta)} dl \\
= \frac{812^2}{3} B_0^2 \Lambda_C n_0^2 \int_0^\infty \frac{1}{\left(1 + \frac{r^2}{r_{\rm c}^2}\right)^{3\beta(1+\eta)}} dl \\
= 2 \frac{812^2}{3} B_0^2 \Lambda_C n_0^2 \int_0^\infty \frac{1}{\left(1 + \frac{r_\perp^2}{r_{\rm c}^2} + \frac{l^2}{r_{\rm c}^2}\right)^{3\beta(1+\eta)}} dl
\end{aligned}$$

where $r^2 = r_\perp^2 + l^2$, see § B.2.1. By using the Beta function:

$$\int_0^\infty \frac{l^a dl}{(m+l^b)^c} = \frac{m^{\frac{a+1-bc}{b}}}{b}\left[\frac{\Gamma(\frac{a+1}{b})\Gamma(c-\frac{a+1}{b})}{\Gamma(c)}\right]; \qquad (a>-1, b>0, m>0, c>\frac{a+1}{b})$$

we obtain:

$$\sigma^2_{\rm RM} = 2\frac{812^2}{3}B_0^2\Lambda_{\rm C}n_0^2\int_0^\infty \frac{dl}{\left(1+\frac{r_\perp^2}{r_{\rm c}^2}+\frac{l^2}{r_{\rm c}^2}\right)^{3\beta(1+\eta)}} =$$

$$= 2\frac{812^2}{3}B_0^2\Lambda_{\rm C}n_0^2 r_{\rm c}\frac{1}{2}\left(1+\frac{r_\perp^2}{r_{\rm c}^2}\right)^{\frac{1-6\beta(1+\eta)}{2}}\Gamma(\frac{1}{2})\frac{\Gamma[3\beta(1+\eta)-\frac{1}{2}]}{\Gamma[3\beta(1+\eta)]} =$$

$$= \frac{812^2}{3}B_0^2\Lambda_{\rm C}n_0^2 r_{\rm c}\left(1+\frac{r_\perp^2}{r_{\rm c}^2}\right)^{\frac{1-6\beta(1+\eta)}{2}}\Gamma(\frac{1}{2})\frac{\Gamma[3\beta(1+\eta)-\frac{1}{2}]}{\Gamma[3\beta(1+\eta)]} =$$

$$= \frac{812^2}{3}B_0^2\Lambda_{\rm C}n_0^2 r_{\rm c}\sqrt{\pi}\left(1+\frac{r_\perp^2}{r_{\rm c}^2}\right)^{\frac{1-6\beta(1+\eta)}{2}}\frac{\Gamma[3\beta(1+\eta)-\frac{1}{2}]}{\Gamma[3\beta(1+\eta)]}.$$

So, the dispersion is:

$$\sigma_{\rm RM}(r_\perp) = KB_0\Lambda_{\rm C}^{\frac{1}{2}}n_0 r_{\rm c}^{\frac{1}{2}}\frac{1}{(1+r_\perp^2/r_{\rm c}^2)^{\frac{6\beta(1+\eta)-1}{4}}}\sqrt{\frac{\Gamma[3\beta(1+\eta)-\frac{1}{2}]}{\Gamma[3\beta(1+\eta)]}}, \tag{B.2}$$

where K has been defined in § 4.2.2. If the magnetic field strength is independent from the thermal gas density ($\eta = 0$), we find the dispersion indicated in Eq. 4.22:

$$\sigma_{\rm RM}(r_\perp) = \frac{KB\Lambda_{\rm C}^{\frac{1}{2}}n_0 r_{\rm c}^{\frac{1}{2}}}{\left(1+\frac{r_\perp^2}{r_{\rm c}^2}\right)^{\frac{6\beta-1}{4}}}\sqrt{\frac{\Gamma(3\beta-\frac{1}{2})}{\Gamma(3\beta)}}. \tag{B.3}$$

A more realistic model requires a magnetic field tangled on a range of scale, as described in Chapter 5. In this case the appropriate scale to use for $\Lambda_{\rm C}$ is the magnetic field auto-correlation length $\Lambda_{\rm B}$, defined in the following.

B.2 Characterization of the magnetic field power spectrum

In this Section we will present the mathematical derivation of the magnetic field and rotation measure structure function, auto-correlation function, auto-correlation length. Moreover, we will show that the magnetic field and the rotation measure power spectra are proportional.

In the following we assume:

- a constant thermal electron density profile;
- an overall size L (from $-L/2$ to $L/2$ with respect to the cluster center) of the system along the line of sight larger than the magnetic field maximum scale of fluctuation $\Lambda_{\rm max}$ ($L >> \Lambda_{\rm max}$). This implies $\langle RM\rangle$=0;
- a null magnetic field on scales larger than the integration domain, that is $\langle B\rangle$=0.

Similar derivations can be found in Enßlin & Vogt (2003).

B.2.1 Auto-correlation functions

As we noted in § 5.3, the rotation measure and magnetic field along the line of sight can be characterized by their auto-correlation functions:

$$C_{\rm RM}(\mathbf{r}_\perp) = \langle RM(\mathbf{r_{0_\perp}}) RM(\mathbf{r_{0_\perp}} + \mathbf{r}_\perp)\rangle_{\mathbf{r}_\perp} \tag{B.4}$$

and

$$C_{\rm B_z}(\mathbf{r}) = \langle B_{\rm z}(\mathbf{r_0}) B_{\rm z}(\mathbf{r_0} + \mathbf{r})\rangle_{\mathbf{r}}. \tag{B.5}$$

Equivalent expressions are

$$C_{\rm RM}(\mathbf{r}_\perp) = \frac{1}{A}\int_{\rm A} RM(\mathbf{r_{0_\perp}}) RM(\mathbf{r_{0_\perp}} + \mathbf{r}_\perp) d\mathbf{r_{0_\perp}} \tag{B.6}$$

and

$$C_{\rm B_z}(\mathbf{r}) = \frac{1}{V}\int_{\rm A}\int_{\rm L} B_{\rm z}(\mathbf{r_{0_\perp}}, \mathbf{l_0}) B_{\rm z}(\mathbf{r_{0_\perp}} + \mathbf{r}_\perp, \mathbf{l_0} + \mathbf{l}) d\mathbf{r_{0_\perp}} d\mathbf{l_0} \tag{B.7}$$

where $\mathbf{r_0}$=$\mathbf{r_{0_\perp}} + \mathbf{l_0}$, $\mathbf{r}$=$\mathbf{r}_\perp + \mathbf{l}$, and $A \times L = V$ is the integration domain.

Since under our assumptions:

$$RM(\mathbf{r_{0_\perp}}) = 812 n_{\rm e} \int_{\rm L} B_{\rm z}(\mathbf{r_{0_\perp}}, \mathbf{l_0}) d\mathbf{l_0}, \tag{B.8}$$

the magnetic field auto-correlation function can be expressed as

$$C_{\rm B_z}(\mathbf{r}) = \frac{1}{812 n_{\rm e} V}\int_{\rm A} RM(\mathbf{r_{0_\perp}}) B_{\rm z}(\mathbf{r_{0_\perp}} + \mathbf{r}_\perp, \mathbf{l_0} + \mathbf{l}) d\mathbf{r_{0_\perp}}. \tag{B.9}$$

By integrating both sides along the line of sight one obtains:

$$812^2 n_{\rm e}^2 \int_{\rm L} C_{\rm B_z}(\mathbf{r}) d\mathbf{l}' = \frac{1}{V}\int_A RM(\mathbf{r_{0_\perp}}) RM(\mathbf{r_{0_\perp}} + \mathbf{r}_\perp) d\mathbf{r_{0_\perp}}$$

$$812^2 n_{\rm e}^2 L \int_{\rm L} C_{\rm B_z}(\mathbf{r}) d\mathbf{l}' = C_{\rm RM}(\mathbf{r}_\perp)$$

where $l' = l_0 + l$. Since $C_{\rm B_z}(\mathbf{r})$ is a cylindrically symmetric function, this integral can be written as

$$C_{\rm RM}(r_\perp) = 812^2 n_{\rm e}^2 L \times \left(2\int_0^{\rm L/2} C_{\rm B_z}(r) dl'\right). \tag{B.10}$$

By considering that $r^2 - r_\perp^2 = (l' - l_0)^2$, if a reference system is selected such that l_0=0, an equivalent expression is

$$C_{\rm RM}(r_\perp) = 812^2 n_{\rm e}^2 L \times \left(2\int_{\rm r_\perp}^{\sqrt{({\rm L}/2)^2 + {\rm r}_\perp^2}} \frac{C_{\rm B_z}(r) r}{\sqrt{r^2 - r_\perp^2}} dr\right). \tag{B.11}$$

This relation indicates a deep connection between the magnetic field and rotation measure power spectra. To better understand this relation an explicit form of these auto-correlation functions has to be found.

B.2.1.1 B_z auto-correlation function

The auto-correlation function along $\hat{\mathbf{k}}_z$ of the component of the magnetic field component B_z is

$$C_{B_z}(r) = \int_{V_k} |\tilde{B}_z|^2(k_x, k_y, k_z) e^{-i\mathbf{k}\cdot\mathbf{r}} dk_x dk_y dk_z \tag{B.12}$$

where $\tilde{B}_z$ is the Fourier transform of the field along $\hat{\mathbf{k}}_z$.

The magnetic field is a solenoidal vector field. Therefore, it can be expressed in Fourier space via the cross product of the wave-number $\mathbf{k}$ and the Fourier transform of the vector potential $\tilde{\mathbf{A}}$ (Eq. 5.4). By indicating the versors in the Fourier space as $\hat{\mathbf{k}}_\mathbf{x}$, $\hat{\mathbf{k}}_\mathbf{y}$, $\hat{\mathbf{k}}_\mathbf{z}$, the power spectrum along the $\hat{\mathbf{k}}_\mathbf{z}$ direction of the magnetic field component B_z will be:

$$|\tilde{B}_z|^2 = |(i\mathbf{k} \times \tilde{\mathbf{A}}(\mathbf{k})) \cdot \hat{\mathbf{k}}_z|^2 \tag{B.13}$$

where $\tilde{\mathbf{A}}(\mathbf{k})$ is isotropic. An equivalent characterization of this triple product is

$$\tilde{\mathbf{B}}_z(\mathbf{k}) = (i\mathbf{k} \times \tilde{\mathbf{A}}(\mathbf{k})) \cdot \hat{\mathbf{k}}_\mathbf{z} = (i\hat{\mathbf{k}}_z \times \mathbf{k}) \cdot \tilde{\mathbf{A}}(\mathbf{k}) \tag{B.14}$$

Because of the isotropy of the magnetic field we can consider a spherical coordinate reference system where the vector $\mathbf{r}$ in Eq. B.12 is along $\hat{\mathbf{k}}_z$. The vector $\hat{\mathbf{k}}_z \times \mathbf{k}$ is in the $\hat{\mathbf{k}}_\mathbf{x}\hat{\mathbf{k}}_\mathbf{y}$ plane, and $\tilde{\mathbf{A}}(\mathbf{k})$ can be written as the sum of a vector along $\hat{\mathbf{k}}_\mathbf{z}$ and a vector in the $\hat{\mathbf{k}}_x\hat{\mathbf{k}}_y$ plane. The only contribution to the scalar product is given by the component of $\tilde{\mathbf{A}}(\mathbf{k})$ in the $\hat{\mathbf{k}}_x\hat{\mathbf{k}}_y$ plane. For these reasons the B_z auto-correlation function becomes

$$\int_0^{2\pi}\int_0^{\pi}\int_0^{\infty} k^2|A_k|^2 \sin^2\theta \cos^2\phi e^{-ikr\cos\theta} k^2 \sin\theta d\theta d\phi dk. \tag{B.15}$$

At first we can carry out the integral in ϕ by parts

$$\int_0^{2\pi} \cos^2\phi d\phi = \left[\frac{\cos\phi \sin\phi}{2}\right]_0^{2\pi} + \frac{1}{2}\int_0^{2\pi} d\phi = \pi \tag{B.16}$$

and we obtain

$$C_{B_z}(r) = \pi \int_0^{\pi}\int_0^{\infty} k^2|A_k|^2 \sin^2\theta e^{-ikr\cos\theta} k^2 \sin\theta d\theta dk. \tag{B.17}$$

The second step is to carry out the integral in θ

$$\int_0^{\pi} \sin^3\theta e^{-ikr\cos\theta} d\theta. \tag{B.18}$$

By using the substitution $\cos\theta = x$

$$-\int_1^{-1} (1-x^2) e^{-ikxr} dx =$$

$$= -\int_1^{-1} e^{-ikxr} dx + \int_1^{-1} x^2 e^{-ikxr} dx =$$

$$= \frac{1}{ikr}(e^{ikr} - e^{-ikr}) - \left[\frac{1}{ikr}(e^{ikr} - e^{-ikr}) - \frac{2}{ikr}\int_1^{-1} xe^{-ikxr} dx\right] =$$

$$= \frac{2}{ikr}\left(\left[-\frac{1}{ikr}xe^{-ikxr}\right]_1^{-1} + \frac{1}{ikr}\int_1^{-1} e^{-ikxr}dx\right) =$$

$$= -\frac{2}{(kr)^2}(e^{-ikr} + e^{ikr}) + \frac{2}{i(kr)^3}(e^{ikr} - e^{-ikr}) =$$

$$= \frac{4}{(kr)^2}\left[\frac{\sin(kr)}{kr} - \cos(kr)\right] \tag{B.19}$$

our integral becomes

$$C_{B_z}(r) = 4\pi\int_0^\infty k^4|A_k|^2\frac{1}{(kr)^2}\left(\frac{\sin(kr)}{kr} - \cos(kr)\right)dk. \tag{B.20}$$

Finally, since $|A_k|^2k^2 = |B_k|^2$, it results

$$C_{B_z}(r) = 4\pi\int_0^\infty k^2|B_k|^2\frac{1}{(kr)^2}\left(\frac{\sin(kr)}{kr} - \cos(kr)\right)dk. \tag{B.21}$$

B.2.1.2 Rotation measure auto-correlation function

The rotation measure auto-correlation function is:

$$C_{RM}(r_\perp) = \int_{A_k}|RM_k|^2(k_x, k_y)e^{-i\mathbf{k}\cdot\mathbf{r}_\perp}dk. \tag{B.22}$$

Because of the isotropy, in polar coordinates we have:

$$C_{RM}(r_\perp) = \int_0^\infty\int_0^{2\pi}|RM_k|^2e^{-ikr_\perp\cos\theta}kdkd\theta. \tag{B.23}$$

Since

$$J_0(kr_\perp) = \frac{1}{2\pi}\int_0^{2\pi}e^{-ikr_\perp\cos\theta}d\theta \tag{B.24}$$

is the zero-order Bessel function (Abramowitz & Stegun 1970), our integral can be expressed as

$$C_{RM}(r_\perp) = 2\pi\int_0^\infty|RM_k|^2J_0(kr_\perp)kdk. \tag{B.25}$$

B.2.2 Proportionality of the magnetic field and rotation measure power spectrum

The auto-correlation function of the magnetic field along the line of sight and of the rotation measure are related by the Eq. B.11. By substituting to $C_{B_z}(r)$ and to $C_{RM}(r_\perp)$ the expressions given by the Eq. B.21 and Eq. B.25, respectively, we obtain

$$2\pi\int_0^\infty|RM_k|^2J_0(kr_\perp)kdk =$$

$$= 812^2n_e^2L4\pi\times2\int_0^\infty\int_{r_\perp}^{\sqrt{(L/2)^2+r_\perp^2}}\frac{k^2|B_k|^2}{(kr)^2}\frac{r}{\sqrt{r^2-r_\perp^2}}\left(\frac{\sin(kr)}{kr} - \cos(kr)\right)drdk. \tag{B.26}$$

The term that appears in the right side of the integral as a function of r is the spherical Bessel function $j_1(kr)$ that can be related to the Bessel function $J_{\frac{3}{2}}(kr)$ by (Oberhettinger 1972)

$$j_1(kr) = \frac{\sin(kr)}{(kr)^2} - \frac{\cos(kr)}{kr} = \sqrt{\frac{\pi}{2kr}} J_{\frac{3}{2}}(kr). \tag{B.27}$$

By using the Eq. B.27 we obtain:

$$\int_0^\infty |RM_k|^2 J_0(kr_\perp) k dk = 812^2 n_e^2 4L \sqrt{\frac{\pi}{2}} \int_0^\infty |B_k|^2 dk \int_{r_\perp}^{\sqrt{(L/2)^2 + r_\perp^2}} \frac{(kr)^{\frac{1}{2}}}{r\sqrt{r^2 - r_\perp^2}} J_{\frac{3}{2}}(kr) dr. \tag{B.28}$$

From Oberhettinger (1972)

$$\int_0^\infty \frac{(kr)^{\frac{1}{2}}}{r(r^2 - r_\perp^2)^{\frac{1}{2}}} J_{\frac{3}{2}}(kr) dr = \sqrt{\frac{\pi}{2}} \frac{J_1(kr_\perp)}{r_\perp} \tag{B.29}$$

therefore, in the limit $L \to \infty$, we find:

$$\int_0^\infty |RM_k|^2 J_0(kr_\perp) k dk = 812^2 n_e^2 2\pi L \int_0^\infty |B_k|^2 \frac{J_1(kr_\perp)}{r_\perp} dk \tag{B.30}$$

that implies

$$|RM_k|^2 = 812^2 n_e^2 2\pi L \frac{J_1(kr_\perp)}{J_0(kr_\perp) kr_\perp} |B_k|^2. \tag{B.31}$$

It means that the rotation measure power spectrum is proportional to the magnetic field power spectrum.

B.2.3 Structure function

As shown in the previous Section, the magnetic field and the rotation measure power spectra are proportional. Therefore the analysis of the rotation measure structure function can give important information about the magnetic field. In the following we will study how the rotation measure structure function varies as a function of the scale distance $r_\perp$ in three different regimes:

- the asymptotic small-separation regime $r_\perp << 2\pi/k_{max}$;
- the intermediate-separation regime $2\pi/k_{max} << r_\perp << 2\pi/k_{min}$;
- the asymptotic large-separation regime $r_\perp >> 2\pi/k_{min}$.

B.2.3.1 Asymptotic small-separation regime

In the small-separation regime the scale distance is smaller than the minimum scale of fluctuation $r_\perp << \Lambda_{min} < \Lambda_{max}$. If the approximation valid in the limit $x << \sqrt{\alpha + 1}$

$$J_\alpha(x) \approx \frac{1}{\Gamma(\alpha + 1)} \left(\frac{x}{2}\right)^\alpha \tag{B.32}$$

is used, the proportionality relation between the rotation measure and magnetic field power spectra becomes:

$$|RM_k|^2 = 812^2 n_e^2 \pi L |B_k|^2. \tag{B.33}$$

Consequently, for a power law magnetic field power spectrum (see Eq. 5.5) the rotation measure auto-correlation function (Eq. B.25) is

$$C_{\rm RM}(r_\perp) = 812^2 n_{\rm e}^2 2\pi^2 LC \int_{k_{\rm min}}^{k_{\rm max}} J_0(kr_\perp) k^{-n+1} dk \tag{B.34}$$

that for $kr_\perp = 0$ becomes

$$C_{\rm RM}(0) = 812^2 n_{\rm e}^2 2\pi^2 LC \int_{k_{\rm min}}^{k_{\rm max}} k^{-n+1} dk. \tag{B.35}$$

By combining these two expression according the Eq. 5.18

$$S_{\rm RM}(r_\perp) = 4\pi^2 812^2 n_{\rm e}^2 LC \int_{k_{\rm min}}^{k_{\rm max}} [1 - J_0(kr_\perp)]\, k^{-n+1} dk. \tag{B.36}$$

By operating the substitution $x = kr_\perp$

$$S_{\rm RM}(r_\perp) = \frac{4\pi^2 812^2 n_{\rm e}^2 LC}{r_\perp^{-n+2}} \int_{\frac{2\pi}{\Lambda_{\rm max}} r_\perp}^{\frac{2\pi}{\Lambda_{\rm min}} r_\perp} [1 - J_0(x)]\, x^{-n+1} dx \tag{B.37}$$

that in the small-separation limit becomes

$$S_{\rm RM}(r_\perp) = 4\pi^2 812^2 n_{\rm e}^2 LC r_\perp^{n-2} \int_0^{\frac{2\pi r_\perp}{\Lambda_{\rm min}}} [1 - J_0(x)] x^{-n+1} dx, \tag{B.38}$$

this integral can be solved considering the behavior of $J_0(x)$ for small arguments. An equivalent expression of the zero-order Bessel function is (Abramowitz & Stegun 1970)

$$J_0(x) = \frac{1}{\pi} \int_0^\pi \cos(-x \sin u) du. \tag{B.39}$$

For small arguments the cosine function behaves as

$$\cos(-x \sin u) = 1 - \frac{(x \sin u)^2}{2} + o((x \sin u)^4). \tag{B.40}$$

By evaluating the zero-order Bessel function in this limit, we obtain

$$J_0(x) = \frac{1}{\pi} \int_0^\pi \left(1 - \frac{(x \sin u)^2}{2}\right) du = \frac{1}{\pi} \int_0^\pi du - \frac{1}{2\pi} \int_0^\pi (x \sin u)^2 du = 1 - \frac{x^2}{4}. \tag{B.41}$$

Some mathematical calculations can be done to get the final result

$$\begin{aligned}
S_{\rm RM}(r_\perp) = 812^2 n_{\rm e}^2 L 4\pi^2 r_\perp^{n-2} C \int_0^{\frac{2\pi r_\perp}{\Lambda_{\rm min}}} x^{-n+1} \left(1 - 1 + \frac{x^2}{4}\right) dx = \\
= 812^2 n_{\rm e}^2 L \pi^2 r_\perp^{n-2} C \int_0^{\frac{2\pi r_\perp}{\Lambda_{\rm min}}} x^{-n+3} dx = \\
= 812^2 n_{\rm e}^2 L \pi^2 r_\perp^{n-2} C \left[\frac{x^{4-n}}{4-n}\right]_0^{\frac{2\pi r_\perp}{\Lambda_{\rm min}}} = \\
= 812^2 n_{\rm e}^2 L \pi^2 r_\perp^{n-2} C \left(\frac{2\pi}{\Lambda_{\rm min}}\right)^{4-n} \frac{r_\perp^{4-n}}{4-n} = \\
= 812^2 n_{\rm e}^2 L \pi^2 C \left(\frac{2\pi}{\Lambda_{\rm min}}\right)^{4-n} \frac{1}{4-n} r_\perp^2.
\end{aligned}$$

This result does not depend on n, therefore on small scales the structure function behavior is proportional to $r_\perp^2$.

B.2.3.2 Intermediate-separation regime

In the intermediate-separation regime the scale distance is larger than the minimum scale of fluctuation but smaller than the maximum scale $\Lambda_{\rm min} << r_\perp << \Lambda_{\rm max}$. By considering Eq. 5.18, and Eq. B.35, we have:

$$S_{\rm RM}(r_\perp) = 8\pi^2 812^2 n_{\rm e}^2 LC \int_{k_{\rm min}}^{k_{\rm max}} \left(\frac{1}{2} - \frac{J_1(kr_\perp)}{kr_\perp}\right) k^{-n+1} dk. \tag{B.42}$$

By substituting $x = kr_\perp$ and considering the approximation $r_\perp << \Lambda_{\rm max}$ and $r_\perp >> \Lambda_{\rm min}$, the integral becomes

$$S_{\rm RM}(r_\perp) = 8\pi^2 812^2 n_{\rm e}^2 LC r_\perp^{n-2} \int_0^\infty \left(\frac{1}{2} - \frac{J_1(x)}{x}\right) x^{-n+1} dx. \tag{B.43}$$

The integral is the sum of two terms. The first can be solved with the residue theorem:

$$\frac{1}{2}\int_0^\infty x^{-n+1} dx = 0. \tag{B.44}$$

Concerning the second one, we can note that it does not depend on $r_\perp$, resulting in a rotation measure structure function depending on $r_\perp^{n-2}$.

B.2.3.3 Asymptotic large-separation regime

In the large-separation regime the scale distance is larger than the maximum scale of fluctuation $r_\perp >> \Lambda_{\rm max} > \Lambda_{\rm min}$. If the approximation valid in the limit $x >> |\alpha^2 - 1/4|$

$$J_\alpha(x) = \sqrt{\frac{2}{\pi x}} \cos\left(x - \frac{\alpha\pi}{2} - \frac{\pi}{4}\right) \tag{B.45}$$

is used, the proportionality relation between the rotation measure and magnetic field power spectra becomes:

$$|RM_{\rm k}| = 812^2 n_{\rm e}^2 2\pi L \frac{\sin(kr_\perp) - \cos(kr_\perp)}{J_0(kr_\perp)\sqrt{\pi(kr_\perp)^3}}. \tag{B.46}$$

The rotation measure auto-correlation function becomes:

$$C_{\rm RM}(r_\perp) = 812^2 n_{\rm e}^2 4\pi^2 LC \int_{k_{\rm min}}^{k_{\rm max}} \frac{\sin(kr_\perp) - \cos(kr_\perp)}{\sqrt{\pi(kr_\perp)^3}} k^{-n+1} dk. \tag{B.47}$$

By operating the substitution $x = kr_\perp$ and in the limit $r_\perp >> \Lambda_{\rm max}$, it results

$$C_{\rm RM}(r_\perp) = 812^2 n_{\rm e}^2 \frac{4\pi^2 LC}{\sqrt{\pi}} r_\perp^{n-2} \int_{\frac{2\pi}{\Lambda_{\rm max}} r_\perp}^\infty [\sin(x) - \cos(x)] x^{-n-\frac{1}{2}} dk. \tag{B.48}$$

If $n > 0$, the expression $[\sin(x) - \cos(x)]/x^{n+1/2} \to 0$ in our limit $x \to \infty$, therefore this integral gives a null contribution. Moreover, when $r_\perp >> \Lambda_{\rm max}$ there is no large scale scale RM contribution, that is $\langle RM \rangle = 0$. Therefore

$$C_{\rm RM}(0) = 812^2 n_{\rm e}^2 2\pi^2 LC \int_{k_{\rm min}}^{k_{\rm max}} k^{-n+1} dk = \sigma_{\rm RM}^2. \tag{B.49}$$

Therefore, by considering Eq. 5.18, the rotation measure structure function in this limit is:

$$S_{\rm RM} \simeq 2\sigma^2_{\rm RM}. \tag{B.50}$$

Overall, in the asymptotic small-separation regime, $r_\perp \ll 2\pi/k_{\rm max}$, the structure function increases as $S_{\rm RM}(r_\perp) \propto r_\perp^2$. In the intermediate regime, where $2\pi/k_{\rm max} \ll r_\perp \ll 2\pi/k_{\rm min}$, $S_{\rm RM}(r_\perp) \propto r_\perp^{n-2}$. Finally for $r_\perp \gg 2\pi/k_{\rm min}$, the structure function saturates to the constant value of $S_{\rm RM} \simeq 2\sigma^2_{\rm RM}$.

B.2.4 Auto-correlation length

The magnetic field and the rotation measure auto-correlation lengths can be derived from their auto-correlation functions.

B.2.4.1 Magnetic field auto-correlation length

Under our assumptions it holds $\langle RM\rangle$=0 and $\langle B\rangle$=0. The total power is given by the auto-correlation function of the magnetic field for a null displacement (r=0). To evaluate the Eq. B.21 in the limit $r \to 0$, we can consider that

$$\sin(kr) \simeq kr - \frac{(kr)^3}{6} \qquad\qquad \cos(kr) \simeq 1 - \frac{(kr)^2}{2}.$$

By combining them as in the Eq. B.21, we get

$$\frac{1}{(kr)^2}\left[\frac{\sin(kr)}{kr} - \cos(kr)\right] = \frac{1}{3} \tag{B.51}$$

and therefore

$$C_{\rm B_z}(0) = \frac{4\pi}{3}\int_0^\infty |B_{\rm k}|^2 k^2 dk = \sigma^2_{\rm B_z}. \tag{B.52}$$

Moreover, in the limit $r_\perp \to 0$, the Eq. B.11 becomes

$$\sigma^2_{\rm RM} = 812^2 n_{\rm e}^2 L \times 2 \int_0^{\rm L/2} C_{\rm B_z}(r) dr. \tag{B.53}$$

By using Eq. B.21, it is

$$\sigma^2_{\rm RM} = 812^2 n_{\rm e}^2 L \times 2 \times 4\pi \int_0^\infty \int_0^{\rm L/2} |B_{\rm k}|^2 \frac{1}{(kr)^2}\left(\frac{\sin(kr)}{kr} - \cos(kr)\right) k^2 dr dk. \tag{B.54}$$

The term that appears in the integral as a function of r can expressed as the Bessel function $J_{\frac{3}{2}}(kr)$ (see Eq. B.27). Therefore, first of all we have to evaluate the integral in r:

$$\int_0^{\rm Lk/2} \frac{1}{(kr)^{\frac{3}{2}}} J_{\frac{3}{2}}(kr) d(kr). \tag{B.55}$$

We can take advantage of the known integral (Oberhettinger 1972)

$$\int_0^\infty \frac{1}{(kr)^{\frac{3}{2}}} J_{\frac{3}{2}}(kr) d(kr) = \frac{2^{-\frac{3}{2}}\pi^{\frac{1}{2}}}{\Gamma(2)}. \tag{B.56}$$

Our integral results in this one in the approximation $Lk/2 \rightarrow \infty$, that is $L >> \Lambda_{max}$, condition verify by our assumptions. Therefore we obtain

$$\sigma^2_{RM} = 812^2 n_e^2 L 2\pi^2 \int_0^\infty |B_k|^2 k dk. \tag{B.57}$$

By multiplying each side by the total power $\sigma^2_{B_z}$ (Eq. B.52), it results

$$\sigma^2_{RM} = 812^2 n_e^2 L \frac{2\pi^2 \int_0^\infty |B_k|^2 k dk}{\frac{4\pi}{3} \int_0^\infty |B_k|^2 k^2 dk} \sigma^2_{B_z} \tag{B.58}$$

that is the same derived by Felten (1996) for a constant n_e and where

$$\frac{3\pi}{2} \frac{\int_0^\infty |B_k|^2 k dk}{\int_0^\infty |B_k|^2 k^2 dk} = \Lambda_B \tag{B.59}$$

is the auto-correlation length. The magnetic field auto-correlation length can be thought as the ratio between the area drawn by the magnetic field auto-correlation function and the value of the magnetic field auto-correlation function in $r = 0$.

B.2.4.2 Rotation measure auto-correlation length

Similarly we can define the rotation measure auto-correlation length as the ratio between the area drawn by the rotation measure auto-correlation function and the value of the rotation measure auto-correlation function in $r_\perp = 0$

$$\Lambda_{RM} = \frac{\int_{-L/2}^{L/2} C_{RM}(r_\perp) dr_\perp}{C_{RM}(0)}. \tag{B.60}$$

Since the function is cylindrically symmetric, we can write

$$\Lambda_{RM} = \frac{2 \int_0^{L/2} C_{RM}(r_\perp) dr_\perp}{C_{RM}(0)}. \tag{B.61}$$

By considering Eq. B.25, we have

$$\Lambda_{RM} = \frac{2 \times 2\pi \int_0^{L/2} \int_0^\infty |RM_k|^2 J_0(kr_\perp) k dk dr_\perp}{C_{RM}(0)}. \tag{B.62}$$

Then we have to evaluate

$$\frac{1}{k} \int_0^{Lk/2} J_0(kr_\perp) d(kr_\perp) \tag{B.63}$$

where to our aims we can assume $Lk/2 \rightarrow \infty$, since $L >> \Lambda_{max}$. In order to do it, we can use the known integral (Oberhettinger 1972)

$$\int_0^\infty J_0(kr_\perp) d(kr_\perp) = 1. \tag{B.64}$$

By noting that

$$C_{RM}(0) = 2\pi \int_{R_k} |RM_k|^2 k dk, \tag{B.65}$$

the rotation measure auto-correlation length becomes

$$\Lambda_{\rm RM} = \frac{2 \times 2\pi \int_0^\infty |RM_{\rm k}|^2 k \frac{1}{k} dk}{2\pi \int_0^\infty |RM_{\rm k}|^2 k dk} \tag{B.66}$$

that is

$$\Lambda_{\rm RM} = 2 \frac{\int_0^\infty |RM_{\rm k}|^2 dk}{\int_0^\infty |RM_{\rm k}|^2 k dk}. \tag{B.67}$$

Bibliography

Abramowitz M., Stegun I.A., 1970, Handbook of mathematical functions : with formulas, graphs, and mathematical tables

Aharonian F., Akhperjanian A.G., Anton G., et al., 2009a, A&A 495, 27

Aharonian F., Akhperjanian A.G., Anton G., et al., 2009b, A&A 502, 437

Aleksić J., Antonelli L.A., Antoranz P., et al., 2010, ApJ 710, 634

Allen S.W., 2000, MNRAS 315, 269

Allen S.W., Taylor G.B., Nulsen P.E.J., et al., 2001, MNRAS 324, 842

Andersson K.E., Madejski G.M., 2004, ApJ 607, 190

Bacchi M., Feretti L., Giovannini G., Govoni F., 2003, A&A 400, 465

Bagchi J., Enßlin T.A., Miniati F., et al., 2002, New Astronomy 7, 249

Bagchi J., Pislar V., Lima Neto G.B., 1998, MNRAS 296, L23

Bagchi J., Sirothia S.K., Werner N., et al., 2011, ApJL 736, L8

Baldi A., Ettori S., Mazzotta P., et al., 2007, ApJ 666, 835

Ballarati B., Feretti L., Ficarra A., et al., 1981, A&A 100, 323

Balogh M.L., Schade D., Morris S.L., et al., 1998, ApJL 504, L75

Bartelmann M., Schneider P., 2001, Physics Reports 340, 291

Beck R., Krause M., 2005, Astronomische Nachrichten 326, 414

Becker R.H., White R.L., Helfand D.J., 1995, ApJ 450, 559

Bekki K., Couch W.J., 2003, ApJL 596, L13

Berezinsky V.S., Blasi P., Ptuskin V.S., 1997, ApJ 487, 529

Biermann L., 1950, Z. Naturforsh. Tiel A5, 65

Bîrzan L., Rafferty D.A., McNamara B.R., et al., 2004, ApJ 607, 800

Blasi P., 2004, Journal of Korean Astronomical Society 37, 483

Blasi P., Colafrancesco S., 1999, Astroparticle Physics 12, 169

Bliton M., Rizza E., Burns J.O., et al., 1998, MNRAS 301, 609

Blumenthal G.R., Gould R.J., 1970, Reviews of Modern Physics 42, 237

Boehringer H., Voges W., Fabian A.C., et al., 1993, MNRAS 264, L25

Böhringer H., Schuecker P., Guzzo L., et al., 2004, A&A 425, 367

Böhringer H., Voges W., Huchra J.P., et al., 2000, ApJS 129, 435

Bonafede A., Feretti L., Giovannini G., et al., 2009a, A&A 503, 707

Bonafede A., Feretti L., Murgia M., et al., 2010, A&A 513, A30

Bonafede A., Giovannini G., Feretti L., et al., 2009b, A&A 494, 429

Bonafede A., Govoni F., Feretti L., et al., 2011, A&A 530, A24

Branduardi-Raymont G., Fabricant D., Feigelson E., et al., 1981, ApJ 248, 55

Broadhurst T., Benítez N., Coe D., et al., 2005a, ApJ 621, 53

Broadhurst T., Takada M., Umetsu K., et al., 2005b, ApJL 619, L143

Brown S., Duesterhoeft J., Rudnick L., 2011, ApJL 727, L25

Brown S., Rudnick L., 2011, MNRAS 412, 2

Brunetti G., 2004, Journal of Korean Astronomical Society 37, 493

Brunetti G., 2009, A&A 508, 599

Brunetti G., 2011, Memorie della Societa Astronomica Italiana 82, 515

Brunetti G., Blasi P., 2005, MNRAS 363, 1173

Brunetti G., Blasi P., Cassano R., Gabici S., 2004, MNRAS 350, 1174

Brunetti G., Lazarian A., 2007, MNRAS 378, 245

Brunetti G., Lazarian A., 2011a, MNRAS 410, 127

Brunetti G., Lazarian A., 2011b, MNRAS 412, 817

Brunetti G., Setti G., Comastri A., 1997, A&A 325, 898

Buote D.A., 2001, ApJL 553, L15

Buote D.A., 2002, In: L. Feretti, I. M. Gioia, & G. Giovannini (ed.) Merging Processes in Galaxy Clusters, Vol. 272. Astrophysics and Space Science Library, p.79

Burn B.J., 1966, MNRAS 133, 67

Burns J.O., 1990, AJ 99, 14

Burns J.O., Hallman E.J., Gantner B., et al., 2008, ApJ 675, 1125

Burns J.O., Schwendeman E., White R.A., 1983, ApJ 271, 575

Burns J.O., Sulkanen M.E., Gisler G.R., Perley R.A., 1992, ApJL 388, L49

Carilli C.L., Taylor G.B., 2002, ARA&A 40, 319

Cassano R., 2009, In: D. J. Saikia, D. A. Green, Y. Gupta, & T. Venturi (ed.) The Low-Frequency Radio Universe, Vol. 407. Astronomical Society of the Pacific Conference Series, p.223

Cassano R., Brunetti G., Setti G., 2006, MNRAS 369, 1577

Cassano R., Brunetti G., Setti G., et al., 2007, MNRAS 378, 1565

Cassano R., Brunetti G., Venturi T., et al., 2008, A&A 480, 687

Cassano R., Ettori S., Giacintucci S., et al., 2010, ApJL 721, L82

Cavaliere A., Fusco-Femiano R., 1976, A&A 49, 137

Chen Y., Reiprich T.H., Böhringer H., et al., 2007, A&A 466, 805

Clarke T.E., 2004, Journal of Korean Astronomical Society 37, 337

Clarke T.E., Ensslin T.A., 2006, AJ 131, 2900

Clarke T.E., Kronberg P.P., Böhringer H., 2001, ApJL 547, L111

Clowe D., Schneider P., 2001, A&A 379, 384

Coe D., Benítez N., Broadhurst T., Moustakas L.A., 2010, ApJ 723, 1678

Colafrancesco S., 1999, In: H. Boehringer, L. Feretti, & P. Schuecker (ed.) Diffuse Thermal and Relativistic Plasma in Galaxy Clusters., p.269

Colgate S.A., Li H., 2000, In: P. C. H. Martens, S. Tsuruta, & M. A. Weber (ed.) Highly Energetic Physical Processes and Mechanisms for Emission from Astrophysical Plasmas, Vol. 195. IAU Symposium, p. 255

Cordey R.A., 1987, MNRAS 227, 695

Crawford C.S., Allen S.W., Ebeling H., et al., 1999, MNRAS 306, 857

Dallacasa D., Brunetti G., Giacintucci S., et al., 2009, ApJ 699, 1288

David L.P., Nulsen P.E.J., McNamara B.R., et al., 2000, In: AAS/High Energy Astrophysics Division #5, Vol. 32. Bulletin of the American Astronomical Society, p. 1208

David L.P., Slyz A., Jones C., et al., 1993, ApJ 412, 479

De Young D.S., 1972, ApJL 173, L7

Deiss B.M., Reich W., Lesch H., Wielebinski R., 1997, A&A 321, 55

Dennison B., 1980, ApJL 239, L93

Dolag K., Bartelmann M., Lesch H., 1999, A&A 348, 351

Dolag K., Bartelmann M., Lesch H., 2002, A&A 387, 383

Dolag K., Bykov A.M., Diaferio A., 2008, Space Science Reviews 134, 311

Dolag K., Enßlin T.A., 2000, A&A 362, 151

Dolag K., Evrard A., Bartelmann M., 2001a, A&A 369, 36

Dolag K., Grasso D., Springel V., Tkachev I., 2005, Journal of Cosmology and Astroparticle Physics 1, 9

Dolag K., Schindler S., Govoni F., Feretti L., 2001b, A&A 378, 777

Donnert J., Dolag K., Brunetti G., et al., 2010a, MNRAS 401, 47

Donnert J., Dolag K., Cassano R., Brunetti G., 2010b, MNRAS 407, 1565

Donnert J., Dolag K., Lesch H., Müller E., 2009, MNRAS 392, 1008

Dressler A., Oemler, Jr. A., Couch W.J., et al., 1997, ApJ 490, 577

Dunn R.J.H., Fabian A.C., Taylor G.B., 2005, MNRAS 364, 1343

Ebeling H., Barrett E., Donovan D., et al., 2007, ApJL 661, L33

Ebeling H., Edge A.C., Bohringer H., et al., 1998, MNRAS 301, 881

Ebeling H., Edge A.C., Mantz A., et al., 2010, MNRAS 407, 83

Ebeling H., Mullis C.R., Tully R.B., 2002, ApJ 580, 774

Ebeling H., Voges W., Bohringer H., et al., 1996, MNRAS 281, 799

Eilek J.A., Owen F.N., 2002, ApJ 567, 202

Enßlin T., Pfrommer C., Miniati F., Subramanian K., 2011, A&A 527, A99

Ensslin T.A., Biermann P.L., Klein U., Kohle S., 1998, A&A 332, 395

Ensslin T.A., Biermann P.L., Kronberg P.P., Wu X.P., 1997, ApJ 477, 560

Enßlin T.A., Gopal-Krishna 2001, A&A 366, 26

Enßlin T.A., Vogt C., 2003, A&A 401, 835

Fabian A.C., 1994, ARA&A 32, 277

Fabian A.C., Hu E.M., Cowie L.L., Grindlay J., 1981, ApJ 248, 47

Fabian A.C., Sanders J.S., Ettori S., et al., 2000, MNRAS 318, L65

Fanaroff B.L., Riley J.M., 1974, MNRAS 167, 31P

Fanti C., Fanti R., de Ruiter H.R., Parma P., 1986, A&AS 65, 145

Feigelson E.D., Laurent-Muehleisen S.A., Kollgaard R.I., Fomalont E.B., 1995, ApJL 449, L149

Felten J.E., 1996, In: V. Trimble & A. Reisenegger (ed.) Clusters, Lensing, and the Future of the Universe, Vol. 88. Astronomical Society of the Pacific Conference Series, p.271

Feretti L., 1999, In: H. Boehringer, L. Feretti, & P. Schuecker (ed.) Diffuse Thermal and Relativistic Plasma in Galaxy Clusters., p.3

Feretti L., 2002, In: A. Pramesh Rao, G. Swarup, & Gopal-Krishna (ed.) The Universe at Low Radio Frequencies, Vol. 199. IAU Symposium, p. 133

Feretti L., 2003, ArXiv Astrophysics e-prints, arXiv:astro-ph/0301576

Feretti L., Bacchi M., Slee O.B., et al., 2006, MNRAS 368, 544

Feretti L., Burigana C., Enßlin T.A., 2004a, New Astronomy Reviews 48, 1137

Feretti L., Comoretto G., Giovannini G., et al., 1993, ApJ 408, 446

Feretti L., Dallacasa D., Giovannini G., Tagliani A., 1995, A&A 302, 680

Feretti L., Fusco-Femiano R., Giovannini G., Govoni F., 2001, A&A 373, 106

Feretti L., Giovannini G., 2008, In: M. Plionis, O. López-Cruz, & D. Hughes (ed.) A Pan-Chromatic View of Clusters of Galaxies and the Large-Scale Structure, Vol. 740. Lecture Notes in Physics, Berlin Springer Verlag, p. 143

Feretti L., Giovannini G., Bohringer H., 1997, New Astronomy 2, 501

Feretti L., Orrù E., Brunetti G., et al., 2004b, A&A 423, 111

Feretti L., Schuecker P., Böhringer H., et al., 2005, A&A 444, 157

Ferrari C., Arnaud M., Ettori S., et al., 2006, A&A 446, 417

Ferrari C., Govoni F., Schindler S., et al., 2008, Space Science Reviews 134, 93

Ferrari C., Intema H.T., Orrù E., et al., 2011, A&A 534, L12

Forman W., Kellogg E., Gursky H., et al., 1972, ApJ 178, 309

Furlanetto S.R., Loeb A., 2001, ApJ 556, 619

Gabici S., Blasi P., 2003, ApJ 583, 695

Gaetz T.J., 1989, ApJ 345, 666

Ge J., Owen F.N., 1994, AJ 108, 1523

Gentile G., Rodríguez C., Taylor G.B., et al., 2007, ApJ 659, 225

Giacintucci S., Dallacasa D., Venturi T., et al., 2011, A&A 534, A57

Giacintucci S., Venturi T., Brunetti G., et al., 2005, A&A 440, 867

Giacintucci S., Venturi T., Brunetti G., et al., 2009, A&A 505, 45

Giacintucci S., Vrtilek J.M., Murgia M., et al., 2008, ApJ 682, 186

Giovannini G., Bonafede A., Feretti L., et al., 2010, A&A 511, L5

Giovannini G., Bonafede A., Feretti L., et al., 2009, A&A 507, 1257

Giovannini G., Cotton W.D., Feretti L., et al., 1998, ApJ 493, 632

Giovannini G., Cotton W.D., Feretti L., et al., 2001, ApJ 552, 508

Giovannini G., Feretti L., 2000, New Astronomy 5, 335

Giovannini G., Feretti L., 2002, In: L. Feretti, I. M. Gioia, & G. Giovannini (ed.) Merging Processes in Galaxy Clusters, Vol. 272. Astrophysics and Space Science Library, p.197

Giovannini G., Feretti L., 2004, Journal of Korean Astronomical Society 37, 323

Giovannini G., Feretti L., Girardi M., et al., 2011, A&A 530, L5

Giovannini G., Feretti L., Venturi T., et al., 1993, ApJ 406, 399

Giovannini G., Tordi M., Feretti L., 1999, New Astronomy 4, 141

Girardi M., Biviano A., 2002, In: L. Feretti, I. M. Gioia, & G. Giovannini (ed.) Merging Processes in Galaxy Clusters, Vol. 272. Astrophysics and Space Science Library, p.39

Girardi M., Boschin W., Barrena R., 2006, A&A 455, 45

Girardi M., Fadda D., Escalera E., et al., 1997, ApJ 490, 56

Gitti M., Brunetti G., Feretti L., Setti G., 2004a, A&A 417, 1

Gitti M., Brunetti G., Setti G., Feretti L., 2004b, In: T. Reiprich, J. Kempner, & N. Soker (ed.) The Riddle of Cooling Flows in Galaxies and Clusters of galaxies., p. 35

Gitti M., Ferrari C., Domainko W., et al., 2007a, A&A 470, L25

Gitti M., Piffaretti R., Schindler S., 2007b, A&A 472, 383

Gómez P.L., Hughes J.P., Birkinshaw M., 2000, ApJ 540, 726

Gomez P.L., Pinkney J., Burns J.O., et al., 1997, ApJ 474, 580

Govoni F., Dolag K., Murgia M., et al., 2010, A&A 522, A105

Govoni F., Enßlin T.A., Feretti L., Giovannini G., 2001a, A&A 369, 441

Govoni F., Feretti L., 2004, International Journal of Modern Physics D 13, 1549

Govoni F., Feretti L., Giovannini G., et al., 2001b, A&A 376, 803

Govoni F., Markevitch M., Vikhlinin A., et al., 2004, ApJ 605, 695

Govoni F., Murgia M., Feretti L., et al., 2005, A&A 430, L5

Govoni F., Murgia M., Feretti L., et al., 2006, A&A 460, 425

Govoni F., Murgia M., Giovannini G., et al., 2011, A&A 529, A69

Govoni F., Murgia M., Markevitch M., et al., 2009, A&A 499, 371

Govoni F., Taylor G.B., Dallacasa D., et al., 2001c, A&A 379, 807

Grasso D., Rubinstein H.R., 2001, Physics Reports 348, 163

Guidetti D., Murgia M., Govoni F., et al., 2008, A&A 483, 699

Guo F., Mathews W.G., 2011, ApJ 728, 121

Harris D.E., Grindlay J.E., 1979, MNRAS 188, 25

Harris D.E., Stern C.P., Willis A.G., Dewdney P.E., 1993, AJ 105, 769

Hoeft M., Brüggen M., 2007, MNRAS 375, 77

Hughes J.P., Birkinshaw M., 1994, In: K. Sato (ed.) Evolution of the Universe and its Observational Quest., p.455

Jeltema T.E., Canizares C.R., Bautz M.W., Buote D.A., 2005, ApJ 624, 606

Johnstone R.M., Allen S.W., Fabian A.C., Sanders J.S., 2002, MNRAS 336, 299

Jones C., Forman W., 1984, ApJ 276, 38

Jones C., Forman W., Vikhlinin A., et al., 2002, ApJL 567, L115

Jones M., Saunders R., 1996, In: H. U. Zimmermann, J. Trümper, & H. Yorke (ed.) Roentgen-strahlung from the Universe., p.553

Kapferer W., Ferrari C., Domainko W., et al., 2006, A&A 447, 827

Kawahara H., Suto Y., Kitayama T., et al., 2007, ApJ 659, 257

Kawano N., Ohto A., Fukazawa Y., 2003, *PASJ*55, 585

Kellogg E., Gursky H., Tananbaum H., et al., 1972, ApJL 174, L65

Kempner J.C., Blanton E.L., Clarke T.E., et al., 2004, In: T. Reiprich, J. Kempner, & N. Soker (ed.) The Riddle of Cooling Flows in Galaxies and Clusters of galaxies., p. 335

Keshet U., 2010, ArXiv e-prints

Keshet U., Loeb A., 2010, ApJ 722, 737

Kim K.T., Kronberg P.P., Dewdney P.E., Landecker T.L., 1990, ApJ 355, 29

Kim K.T., Tribble P.C., Kronberg P.P., 1991, ApJ 379, 80

Klein U., Wielebinski R., Beck R., 1984, A&A 135, 213

Kolokotronis V., Basilakos S., Plionis M., Georgantopoulos I., 2001, MNRAS 320, 49

Kotov O., Vikhlinin A., 2005, ApJ 633, 781

Kronberg P.P., 2002, Physics Today 55, 120000

Kronberg P.P., Dufton Q.W., Li H., Colgate S.A., 2001, ApJ 560, 178

Kronberg P.P., Lesch H., Hopp U., 1999, ApJ 511, 56

Kuchar P., Enßlin T.A., 2011, A&A 529, A13

Kulsrud R.M., Cen R., Ostriker J.P., Ryu D., 1997, ApJ 480, 481

Kunz M.W., Schekochihin A.A., Cowley S.C., et al., 2011, MNRAS 410, 2446

Kushnir D., Katz B., Waxman E., 2009, Journal of Cosmology and Astroparticle Physics 9, 24

Laing R.A., Bridle A.H., Parma P., Murgia M., 2008, MNRAS 391, 521

Laing R.A., Riley J.M., Longair M.S., 1983, MNRAS 204, 151

Lara L., Giovannini G., Cotton W.D., et al., 2002, New Astronomy Reviews 46, 89

Large M.I., Mathewson D.S., Haslam C.G.T., 1959, Nat 183, 1663

Lawler J.M., Dennison B., 1982, ApJ 252, 81

Leahy J.P., Perley R.A., 1991, AJ 102, 537

Ledlow M.J., Voges W., Owen F.N., Burns J.O., 2003, AJ 126, 2740

Lemze D., Barkana R., Broadhurst T.J., Rephaeli Y., 2008, MNRAS 386, 1092

Leonard A., King L.J., Goldberg D.M., 2011, MNRAS 413, 789

Liang H., 1999, In: H. Boehringer, L. Feretti, & P. Schuecker (ed.) Diffuse Thermal and Relativistic Plasma in Galaxy Clusters., p.33

Liang H., Hunstead R.W., Birkinshaw M., Andreani P., 2000, ApJ 544, 686

Limousin M., Richard J., Jullo E., et al., 2007, ApJ 668, 643

Loken C., Roettiger K., Burns J.O., Norman M., 1995, ApJ 445, 80

Longair M.S., 1981, High energy astrophysics

Lyutikov M., 2006, MNRAS 373, 73

Markevitch M., Forman W.R., Sarazin C.L., Vikhlinin A., 1998, ApJ 503, 77

Markevitch M., Gonzalez A.H., David L., et al., 2002, ApJL 567, L27

Markevitch M., Govoni F., Brunetti G., Jerius D., 2005, ApJ 627, 733

Markevitch M., Ponman T.J., Nulsen P.E.J., et al., 2000, ApJ 541, 542

Markevitch M., Vikhlinin A., 2001, ApJ 563, 95

Markevitch M., Vikhlinin A., 2007, Physics Reports 443, 1

Markovic K., Bridle S., Slosar A., Weller J., 2011, Journal of Cosmology and Astroparticle Physics 1, 22

Maughan B.J., Jones C., Forman W., Van Speybroeck L., 2008, ApJS 174, 117

McNamara B.R., Bîrzan L., Rafferty D.A., et al., 2008, In: T. A. Rector & D. S. De Young (ed.) Extragalactic Jets: Theory and Observation from Radio to Gamma Ray, Vol. 386. Astronomical Society of the Pacific Conference Series, p. 311

McNamara B.R., Nulsen P.E.J., 2007, ARA&A 45, 117

Meisenheimer K., Roser H.J., Hiltner P.R., et al., 1989, A&A 219, 63

Million E.T., Allen S.W., 2009, MNRAS 399, 1307

Miralda-Escude J., Babul A., 1995, ApJ 449, 18

Moffet A.T., Birkinshaw M., 1989, AJ 98, 1148

Mohr J.J., Mathiesen B., Evrard A.E., 1999, ApJ 517, 627

Murgia M., Eckert D., Govoni F., et al., 2010a, A&A 514, A76

Murgia M., Govoni F., Feretti L., Giovannini G., 2010b, A&A 509, A86

Murgia M., Govoni F., Feretti L., et al., 2004, A&A 424, 429

Murgia M., Govoni F., Markevitch M., et al., 2009, A&A 499, 679

Murgia M., Parma P., Mack K.H., et al., 2011, A&A 526, A148

Navarro J.F., Frenk C.S., White S.D.M., 1996, ApJ 462, 563

Neumann D.M., Arnaud M., 1999, A&A 348, 711

Neumann D.M., Arnaud M., 2001, A&A 373, L33

Oberhettinger F., 1972, Tables of Bessel Transforms

Orrù E., Murgia M., Feretti L., et al., 2007, A&A 467, 943

Owen F., Morrison G., Voges W., 1999, In: H. Boehringer, L. Feretti, & P. Schuecker (ed.) Diffuse Thermal and Relativistic Plasma in Galaxy Clusters., p.9

Pacholczyk A.G., 1970, Radio astrophysics. Nonthermal processes in galactic and extragalactic sources

Parma P., Murgia M., de Ruiter H.R., et al., 2007, A&A 470, 875

Parrish I.J., Quataert E., Sharma P., 2009, ApJ 703, 96

Parrish I.J., Quataert E., Sharma P., 2010, ApJL 712, L194

Pedlar A., Ghataure H.S., Davies R.D., et al., 1990, MNRAS 246, 477

Peng E.H., Andersson K., Bautz M.W., Garmire G.P., 2009, ApJ 701, 1283

Peres C.B., Fabian A.C., Edge A.C., et al., 1998, MNRAS 298, 416

Perley R.A., Taylor G.B., 1991, AJ 101, 1623

Petrosian V., 2001, ApJ 557, 560

Pfrommer C., 2008, MNRAS 385, 1242

Pfrommer C., Enßlin T.A., 2004a, A&A 413, 17

Pfrommer C., Enßlin T.A., 2004b, MNRAS 352, 76

Pfrommer C., Enßlin T.A., Miniati F., Subramanian K., 2011, Memorie della Societa Astronomica Italiana 82, 598

Pfrommer C., Enßlin T.A., Springel V., 2008, MNRAS 385, 1211

Pizzo R.F., de Bruyn A.G., Bernardi G., Brentjens M.A., 2011, A&A 525, A104

Press W.H., Flannery B.P., Teukolsky S.A., 1986, Numerical recipes. The art of scientific computing

Reid A.D., Hunstead R.W., Lemonon L., Pierre M.M., 1999, MNRAS 302, 571

Reimer O., Pohl M., Sreekumar P., Mattox J.R., 2003, ApJ 588, 155

Reiprich T.H., Böhringer H., 2002, ApJ 567, 716

Rengelink R.B., Tang Y., de Bruyn A.G., et al., 1997, A&AS 124, 259

Rephaeli Y., 2001, In: F. A. Aharonian & H. J. Völk (ed.) American Institute of Physics Conference Series, Vol. 558. American Institute of Physics Conference Series, p.427

Rephaeli Y., Gruber D.E., Rothschild R.E., 1987, ApJ 320, 139

Riemer-Sørensen S., Paraficz D., Ferreira D.D.M., et al., 2009, ApJ 693, 1570

Roettgering H.J.A., Wieringa M.H., Hunstead R.W., Ekers R.D., 1997, MNRAS 290, 577

Roettiger K., Burns J.O., Stone J.M., 1999a, ApJ 518, 603

Roettiger K., Stone J.M., Burns J.O., 1999b, ApJ 518, 594

Rossetti M., Eckert D., Cavalleri B.M., et al., 2011, A&A 532, A123

Roussel H., Sadat R., Blanchard A., 2000, A&A 361, 429

Roychowdhury S., Ruszkowski M., Nath B.B., Begelman M.C., 2004, ApJ 615, 681

Rudnick L., Blundell K.M., 2003, ApJ 588, 143

Rudnick L., Lemmerman J.A., 2009, ApJ 697, 1341

Russell H.R., van Weeren R.J., Edge A.C., et al., 2011, MNRAS 417, L1

Ruszkowski M., Oh S.P., 2010, ApJ 713, 1332

Ryu D., Kang H., Cho J., Das S., 2008, Science 320, 909

Sarazin C.L., 2002, In: L. Feretti, I. M. Gioia, & G. Giovannini (ed.) Merging Processes in Galaxy Clusters, Vol. 272. Astrophysics and Space Science Library, p.1

Sarazin C.L., Bahcall J.N., 1977, ApJS 34, 451

Schlickeiser R., Sievers A., Thiemann H., 1987, A&A 182, 21

Schuecker P., Finoguenov A., Miniati F., et al., 2004, A&A 426, 387

Sehgal N., Hughes J.P., Wittman D., et al., 2008, ApJ 673, 163

Sijbring D., 1993, Ph.D. thesis

Simard-Normandin M., Kronberg P.P., Button S., 1981, ApJS 45, 97

Skillman S.W., Hallman E.J., O'Shea B.W., et al., 2011, ApJ 735, 96

Skillman S.W., O'Shea B.W., Hallman E.J., et al., 2008, ApJ 689, 1063

Slee O.B., Roy A.L., Murgia M., et al., 2001, AJ 122, 1172

Smith R.J., Lucey J.R., Steel J., Hudson M.J., 1997, MNRAS 291, 461

Struble M.F., Rood H.J., 1999, ApJS 125, 35

Subramanian K., Shukurov A., Haugen N.E.L., 2006, MNRAS 366, 1437

Taylor A.R., Stil J.M., Sunstrum C., 2009, ApJ 702, 1230

Taylor G.B., Fabian A.C., Allen S.W., 2002, MNRAS 334, 769

Thierbach M., Klein U., Wielebinski R., 2003, A&A 397, 53

Tribble P.C., 1991a, MNRAS 250, 726

Tribble P.C., 1991b, MNRAS 253, 147

Tucker W.H., Rosner R., 1983, ApJ 267, 547

Tyson J.A., Wenk R.A., Valdes F., 1990, ApJL 349, L1

Umetsu K., Broadhurst T., 2008, ApJ 684, 177

Vacca V., Govoni F., Murgia M., et al., 2011, A&A 535, A82

Vacca V., Murgia M., Govoni F., et al., 2010, A&A 514, A71

Vacca V., Murgia M., Govoni F., et al., 2012, ArXiv e-prints, 1201.4119

van Weeren R.J., Brüggen M., Röttgering H.J.A., et al., 2011a, A&A 533, A35

van Weeren R.J., Hoeft M., Röttgering H.J.A., et al., 2011b, A&A 528, A38

van Weeren R.J., Röttgering H.J.A., Brüggen M., Cohen A., 2009, A&A 505, 991

van Weeren R.J., Röttgering H.J.A., Brüggen M., Hoeft M., 2010, Science 330, 347

Vazza F., Brunetti G., Gheller C., 2009, MNRAS 395, 1333

Vazza F., Brunetti G., Gheller C., et al., 2011, A&A 529, A17

Venturi T., Bardelli S., Dallacasa D., et al., 2003, A&A 402, 913

Venturi T., Giacintucci S., Brunetti G., et al., 2007, A&A 463, 937

Venturi T., Giacintucci S., Dallacasa D., et al., 2008, A&A 484, 327

Vestrand W.T., 1982, AJ 87, 1266

Vikhlinin A., Markevitch M., Murray S.S., 2001a, ApJ 551, 160

Vikhlinin A., Markevitch M., Murray S.S., 2001b, ApJL 549, L47

Vogt C., Enßlin T.A., 2003, A&A 412, 373

Völk H.J., Aharonian F.A., Breitschwerdt D., 1996, Space Science Reviews 75, 279

Völk H.J., Atoyan A.M., 2000, ApJ 541, 88

Widrow L.M., 2002, Reviews of Modern Physics 74, 775

Wu X.P., Xue Y.J., Fang L.Z., 1999, ApJ 524, 22

Xu H., Li H., Collins D.C., et al., 2009, ApJL 698, L14

Xu H., Li H., Collins D.C., et al., 2010, ApJ 725, 2152

Xu H., Li H., Collins D.C., et al., 2011, ApJ 739, 77

Zhang Y.Y., Böhringer H., Finoguenov A., et al., 2006, A&A 456, 55

Zhang Y.Y., Finoguenov A., Böhringer H., et al., 2008, A&A 482, 451

Zwicky F., 1937, ApJ 86, 217

Acknowledgements

I am extremely grateful to Dr. Federica Govoni and Dr. Matteo Murgia for all their precious teachings. They made this work possible and their constant help and presence during its achievement has been of fundamental importance. Moreover, they have been and still are for me a model to take from a professional but mainly human point of view. They deserve all my admiration. I am grateful as well to Prof. L. Burderi for his support and help during these three years.

I sincerely thank Chiara Ferrari for her precious contribution, all her suggestions have been extremely important for improving the presentation of this work. I am particularly grateful also to Prof. G. Giovannini and Dr. L. Feretti for their fundamental and continuous presence and help, to Prof. G. B. Taylor, Dr. R. A. Perley, Annalisa Bonafede, Emanuela Orrù, and Roberto Pizzo for useful discussions. In particular, I thank Prof. G. B. Taylor for supervising me during my stay in USA and Roberto Pizzo for supervising me during my stay in the Netherlands. A special thank to Dr. Andrea Tarchi for the suggestions about my future research activity and all his help during these years.

I acknowledge Prof. N. D′Amico and Dr. A. Possenti for the hospitality at the "Osservatorio Astronomico di Cagliari-INAF" where this work was done, the hospitality of the Netherlands Institute for Radio Astronomy (ASTRON) and of the Department of Physics and Astronomy at the University of New Mexico where fruitful collaborations have been developed and part of this work was done.

I am grateful to all the staff of the "Osservatorio Astronomico di Cagliari-INAF" for all the really enjoyable time spent together with a special thought for Sabrina and Noemi whose presence has been fundamental during these three years, and to all those that supported me from a logistical point of view. I am grateful to Antonella Fara and Riccardo Pittau for the assistance with the CyberSAR-OAC computer cluster. I am grateful as well to Antonio Poddighe for all the computer science support.

A hearty thank you to all the other friends, both the long-standing ones and those I met in the last years, in particular to Daniela, Claudia, Katia, Deborah, Ilaria and Cristina.

At last but not least I would like to thank my family that makes my days worth living and *you*, who are the best present of this PhD.

This research was supported by the INFN, "Università degli studi di Cagliari", PRIN - INAF2008 and PRIN - INAF2009. I acknowledge financial contribution from the agreement ASI - INAF I/009/10/0 and ASI - INAF I/088/06/0 -High Energy Astrophysics.

This work made use of results produced by the CyberSAR Project managed by the Consorzio COSMOLAB, a project cofunded by the Italian Ministry of University and Research (MIUR) within the Programma Operativo Nazionale 2000-2006 "Ricerca Scientifica, Sviluppo Tecnologico, Alta Formazione" per le Regioni Italiane dell' Obiettivo 1 (Campania, Calabria, Puglia, Basilicata, Sicilia, Sardegna) - Asse II, Misura II.2 "Società dell′Informazione", Azione a "Sistemi di calcolo e simulazione ad alte prestazioni". More information is available at http://www.cybersar.com.

The National Radio Astronomy Observatory (NRAO) is a facility of the National Science Foundation, operated under cooperative agreement by Associated Universities, Inc. Funding for

the SDSS and SDSS-II has been provided by the Alfred P. Sloan Foundation, the Participating Institutions, the National Science Foundation, the U.S. Department of Energy, the National Aeronautics and Space Administration, the Japanese Monbukagakusho, the Max Planck Society, and the Higher Education Funding Council for England. The SDSS Web Site is http://www.sdss.org/. This research made use of Montage, funded by the National Aeronautics and Space Administration's Earth Science Technology Office, Computational Technologies Project, under Cooperative Agreement Number NCC5-626 between NASA and the California Institute of Technology. The code is maintained by the NASA/IPAC Infrared Science Archive.